Precise Relative Positioning of Formation Flying Spacecraft using GPS

Precise Relative Positioning of Formation Flying Spacecraft using GPS

Remco Kroes

Publications on Geodesy 61

NCG Nederlandse Commissie voor Geodesie Netherlands Geodetic Commission

Delft, March 2006

Precise Relative Positioning of Formation Flying Spacecraft using GPS
Remco Kroes
Publications on Geodesy 61
ISBN-10: 90 6132 296 0
ISBN-13: 978 90 6132 296 2
ISSN: 0165 1706

Published by: NCG, Nederlandse Commissie voor Geodesie, Netherlands Geodetic Commission, Delft, The Netherlands.
Printed by: Optima Grafische Communicatie, Optima Graphic Communication, Rotterdam, The Netherlands.
Cover illustration: Illustration of the viewing geometry for relative spacecraft positioning using differenced GPS observations.

NCG, Nederlandse Commissie voor Geodesie, Netherlands Geodetic Commission
P.O. Box 5058, 2600 GB Delft, The Netherlands
T: +31 (0)15 278 28 19
F: +31 (0)15 278 17 75
E: info@ncg.knaw.nl
W: www.ncg.knaw.nl

The NCG, Nederlandse Commissie voor Geodesie, Netherlands Geodetic Commission is part of the Royal Netherlands Academy of Arts and Sciences (KNAW)

Contents

Acknowledgements **ix**

Important Acronyms **xi**

Summary **xiii**

Samenvatting (Summary in Dutch) **xv**

1 Introduction **1**
1.1 Spacecraft formation flying using GPS 2
1.2 Research objective and motivation 4
1.3 The CHAMP and GRACE satellite missions 6
1.4 Outline 8

2 GPS observations **9**
2.1 Observation types 9
2.1.1 Pseudorange 10
2.1.2 Carrier phase 11
2.2 Dual frequency observation model 12
2.3 Linear data combinations 14
2.3.1 Ionosphere free linear combination 14
2.3.2 Wide-lane and narrow-lane 14
2.3.3 Multipath combinations 15
2.4 Linearization for positioning 16
2.5 Relative positioning models 17
2.5.1 Single difference model 17
2.5.2 Double difference model 21
2.6 GPS data quality 23
2.6.1 Biases and correlations 23
2.6.2 Multipath and systematic effects 24
2.6.3 Measurement noise 31

3 Precise orbit determination **35**
3.1 GPS orbit and clock products . . . 36
3.2 Reference frame transformations . . . 39
3.3 Kinematic orbit determination . . . 40
3.4 Reduced dynamic orbit determination . . . 45
3.4.1 Dynamical modeling . . . 46
3.4.2 Empirical accelerations . . . 48
3.4.3 Batch LSQ . . . 49
3.4.4 Extended Kalman filter . . . 54
3.5 GHOST toolkit . . . 59
3.5.1 Processing scheme . . . 59
3.5.2 GPS data editing . . . 61
3.6 POD results . . . 63
3.6.1 Settings and input data . . . 63
3.6.2 Empirical accelerations . . . 67
3.6.3 Post-fit residuals . . . 68
3.6.4 Orbit comparisons . . . 70
3.6.5 SLR validation . . . 75
3.6.6 Conclusion . . . 78

4 Relative spacecraft positioning **79**
4.1 Integer ambiguity resolution . . . 80
4.1.1 Integer ambiguity estimation . . . 80
4.1.2 Integer ambiguity validation . . . 83
4.2 Proposed processing strategies . . . 87
4.2.1 Sequential kinematic filter . . . 89
4.2.2 Kinematic batch LSQ . . . 90
4.2.3 Reduced dynamic batch LSQ . . . 92
4.2.4 Extended Kalman filter . . . 94
4.3 Details of the extended Kalman filter . . . 95
4.4 Extended Kalman filter results . . . 104
4.4.1 Filter settings . . . 105
4.4.2 Empirical accelerations . . . 107
4.4.3 Ionospheric path delays . . . 109
4.4.4 GRACE K/Ka-Band Ranging System modeling . . . 110
4.4.5 KBR comparison of the GRACE POD solutions . . . 111
4.4.6 Float ambiguity solution . . . 113
4.4.7 Fixed ambiguity solution . . . 115
4.4.8 Relative position comparisons . . . 123
4.5 Some words on 131
4.5.1 ... the effects of higher systematic or multipath errors . . . 131
4.5.2 ... using the C/A code and carrier phase observations . . . 133
4.5.3 ... testing different ambiguity resolution approaches . . . 135

5 Conclusions and outlook **139**

A Integer Ambiguity Estimation **145**
A.1 Integer rounding 146
A.2 Integer bootstrapping 146
A.3 Integer Least-Squares 148
A.4 Optimized Integer Least Squares: The LAMBDA Method 151

B Lower boundary for the bootstrapping success rate **155**

Bibliography **157**

Curriculum Vitae **165**

Acknowledgements

I owe my gratitude to many people who helped me on all kinds of levels and with all kinds of issues during the coarse of my PhD research. Without them this dissertation would simply not be. First and foremost I would especially like to thank Oliver Montenbruck from the DLR, and Pieter Visser and Boudewijn Ambrosius from the TU Delft for their great guidance and supervision during the entire research and for the many fruitful discussions. In addition, Boudewijn Ambrosius and Pieter Visser are greatly acknowledged for allowing me to spent nearly one and a half years of my entire PhD research at two renomated foreign research institutions, the DLR German Space Operations Center in Oberpfaffenhofen, Germany, and the NASA Jet Propulsion Laboratory in Pasadena, CA. These visits really helped to shape the dissertation to what it is right now, and provided me with lots of inspiration. To this extent my deepest gratitude also goes to the host institutions for receiving me. At the DLR I would again like to thank Oliver Montenbruck for arranging both visits, from September through December 2002 and July through December 2004, and for the close cooperation and many discussions during the time of my stay. At JPL I would like to thank Yoaz Bar-Sever for all his efforts in arranging my six month visit, from September 2003 through February 2004, and for all his support during the time I was present. At JPL I would furthermore like to thank William Bertiger for the many discussions on my research topic, and Gerhard Kruizinga for also helping me with many non-work related issues during my stay.

I furthermore really enjoyed the many fruitful discussions with my colleagues Christian Tiberius, Peter Joosten and Sandra Verhagen on the topic of integer ambiguity resolution and relative positioning. Last but not least I want to thank all my colleagues at the Astrodynamics and Satellite Systems group. I really enjoyed working with them. In particular I would like to mention Jose van den IJssel who performed the SLR validation of the different orbits computed for this research, Marc Naije for his great (computer) support and Ernst Schrama for the many discussions and his interest in my work.

Delft, The Netherlands, November 2005
Remco Kroes

Important Acronyms

CHAMP	Challenging Mini Satellite Payload
CODE	Center for Orbit Determination Europe
DD	Double Difference
DEOS	Delft Institute for Earth Observation and Satellite Systems
EKF	Extended Kalman Filter
FAST	Filter for Adjustment of Satellite Trajectories
FRNS	Filter for Relative Navigation of Spacecraft
GHOST	GPS High Precision Orbit Determination Software Tools
GPS	Global Positioning System
GRACE	Gravity Recovery and Climate Experiment
ILS	Integer Least-Squares
JPL	Jet Propulsion Laboratory
LAMBDA	Least-squares AMBiguity Decorrelation Adjustment
LEO	Low Earth Orbiter/Orbiting
LSQ	Least-Squares
PDOP	Position Dilution Of Precision
POD	Precise Orbit Determination
PosFit	Position Fitting (of discrete SPPLEO positions)
RDOD	Reduced Dynamic Orbit Determination
S/C	Spacecraft
SD	Single Difference
SLR	Satellite Laser Ranging
SPP	Single Point Positioning
SPPLEO	Single Point Positioning for LEO spacecraft
TUM	Technical University Munich
UD	Undifferenced

Summary

Spacecraft formation flying is currently considered as a key technology for advanced space missions. Compared to large individual spacecraft, the distribution of sensor systems amongst multiple platforms offers improved flexibility and redundancy, shorter times to mission and the prospect of being more cost effective. Besides these advantages, satellite formations in low Earth orbit provide advanced science opportunities that cannot, or not easily, be realized with single spacecraft. One of the fundamental issues of spacecraft formation flying is the determination of the relative state (position and velocity) between the satellite vehicles within the formation. Knowledge of these relative states in (near) real-time is important for operational aspects. In addition, some of the scientific applications, such as high resolution interferometry, require an accurate post-facto knowledge of these states. The goal of this dissertation is therefore to develop, implement and test a method for high precise post-facto relative positioning of formation flying spacecraft, using GPS observation data. The need for such a methodology comes from scientific satellite formation flying missions that are currently being planned. A good example here is the Synthetic Aperture Radar (SAR) interferometry formation consisting of the TerraSAR-X and TanDEM-X satellites. The primary mission objective here requires the relative position to be known within a 2 mm precision (1-dimensional).

GPS receivers are often considered as the primary instruments for precise relative navigation in future satellite formation flying missions. As is commonly known, precise relative positioning between GPS receivers in geodetic networks is exercised on a routine basis. Furthermore, GPS receivers are already frequently used onboard satellites to perform all kinds of navigational tasks, are suitable for real-time applications and provide measurements with a 3-dimensional nature.

Previous studies carried out in this research area focussed on the real-time or operational aspects, and all used GPS data obtained from software or hardware-in-the-loop simulations. This dissertation clearly distinguishes itself due to the fact that the developed methodology has been tested using real-world GPS data from the GRACE mission, which in addition also provides a precise way to validate the obtained results by means of the GRACE K/Ka-Band Ranging System (KBR) observations.

One of the key aspects of any GPS positioning application is the quality of the

observation data used. To this extent an in-flight performance analysis of the used GRACE (and CHAMP) GPS data has been carried out. The results show that the GRACE GPS pseudorange observations, on the individual frequencies, are subject to systematic errors in the order of 10-15 cm. Furthermore, an assessment of the noise of both the GPS pseudorange and carrier phase data demonstrates that the noise of the GRACE B observation data is significantly lower.

When using GPS for precise relative spacecraft positioning, the trajectory or orbit of one of the spacecraft, serving as the reference, has to be known to the best possible extent. In order to facilitate this, a total of three precise orbit determination strategies, using undifferenced ionosphere free GPS pseudorange and carrier phase observations, have been implemented and tested. They comprise a kinematic and reduced dynamic batch LSQ estimation method, as well as an extended Kalman filter/smoother (EKF), that also form the conceptual basis for the relative spacecraft positioning strategies. Each of the precise orbit determination concepts has been tested using GPS data from the CHAMP and GRACE missions. The reduced dynamic batch LSQ orbits were validated with Satellite Laser Ranging data, where the residuals showed an RMS of 3-4 cm.

Out of a total of four possible processing strategies that have been identified for relative spacecraft positioning, only an extended Kalman filter/smoother has proven to work satisfactorily when tested on the real-world GRACE GPS data. The EKF processes single difference GPS pseudorange and carrier phase observations and uses (pseudo) relative spacecraft dynamics to propagate the relative satellite state over the observation epochs. Despite its single difference parametrization the EKF can still resolve and incorporate the integer double difference carrier phase ambiguities, which is commonly regarded as, and has proven to be in this dissertation, the key to precise GPS based relative positioning. Estimation of the integer ambiguities is accomplished by the well known Least Squares Ambiguity Decorrelation Adjustment (LAMBDA) method. Due to the presence of systematic errors in the GRACE GPS data, a relatively conservative validation of the estimated integer ambiguity parameters was found to be required prior to their incorporation in the filter. When validating the daily ambiguity fixed GRACE relative position solutions from the EKF with the KBR observations, it has been shown that an actual overall relative position precision of 0.9 mm (1-dimensional) over a 101 day data arc is achieved. This dissertation is the first that proves that such precision can be truly obtained for real-world relative spacecraft positioning applications.

Samenvatting

Op dit moment wordt het in formatie vliegen van ruimtevaartuigen, of satellieten, gezien als een van de meest veelbelovende technieken voor toekomstige en geavanceerde ruimtevaartmissies. Een van de voordelen is onder meer de verdeling van meetinstrumenten en sensoren over verschillende kleine satellieten. Naast het feit dat dit de flexibiliteit verhoogt zal dit waarschijnlijk ook leiden tot een kortere ontwikkelingstijd en een kostenreductie. Buiten deze voordelen bieden satellietformaties in een lage aardbaan geavanceerde wetenschappelijke onderzoeksmogelijkheden die niet, of zeer moeilijk, kunnen worden gerealiseerd wanneer er slechts van een enkele satelliet gebruik wordt gemaakt. Een van de fundamentele kwesties bij het in formatie vliegen van satellieten is het bepalen van de onderlinge, of relatieve, afstanden tussen de satellieten in deze formatie. Kennis van deze relatieve afstanden in real time is belangrijk voor onder meer operationele aspecten. Sommige wetenschappelijke toepassingen vereisen echter een hoogprecieze of -nauwkeurige kennis van deze afstanden achteraf. Het doel van dit proefschrift, en het onderliggende onderzoek, is de ontwikkeling, de implementatie en het testen van een methode die deze afstanden met een hoge precisie achteraf kan bepalen, gebruikmakend van GPS metingen. De vraag naar zulk een methode komt van enkele wetenschappelijke missies die momenteel voorbereid worden. Een goed voorbeeld is de nieuwe 'Synthetic Aperture Radar' (SAR) interferometrie missie bestaande uit twee in formatie vliegende satellieten, TerraSAR-X en TanDEM-X. Het primaire missiedoel, het genereren van hoognauwkeurige digitale hoogtemodellen, vereist dat de relatieve afstand tussen beide satellieten achteraf kan worden bepaald met een precisie van 2 mm (1-dimensionaal).

GPS ontvangers worden vaak overwogen als het primaire meetinstrument voor het precies bepalen van de relatieve afstanden tussen in formatie vliegende satellieten. Dat komt onder meer doordat precieze onderlinge afstandsbepalingen tussen GPS ontvangers in geodetische netwerken al routinewerk is, en het dus is aangetoond dat dit meetinstrument hiervoor geschikt is. Verder worden GPS ontvangers al zeer frequent gebruikt aan boord van satellieten voor allerlei soorten navigatietaken. Het GPS systeem is bovendien geschikt voor real time toepassingen en de metingen zijn 3-dimensionaal van aard.

Het merendeel van de eerder uitgevoerde studies in dit vakgebied had betrekking

op de real time of operationele aspecten van het in formatie vliegen. Bovendien was de gebruikte GPS meetdata altijd verkregen uit simulaties, zij het door middel van software of 'hardware-in-the-loop'. Dit proefschrift onderscheidt zich duidelijk door het feit dat de ontwikkelde methoden getest zijn met GPS observatiedata afkomstig van de GRACE missie, en doordat de verkregen relatieve afstanden precies kunnen worden gevalideerd met behulp van de GRACE K/Ka-Band Ranging System (KBR) metingen.

Een van de belangrijkste aspecten van GPS toepassingen is de kwaliteit van de gebruikte observatiedata. Om een beter inzicht hierin te krijgen zijn er eerst een aantal analyses uitgevoerd om de prestaties van de GPS ontvangers aan boord van de CHAMP en GRACE satellieten te bepalen. De resultaten laten onder meer zien dat de systematische fouten van de GPS code metingen afkomstig van de GRACE GPS ontvangers in de orde van 10-15 cm zijn. Verder is gebleken dat de meetruis van de GPS observatiedata afkomstig van GRACE B significant lager is dan voor CHAMP of GRACE A.

Wanneer GPS wordt gebruikt voor relatieve satelliet-afstandsbepaling moet de baan van een van de satellieten, die als referentiepunt dient, met de hoogst mogelijke precisie bekend zijn. Daarom zijn er in totaal drie methoden voor precieze satelliet baanbepaling ontwikkeld en getest, die gebruik maken van ionosfeervrije GPS code en fase metingen. Deze bestaan uit een kinematische en een gereduceerd dynamische 'batch LSQ' schattingsmethode, alsmede een 'Extended Kalman Filter/Smoother' (EKF). Deze methoden vormen ook de conceptuele basis van de later ontwikkelde strategieën voor relatieve satelliet afstandsbepaling. Elk van de precieze baanbepalingsmethoden is uitvoerig getest met GPS observatiedata van de CHAMP en GRACE missie. De satelliet banen verkregen met de gereduceerd dynamische 'batch LSQ' schattingsmethode zijn gevalideerd met 'Satellite Laser Ranging' metingen, waar de residuen een RMS van 3-4 cm vertonen.

Van de totaal vier strategieën die geïdentificeerd en uitgeprobeerd zijn voor precieze relatieve afstandsbepaling van satellieten bleek alleen de 'Extended Kalman Filter/Smoother' robuust genoeg voor toepassing op de GRACE GPS data. De EKF verwerkt de zogenaamde enkelverschillen ('single differences') van de GPS code en fase metingen op de individuele frequenties, en gebruikt een 'pseudo' modellering van de relatieve satellietdynamica om de toestandsvector tussen de meetepochen te propageren. Ondanks de parametrisatie, behorende bij de enkelverschil metingen, is de filter nog steeds in staat om de geheeltallige fase-meerduidigheden behorende bij dubbelverschil GPS fase metingen op te lossen en te gebruiken. Dit laatste wordt algemeen gezien als de sleutel tot hoogprecieze relatieve GPS plaatsbepaling, wat ook gedurende dit onderzoek duidelijk gebleken is waar te zijn. Schatting van deze geheeltallige meerduidigheden gebeurd met behulp van de bekende Least Squares Ambiguity Decorrelation Adjustment (LAMBDA) methode. Voordat de geschatte meerduidigheden gebruikt kunnen worden door de filter worden ze door een vrij conservatief validatieschema getoetst op juistheid. Dit is noodzakelijk gebleken door de aanwezigheid van niet gemodelleerde fouten in de GPS observatiedata. Wanneer de dagelijkse oplossingen voor de relatieve positie tussen beide GRACE satellieten,

verkregen uit de EKF waarbij de geheeltallige fase-meerduidigheden worden geschat en gebruikt, worden gevalideerd met de KBR metingen blijkt, dat de algehele precisie van de oplossingen op 0.9 mm (1-dimensionaal) ligt voor een testperiode van 101 dagen. Dit proefschrift is het eerste waarin wordt bewezen dat zulke precisie in de werkelijkheid te halen valt voor relatieve satelliet-afstandsbepaling.

Chapter 1
Introduction

Although initially only intended for terrestrial positioning applications, the use of the Global Positioning System (GPS) for space applications, especially in low Earth orbits (LEOs), was recognized early on as well. In 1982 the LandSat-4 satellite carried the first GPS receiver into orbit [*Birmingham et al.*, 1983]. With only a few of the prototype Block I GPS satellites available at the time, LandSat-4's GPS receiver demonstrated that a spacecraft could be navigated to an accuracy better than 50 meters in real-time.

Since that inaugural flight GPS receivers have gradually evolved into well-accepted standard tools for spacecraft navigation. Aside from onboard applications like real-time positioning, attitude determination or time-synchronization of spacecraft sensors, GPS receivers are nowadays considered as primary tracking system for precise orbit determination in many satellite missions. Here, the accuracy, global coverage and three-dimensional nature of GPS measurements makes this system highly competitive to other, more traditional, spacecraft tracking systems such as Satellite Laser Ranging (SLR) and DORIS.

In accordance with geodetic applications, dual-frequency GPS receivers are preferred for precise orbit determination and navigation of LEO spacecraft. As opposed to single frequency GPS receivers, the dual frequency ones are capable of eliminating the ionospheric signal errors and thus to make best use of the high accuracy GPS carrier phase measurements. Single frequency GPS receivers, such as Surrey's SGR series [*SSTL*, 2003], the DLR Phoenix [*Montenbruck et al.*, 2004] and Astrium's Mosaic [*Astrium*, 2002], are generally used for small satellite missions when medium navigational precision is required. Driven by the need of various scientific missions, a growing number of suitable dual frequency GPS receivers is being made available for space applications. Aside from the Jet Propulsion Laboratory's (JPL) BlackJack GPS receiver [*Montenbruck and Kroes*, 2003], which is already flown on CHAMP, GRACE, IceSat and Jason-1, the European Lagrange receiver [*Marradi et al.*, 2001] and the GRAS instrument [*Silvestrin et al.*, 2000] are currently prepared for use on Radarsat-2, GOCE and METOP. Recently, a Soyuz-2 capsule

travelling to the International Space Station already carried a Lagrange GPS receiver, as a test experiment [*ENEIDE*, 2005] for differential GPS (DGPS) using the European Geostationary Navigation Overlay System (EGNOS). Furthermore, the validation of commercial-off the-shelf receivers (NovAtel OEM4-G2L) is in progress for use onboard the Canadian CASSIOPE mission [*Langley et al.*, 2004].

Besides their use for precise navigational tasks, dual frequency spaceborne GPS receivers are slowly becoming stand-alone scientific instruments as well. They have successfully profiled the atmosphere, by observing GPS signals as they are occulted by the Earth's limb [*Kursinski et al.*, 1997], and are used to study the Earth's gravity field [*Reigber et al.*, 2002]. Furthermore the use of GPS for altimetry purposes, where backscattered GPS signals from the sea surface are measured, is currently being investigated [*Yunck*, 2003].

This research work focusses on yet another space application of GPS, namely its use for precise relative navigation of formation flying satellites. The rationale of this relatively new application and an overview of previous research conducted in this field are provided in the next section. Followed by this is the objective and motivation of the current study and its contribution to this area of research. A brief introduction of two satellite missions, CHAMP and GRACE, of which GPS data is frequently used for this research, is given thereafter. Finally, the chapter is concluded with a detailed outline of the rest of this dissertation.

1.1 Spacecraft formation flying using GPS

Spacecraft formation flying is currently considered as a key technology for advanced space missions. Compared to large individual spacecraft, the distribution of sensor systems amongst multiple platforms offers improved flexibility and redundancy, shorter times to mission and the prospect of being more cost effective. Besides these advantages, satellite formations in low Earth orbit provide advanced science opportunities that cannot, or not easily, be realized with single spacecraft, such as measuring small scale variations in the Earth's gravity field or higher resolution imagery and interferometry.

One of the fundamental issues of spacecraft formation flying is the determination of the relative state (position and velocity) between the satellite vehicles within the formation. Knowledge of these relative states in (near) real-time is important for operational aspects. In addition some of the scientific applications, such as high resolution interferometry, require an accurate post-facto knowledge of these states instead. Therefore a suitable sensor system needs to be selected for each mission. The highest precision is obtained with optical metrology. Here, use is made of a laser interferometer, which measures the relative distances between satellites with mm to μm precision. A custom tailored radio frequency (RF) system, such as the Ka-Band Ranging system on GRACE, obtains the same kind of precision, but measures a biased range instead. The major drawbacks of both systems are the relatively narrow field of view, certainly for the optical system, and the fact that

only 1-dimensional measurements (ranges) are provided. This is where GPS, used as an RF metrology system, clearly makes a difference.

As commonly known, precise relative positioning between GPS receivers in geodetic networks is exercised on a routine basis. Furthermore GPS receivers are already frequently used onboard satellites to perform all kinds of navigational tasks, are suitable for real-time applications and provide measurements with a 3-dimensional nature. Therefore they are often considered as the primary instrument for relative navigation in future satellite formation flying missions.

Most of the research on GPS based spacecraft relative navigation conducted over the past decade focused on the needs and aspects of formation control and maintenance in (near) real-time. For this a single frequency GPS receiver is generally sufficient when the inter-satellite distance, or baseline, is restricted to a maximum of about 10 km. A few studies regarding rendez-vous and docking applications used GPS data from actual demonstration missions. The most well known is probably the Automated Transfer Vehicle (ATV) Rendez-Vous Predevelopment Program (ARP). The ATV is ESA's logistic and supply vehicle for the International Space Station. It uses GPS for relative navigation during the long and medium distances (40 km to 200 m) of the approach. The program consisted of 3 demonstration missions, all involving the Space Shuttle (STS-80, STS-84 and STS-86) as the chaser spacecraft. The real-time relative position accuracy obtained varied from 8.7 to 10.0 m [*Highsmith and Axelrad*, 2002] compared to precise laser ranges. This limited accuracy is the result of solely processing GPS pseudorange data, subject to large multipath errors, whilst using the first order Clohessy-Wiltshire equations [*Clohessy and Wiltshire*, 1960] for propagation of the relative state.

Due to the unavailability of real-world GPS data from other types of formation flying scenarios most of the previous research is based on software or hardware-in-the-loop (HWIL) simulations. Studies performed by *Ebinuma* [2001], *Leung and Montenbruck* [2005], *Busse* [2003] and *Hartrampf et al.* [2002] used single frequency GPS receivers in HWIL simulations, where the first two studies focussed on real-time relative positioning. *Ebinuma* [2001] has demonstrated precise closed loop rendezvous of two spacecraft and achieved a relative position accuracy of 5 cm (3D RMS). In order to achieve this he used double differenced carrier phase data. No attempts were made to fix the accompanying carrier phase ambiguities to integer values, as is commonly regarded to be the key to precise relative GPS positioning. Of the other studies mentioned here, only *Leung and Montenbruck* [2005] and *Hartrampf et al.* [2002] made efforts to fix the double difference carrier phase ambiguities to integer values. *Busse* [2003] and *Leung and Montenbruck* [2005] both used modified versions of the Zarlink Orion GPS receiver, with the difference that *Leung and Montenbruck* [2005] implemented the processing algorithms on a flight proven onboard navigation computer. For respective baselines of 1 km [*Busse*, 2003] and 12 km [*Leung and Montenbruck*, 2005] both studies obtained a relative positioning accuracy of 1 cm (3-dimensional root-mean-square (RMS)), where the latter clearly shows the accuracy improvement from fixing ambiguities over longer baselines. Finally, *Hartrampf et al.* [2002] performed an HWIL simulation using

Astrium Mosaic receivers. Here, an accuracy of 1 cm was obtained for a 1 km baseline with purely kinematic processing of double difference carrier phase data with, as mentioned before, the ambiguities fixed to integer values.

A study using dual frequency GPS data from both software and HWIL simulations was carried out by *Binning* [1997]. Here, the employed filtering scheme only processes the wide lane combination of the double difference carrier phase observations, and fixes the accompanying ambiguities to integer values. Although this somewhat improves the accuracy of the relative position solution, high precision comes from correctly fixing the ambiguities on both carrier frequencies and processing the ionosphere free combination of the carrier phase data instead. The resulting relative position accuracy in this study therefore remains limited to 3 cm (3-dimensional RMS) for a 50 km baseline.

More recently, some studies were carried out focussing on high accurate post facto relative S/C positioning, all using dual frequency GPS data. A study by *Flechtner* [2003], purely based on software simulations, suggests that for two along-track separated formation flying S/C (separation up to 80 km) the relative position can most of the time be determined with an accuracy of 1 mm. Furthermore, with the coming of the GRACE mission, a study by *Svehla and Rothacher* [2004*a*] finally presents non-simulated results of highly precise post-facto relative spacecraft positioning using GPS. Here it is demonstrated that the relative position between the GRACE satellites can be determined with a precision of 3 mm (1-dimensional, along-track) when comparing to the measurements obtained from the Ka-Band Ranging System.

1.2 Research objective and motivation

The objective of this research work is to develop, implement and validate a strategy for high precision post-facto relative positioning of formation flying satellites, using dual frequency differenced GPS observations. The demand for such a method is driven by near future scientific applications requiring these high precision solutions in order to satisfy the mission objectives. A good example here is the planned Synthetic Aperture Radar (SAR) interferometry formation consisting of the TerraSAR-X and TanDEM-X satellites (Fig. 1.1).

TerraSAR-X is an advanced interferometric SAR mission, which is planned to be launched into a near polar, near circular orbit with an altitude of 515 km, in 2006. The formation is completed in 2008 when an identical satellite, TanDEM-X [*Moreira*, 2003], shall be put into orbit. The formation can be operated in two modes; bistatic mode, where both spacecraft will be separated by approximately 3 km, and a mono-static pursuit mode for along-track interferometry, where the separation will vary between 30 - 50 km. In bistatic operation mode the mission objective is to generate highly accurate Digital Elevation Models (DEMs) on a global scale, satisfying DTED-3 [*Moreira et al.*, 2004] specifications. This translates to a vertical mapping accuracy of 2 m or better, which can only be achieved if the

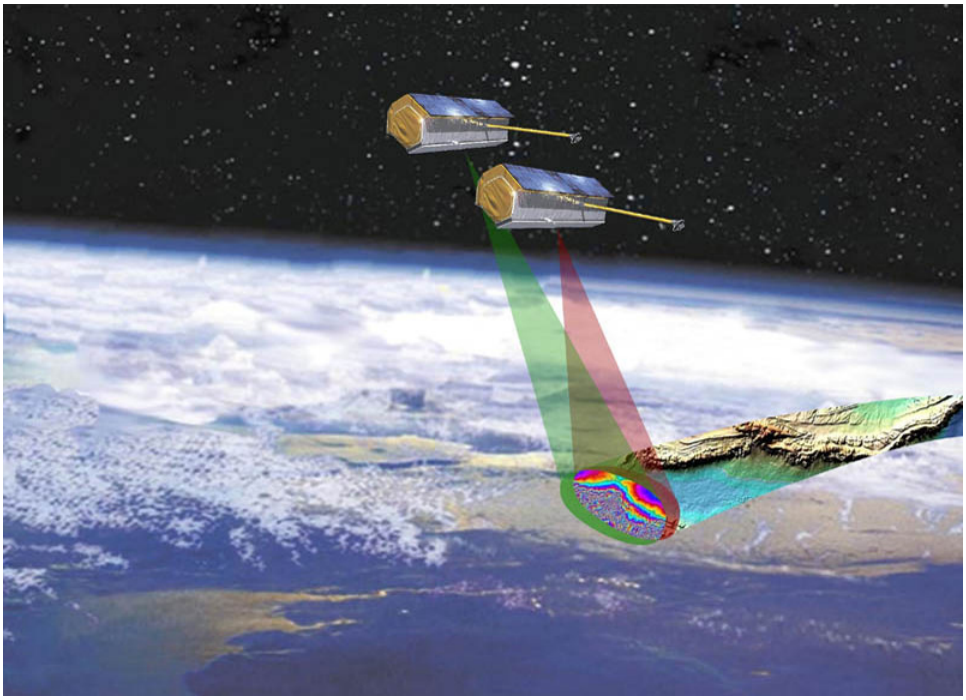

Figure 1.1 Artist's impression of the TerraSAR-X and TanDEM-X satellites in bistatic operation mode (Source: Astrium GmbH).

relative distance between both spacecraft is known within 2 mm (1-dimensional RMS), cf. [*Moreira et al.*, 2004].

None of the studies conducted so far were able to proof that such precision is feasible, due to inadequacies in the filter design and measurement processing. In addition, all obtained results, except for the ones obtained by *Svehla and Rothacher* [2004*b*], remain based on simulations, which even if they involve flight proven GPS hardware still resemble an ideal environment. This study clearly distinguishes itself on several critical issues, which are also the main contributions to this area of research. First of all, the developed filtering scheme processes single difference dual-frequency GPS pseudorange and carrier phase observations in a reduced dynamic way. Using high precision force models to generate 'pseudo' relative spacecraft dynamics, the relative state is propagated. In order to compensate for dynamical modeling deficiencies, empirical accelerations, employing a first order Gauss Markov noise process, are estimated. Second and more important, despite a single difference formulation, the double difference integer carrier phase ambiguities on both frequencies are estimated and used by the filter in order to achieve the highest obtainable precision. Finally, and perhaps most important, the developed method is tested with actual GPS data from the GRACE mission, and the result-

ing relative position solutions can be precisely validated using Ka-Band Ranging system observations. This assures that the developed strategy is viable for use in real-world situations, and will truly provide baseline solutions with the precision (1-dimensional) presented in this dissertation.

1.3 The CHAMP and GRACE satellite missions

Throughout this research extensive use is made of GPS data from both the CHAMP and GRACE satellite missions. A brief overview of both missions is therefore given in the following.

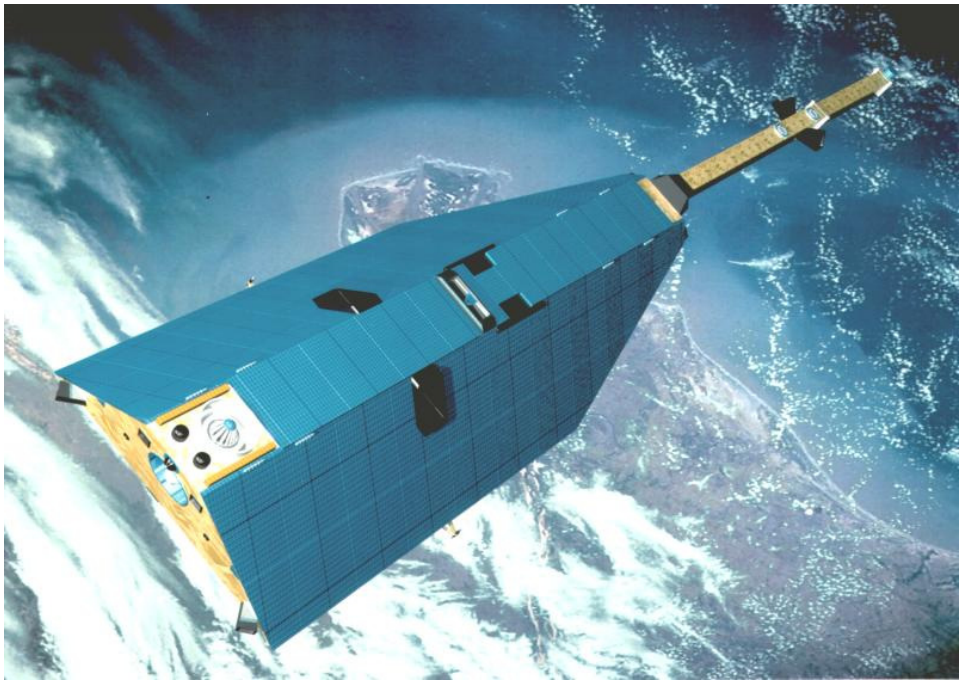

Figure 1.2 Artist's impression of the CHAMP satellite in orbit (Source: Astrium GmbH).

The Challenging Minisatellite Payload (CHAMP), illustrated in Fig. 1.2, is a German small satellite mission for geoscientific and atmospheric research and applications [*Reigber et al.*, 2003]. On 15 July 2000 CHAMP was launched into an almost circular, near polar orbit with an initial altitude of approximately 454 km. The primary mission objectives comprise the accurate determination of the Earth's gravity field, the estimation of the magnetic field including its spatial and temporal variations, as well as the collection of refraction data for modeling the physical properties of the troposphere and ionosphere. To achieve these science goals, the satellite is equipped with a number of highly accurate instruments, such as the

STAR accelerometer (ONERA, France), the JPL BlackJack GPS receiver, multiple magnetometers and an autonomous star sensor. A more detailed description of the CHAMP mission and its scientific goals can be found in [*Reigber et al.*, 1996].

The JPL BlackJack GPS receiver onboard of the CHAMP satellite is connected to a total of four GPS antennas. A zenith-mounted patch antenna equipped with a choke ring and a typical cone of 80° serves as prime antenna for precise orbit determination (POD). A backup POD antenna is mounted next to the prime one, but not equipped with a choke ring. On the rear side of the spacecraft (S/C) a helix antenna for occultation measurements can be found, exhibiting a 20° nadir tilt. The last antenna, a helix antenna with left-hand circular polarization, is mounted on the bottom side (nadir pointing) and is planned to be used for GPS altimetry. For this research only the GPS data collected by the primary POD antenna are used, for both precise orbit determination and data quality assessment.

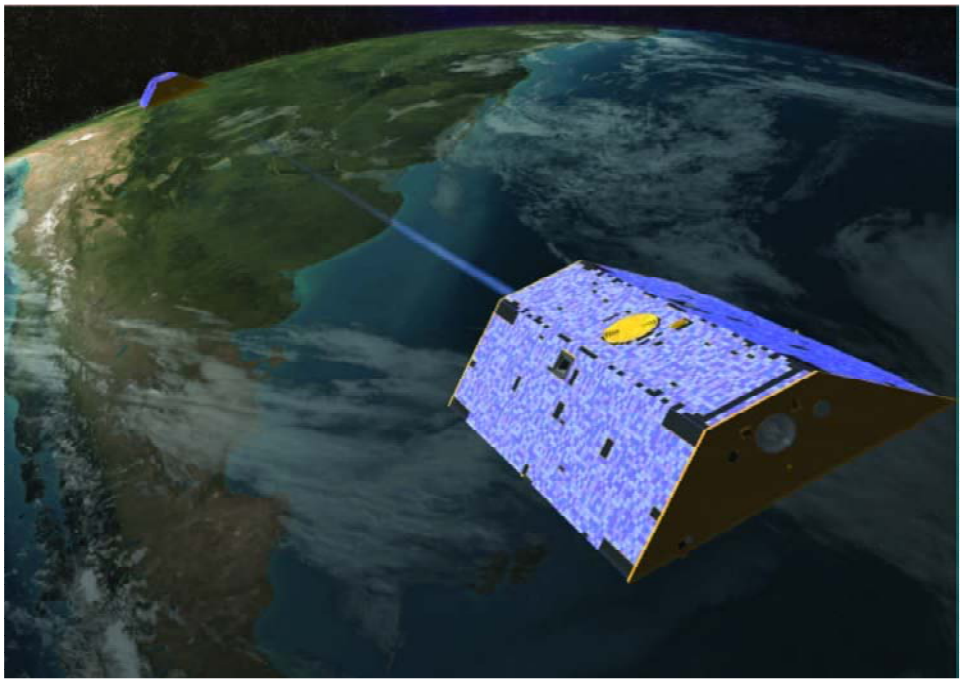

Figure 1.3 Artist's impression of the GRACE satellites in orbit (Source: CSR at the University of Texas). The KBR link between both S/C is clearly illustrated.

The Gravity Recovery and Climate Experiment (GRACE) mission consists of two identical formation flying spacecraft in a near polar, near circular orbit with an initial altitude of approximately 500 km (Fig. 1.3). The spacecraft have a nominal separation of 220 km. The primary mission objective is to measure the time varying changes in the Earth's gravity field [*Tapley et al.*, 2004*b*], which is accomplished by the mission's key instruments, the Ka-Band Ranging System (KBR) and the

accelerometers. The KBR instrument measures the change in distance (biased range) between both S/C, which is a measure for the change in gravity, within a precision of 10 μm at 1Hz samples (10 $\mu m/\sqrt{Hz}$) [*Dunn et al.*, 2003]. Both S/C are equipped with the Instrument Processing Unit (IPU), which is a modified version of the JPL BlackJack GPS receiver. In addition to making the usual GPS observations, the IPU also processes the Star Camera and KBR signals. Frequency generation for both the KBR (24 & 32 GHz) and GPS reference signals is accomplished by an ultra stable oscillator (USO). A complete overview of the entire GRACE mission can be found in *NASA* [2002]. Within this research the KBR observations are used to independently validate the precision of the along-track component of the relative S/C positions computed by solely using GPS observations.

1.4 Outline

Chapter 2 provides a detailed overview of the GPS observation types used throughout this research. It deals with observation modeling for both absolute and relative spaceborne positioning applications, as well as with data quality aspects, including the analysis of systematic errors and thermal noise in the GPS observation data.

In order to obtain an accurate relative position solution, the absolute position of one of the S/C, serving as the reference for modeling, has to be known with good precision as well. Furthermore, due to the great similarities in modeling and handling of GPS measurements for both absolute and relative GPS positioning, the developed concepts for POD serve as a reference for the relative S/C positioning problem. Therefore, a thorough discussion of the developed precise orbit determination (absolute positioning) techniques using GPS observations is given in chapter 3. Here, a kinematic and reduced dynamic batch Least-Squares (LSQ) estimator and an extended Kalman filter are discussed in detail, together with a comparison of the results of each method when tested with CHAMP and GRACE data.

Chapter 4 is devoted to the problem of relative positioning between formation flying spacecraft. It starts with an overview of the integer carrier phase ambiguity estimation and validation problem, followed by a description of promising strategies for relative positioning. The most viable processing strategy, an extended Kalman filter (EKF), is presented in full detail, including extensive test and validation results of this method using GRACE data.

Finally the conclusions, recommendations and the issues for future study are given in chapter 5.

Chapter 2
GPS observations

The Global Positioning System nominally consist of a constellation of 24 satellites in near circular orbits with a radius of approximately 26500 km. The satellites are divided over 6 orbital planes, equally spaced around the equator with an inclination of approximately 55°. Each satellite continuously transmits data on 2 L-band frequencies denoted as f_1, at 1575.42 MHz, and f_2, at 1272.60 MHz, corresponding to wavelengths of approximately 19.0 cm, λ_1, and 24.4 cm, λ_2. Both frequencies are modulated with so-called Pseudo Random Noise (PRN) codes used for acquisition and tracking of the GPS signal. The first frequency is modulated with the Coarse Acquisition (C/A) and the Precision (P) code, the second frequency only with the P-code. The C/A-code is accessible to all users whereas the P-code is normally encrypted to the P(Y)-code, which can only be directly observed by authorized users. The GPS navigation data message is distributed using the code observations and contains information about the actual GPS time and the position and clock errors of the GPS satellites, making the system suitable for real-time positioning applications. More detailed information about the GPS system itself can be found in several literature sources such as [*Hofmann-Wellenhof et al.*, 2001] and [*Parkinson and Spilker*, 1995].

This chapter primarily deals with the GPS observation types used throughout this research, what affects them and how they are modeled for the different positioning applications. In addition, the final section of this chapter is devoted to GPS data quality aspects. For this an in-flight performance analysis of the GPS data obtained from the main POD antenna of the BlackJack GPS receiver onboard the CHAMP and GRACE satellites has been conducted to visualize systematic errors and noise influencing the different GPS observations.

2.1 Observation types

Generally there are 3 types of GPS observations, the code or pseudorange observation, the carrier phase or integrated Doppler observation, and the range-rate or

instantaneous Doppler observation. Not every receiver supports or gives out all types of observations. As mentioned earlier all real-world GPS observation data used in this research comes from the CHAMP and GRACE mission, and is therefore obtained from the JPL BlackJack GPS receiver, which supports tracking of all 3 code and accompanying carrier phase observations.

GPS positioning is primarily based on one way measurements of the signal travelling time. For this purpose a common reference time, called GPS time, has been defined, which has a constant offset of -19 seconds with respect to the international atomic time (TAI). The GPS satellites are equipped with redundant atomic clocks of either Cesium or Rubidium (see section 3.1), whereas GPS receivers use temperature compensated crystal oscillators (TCXOs) in most cases. Both the GPS satellite (superscript s) and GPS receiver (subscript r) experience a clock offset (δt) causing the respective internal times to become

$$\begin{aligned} t^s(t) &= t + \delta t^s(t) \\ t_r(t) &= t + \delta t_r(t) \end{aligned} \tag{2.1}$$

as function of the overall GPS system time t. The clock offsets are subject to a drift and therefore only valid on a certain epoch. This fact has to be taken into account when modeling the different observation types throughout this research.

2.1.1 Pseudorange

The code observations are a direct, but coarse, measure of the signal travelling time, and thus of the range between the antenna phase centers of the GPS satellite and the GPS receiver. They are also referred to as pseudoranges because they are still subject to clock offsets from both the GPS satellite and GPS receiver. Although the P(Y)-code is encrypted, several techniques, such as (semi-)codeless tracking, have been developed allowing P(Y)-code observations to be made without the decryption key and hardware, at the expense of a loss in Signal to Noise Ratio (SNR), and thus a reduced precision [*Woo*, 1991]. As mentioned above the GPS receivers used in this study are capable of making these observations on both frequencies.

Following *Husti* [2000], the observed signal travelling time, $t_r^s(t)$, at epoch t is written as:

$$t_r^s(t) = t_r(t) - t^s(t - \tau_r^s(t)), \tag{2.2}$$

in which $t_r(t)$ is the receiver time of reception and $t^s(t-\tau_r^s(t))$ is the satellite time of signal transmission. The true signal travelling time is denoted as $\tau_r^s(t)$. Substitution of eqn. 2.1 into eqn. 2.2 yields,

$$t_r^s(t) = \tau_r^s(t) + \delta t_r(t) - \delta t^s(t - \tau_r^s(t)). \tag{2.3}$$

Multiplication of this expression with the speed of light and substitution of the geometric range between the GPS satellite and receiver antenna phase centers, $\rho_r^s(t) = c\tau_r^s(t)$, results in a first approximation of the pseudorange observation

$$P_r^s(t) = \rho_r^s(t) + c(\delta t_r(t) - \delta t^s(t - \tau_r^s(t))). \tag{2.4}$$

The actual observation however is still affected by atmospheric effects, instrumental delays in the GPS receiver and GPS satellite, signal multipath and other systematic errors, and of course thermal measurement noise. Since this study solely focuses on space applications the only atmospheric effect influencing the observations is the one caused by the ionosphere. The ionosphere stretches from roughly 50 to 1000 km above the Earth's surface and consists of ions and free electrons. Its effect on radio waves is frequency dependent. From [*Hofmann-Wellenhof et al.*, 2001] it is learned that for GPS observations the so called ionospheric path delay, $I_r^s(t, f)$, in units of meters, is given by

$$I_r^s(t, f) = \frac{40.3}{f^2}\mathrm{TEC}_r^s(t), \tag{2.5}$$

where TEC stands for the Total Electron Content i.e. the total electron density along the signal path length. Although this term only covers the first order ionospheric effect, it comprises the dominant error induced by the ionosphere. Higher order effects are generally on the sub-mm level [*Kedar et al.*, 2003] and are ignored here.

The measurement thermal noise of the code observation, $\epsilon_{rP}^s(t)$, is assumed to be purely random with a zero mean and is typically on the decimeter level for modern geodetic grade receivers. All other errors and biases are contained in one term,

$$M_{rP}^s(t) = b_{r(i)P}^s(t) + m_{rP}^s(t) + s_{rP}^s(t), \tag{2.6}$$

where the GPS receiver and GPS satellite hardware delays are grouped into a code bias on receiver tracking channel i, $b_{r(i)P}(t)$, and the code multipath and other systematic effects are respectively given by $m_{rP}^s(t)$ and $s_{rP}^s(t)$. Finally the observation equation for a pseudorange observation on any of the two transmitting frequencies yields

$$P_r^s(t) = \rho_r^s(t) + c(\delta t_r(t) - \delta t^s(t - \tau_r^s(t))) + I_r^s(t, f) + M_{rP}^s(t) + \epsilon_{rP}^s(t). \tag{2.7}$$

2.1.2 Carrier phase

Besides making code observations most GPS receivers also support accurate tracking of the carrier onto which the code was modulated. The observed carrier beat phase on one of the frequencies can be expressed as

$$\phi_r^s(t) = \phi_r(t) - \phi^s(t - \tau_r^s(t)) + N_r^s. \tag{2.8}$$

and basically consists of a phase difference, $\phi_r - \phi^s$, and an integer number of carrier cycles, N_r^s. The GPS receiver carrier phase at the moment of signal reception is denoted by $\phi_r(t)$, and $\phi^s(t - \tau_r^s(t))$ represents the carrier phase of the GPS satellite at time of transmission. These last two terms can furthermore be written as

$$\begin{array}{ll} \phi_r(t) & = \phi_r(t_0) + f(t - t_0) + f(\delta t_r(t) - \delta t_r(t_0)) \\ \phi^s(t - \tau_r^s(t)) & = \phi^s(t_0) + f(t - \tau_r^s(t) - t_0) + f(\delta t^s(t - \tau_r^s(t)) - \delta t^s(t_0)) \end{array}, \tag{2.9}$$

where $\phi_r(t_0)$ and $\phi^s(t_0)$ resemble the initial phases, at t_0, of the GPS receiver and GPS satellite and f the transmitting frequency. Substitution of these expressions into eqn. 2.8 yields

$$\phi_r^s(t) = f\tau_r^s(t) + f(\delta t_r(t) - \delta t^s(t - \tau_r^s(t)) + A_r^s, \tag{2.10}$$

in which the ambiguity or bias term,

$$A_r^s = N_r^s + \phi_r(t_0) - f\delta t_r(t_0) - \phi^s(t_0) + f\delta t^s(t_0), \tag{2.11}$$

is a real valued parameter, which is constant over a continuous tracking arc.

Similar as for the code observation the carrier phase measurement is also affected by the ionosphere and subject to hardware delays, systematic errors and multipath, and of course thermal measurement noise. In addition, carrier phase observations can be subject to polarization induced wind-up [*Xu*, 2003]. This effect occurs when a GPS antenna receives a polarized GPS signal while at the same time the antenna is rotating around the line of sight vector. For spaceborne GPS this effect can occur when e.g. the satellite's attitude is not actively controlled.

The first order ionospheric correction to the phase observation is the same as for the code observation, but has the opposite sign. This is due to the fact that the ionosphere causes an advance on the phase and similarly a delay on the modulated code observation. Furthermore, the thermal noise of the carrier phase measurement is on the mm level and multipath errors are confined to a quarter of the signal wavelength ([*Leva et al.*, 1996]; [*Braasch*, 1995]), making this observation type much more accurate than pseudoranges. After multiplication of eqn. 2.10 with the signal wavelength, λ, and applying the above mentioned corrections, the carrier phase observation equation, for any of the frequencies, is given by

$$L_r^s(t) = \rho_r^s(t) + c(\delta t_r(t) - \delta t^s(t - \tau_r^s(t))) - I_r^s(t, f) + \lambda A_r^s + M_{rL}^s(t) + \epsilon_{rL}^s(t), \tag{2.12}$$

where the measurement noise, captured in $\epsilon_{Lr}^s(t)$, is again assumed as purely random with a zero mean and where all other (systematic) errors are given by

$$M_{rL}^s(t) = b_{r(i)P}(t) + w_{rL}^s(t) + m_{rL}^s(t) + s_{rL}^s(t). \tag{2.13}$$

Here, similar to the code observation, the hardware delays from both the GPS receiver and GPS satellite for the phase observable are grouped into an additional phase bias on receiver tracking channel i, $b_{r(i),L}(t)$, and the carrier phase multipath and systematic errors are given by $m_{rL}^s(t)$ and $s_{rL}^s(t)$. Furthermore, the effect of phase wind up is captured in $w_{rL}^s(t)$.

The major differences between the code and carrier phase observations are the overall accuracy, the opposite influence of the ionosphere and the fact that the carrier phase observations are ambiguous.

2.2 Dual frequency observation model

After having derived the observation equations in the previous section, the overall dual frequency model for the P-code and accompanying carrier phase measurements

obtained from GPS satellite s, is summarized as

$$\begin{aligned}
P^s_{1r}(t) &= \rho^s_r(t) + c(\delta t_r(t) - \delta t^s(t - \tau^s_r(t))) + \quad I^s_r(t) \qquad\quad + M^s_{rP_1}(t) + \epsilon^s_{rP_1}(t) \\
P^s_{2r}(t) &= \rho^s_r(t) + c(\delta t_r(t) - \delta t^s(t - \tau^s_r(t))) + \tfrac{f_1^2}{f_2^2} I^s_r(t) \qquad + M^s_{rP_2}(t) + \epsilon^s_{rP_2}(t) \\
L^s_{1r}(t) &= \rho^s_r(t) + c(\delta t_r(t) - \delta t^s(t - \tau^s_r(t))) - \quad I^s_r(t) + \lambda_1 A^s_{1r} + M^s_{rL_1}(t) + \epsilon^s_{rL_1}(t) \\
L^s_{2r}(t) &= \rho^s_r(t) + c(\delta t_r(t) - \delta t^s(t - \tau^s_r(t))) - \tfrac{f_1^2}{f_2^2} I^s_r(t) + \lambda_2 A^s_{2r} + M^s_{rL_2}(t) + \epsilon^s_{rL_2}(t)
\end{aligned}, \tag{2.14}$$

with the carrier phase ambiguities

$$\begin{aligned}
A^s_{1r} &= N^s_{1r} + \phi_{1r}(t_0) - f_1 \delta t_r(t_0) - \phi^s_1(t_0) + f_1 \delta t^s(t_0) \\
A^s_{2r} &= N^s_{2r} + \phi_{2r}(t_0) - f_2 \delta t_r(t_0) - \phi^s_2(t_0) + f_2 \delta t^s(t_0)
\end{aligned}. \tag{2.15}$$

Here, the subscripts 1 and 2 denote the different frequencies, f_1 and f_2. It can be seen that the ionospheric path delay on f_1, given as $I^s_r(t)$, is mapped to f_2 with the factor f_1^2/f_2^2, derived from eqn. 2.5. Although not further discussed here, when needed the C/A code and carrier phase observables can be modeled in exactly the same way as the P_1 and L_1 observables respectively. Furthermore, it must be pointed out that in the dual frequency model the geometric range, $\rho^s_r(t)$, is assumed to be the same for each observation. As pointed out by *Teunissen and Kleusberg* [1998] this is not the case in reality, since the signal travelling time slightly varies for each of the frequencies, but with less than $0.1\mu s$. This results in sub-mm position differences for the GPS satellites, which are negligible compared to the other errors that are present in the observations.

As stated earlier, the thermal noise, $\epsilon^s_r(t)$, for each of the observations is assumed to be purely random with a zero mean. Furthermore, a very important assumption is that individual observations from a single GPS receiver are completely uncorrelated temporally, spatially and also between the different observation types and frequencies. This means that the covariance matrix, $\mathbf{Q_z}$, of the observation vector

$$\mathbf{z}(t) = \begin{pmatrix} P^s_{1r}(t) \\ P^s_{2r}(t) \\ L^s_{1r}(t) \\ L^s_{2r}(t) \end{pmatrix} \tag{2.16}$$

is completely diagonal

$$\mathbf{Q_z} = \begin{pmatrix} (\sigma^s_{rP_1})^2 & 0 & 0 & 0 \\ 0 & (\sigma^s_{rP_2})^2 & 0 & 0 \\ 0 & 0 & (\sigma^s_{rL_1})^2 & 0 \\ 0 & 0 & 0 & (\sigma^s_{rL_2})^2 \end{pmatrix}, \tag{2.17}$$

where the entries resemble the assumed precision of the observations. The individual measurement variances are kept constant for now, under the assumption $\sigma^s_{rP_1} = \sigma^s_{rP_2}$ and $\sigma^s_{rL_1} = \sigma^s_{rL_2}$.

Although the dual frequency GPS observation model presented here can not be used for positioning applications in its current form it serves as an overall reference in the derivation of linear data combinations and positioning models throughout this chapter.

2.3 Linear data combinations

Several linear data combinations, useful for positioning as well as data analysis and editing applications, can be derived from the previously presented dual frequency model. The linear combinations used throughout this study are briefly discussed in the following.

2.3.1 Ionosphere free linear combination

As the name suggests this linear combination eliminates the first order ionospheric path delay. It is extensively used in absolute GPS positioning applications since it simplifies measurement modeling and data handling. For the code and carrier phase observations the ionosphere free (subscript 'IF') combination yields

$$\begin{aligned} P^s_{\mathrm{IF}r}(t) &= \tfrac{f_1^2}{f_1^2-f_2^2} P^s_{1r}(t) - \tfrac{f_2^2}{f_1^2-f_2^2} P^s_{2r}(t) \approx 2.546 P^s_{1r}(t) - 1.546 P^s_{2r}(t) \\ L^s_{\mathrm{IF}r}(t) &= \tfrac{f_1^2}{f_1^2-f_2^2} L^s_{1r}(t) - \tfrac{f_2^2}{f_1^2-f_2^2} L^s_{2r}(t) \approx 2.546 L^s_{1r}(t) - 1.546 L^s_{2r}(t) \end{aligned} . \tag{2.18}$$

Applying this to the dual frequency observation model results in the following parametrization

$$\begin{aligned} P^s_{\mathrm{IF}r}(t) &= \rho^s_r(t) + c(\delta t_r(t) - \delta t^s(t - \tau^s_r(t))) + M^s_{rP_{\mathrm{IF}}}(t) + \epsilon^s_{rP_{\mathrm{IF}}}(t) \\ L^s_{\mathrm{IF}r}(t) &= \rho^s_r(t) + c(\delta t_r(t) - \delta t^s(t - \tau^s_r(t))) + \lambda_{\mathrm{IF}} A^s_{\mathrm{IF}r} + M^s_{rL_{\mathrm{IF}}}(t) + \epsilon^s_{rL_{\mathrm{IF}}}(t) \end{aligned} , \tag{2.19}$$

where it must be noted that the carrier phase ambiguity, $A^s_{\mathrm{IF}r}$, does not any longer contain an integer part as a result of the non-integer multiplication. Propagation of the covariance however still results in an uncorrelated observation model, but the noise is roughly a factor 3 higher than for the measurements on the individual frequencies.

2.3.2 Wide-lane and narrow-lane

The wide-lane (subscript 'WL') and narrow-lane (subscript 'NL') combinations are only related to the carrier phase observations and are often used in ambiguity resolution applications. When the carrier phase observations are again expressed in cycles, the combinations yield

$$\begin{aligned} \phi^s_{r\mathrm{WL}}(t) &= \phi^s_{1r}(t) - \phi^s_{2r}(t) \\ \phi^s_{r\mathrm{NL}}(t) &= \phi^s_{1r}(t) + \phi^s_{2r}(t) \end{aligned} . \tag{2.20}$$

These combinations have a (virtual) wavelength of approximately 86.2 cm, λ_{WL}, and 10.7 cm, λ_{NL}, hence the names. When expressed in units of length and combined with pseudorange measurements, observations yielding the wide-lane and narrow-lane carrier phase ambiguity remain. The expression for the wide-lane carrier phase ambiguity, $\lambda_{\mathrm{WL}} A^s_{r\mathrm{WL}}$,

$$MW^s_r(t) = \frac{1}{f_1 - f_2}\big(f_1 L^s_{1r}(t) - f_2 L^s_{2r}(t)\big) - \frac{1}{f_1 + f_2}\big(f_1 P^s_{1r}(t) + f_2 P^s_{2r}(t)\big) \quad (2.21)$$

is also referred to as the Melbourne-Wübbena linear combination, cf [*Melbourne*, 1985]; [*Wübbena*, 1985]. The long virtual wavelength, in combination with a noise of approximately 0.7 times the noise on the individual code observations, makes this combination very suitable for (real-time) data editing purposes, such as carrier phase cycle slip detection, or for use in integer ambiguity resolution.

2.3.3 Multipath combinations

The so-called multipath combinations [*Estey and Meertens*, 1999] can be used to, as the name suggests, assess multipath and systematic errors in, and the noise level of, the pseudorange observations. They are constructed using a mix of code and carrier phase observations, where it is assumed that the systematic errors and noise of the carrier phase measurements are negligible compared to the ones on the code observations. The first step is to derive an expression for the ionospheric path delay based on the carrier phase observations:

$$I^s_r(t) = \frac{1}{\alpha - 1}\big(L^s_{1r}(t) - L^s_{2r}(t)\big) - \frac{1}{\alpha - 1}\big(\lambda_1 A^s_{1r} - \lambda_2 A^s_{2r}\big). \quad (2.22)$$

Here, α is the factor describing the relation between the ionospheric path delays on both frequencies, $\alpha = f_1^2/f_2^2$. The multipath combinations are now formed by subtracting the respective carrier phase observations from their accompanying pseudoranges and substituting eqn. 2.22 for the ionosphere. When neglecting the carrier phase noise and systematic errors, the multipath observations,

$$\begin{aligned} MP1^s_r(t) &= P^s_{1r}(t) - \left(1 + \frac{2}{\alpha - 1}\right) L^s_{1r}(t) + \left(\frac{2}{\alpha - 1}\right) L^s_{2r}(t) \\ MP2^s_r(t) &= P^s_{2r}(t) - \left(\frac{2\alpha}{\alpha - 1}\right) L^s_{1r}(t) + \left(\frac{2\alpha}{\alpha - 1} - 1\right) L^s_{2r}(t) \end{aligned}, \quad (2.23)$$

are parameterized as

$$\begin{aligned} MP1^s_r(t) &\approx -\left(1 + \frac{2}{\alpha - 1}\right)\lambda_1 A^s_{1r} + \left(\frac{2}{\alpha - 1}\right)\lambda_2 A^s_{2r} + M^s_{rP1}(t) + \epsilon^s_{rP1}(t) \\ MP2^s_r(t) &\approx -\left(\frac{2\alpha}{\alpha - 1}\right)\lambda_1 A^s_{1r} + \left(\frac{2\alpha}{\alpha - 1} - 1\right)\lambda_2 A^s_{2r} + M^s_{rP2}(t) + \epsilon^s_{rP2}(t) \end{aligned}, \quad (2.24)$$

consisting of a constant combined carrier phase bias and the systematic errors and the thermal noise of the pseudorange observations. These linear combinations are

used in section 2.6 for assessing the pseudorange data quality of the CHAMP and GRACE GPS receivers.

2.4 Linearization for positioning

So far the dual frequency and ionosphere free GPS observation models are completely linear, but are still parameterized with the geometric ranges, $\rho_r^s(t)$, between the phase centers of the GPS receiver and GPS satellite antennas. Parametrization in terms of antenna phase center positions, required for positioning applications, however, introduces a non-linearity. The geometric range

$$\rho_r^s(t) = \|\mathbf{r}^s(t - \tau_r^s(t)) - \mathbf{r}_r(t)\| \tag{2.25}$$

is simply given as the distance between the antenna phase center position of the GPS receiver, $\mathbf{r}_r(t)$, and the GPS satellite, $\mathbf{r}^s(t-\tau_r^s(t))$, at the time of signal reception and transmission respectively. When approximate values of both positions are obtained (subscript 0), a linearization around them yields

$$\rho_r^s(t) = \rho_{r0}^s(t) - \mathbf{e}_r^s(t) \cdot \Delta\mathbf{r}_r(t) + \mathbf{e}_r^s(t) \cdot \Delta\mathbf{r}^s(t), \tag{2.26}$$

where

$$\rho_{r0}^s(t) = \|\mathbf{r}_0^s(t - \tau_r^s(t)) - \mathbf{r}_{r0}(t)\| \tag{2.27}$$

and where $\Delta\mathbf{r}_r(t)$ and $\Delta\mathbf{r}^s(t)$ are the phase center position increments of the GPS receiver and GPS satellite respectively. Furthermore, the partial derivatives, also known as the line of sight vector (Fig. 2.1), are given by

$$\mathbf{e}_r^s(t) = \frac{\mathbf{r}_0^s(t - \tau_r^s(t)) - \mathbf{r}_{r0}(t)}{\|\mathbf{r}_0^s(t - \tau_r^s(t)) - \mathbf{r}_{r0}(t)\|}. \tag{2.28}$$

Substitution of this linearized range into the observation equations again results in linear observation models, which are now suitable for use in positioning applications.

At this point it has to be noted that although the GPS observations are parameterized with the antenna phase center position(s) (increments), these are in general not the points of interest for positioning. Throughout this study all positions that are provided or estimated refer to the center of mass of either the GPS satellites or the spacecraft onto which the GPS receiver is mounted. The antenna phase center offsets with respect to the centers of mass of all satellites involved are accounted for in the different positioning applications. These offsets however, have virtually no impact on the linearization presented here.

Throughout this research the GPS satellite positions and clock offsets are obtained from external resources and are assumed known on every epoch, resulting in $\Delta\mathbf{r}^s(t) = 0$, and thus $\mathbf{r}^s(t) = \mathbf{r}_0^s(t)$. A discussion of these so-called GPS ephemerides is provided later in section 3.1. It must however be noted that this introduces an

additional uncertainty in the observation model since the externally generated GPS ephemerides data is only accurate to a certain level (see section 3.1). Any error in a provided GPS satellite clock offset propagates directly into the concerning observation equations, whereas GPS satellite position errors, $\epsilon_{\mathbf{r}^s}(t)$, affect the observations according to the previously derived linearization, $\mathbf{e}_r^s(t) \cdot \epsilon_{\mathbf{r}^s}(t)$.

For the different absolute positioning applications in this research it is assumed that the biases and errors, captured in the M_r^s terms of the different observations, are zero. No corrections whatsoever are applied to compensate for any of the previously discussed errors concerned. They are simply accounted for in the measurement variances, for which realistic values are determined using the analysis in section 2.6. The different observations however are still assumed to be uncorrelated.

The ionosphere free observation model, used for the absolute positioning applications, is now parameterized with the position increment of the GPS receiver antenna phase center, the GPS receiver clock offset and the ionosphere free carrier phase ambiguity. When these parameters are adjusted for using observations from multiple GPS satellites, it must be noted that the mean value of all unmodeled biases and errors over all observations cannot be separated from the GPS receiver clock offset and will therefore bias it. Since this will in general only result in a very slight time offset the impact of this effect on the accuracy of the final position is negligible, even for spaceborne GPS positioning applications where the GPS receiver in general moves faster than the GPS satellite. For completeness it has to be stated that constant phase channel biases can also not be separated from the carrier phase ambiguities. Again this has no direct consequence for the resulting position accuracy.

2.5 Relative positioning models

When only the relative position between two GPS receivers is required, use is made of GPS data differences between observations taken by both GPS receivers. Differenced GPS observation data has the advantage of eliminating or reducing common error sources, such as the GPS satellite clock offsets and common biases due to hardware delays.

In the following the so called single difference (SD) and double difference (DD) GPS observation and positioning models, used within this research, are described using Fig. 2.1 for illustration purposes.

2.5.1 Single difference model

A SD observation is formed by subtracting two GPS observations of the same type and on the same frequency, taken by two GPS receivers at the same instant and originating from a mutually observed GPS satellite. In general a SD parameter or observation between GPS receivers A and B, and with respect to GPS satellite j (Fig. 2.1) is denoted as $\square_{AB}^j = \square_B^j - \square_A^j$, where $\square$ can be any observation or parameter. Applying this to the dual frequency observation model from eqn. 2.14,

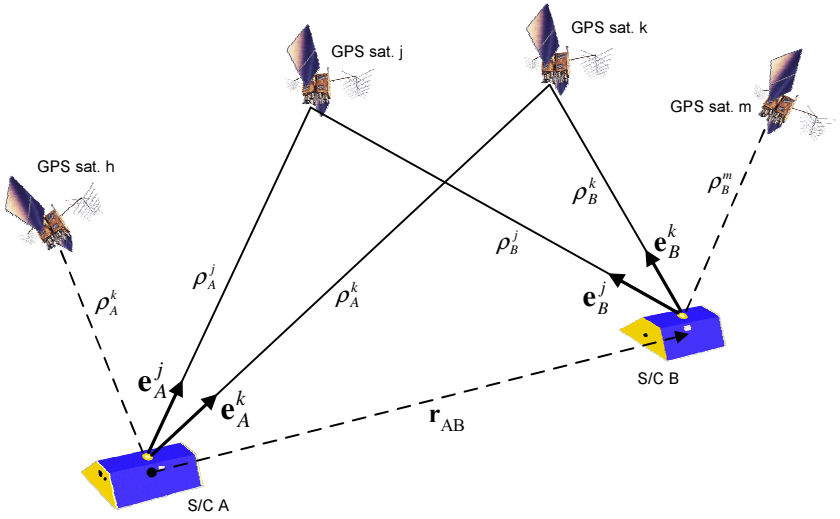

Figure 2.1 Overall viewing geometry for relative (spacecraft) positioning using differenced GPS observations. GPS satellites j and k are commonly observed by both receivers and thus SD and DD observations can be formed. This is not the case for GPS satellites h and m, which are only observed by one receiver.

which from now on will be referred to as the undifferenced (UD) model, results in the SD observation model

$$\begin{aligned}
P^j_{1AB}(t) &= \rho^j_{AB}(t) + c\delta t_{AB}(t) + \quad I^j_{AB}(t) \quad + M^j_{AB,P_1}(t) + \epsilon^j_{AB,P_1}(t) \\
P^j_{2AB}(t) &= \rho^j_{AB}(t) + c\delta t_{AB}(t) + \tfrac{f_1^2}{f_2^2} I^j_{AB}(t) \quad + M^j_{AB,P_2}(t) + \epsilon^j_{AB,P_2}(t) \\
L^j_{1AB}(t) &= \rho^j_{AB}(t) + c\delta t_{AB}(t) - \quad I^j_{AB}(t) + \lambda_1 A^j_{1AB} + M^j_{AB,L_1}(t) + \epsilon^j_{AB,L_1}(t) \\
L^j_{2AB}(t) &= \rho^j_{AB}(t) + c\delta t_{AB}(t) - \tfrac{f_1^2}{f_2^2} I^j_{AB}(t) + \lambda_2 A^j_{2AB} + M^j_{AB,L_2}(t) + \epsilon^j_{AB,L_2}(t)
\end{aligned} \quad , \tag{2.29}$$

which is parameterized with the SD or 'relative' parameters instead of the 'absolute' ones. As can be seen the GPS satellite clock offset is eliminated when forming single differences. The SD carrier phase ambiguities,

$$\begin{aligned}
A^j_{1AB} &= N^j_{1AB} + \phi_{1AB}(t_0) - f\delta t_{AB}(t_0) \\
A^j_{2AB} &= N^j_{2AB} + \phi_{2AB}(t_0) - f\delta t_{AB}(t_0)
\end{aligned} \quad , \tag{2.30}$$

are still real valued with the difference that the initial phase and clock offset of the GPS satellite have been removed. In addition, any common errors captured in the M^s_r terms of the individual receivers that are caused by the GPS satellite, such as biases due to hardware delays, also cancel out. Multipath and other systematic errors however still remain present since they generally have a different pattern for

the individual receivers. It must furthermore be noted that if the relative position between both spacecraft would be small (several km) the SD ionospheric path delays might become very small as well (a few cm). Similar to many terrestrial applications such small atmospheric effects, SD or their DD equivalents, could potentially be ignored to speed up the resolution of the integer DD carrier phase ambiguities (eqn. 2.35). However, for the 220 km separation of the GRACE satellites the SD ionospheric path delays, as well as the DD ones, can still be in the order of meters (Fig. 4.7 on page 109) and thus have to be accounted for.

As already stated before all UD GPS observations are assumed to be uncorrelated, resulting in a diagonal covariance matrix, $\mathbf{Q}_{UD}$. In general the relation between e.g. the SD and UD P_1-code observations taken by GPS receivers A and B from GPS satellites h, j, k, and m is given by

$$\begin{pmatrix} P^j_{1AB}(t) \\ P^h_{1AB}(t) \\ P^k_{1AB}(t) \\ P^m_{1AB}(t) \end{pmatrix} = \begin{pmatrix} 1 & 0 & 0 & 0 & -1 & 0 & 0 & 0 \\ 0 & 1 & 0 & 0 & 0 & -1 & 0 & 0 \\ 0 & 0 & 1 & 0 & 0 & 0 & -1 & 0 \\ 0 & 0 & 0 & 1 & 0 & 0 & 0 & -1 \end{pmatrix} \begin{pmatrix} P^j_{1B}(t) \\ P^h_{1B}(t) \\ P^k_{1B}(t) \\ P^m_{1B}(t) \\ P^j_{1A}(t) \\ P^h_{1A}(t) \\ P^k_{1A}(t) \\ P^m_{1A}(t) \end{pmatrix}, \tag{2.31}$$

which can also be written as $\mathbf{z}^{P_1}_{SD} = \mathbf{T}_{SD}\mathbf{z}^{P_1}_{UD}$. The covariance matrix for these SD observations, $\mathbf{Q}^{P_1}_{SD}$, can now be propagated from the UD model and yields

$$\mathbf{Q}^{P_1}_{SD} = \mathbf{T}_{SD}\mathbf{Q}^{P_1}_{UD}\mathbf{T}^T_{SD} = \begin{pmatrix} (\sigma^j_{AB,P_1})^2 & 0 & 0 & 0 \\ 0 & (\sigma^h_{AB,P_1})^2 & 0 & 0 \\ 0 & 0 & (\sigma^k_{AB,P_1})^2 & 0 \\ 0 & 0 & 0 & (\sigma^m_{AB,P_1})^2 \end{pmatrix} \tag{2.32}$$

with the single difference variances of e.g. GPS satellite j defined as $(\sigma^j_{AB,P_1})^2 = (\sigma^j_{A,P_1})^2 + (\sigma^j_{B,P_1})^2$. This shows that the single difference observations of one type and frequency remain uncorrelated but experience an increase in noise level with a factor of $\sqrt{2}$ when the noise of the observations from both receivers is assumed to be equal. Since no SD combinations between the different data types or frequencies are formed, the entire SD observation model from 2.29 remains uncorrelated, resulting in again a purely diagonal covariance matrix, $\mathbf{Q}_{SD}$.

In analogy with the UD observation model a linearization has to take place before the SD observations can be used in relative positioning applications. For this the relative position between the antenna phase centers of GPS receivers A and B is defined as $\mathbf{r}_{AB}(t) = \mathbf{r}_B(t) - \mathbf{r}_A(t)$. When now using eqn. 2.26, the linearized SD

geometric range becomes

$$\begin{aligned}\rho^j_{AB}(t) &= \rho^j_B(t) - \rho^j_A(t) \\ &= \rho^j_{AB0}(t) - \mathbf{e}^j_B(t) \cdot \Delta\mathbf{r}_B(t) + \mathbf{e}^j_A(t) \cdot \Delta\mathbf{r}_A(t) \\ &\quad + (\mathbf{e}^j_B(t) - \mathbf{e}^j_A(t)) \cdot \Delta\mathbf{r}^j(t) \\ &= \rho^j_{AB0}(t) - \mathbf{e}^j_B(t) \cdot \Delta\mathbf{r}_{AB}(t) - \mathbf{e}^j_{AB}(t) \cdot \Delta\mathbf{r}_A(t) + \mathbf{e}^j_{AB}(t) \cdot \Delta\mathbf{r}^j(t),\end{aligned} \tag{2.33}$$

where it can be seen that the relative position is incremented using the line of sight vector from GPS receiver B exclusively. As mentioned before the GPS satellite positions are assumed to be known on every epoch, and thus again $\Delta\mathbf{r}^j(t) = 0$. It can also be seen here that any uncertainties in them, $\epsilon_{\mathbf{r}^j}(t)$, affect the SD observations by the relation $\mathbf{e}^j_{AB}(t) \cdot \epsilon_{\mathbf{r}^j}(t)$, which is many times smaller than for the absolute positioning case. Furthermore, relative positioning applications require the knowledge of the absolute position of the reference GPS receiver, A in this case, which is then kept fixed to its given value, resulting in $\Delta\mathbf{r}_A(t) = 0$. From the linearization it is learned that any errors in the assumed reference position, $\epsilon_{\mathbf{r}_A}(t)$, affect the SD observations in the same way as the uncertainties of the GPS satellite position, $\mathbf{e}^j_{AB}(t) \cdot \epsilon_{\mathbf{r}_A}(t)$. By applying the cosine rule, an upper limit for this expression is derived in *Teunissen and Kleusberg* [1998] as

$$\mathbf{e}^j_{AB}(t) \cdot \epsilon_{\mathbf{r}_A}(t) \leq \frac{\|\mathbf{r}_{AB}(t)\|}{\|\mathbf{r}^j(t) - \mathbf{r}_B(t)\|} \|\epsilon_{\mathbf{r}_A}(t)\|. \tag{2.34}$$

It can now be shown that in e.g. the case of GRACE where the relative position between both receivers is roughly 220 km, a 1 m error in the position of the reference spacecraft could possibly affect the SD observations by 1 cm. In order to reduce errors induced by this effect the trajectory of the reference spacecraft should be known with high precision, e.g. a 3-dimensional position accuracy of 10 cm or better.

Substitution of the linearized range (eqn. 2.33) into the SD observation model results in the linear SD positioning model. Similar to the absolute positioning case, the remaining systematic errors, captured in the SD M^j_{AB} terms, are assumed to be zero. The presence of these unmodeled effects is now again accounted for by the variances, which remain uncorrelated. The SD positioning model is now parameterized with the relative position (increment) between the GPS receiver antenna phase centers, the relative GPS receiver clock offset, the SD carrier phase ambiguities on both frequencies and the SD ionospheric path delays. When, in full analogy with the discussion in the previous section, these parameters are adjusted for, the mean value of all unmodeled errors will again bias the relative GPS receiver clock offset, and in a similar way constant phase channel biases cannot be separated from the SD carrier phase ambiguities.

If closely observed it can be seen that despite the fact that everything is modeled with 'relative' parameters instead of 'absolute' ones, the dual frequency SD and UD positioning models have exactly the same structure.

2.5.2 Double difference model

A double difference observation is formed by subtracting two SD observations of the same type and frequency, taken by the same two GPS receivers at the same instant, but each relating to a different GPS satellite. When in general a DD parameter or observation between GPS receivers A and B with respect to GPS satellites j and k (Fig. 2.1) is denoted as $\square_{AB}^{jk} = \square_{AB}^{k} - \square_{AB}^{j}$, where $\square$ again stands for any parameter or observation, the DD observation model is obtained from the SD one (eqn. 2.29) as

$$\begin{array}{lll} P_{1AB}^{jk}(t) = \rho_{AB}^{jk}(t) + & I_{AB}^{jk}(t) & + M_{AB,P1}^{jk}(t) + \epsilon_{AB,P1}^{jk}(t) \\ P_{2AB}^{jk}(t) = \rho_{AB}^{jk}(t) + & \frac{f_1^2}{f_2^2} I_{AB}^{jk}(t) & + M_{AB,P2}^{jk}(t) + \epsilon_{AB,P2}^{jk}(t) \\ L_{1AB}^{jk}(t) = \rho_{AB}^{jk}(t) - & I_{AB}^{jk}(t) + \lambda_1 N_{1AB}^{jk} & + M_{AB,L1}^{jk}(t) + \epsilon_{AB,L1}^{jk}(t) \\ L_{2AB}^{jk}(t) = \rho_{AB}^{jk}(t) - & \frac{f_1^2}{f_2^2} I_{AB}^{jk}(t) + \lambda_2 N_{2AB}^{jk} & + M_{AB,L2}^{jk}(t) + \epsilon_{AB,L2}^{jk}(t) \end{array} . \tag{2.35}$$

As can be seen this removes the relative GPS receiver clock offset still present in the SD observations as well as any common biases in the SD error terms, M_{AB}^{j}. It must be noted that in the presence of inter-channel biases that are different for both receivers a bias remains in the resulting DD error terms, M_{AB}^{jk}. In a similar way multipath and systematic errors remain present in the DD observation data, since their patterns are generally different between the individual receivers. It can however be seen that the initial receiver phase and clock offset are removed from the carrier phase ambiguities, transforming them to integers. The model shows that once these integer carrier phase ambiguities are correctly resolved the accompanying observations are transformed to highly accurate relative ranges, allowing for precise relative positioning.

The removal of the relative GPS receiver clock offset in the DD model however is done at the expense of one observation and the introduction of a correlation between the observations of the same type and frequency. This is demonstrated by taking the SD P_1-code observations of the previous subsection and transforming them to their DD equivalents, using the SD observation from GPS satellite j as a common reference,

$$\begin{pmatrix} P_{1AB}^{jh}(t) \\ P_{1AB}^{jk}(t) \\ P_{1AB}^{jm}(t) \end{pmatrix} = \begin{pmatrix} -1 & 1 & 0 & 0 \\ -1 & 0 & 1 & 0 \\ -1 & 0 & 0 & 1 \end{pmatrix} \begin{pmatrix} P_{1AB}^{j}(t) \\ P_{1AB}^{h}(t) \\ P_{1AB}^{k}(t) \\ P_{1AB}^{m}(t) \end{pmatrix} . \tag{2.36}$$

This is equally expressed as $\mathbf{z}_{DD}^{P_1} = \mathbf{T}_{DD}\mathbf{z}_{SD}^{P_1}$, and the accompanying measurement covariance matrix, $\mathbf{Q}_{DD}^{P_1}$, is obtained by propagating the SD one,

$$\mathbf{Q}_{DD}^{P_1} = \mathbf{T}_{DD}\mathbf{Q}_{SD}^{P_1}\mathbf{T}_{DD}^{T} = \begin{pmatrix} (\sigma_{AB,P_1}^{jh})^2 & (\sigma_{AB,P_1}^{j})^2 & (\sigma_{AB,P_1}^{j})^2 \\ (\sigma_{AB,P_1}^{j})^2 & (\sigma_{AB,P_1}^{jk})^2 & (\sigma_{AB,P_1}^{j})^2 \\ (\sigma_{AB,P_1}^{j})^2 & (\sigma_{AB,P_1}^{j})^2 & (\sigma_{AB,P_1}^{jm})^2 \end{pmatrix} , \tag{2.37}$$

where e.g. $(\sigma^{jh}_{AB,P_1})^2 = (\sigma^{h}_{AB,P_1})^2 + (\sigma^{j}_{AB,P_1})^2$. Here it can immediately be seen that all DD observations are correlated with the variance of the reference SD observation, σ^{j}_{AB,P_1}. Since the DD observations are only formed between SD observations of the same type and frequency, no further cross-correlations are introduced. The overall covariance matrix of the DD observation model is thus block diagonal:

$$\mathbf{Q}_{DD} = \begin{pmatrix} \mathbf{Q}^{P_1}_{DD} & \mathbf{0} & \mathbf{0} & \mathbf{0} \\ \mathbf{0} & \mathbf{Q}^{P_2}_{DD} & \mathbf{0} & \mathbf{0} \\ \mathbf{0} & \mathbf{0} & \mathbf{Q}^{L_1}_{DD} & \mathbf{0} \\ \mathbf{0} & \mathbf{0} & \mathbf{0} & \mathbf{Q}^{L_2}_{DD} \end{pmatrix}, \tag{2.38}$$

where the sub-matrices are of the same structure as in eqn. 2.37.

Again a linearization of the DD geometric ranges, $\rho^{jk}_{AB}(t)$, between the respective antenna phase centers has to take place before the DD observations can be used in relative positioning applications. When using eqn. 2.33, the linearization reads

$$\begin{aligned} \rho^{jk}_{AB}(t) &= \rho^{k}_{AB}(t) - \rho^{j}_{AB}(t) \\ &= \rho^{jk}_{AB0}(t) - (\mathbf{e}^{k}_{B}(t) - \mathbf{e}^{j}_{B}(t)) \cdot \Delta\mathbf{r}_{AB}(t) \\ &\quad + (\mathbf{e}^{k}_{AB}(t) - \mathbf{e}^{j}_{AB}(t)) \cdot \Delta\mathbf{r}_{A}(t) \\ &\quad + \mathbf{e}^{k}_{AB}(t) \cdot \Delta\mathbf{r}^{k}(t) - \mathbf{e}^{j}_{AB}(t) \cdot \Delta\mathbf{r}^{j}(t), \end{aligned} \tag{2.39}$$

where again $\Delta\mathbf{r}_A(t) = 0$, $\Delta\mathbf{r}^k(t) = 0$ and $\Delta\mathbf{r}^j(t) = 0$ due to the fact that the positions of the reference GPS receiver A and GPS satellites are assumed known. The relative position is still incremented using exclusively the line of sight vectors of GPS receiver B. Substitution of the linearized DD geometric range into the dual frequency DD observation model results in the DD positioning model. Here, similar as in the UD and SD case, it is assumed that all (systematic) errors and biases, captured in the M^{jk}_{AB} terms, are zero. This assumption is again not expected to change anything in the correlations derived earlier. The dual frequency DD positioning model is now exclusively parameterized with the relative position (increment) between the phase centers of GPS receivers A and B, the DD ionospheric path delays and the (integer) DD carrier phase ambiguities.

When comparing the SD and DD models one might suggest that in the DD formulation there is even further error reduction, positively influencing the results in positioning applications. This is however not true since in the SD case the mean value of all unmodeled effects was absorbed by the relative receiver clock, which is now eliminated at the cost of one observation. When the earlier derived DD correlations are correctly taken into account the result of a position adjustment in both models is the same. However, the DD formulation has the advantage that it allows for a direct estimation of the integer DD carrier phase ambiguities, which, as pointed out earlier, transform the accompanying DD observations to highly accurate relative ranges, allowing for precise relative positioning.

2.6 GPS data quality

For all precise GPS positioning applications the quality of the GPS observation data used is of utmost importance. Ideally the data is only subject to a random noise with zero mean and a small standard deviation. However, as discussed in the previous sections, with real-world GPS applications channel biases and multipath and/or other types of systematic errors are most likely to be present and can influence the final position solution accuracy, if not properly accounted for. Since for this research all these errors are neglected in the functional part of the positioning model, they have to be accounted for in the stochastic part. Here the combination of the unmodeled errors and the thermal measurement noise is still assumed to be uncorrelated and to have a zero mean, but with a higher variance than for thermal noise only.

This section gives an overview of the unmodeled errors to the best possible extent in an effort to provide some background and physical interpretation of the observation variances used for the different CHAMP and GRACE positioning applications throughout this research. This is accomplished by in-flight performance analyses, using data obtained from the main POD antennas, of the BlackJack GPS receivers onboard the CHAMP and GRACE spacecraft in the analogy of *Montenbruck and Kroes* [2003], as well as by a pre-flight validation of the BlackJack follow-up, the Integrated GPS Occultation Receiver (IGOR), for the TerraSAR-X mission [*Montenbruck et al.*, 2005*c*].

2.6.1 Biases and correlations

Since the IGOR pre-flight validation test is executed on a GPS signal simulator (Spirent STR4760), using a two hour spaceborne scenario, it allows for some analysis on inter-frequency and inter-channel code biases and correlations of the thermal noise, that cannot, or not easily, be assessed with the in-flight performance analysis. Both the in-flight and pre-flight analysis conducted show a constant differential code bias between the C/A and P_1-code observations, $P_1 - C/A \approx +0.3$ m, which is more or less the same for all satellites and all receivers involved. In addition, in the pre-flight validation test [*Montenbruck et al.*, 2005*c*] a constant bias between the P_2 and P_1 code observations, $P_2 - P_1 \approx +4.5$ m, again constant over time for all GPS satellites, was observed. This resembles a difference in the geometric range, and thus in the signal travelling time of approximately 0.015 μs, resulting in displacements of 0.05 mm for the GPS satellites and 0.14 mm for the LEO spacecraft that can be neglected in POD applications, and even cancels out in relative positioning when the same for all GPS receivers involved. In addition, a larger systematic timing error of approximately 0.45 μs was found for the carrier phase observables, corresponding to a roughly 4 mm displacement. Again, for relative positioning applications this error cancels out if the same receivers are used (which is the case for this research since both GRACE S/C are equipped with the BlackJack GPS receiver). Furthermore the pre-flight validation test showed that inter-channel biases are mostly small and

around zero, but can have a maximum of 0.10 m for the P_1, and 0.40 m for the P_2 code. It remains unclear though, to which extent uncalibrated biases inside the employed GPS signal simulator are responsible for part, or all, of these observed inter-channel code biases.

In addition, no evidence for correlations between the noise of the P_1 and P_2 code observations was found in *Montenbruck et al.* [2005*c*]. This is expected since for codeless tracking the individual P codes are still used to track the encrypted signal, making the process uncorrelated. The carrier phases of the encrypted codes however cannot be properly tracked without help of the C/A code phase and each other, and correlations between the inter-frequency carrier phase observations are expected at this point, as was shown earlier for several geodetic GPS receivers [*Tiberius et al.*, 1999] and during a performance assessment of the NovAtel OEM4-G2 receiver [*Montenbruck*, 2003]. Unfortunately a zero baseline test, required for finding such correlations, could not be carried out in the limited time available for the pre-flight validation test, and correlations between the carrier phase observables within the BlackJack GPS receiver can therefore only be suspected at this point. Nevertheless, as stated earlier, all observations from a single GPS receiver are still treated as uncorrelated throughout this research.

2.6.2 Multipath and systematic effects

Multipath errors in a GPS receiver are caused by the superposition of the direct signal with interfering signals taking a different signal path. They are typically associated with signal reflections in the vicinity of the receiving antenna, in which case the resulting errors depend on the path difference, the strength and polarization of the reflected radiation as well as receiver internal properties. While carrier-phase multipath is confined to a quarter wavelength, code multipath may be as large as 0.5 code chips for distant reflectors ([*Leva et al.*, 1996]; [*Braasch*, 1995]). This makes carrier phase multipath harder to visualize. In case of a spaceborne GPS receiver, multipath reflections are exclusively caused by the satellite's surfaces, excluding rendezvous and docking type of applications, and the maximum path delay is thus of the order of the linear spacecraft dimension. Still choke-ring antennas are used for most scientific satellite missions in an effort to minimize the already restricted multipath.

Other types of systematic errors, such as electronic signal interference, cannot be separated easily from pure multipath errors, because they mostly exhibit a similar pattern. However, the only concern with both types of errors is the impact they have on positioning applications. This is especially true in the case of relative positioning, where these errors influence on two different levels. First of all, the integer carrier phase ambiguities have to be resolved, for which the pseudorange observations are heavily needed. Large errors in the pseudoranges can therefore lead to erroneous integer estimates, dramatically degrading the relative position solution. Second, after resolution of the integers, the carrier phases can be used

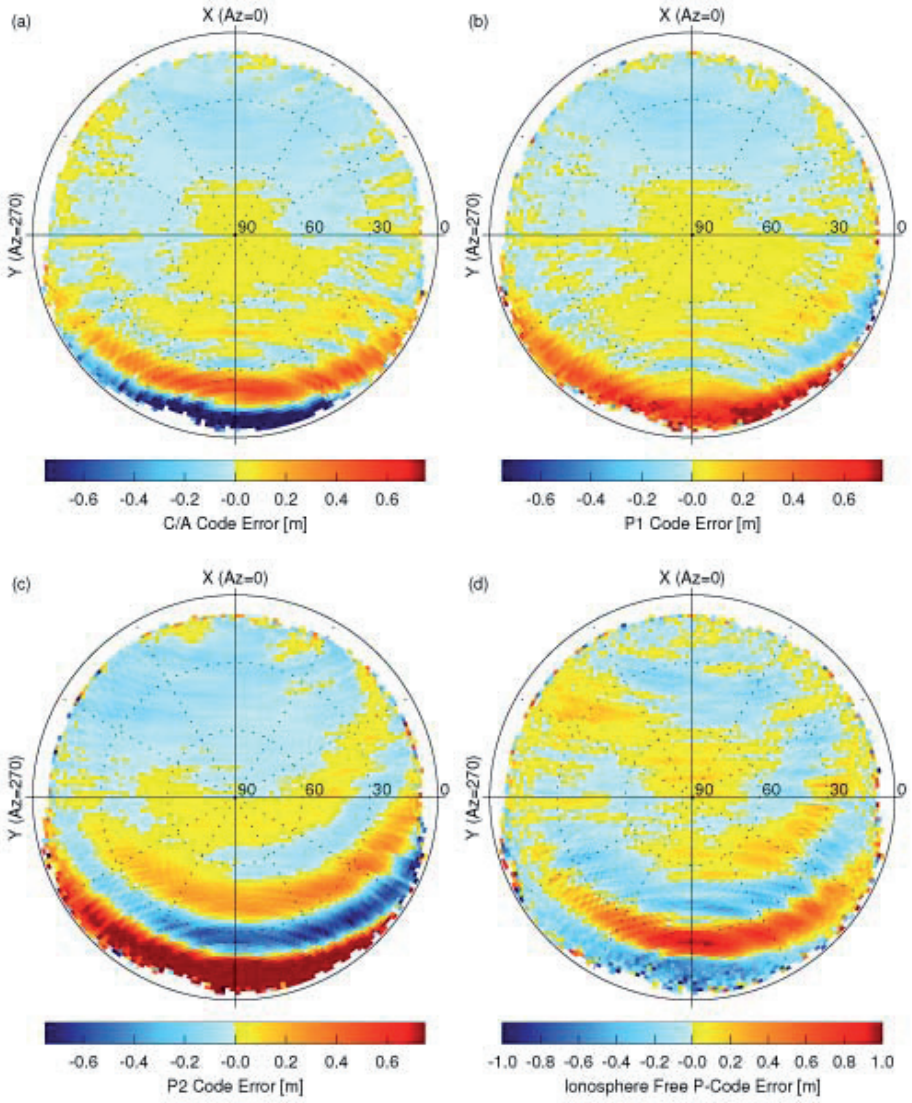

Figure 2.2 Systematic errors on the C/A (a), P_1 (b), P_2 (c) and ionosphere free (d) pseudorange observation data obtained from the main POD antenna of the CHAMP BlackJack GPS receiver. The errors are expressed in the body fixed antenna diagram (see text).

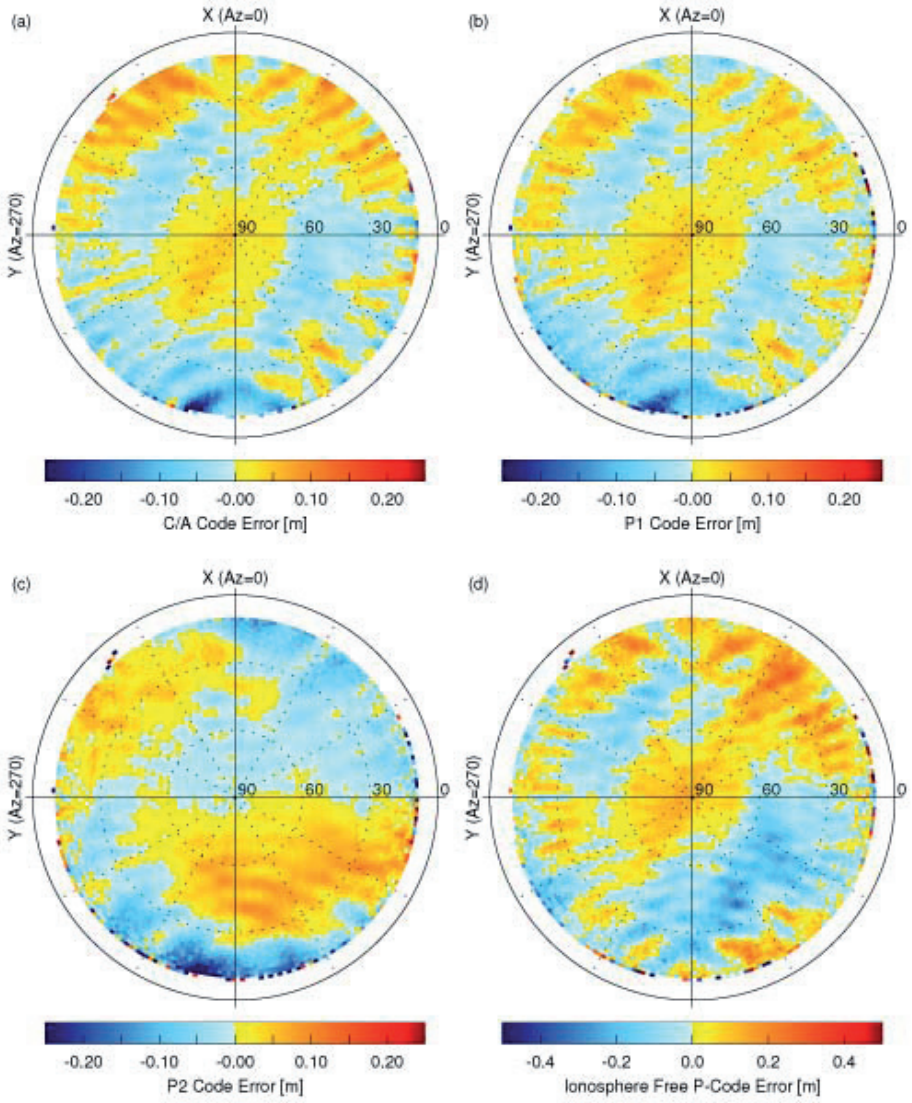

Figure 2.3 Systematic errors on the C/A (a), P_1 (b), P_2 (c) and ionosphere free (d) pseudorange observation data obtained from the the main POD antenna of the GRACE A BlackJack GPS receiver. The errors are expressed in the body fixed antenna diagram (see text).

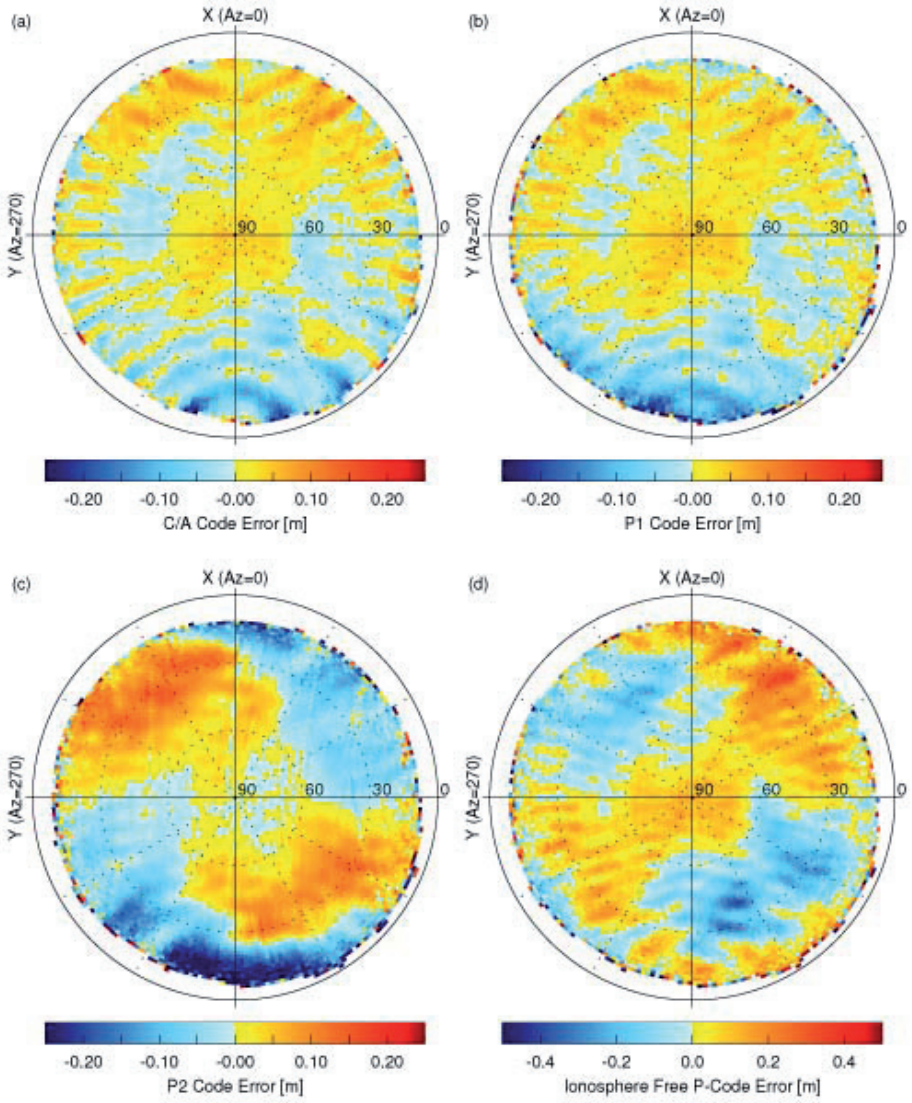

Figure 2.4 Systematic errors on the C/A (a), P_1 (b), P_2 (c) and ionosphere free (d) pseudorange observation data obtained from the the main POD antenna of the GRACE B BlackJack GPS receiver. The errors are expressed in the body fixed antenna diagram (see text).

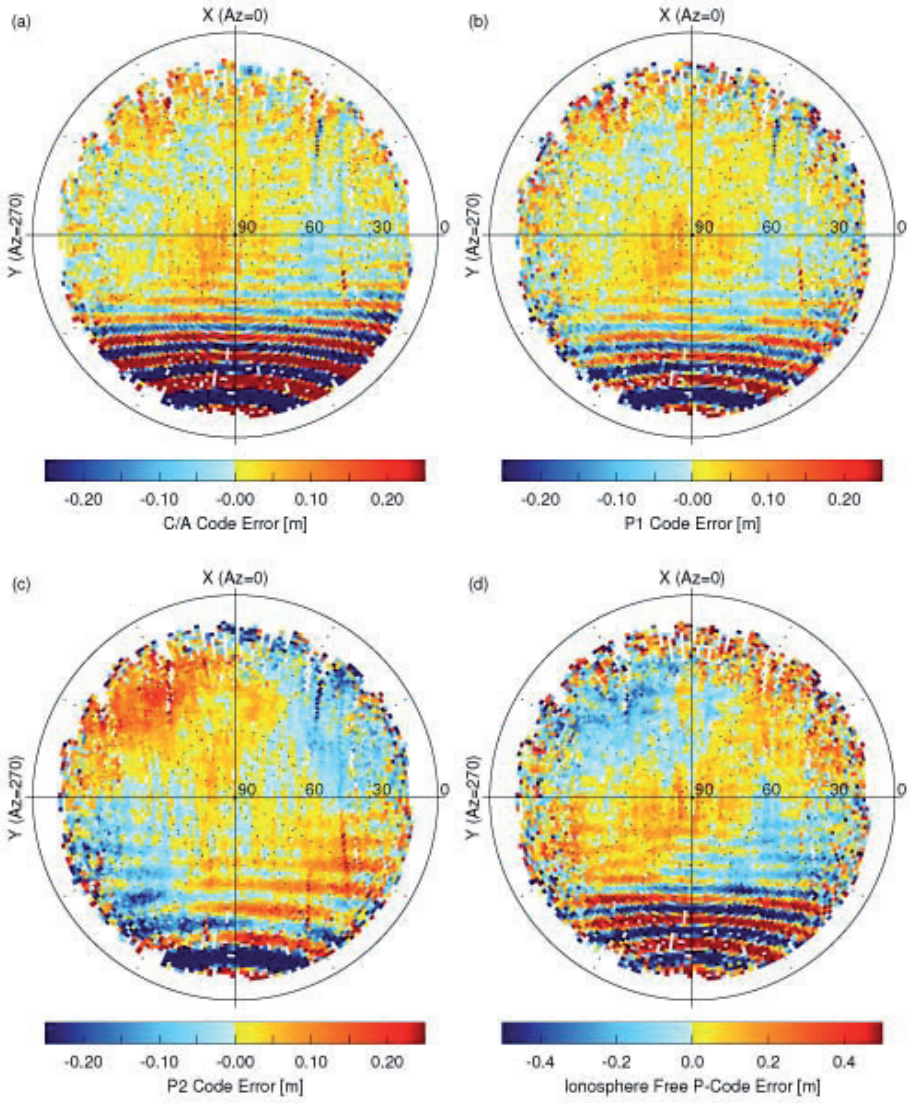

Figure 2.5 Systematic errors on the C/A (a), P_1 (b), P_2 (c) and ionosphere free (d) pseudorange observation data obtained from the the main POD antenna of the GRACE B BlackJack GPS receiver during the time the occultation antenna was active. The errors are expressed in the body fixed antenna diagram (see text).

as highly accurate relative ranges. Here carrier phase multipath easily exhibits the noise level and can deteriorate the desired positioning accuracy.

In this subsection the combined multipath and systematic errors present in the pseudorange observations of the CHAMP and GRACE GPS data are analyzed using the multipath equations derived earlier (eqn. 2.23). Besides the individual P-code observations the errors in the ionosphere free combination and in the C/A code are also presented. Since the errors concerned are generally of a repetitive nature they are best expressed in an antenna diagram as function of the azimuth and elevation in the S/C body frame. This is accomplished as follows. First, the carrier phase biases of the multipath equations are calibrated over an entire (continuous tracking) pass, using good quality pseudoranges. Then, for each pseudorange observation the combined multipath and systematic errors and measurement thermal noise are obtained, using the calibrated carrier phase biases, which are saved into the corresponding azimuth/elevation bin. The azimuth and elevation bins are defined in the respective CHAMP and GRACE body fixed reference systems that can be obtained using the transformations from section 3.2. After having processed all data the average value of each bin is taken as the combined systematic/multipath error, where the average contribution of the noise per bin is assumed to be zero. It must be mentioned that the mean contribution of the pseudorange errors over a single satellite pass will be absorbed by the bias in the calibration process. Within this research, the results of this analysis are therefore purely intended for visualization of errors present in the pseudorange data and not for the creation of a corrective model of any kind.

For a good visualization the azimuth/elevation grid should first of all be dense enough, but also contain enough data points per bin and has to cover a larger time span to be able to observe if there is any pattern change over time. Therefore, a data arc of 51 consecutive days, covering July 9 through August 28 2003, has been processed for each individual S/C according to the previously described scheme. The results can be found in Figures 2.2 (CHAMP), 2.3 (GRACE A) and 2.4 (GRACE B), where each bin contains at least 10 data points for elevations above 20 degrees and 5 data points below this mask. The error plots presented here were found to be constant over time when comparing them with plots of other, shorter time spans.

It has already been shown by *Montenbruck and Kroes* [2003] that the pseudorange data obtained from the POD antenna on CHAMP, Fig. 2.2, is severely influenced by systematic errors, which again are seen here. The errors on the individual code observations have maximum values of approximately 0.6 m, both positive and negative, for low elevations. Due to the different pattern, these errors are only slightly amplified in the ionosphere free combination where a maximum of 0.8 m is observed. These observed errors are not caused by multipath but were earlier related to cross-talk interference between the GPS occultation and POD antenna strings in the GPS receiver front end [*Montenbruck and Kroes*, 2003]. The effect confines itself to the aft looking hemisphere, since it only occurs if GPS signals from the same GPS satellite are simultaneously received by both antennas.

When examining the results for the GRACE satellites the systematic patterns are generally on the sub-dm level with maximum values of approximately 0.2 m in both positive and negative direction for the individual pseudorange observations. The absence of the large systematic interference as seen on CHAMP is explained by the fact that, although physically present, the GPS occultation antenna is not activated on either of the S/C. Although the errors on GRACE B are slightly higher, the overall patterns of both spacecraft show great similarity, which, due to the fact that the GRACE S/C are identical, might actually be the visualization of true signal multipath.

The ionosphere free pseudorange error plots for the GRACE S/C, Fig. 2.3d and 2.4d, show great similarities with the ones derived by *Haines et al.* [2005]. Here, similar plots were created using ionosphere free pseudorange and carrier phase post-fit measurement residuals, resulting from the GRACE spacecraft reduced-dynamic POD process, over a period of two years. In addition to the pseudorange error visualization, collecting post-fit residuals also allows for a visualization of multipath and systematic errors on the ionosphere free carrier phase observation, which cannot be created using the multipath equations. However, these residuals are generally small and can easily be affected by errors from e.g. the dynamic modeling or in the GPS satellite clock offsets. Therefore care should be taken when interpreting them. Nevertheless, it is learned that for ionosphere free carrier phase observations, the systematic errors are generally small and appear to have maximum values of around 1 cm, both positive and negative. Furthermore, in *Haines et al.* [2005] the systematic error plots of both ionosphere free observation types were also compared with the results of a multipath simulation. For the carrier phase the simulation and the residual plots show great similarity, which can unfortunately not be said for the pseudorange. It therefore remains unclear if the systematic pseudorange errors found for the GRACE S/C are truly the result of multipath or of something else.

As mentioned before, the GRACE GPS occultation antennas were not activate during the period for multipath analysis. More specifically, until the time of writing only the GPS occultation antenna on GRACE B has been activated for testing purposes on two occasions. The first test conducted covered a time span of slightly over 24 hours during July 28 and 29 2004, The second test period on the other hand covers over a week, December 2 to 9 2004. Although for an analysis of the systematic errors the second test period is favored, any GRACE data beyond August 1 2004 has not been made public so far. Therefore the results of the multipath analysis of GRACE B, shown in Fig. 2.5, are obtained using the 24 hour test period from July 2004. Although the plots are a bit noisy due to the limited data available it can be clearly observed that a similar type of interference as for CHAMP is now also present in the GRACE B pseudorange observations. This effect is basically added to the systematic errors already present. Again the effect is confined to the aft looking hemisphere, where the signals from a GPS satellite are observed by both the POD and the occultation antenna. It appears however that the fringes of the effect are smaller and are repeated multiple times in comparison to CHAMP. This can be attributed to the fact that the physical separation between the GPS

POD and occultation antennas is larger on the GRACE S/C than it is on CHAMP. However, more data should be accumulated, and a more thorough analysis should be conducted, before any conclusive statement on this matter can be made.

2.6.3 Measurement noise

All GPS observations are subject to a random thermal noise with zero mean and a standard deviation (σ). The noise level depends on the observation type and on the signal strength at which the observation was taken. Pseudoranges typically have an average noise on the dm level, whereas carrier phase observations are well known to have a maximum noise error of only a few mm. In order to allow a proper interpretation of the noise characteristics for both observation types, the noise standard deviation can best be expressed as a function of the carrier to noise density ratio (C/N_0), in order to e.g. relate it to tracking loop characteristics [*Ward*, 1996].

In the case of CHAMP and GRACE the Signal to Noise Ratio (SNR) of all code and accompanying carrier phase observation types are also provided in the GPS data file. This allows for the derivation of the carrier to noise density ratio, which in case of the BlackJack GPS receiver is specified as [*Montenbruck and Kroes*, 2003]:

$$C/N_0 = 20 \log_{10} \left(\frac{\mathrm{SNR}}{\sqrt{2}} \right). \tag{2.40}$$

For the in-flight GPS pseudorange data, the noise level can be assessed by using the pseudorange residuals from each of the azimuth/elevation data bins in the multipath and systematic error analysis and group them into carrier to noise density ratio data bins. Due to the fact that small systematic errors can still be present, the RMS of each of these bins represents an upper limit of the pseudorange measurement noise standard deviation. The results of this analysis is shown in Fig. 2.6, for CHAMP (top), GRACE A (middle) and GRACE B (bottom) respectively. The low noise on the C/A code is caused by the fact that this observation can be tracked directly, whereas the P_1 and P_2 code observations are obtained using a form of semi-codeless tracking. Another result of the semi-codeless tracking process is the lower C/N_0 for the concerned observations at the same elevations. Typically, for C/A code observations an elevation of 10° corresponds to a C/N_0 of 40 dB-Hz, whereas for the P_1 and P_2 the corresponding C/N_0 values are respectively 25 dB-Hz and 20 dB-Hz. The figure shows a large difference between especially the code noise for GRACE A and GRACE B, which remains unexplained for now. The same type of noise figures were also derived in the pre-flight IGOR validation test [*Montenbruck et al.*, 2005*c*]. Here, the C/A code noise ranges from 20 cm at a C/N_0 of 40 dB-Hz to 5 cm at 58 dB-Hz. For the P_1 and P_2 code observations the noise respectively varied from 60 cm and 45 cm at a C/N_0 of 20 dB-Hz to 5 cm for both at a C/N_0 of 53 dB-Hz. As can be seen here the noise on the P_2 code is actually lower than

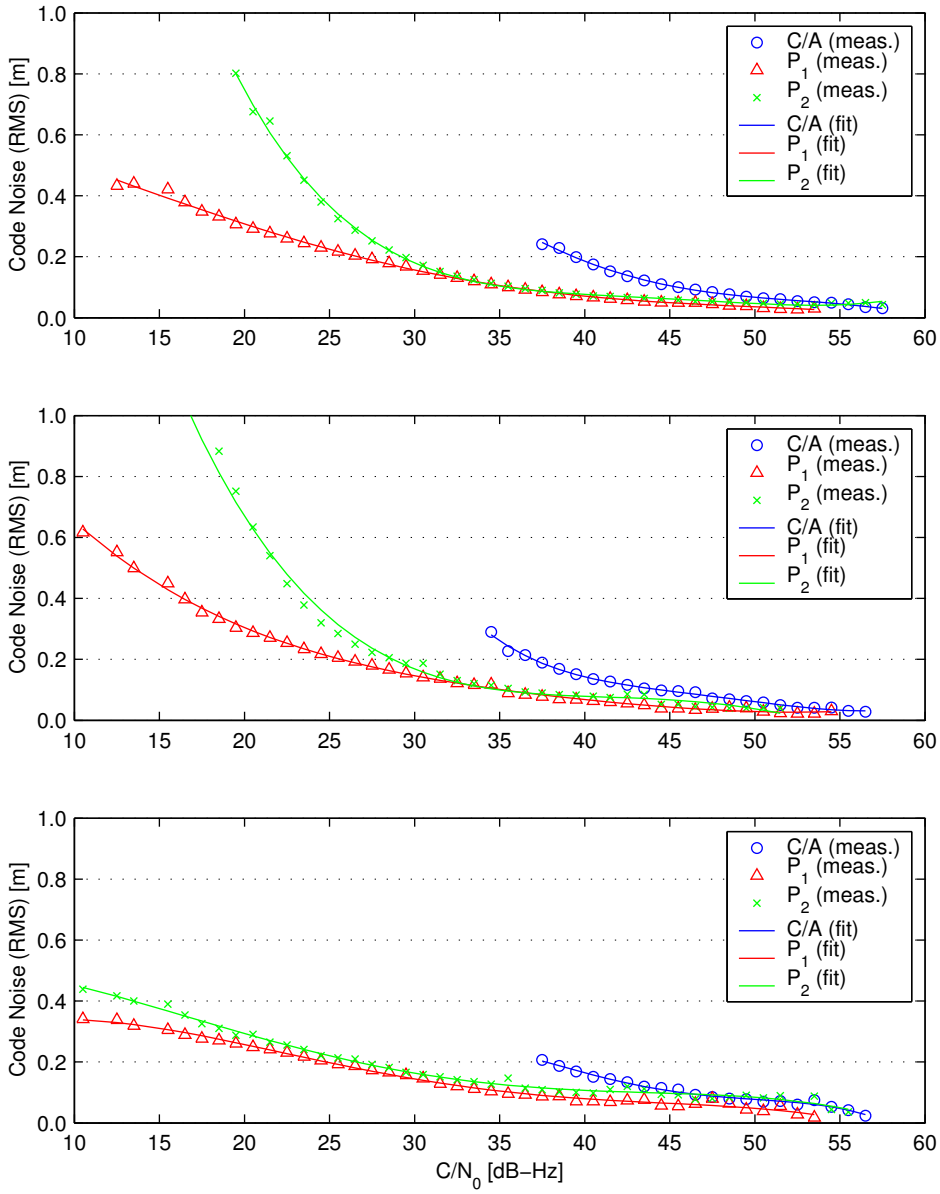

Figure 2.6 Pseudorange noise (measured and fitted), after the removal of the systematic effects, as function of the carrier to noise density ratio (C/N_0) for CHAMP (top), GRACE A (middle) and GRACE B (bottom).

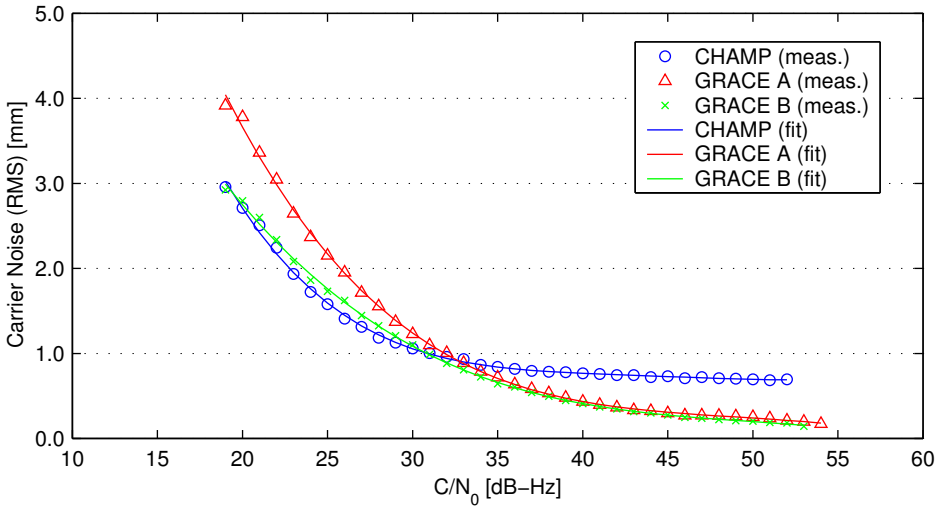

Figure 2.7 Upper limit of the carrier phase noise (measured and fitted) on the L_1 observation, as function of the carrier to noise density ratio (C/N_0) for CHAMP, GRACE A and GRACE B.

the one on the P_1 code. An explanation for this was not given, and contradicts the results of all three in-flight analyses.

Unfortunately the carrier phase noise was not assessed in the pre-flight validation test, but some information on this can be obtained from the in-flight scenarios. Each of the BlackJack GPS receivers gives out the carrier phase observation of the P_1 and C/A codes, L_1 and L_A respectively. Since they are taken on the same frequency the ionospheric path delay and multipath and systematic errors are the same. When taking the difference of these observations the only parameters remaining are the difference between the (constant) carrier phase biases on each of the observations and the combined thermal noise. When again assuming no correlation, the combined noise

$$\sigma_{(L_1-L_A)} = \sqrt{\sigma_{L_1}^2 + \sigma_{L_A}^2} > \sigma_{L_1} > \sigma_{L_A}, \tag{2.41}$$

can now serve as an upper limit of the noise on L_1, when this noise is assumed larger than the one on the C/A code phase observable. For each continuous pass this carrier phase difference is constructed and corrected for its bias. The resulting carrier phase noise is then again grouped into C/N_0 data bins, from which a curve in analogy with the code noise is created. For all three in-flight scenarios the carrier phase noise curves are presented in Fig 2.7. As can be seen here the noise RMS is 3 to 4 mm for observations taken at low elevations (20 dB-Hz) whereas a sub-mm noise, 0.3 to 0.7 mm, is found for observations taken at high elevations (53 dB-Hz).

Overall it can be said that the empirically derived noise curves, for each of the in-flight data sets, could be used for proper data weighting if the multipath and systematic errors would be corrected or modeled for as well. Since this is not the case, these curves, and the multipath analysis from the previous subsection, are merely presented here for motivating the order of magnitude of the observation data weights used for the different positioning applications later on.

Chapter 3
Precise orbit determination

Nowadays most Earth observation satellites require a precise post-facto knowledge of the orbit in order to fulfill the scientific mission requirements. This is especially true for remote sensing applications like satellite altimetry and SAR interferometry, but also for gravity missions. Furthermore, as already mentioned in the previous chapter (section 2.5.1), spacecraft formation flying applications also require an accurate knowledge of the position of the reference spacecraft, in order to minimize errors in the relative position computation.

For this study a total of three proposed precise orbit determination strategies using undifferenced ionosphere free GPS observations have been implemented and tested. They comprise purely kinematic as well as reduced dynamic data processing schemes. Since these POD techniques also form the conceptual bases for the developed relative positioning methodologies, that are presented in the next chapter, a detailed overview of them is provided here.

The choice of using undifferenced GPS observation data for the developed POD techniques is primarily motivated by the deactivation of Selective Availability, i.e. the intentional dithering of the GPS satellite clock and manipulation of the broadcast ephemerides [*Hofmann-Wellenhof et al.*, 2001]. As a result precise (high rate) post-facto GPS satellite clock products and ephemerides data, required for precise positioning using undifferenced GPS data, are available nowadays (section 3.1). In order to obtain a high precise satellite orbit, there is thus no longer a direct need for single, double or even triple difference GPS based POD schemes, see e.g. *Svehla and Rothacher* [2003] or *Van den IJssel et al.* [2003], which require the usage of GPS data from a network of ground based GPS reference stations. The complex data handling, associated with such schemes, can thus be avoided, which is found to be one of the major benefits of using undifferenced GPS observation data.

This chapter starts with an overview of the GPS orbit and clock products, the GPS ephemerides, used for the developed GPS POD applications. This is followed by a description of reference frame conventions and transformations used throughout the rest of this thesis. A detailed description of each of the different

POD strategies, a kinematic and a reduced dynamic batch least-squares estimator and an extended Kalman filter, is given thereafter. The chapter is concluded with an analysis of the POD results from each of the developed strategies using data from the CHAMP and GRACE mission.

3.1 GPS orbit and clock products

Any type of precise positioning application using undifferenced GPS data requires an accurate knowledge of the GPS satellite positions and clock offsets. These so called GPS ephemerides are provided by the International GNSS Service (IGS), formerly known as the International GPS Service. The IGS began to provide precise GPS ephemerides information for geodetic users and surveyors as early as 1994 [*Kouba*, 2002] when GPS had almost reached its fully operational status. Within the IGS, various Analysis Centers derive their own, independent GPS orbit and clock solutions. These are subsequently merged into combined IGS products applying proper weighting and quality control. Both the network of IGS ground stations and the quality of the resulting products have continuously increased over the past decade.

The IGS currently provides three types of GPS ephemerides products; the final, rapid and ultra-rapid ephemerides. The final IGS ephemerides are released some 13 days after the end of a GPS week and have a reported position and clock accuracy of better than 5 cm [*IGSCB*, 2005]. The rapid products, in contrast, are available within 17 hours past the end of each day and, meanwhile, achieve an almost identical accuracy. The ultra-rapid orbit and clock products were created in response to the increasing need of near real-time GPS processing. They are made available four times per day and have a latency of 3 hours past the last GPS observations. In addition to the GPS orbit and clock data based on actual GPS observation data, the ultra-rapid ephemerides also contain a 24 hour prediction. The predicted orbit information is presently accurate to roughly one decimeter, whereas irregularities of the clock drift cause prediction errors on the order of one meter [*IGSCB*, 2005].

All types of IGS ephemerides products provide GPS orbit and clock offset data in the standard SP3 format [*Remondi*, 1991] on a regular 15 min grid. The positions and velocities in the SP3 format are provided in the Inertial Terrestrial Reference Frame (ITRF) [*McCarthy*, 1996] and relate to the center of gravity of the GPS satellites. The regular grid point spacing allows for accurate polynomial interpolation of the GPS satellite position at the time of a measurement, which for this research is accomplished using an 8^{th}-order Lagrange interpolation method. After interpolation to the epoch of interest the GPS satellite position needs to be corrected for the antenna phase center offset before it can be used in positioning. Throughout this research these offsets are assumed to be constant. Phase center variations for the different observation types and GPS satellites, such as mentioned by *Haines et al.* [2005], are ignored here. For all IGS ephemerides products the

antenna phase center offsets, defined in the GPS satellite body coordinate system which originates in the center of gravity of the satellite, are specified in Table 3.1.

Table 3.1 Antenna phase center offsets for the GPS satellites it their body coordinate system.

	X [m]	Y[m]	Z[m]
Block II/IIA	0.279	0.000	1.023
Block IIR	0.000	0.000	0.000

As can be seen here, the assumed antenna phase center positions coincide with the satellite center of mass for the newer Block IIR satellites. For the other GPS satellites the offset correction still needs to be applied. The attitude model used for this is described in *Xu* [2003]. Here, the z-axis of the satellite always points towards the center of the Earth, the y-axis is perpendicular to the vector between the Sun and the GPS satellite and the x-axis completes the right-handed coordinate system.

In contrast to orbital data, high-order polynomial interpolation is not suitable for clock parameters due to the underlying random noise processes, and linear interpolation is therefore advisable. The errors resulting from the interpolation of clock data depend on the interval size and the Allan variance of the respective clock, cf. [*Kouba*, 2002], [*Zumberge and Gendt*, 2001]. Therefore, supplementary to the SP3 ephemerides products, clock offset data at 5 min intervals are made available as part of separate (final and rapid) clock products. In response to the demand for even higher rate clock data, several IGS Analysis Centers, such as the Center for Orbit Determination in Europe (CODE) and JPL, have made their clock solutions, at 30 second intervals, and accompanying orbits publicly available.

The different POD applications described in this chapter process the GPS data at intervals of nominally 30 seconds. In order to achieve the best results use is made of the CODE high rate clocks and accompanying orbits, to which the same antenna offset and attitude model is applied as for the IGS products. When not available they are replaced with final IGS ephemerides supplemented with the 5 minute clock corrections. In *Montenbruck et al.* [2005*b*] an assessment of the error associated with linear interpolation of the 5 minute, and for completeness also the 15 minute, clock data set, is presented using the high rate 30 second CODE clock solutions. Different test data sets were first reduced to 5 min and 15 min intervals, then interpolated linearly to 30 s steps and finally compared with the original data. To explore the dependence on the employed clock type, Block II/IIA satellites operating cesium clocks, Block II/IIA satellites working with rubidium clocks and Block IIR satellites that use rubidium clocks exclusively have been distinguished in the analysis presented in *Montenbruck et al.* [2005*b*]. Comparisons conducted at different epochs in the 2000-2004 time frame did not indicate a general trend in the clock noise characteristics. It was therefore stated that it is appropriate to work with time-averaged values for the clock interpolation error that are summarized in Fig. 3.1 for the individual clock types.

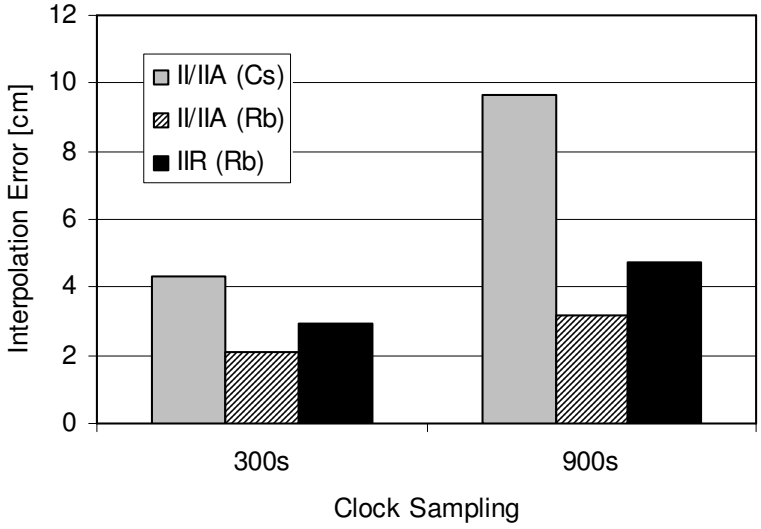

Figure 3.1 RMS error of GPS clock interpolation for 5 and 15 minute intervals. (Source: [*Montenbruck et al.*, 2005*b*])

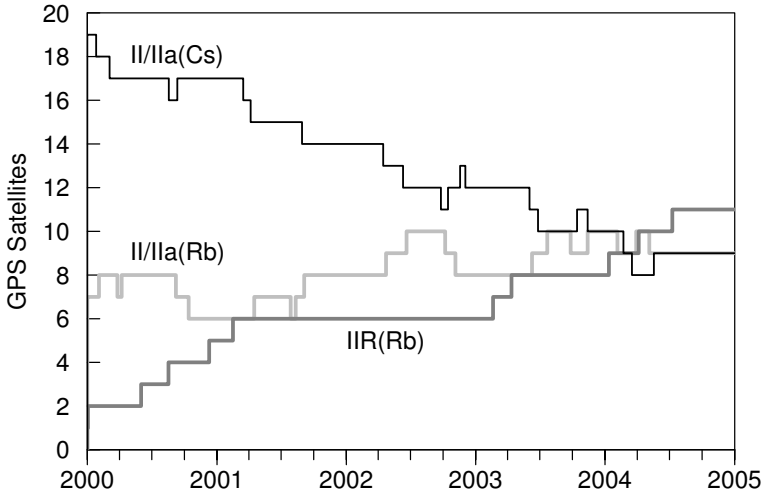

Figure 3.2 Number of GPS satellites operating cesium (Cs) and rubidium (Rb) clocks over time. (Source: [*Montenbruck et al.*, 2005*b*])

The biggest errors are clearly encountered for Block II/IIA cesium clocks, which exhibit an RMS interpolation error of almost 10 cm at 15 min intervals. This notably exceeds the accuracy of IGS final and rapid clock solutions and underlines the need for 5 min or even higher-rate clock products for undifferenced GPS data processing. Among the rubidium clocks, the best interpolation results are obtained

for Block II/IIA satellites. For 5 min intervals the interpolations error decreases to a few centimeters for all clock types, even though the relative gain for rubidium clocks is less pronounced than for the Block II/IIA cesium clocks. Over the past five years, a notable number of Block II/IIA satellites have been replaced by the follow-on IIR model. Also, numerous II/IIA satellites no longer operate their cesium clocks but have switched to one of their backup rubidium clocks. The fraction of GPS satellites operating cesium clocks has thus decreased from 2/3 in early 2000 to about 1/3 in late 2004 (Fig. 3.2). According to *Montenbruck et al.* [2005*b*], this change has resulted in a continuous reduction of the average clock interpolation error for the entire GPS constellation from about 8 cm to 6 cm for 15 min interpolation and from 4 cm to 3 cm for 5 min interpolation. The results presented here are in good consistency with an analysis of GPS clock data performed by *Zumberge and Gendt* [2001] right after the deactivation of Selective Availability. Based on a two weeks data set in May 2000, these authors determined an average interpolation error of 3.5 cm for 5 min interpolation that decreases linearly to 4 mm at 30 s sampling.

3.2 Reference frame transformations

Throughout the various applications discussed in this chapter and the next one position coordinates are expressed in different reference systems. The just mentioned GPS ephemerides data for example are provided in the ITRF, whereas the reduced dynamic orbit determination applications require the integration of the equations of motion of the user spacecraft, i.e. CHAMP and/or GRACE, in the International Celestial Reference Frame (ICRF) [*McCarthy*, 1996]. In addition, the phase center offset of the receiving GPS antenna with respect to the center of mass of the user spacecraft also has to be accounted for. To this extent two reference frame transformations, used throughout this entire research are provided in the following.

First, whenever a position vector in the ICRF, $\mathbf{r}_{\mathrm{ICRF}}$, requires transformation to the ITRF, $\mathbf{r}_{\mathrm{ITRF}}$, this is accomplished by

$$\mathbf{r}_{\mathrm{ITRF}} = \mathbf{U}(t)\mathbf{r}_{\mathrm{ICRF}}, \tag{3.1}$$

where $\mathbf{U}(t)$ is a 3×3 orthonormal matrix more specifically defined as

$$\mathbf{U}(t) = \mathbf{\Pi}(t)\mathbf{\Theta}(t)\mathbf{N}(t)\mathbf{P}(t). \tag{3.2}$$

Here, the individual matrices describe the coordinate change due to precession, $\mathbf{\Pi}(t)$, nutation $\mathbf{N}(t)$, Earth rotation, $\mathbf{\Theta}(t)$, and polar motion, $\mathbf{P}(t)$. The International Astronomical Union (IAU) conventions used to compute each of these matrices are summarized in Table 3.2 and can be found in *McCarthy* [1996] or *Montenbruck and Gill* [2000]. The required input for these models, such as polar motion parameters or the UT1-UTC time offsets, are captured in the so called Earth rotation parameters. For this research these parameters are obtained from either the International Earth Rotation Service (IERS) or from the IGS. For the POD applications in this chapter and the relative positioning applications in the next

Table 3.2 Reference system transformation conventions used for this research.

Item	Description
$\mathbf{\Pi}(t)$	IAU 1976 Precession
$\mathbf{N}(t)$	IAU 1980 Nutation
$\mathbf{\Theta}(t)$	IAU 1982 Sidereal Time
$\mathbf{\Pi}(t)$	Polar motion (IERS/IGS)

one, the ITRF convention used is ITRF2000, which is implied by the used IGS or CODE GPS ephemerides data. When following the reference frame transformations from Table 3.2 the ICRF convention used then becomes the Earth Mean Equator of J2000 (EME2000), also known as the J2000 inertial system.

The second transformation concerns the user spacecraft GPS antenna phase center offset. This offset is provided in the user S/C body system, which has its origin in the center of mass of the user S/C. Similar to the GPS satellites this offset is assumed to be constant, meaning that possible phase center variations are ignored. For this research, the 3×3 orthonormal matrix $\mathbf{C}(t)$ describes the transformation between a position, or antenna offset, in the S/C body frame, $\mathbf{r}_{\mathrm{BODY}}$, and in the ICRF, here EME2000, as

$$\mathbf{r}_{\mathrm{ICRF}} = \mathbf{C}(t)\mathbf{r}_{\mathrm{BODY}}. \tag{3.3}$$

Within the various applications this transformation matrix is constructed using precise S/C attitude data, which is obtained from star camera observations, and provided as quaternions. The exact definition of how the quaternions are handled for this research can be found in *Montenbruck* [2000]. When required, a transformation between the S/C body frame and the ITRF can now be simply handled by

$$\mathbf{r}_{\mathrm{ITRF}} = \mathbf{U}(t)\mathbf{C}(t)\mathbf{r}_{\mathrm{BODY}}. \tag{3.4}$$

Due to the fact that both $\mathbf{U}(t)$ and $\mathbf{C}(t)$ are orthonormal, their inverse, required for a transformation in the other direction, is simply given by their transposed.

3.3 Kinematic orbit determination

The Global Positioning System is the only tracking system to date allowing purely kinematic 3-dimensional positioning of LEO spacecraft. The real-time GPS receiver internal position solution, or navigation solution, is often a kinematic one constructed using solely pseudorange data. For onboard applications this position solution with a typical accuracy of several to tens of meters mostly suffices. Post facto kinematic POD applications on the other hand should provide reliable high accuracy position solutions and still have the benefit of relative simplicity, since no prior knowledge of the spacecraft trajectory is required. This means that carrier

phase observations must be included and an adequate processing technique has to be used.

Within this research kinematic GPS based POD is accomplished using a weighted linearized batch least-squares (LSQ) estimator, processing all ionosphere free carrier phase and pseudorange measurements, collected over data arcs with a typical length of a day (24 hours), at once. Subsequently, the parameters of interest, also referred to as the estimation parameters, used in modeling the GPS observations are then resolved from an overdetermined system of linear equations. This is done in such a way that the squares of the measurement residuals, in the metric of the measurement covariance, are minimized. Aside from the following brief overview, the fundamental concept of weighted linearized LSQ is extensively covered in literature, such as *Teunissen* [2000] and *Montenbruck and Gill* [2000], where in the latter the problem is discussed in the context of satellite orbit adjustment. Therefore, the focuss here is on those aspects that are of prime relevance for GPS based orbit determination.

When considering a linearization of the modeled GPS measurements, $\mathbf{h}(\mathbf{y})$, around an initial value, $\mathbf{y}_0$, of the estimation parameters, $\mathbf{y}$, the LSQ update of this initial value is given by

$$\Delta\mathbf{y} = (\mathbf{H}^T\mathbf{W}\mathbf{H})^{-1}\mathbf{H}^T\mathbf{W}(\mathbf{z} - \mathbf{h}(\mathbf{y}_0)), \tag{3.5}$$

resulting in the updated estimation parameters, $\mathbf{y} = \mathbf{y}_0 + \Delta\mathbf{y}$. Here, $\mathbf{z}$ is the vector containing the actual GPS observations and $\mathbf{W} = \mathbf{Q}_\mathbf{z}^{-1}$ is the accompanying weighting matrix, given by the inverse of their covariance matrix. Furthermore, the design matrix, $\mathbf{H} = (\partial\mathbf{h}(\mathbf{y}_0)/\partial\mathbf{y}_0)$, contains the linearized partial derivatives of the modeled measurements with respect to the estimation parameters. The part requiring inversion, $\mathbf{N} = \mathbf{H}^T\mathbf{W}\mathbf{H}$, is also referred to as the normal equations. Nonlinear estimation problems, such as GPS positioning applications, can be coped with by means of multiple iterations, where the updated estimation parameters are used as the initial values for the next iteration.

For spaceborne kinematic GPS positioning applications parametrization of pseudorange and carrier phase observations is relatively straightforward, and is done according to the UD ionosphere free GPS observation model, eqn. 2.19, and the linearization from eqn. 2.26. At any given measurement epoch t_i both observation types are parameterized with the phase center position of the GPS receiver antenna and the GPS receiver clock offset, $\mathbf{x}_i = (x_i; y_i; z_i; c\delta t_i)$. Since the spacecraft is continuously moving a new position and clock offset have to be determined at every epoch. In addition, the carrier phase observations also contain the ionosphere free ambiguity or bias parameter, $b_j = (\lambda_{\mathrm{IF}} A_{\mathrm{IF}})_j$, which remains constant over time until a cycle slip or phase break occurs. In the absence of data gaps a typical one day (24 hour) data arc now requires a total of $n_X = 2880$ epochs to be processed, when the measurements are processed at 30 second intervals. Due to the fast changing viewing geometry for LEO spacecraft GPS satellites are observed for a maximum of about 40 minutes resulting in typically 15 (phase connected) passes with constant ambiguities for a single GPS satellite. Most of the time the

total number of independent ambiguity parameters over 24 hours is approximately $n_B \approx 450 - 500$ for spaceborne scenarios. Together this results in a total number of roughly $4n_X + n_B \approx 12000$ estimation parameters that need to be adjusted on a single day. With an average number of 6 good quality pseudorange and carrier phase observations per epoch, the total number of measurements adds up to approximately 35000, making the system in principle overdetermined.

Although the total number of estimation parameters is quite large, they can be efficiently solved for when grouped into the $4n_X$ dimensional position and clock offset vector

$$\mathbf{X} = \big(\mathbf{x}_0; \cdots ; \mathbf{x}_i; \cdots ; \mathbf{x}_{n_X-1}\big), \tag{3.6}$$

and the n_B dimensional carrier phase ambiguity vector

$$\mathbf{B} = \big(b_0; \cdots ; b_j; \cdots ; b_{n_B-1}\big), \tag{3.7}$$

allowing a partitioned solution of the normal equations later on. In accord with the partitioned formulation the design matrix $\mathbf{H}$ is split up into a part containing the modeled linearized measurement partials with respect to the position and clock offset, $\mathbf{H}_X$, and the carrier phase ambiguities, $\mathbf{H}_B$. The partials of a modeled measurement of GPS satellite s with respect to the position and clock offset,

$$\frac{\partial h_i^s}{\partial \mathbf{X}} = \big(\mathbf{0}_{(0)}^T, \ldots, \mathbf{0}_{(i-1)}^T, \big(\,\mathbf{e}^s(t_i)\,;\,1\,\big)_{(i)}^T, \mathbf{0}_{(i+1)}^T, \ldots, \mathbf{0}_{(n_X-1)}^T\big), \tag{3.8}$$

only relate to the epoch t_i the measurement was taken. The same is true for the partials of the modeled carrier phase measurement of GPS satellite s with respect to the ambiguity parameters

$$\frac{\partial h_i^s}{\partial \mathbf{B}} = \big(0_{(0)}, \ldots, 0_{(j-1)}, 1_{(j)}, 0_{(j+1)}, \ldots, 0_{(n_B-1)}\big). \tag{3.9}$$

Here, the only non-zero entry is for the bias parameter (j) relating to the carrier phase observation from satellite s at epoch t_i. As can be seen in these last two equations the only non-linear part of the model is formed by the position partials, seen earlier in eqn. 2.28 as the line of sight vector. If the initial positions, $\mathbf{X}_0$, are not chosen close enough to the final ones, multiple iterations might be required for this part of the model to become linear.

The GPS observation model is linearized around initial values of the epoch wise position and clock offset ($\mathbf{X}_0$) and ambiguity values ($\mathbf{B}_0$),

$$\begin{aligned} \mathbf{X} &= \mathbf{X}_0 + \Delta\mathbf{X} \\ \mathbf{B} &= \mathbf{B}_0 + \Delta\mathbf{B} \end{aligned}. \tag{3.10}$$

for which respective updates, $\Delta\mathbf{X}$ and $\Delta\mathbf{B}$, are computed during the LSQ solution process. Using the initial values to compute the partial derivatives and the modeled

observations, the LSQ estimation problem now reads

$$\begin{aligned}&\left(\frac{\partial \mathbf{h}}{\partial(\mathbf{X}_0,\mathbf{B}_0)}\right)^T \mathbf{W}\left(\frac{\partial \mathbf{h}}{\partial(\mathbf{X}_0,\mathbf{B}_0)}\right)\begin{pmatrix}\Delta\mathbf{X}\\ \Delta\mathbf{B}\end{pmatrix}\\ &\quad=\left(\frac{\partial \mathbf{h}}{\partial(\mathbf{X}_0,\mathbf{B}_0)}\right)^T \mathbf{W}\big(\mathbf{z}-\mathbf{h}(\mathbf{X}_0,\mathbf{B}_0)\big).\end{aligned} \tag{3.11}$$

When substituting the partitioned notation of the design matrix,

$$\left(\frac{\partial \mathbf{h}}{\partial(\mathbf{X}_0,\mathbf{B}_0)}\right)=\begin{pmatrix}\mathbf{H}_X & \mathbf{H}_B\end{pmatrix}, \tag{3.12}$$

the LSQ estimation is rewritten as

$$\begin{pmatrix}\mathbf{H}_X^T\mathbf{W}\mathbf{H}_X & \mathbf{H}_X^T\mathbf{W}\mathbf{H}_B\\ \mathbf{H}_B^T\mathbf{W}\mathbf{H}_X & \mathbf{H}_B^T\mathbf{W}\mathbf{H}_B\end{pmatrix}\begin{pmatrix}\Delta\mathbf{X}\\ \Delta\mathbf{B}\end{pmatrix}=\begin{pmatrix}\mathbf{H}_X^T\mathbf{W}\big(\mathbf{z}-\mathbf{h}(\mathbf{X}_0,\mathbf{B}_0)\big)\\ \mathbf{H}_B^T\mathbf{W}\big(\mathbf{z}-\mathbf{h}(\mathbf{X}_0,\mathbf{B}_0)\big)\end{pmatrix}. \tag{3.13}$$

which can furthermore be reduced to

$$\begin{pmatrix}\mathbf{N}_{XX} & \mathbf{N}_{XB}\\ \mathbf{N}_{BX} & \mathbf{N}_{BB}\end{pmatrix}\begin{pmatrix}\Delta\mathbf{X}\\ \Delta\mathbf{B}\end{pmatrix}=\begin{pmatrix}\mathbf{n}_X\\ \mathbf{n}_B\end{pmatrix}. \tag{3.14}$$

Due to the partitioned formulation of the problem, the normal equations can be solved for more efficiently than by direct inversion of the full matrix with dimension 12000×12000. The general structure of the normal equations from eqn. 3.3 is visualized in Fig. 3.3 for a 1-hour data arc, processed in 60 second measurement intervals. It can be seen in the structure of $\mathbf{N}_{XB}$, or $\mathbf{N}_{BX}$, that all positions and clock offsets are interconnected through the carrier phase biases. Furthermore, it shows that the part relating to the positions and clock offsets, $\mathbf{N}_{XX}$, is a block diagonal matrix with 4×4 elements. Inversion of this matrix ($\mathbf{N}_{XX}^{-1}$) is easily accomplished by a simple inversion of the individual 4×4 diagonal sub-matrices. It is now possible to first resolve the bias parameter updates,

$$\Delta\mathbf{B}=\big(\mathbf{N}_{BB}-\mathbf{N}_{BX}\mathbf{N}_{XX}^{-1}\mathbf{N}_{XB}\big)^{-1}\big(\mathbf{n}_B-\mathbf{N}_{BX}\mathbf{N}_{XX}^{-1}\mathbf{n}_X\big), \tag{3.15}$$

which are subsequently back-substituted to find the updates for the positions and clock offsets,

$$\Delta\mathbf{X}=\mathbf{N}_{XX}^{-1}\big(\mathbf{n}_X-\mathbf{N}_{XB}\Delta\mathbf{B}\big). \tag{3.16}$$

Note that this only requires the direct inversion of a matrix with the approximate dimension 500×500, in addition to the 2880 inversions of the 4×4 sub-matrices. The formal covariances of the estimation parameters are given by

$$\mathbf{Q}_{BB}=\big(\mathbf{N}_{BB}-\mathbf{N}_{BX}\mathbf{N}_{XX}^{-1}\mathbf{N}_{XB}\big)^{-1}, \tag{3.17}$$

which was already computed when solving for the bias parameter updates, and by

$$\mathbf{Q}_{XX}=\mathbf{N}_{XX}^{-1}+\big(\mathbf{N}_{XX}^{-1}\mathbf{N}_{XB}\big)\mathbf{Q}_{BB}\big(\mathbf{N}_{XX}^{-1}\mathbf{N}_{XB}\big)^T. \tag{3.18}$$

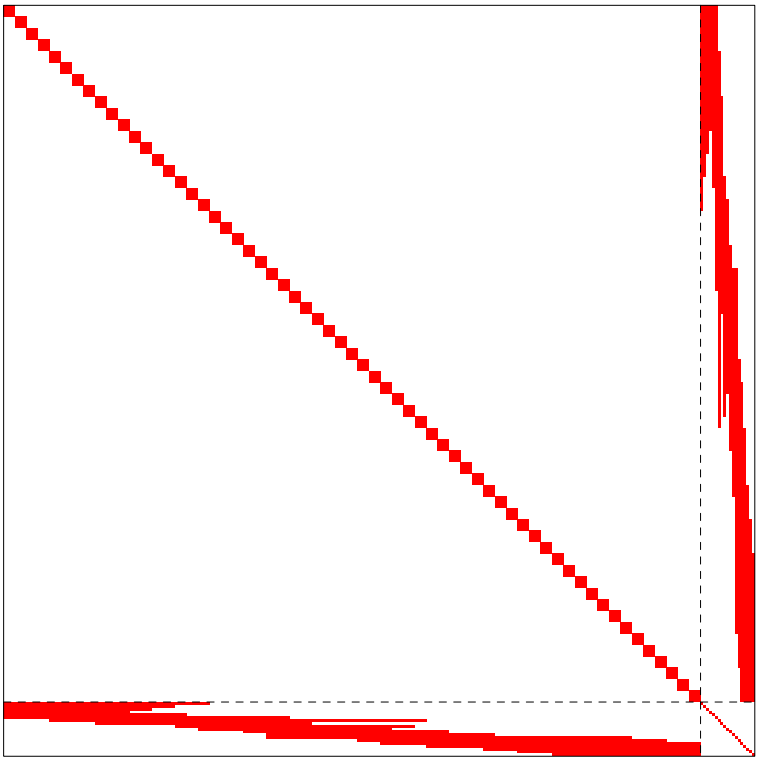

Figure 3.3 Structure of the normal equations for kinematic least-squares batch estimation of epoch-wise position and clock corrections, as well as carrier phase biases over continuous tracking arcs.

Due to the fact that both GPS pseudorange and carrier phase observations are processed the normal equations can be readily inverted, allowing for a parameter adjustment. It is however also possible to process solely ionosphere free carrier phase data, which could be more accurate. This requires the same parameters to be adjusted, but with roughly half of the observation data available. The resulting system however is no longer overdetermined since a singularity is now introduced. A common shift in the carrier phase bias parameters can namely no longer be separated from a common shift in all receiver clock offsets and vice versa. A solution to this is adding (uncorrelated) a-priori information to e.g. the bias parameters. The a-priori bias values, $\mathbf{B}_{apr}$, and their accompanying data weights, or information matrix, $\mathbf{\Lambda}_B$, are added to the normal equations as

$$\begin{pmatrix} \mathbf{N}_{XX} & \mathbf{N}_{XB} \\ \mathbf{N}_{BX} & \mathbf{N}_{BB} + \mathbf{\Lambda}_B \end{pmatrix} \begin{pmatrix} \Delta\mathbf{X} \\ \Delta\mathbf{B} \end{pmatrix} = \begin{pmatrix} \mathbf{n}_X \\ \mathbf{n}_B + \mathbf{\Lambda}_B\mathbf{B}_{apr} \end{pmatrix}, \tag{3.19}$$

which can still be solved in the same way as before, since the general structure depicted in Fig. 3.3 does not change. It must be noted however that if multiple

bias parameters are given a-priori information, whilst being interconnected with each other, there is no longer a free estimation of the parameters. Therefore, ideally, only one of the bias parameters should be given a-priori information for each interconnected batch of carrier phase biases.

After having obtained the final position solutions they still need to be expressed in the center of mass of the concerning spacecraft. This is accomplished using the GPS antenna phase center offset and the transformation described in eqn. 3.4. Results of the kinematic batch LSQ for POD can be found later on in this chapter when tested with CHAMP and GRACE GPS observation data.

3.4 Reduced dynamic orbit determination

As made clear in the previous section kinematic POD requires no a-priori knowledge of the spacecraft motion and can thus be applied to a wide range of scenarios. On the other hand, kinematic methods are particularly sensitive to erroneous measurements, unfavorable viewing geometry and data outages, which sometimes restrict their value in practice. Dynamic orbit determination, in contrast, makes use of known physical models of the spacecraft motion to constrain the resulting position estimates. This allows an averaging of measurements from different epochs and the satellite trajectory can even be propagated across data gaps.

However, the dynamics of real-world LEO spacecraft are hardly known to a level that matches the accuracy of GPS pseudorange and carrier phase measurements. Particularly aerodynamic forces are not well predictable at altitudes of 300-600 km due to limitations of upper atmosphere density models [*Bruinsma et al.*, 2003] and the complicated interaction of neutral gases and charged particles with the spacecraft surface.

Due to the limitations of both pure kinematic and pure dynamic orbit determination the concept of reduced dynamic orbit determination has been introduced in the previous decades ([*Wu et al.*, 1991]; [*Yunck et al.*, 1990]). Here, the deterministic (numerical) model of the spacecraft dynamics is complemented by stochastic parameters, in the form of empirical accelerations or impulsive shots, that are adjusted along with other parameters in the orbit determination process. In this way, the available accuracy of the GPS measurements may be fully exploited without sacrificing the robustness offered by dynamical orbit determination techniques.

This section starts with an overview of the dynamical models and their partial derivatives used for the actual orbit determination process, followed by the theory of the empirical accelerations. Furthermore, two different concepts for reduced dynamic orbit determination are discussed, a batch LSQ estimator and an extended Kalman filter. The measurement processing and handling of the orbit parameters and empirical accelerations differ for each of these methods. The merits and disadvantages of both approaches are discussed in the next section, where the orbit determination results are presented.

3.4.1 Dynamical modeling

When considering reduced dynamic orbit determination, dynamic force models are first of all used to accurately propagate the satellite (initial) state vector, in EME2000,

$$\mathbf{y}(t) = \begin{pmatrix} \mathbf{r}(t) \\ \mathbf{v}(t) \end{pmatrix}, \tag{3.20}$$

over time by means of numerical integration of the first order differential equation

$$\frac{d}{dt}\mathbf{y}(t) = \mathbf{f}(t, \mathbf{y}(t), \mathbf{p}) = \begin{pmatrix} \mathbf{v}(t) \\ \mathbf{a}(t, \mathbf{r}, \mathbf{v}, \mathbf{p}) \end{pmatrix}. \tag{3.21}$$

More specifically the dynamic force models are used to compute the gravitational and non-gravitational accelerations, $\mathbf{a}(t, \mathbf{r}, \mathbf{v}, \mathbf{p})$, acting on the spacecraft. These on their turn depend on the time, t, the position, $\mathbf{r}$, and velocity, $\mathbf{v}$, of the spacecraft as well as the force model parameters, $\mathbf{p}$. Since the initial state vector at t_0, $\mathbf{y}(t_0)$, and the force model parameters are actually being estimated as part of the orbit determination process, linearized expressions for the partial derivatives of the satellite state at an arbitrary time t with respect to the estimation parameters are required for GPS measurement modeling later on. The computation of these partials again requires the use of the dynamic force models.

Following *Montenbruck and Gill* [2000], the partial derivatives of the spacecraft state at arbitrary time t with respect to the initial state vector are captured in the state transition matrix,

$$\mathbf{\Phi}(t, t_0) = \frac{\partial \mathbf{y}(t)}{\partial \mathbf{y}(t_0)}, \tag{3.22}$$

which is 6×6 dimensional and can be obtained by differentiating eqn. 3.21 to the initial state:

$$\frac{\partial}{\partial \mathbf{y}(t_0)}\frac{d}{dt}\mathbf{y}(t) = \frac{\partial \mathbf{f}(t, \mathbf{y}(t), \mathbf{p})}{\partial \mathbf{y}(t_0)} = \frac{\partial \mathbf{f}(t, \mathbf{y}(t), \mathbf{p})}{\partial \mathbf{y}(t)} \cdot \frac{\partial \mathbf{y}(t)}{\partial \mathbf{y}(t_0)}. \tag{3.23}$$

This last equation can be rewritten to

$$\frac{d}{dt}\mathbf{\Phi}(t, t_0) = \frac{\partial \mathbf{f}(t, \mathbf{y}(t), \mathbf{p})}{\partial \mathbf{y}(t)} \cdot \mathbf{\Phi}(t, t_0), \tag{3.24}$$

or more specifically

$$\frac{d}{dt}\mathbf{\Phi}(t, t_0) = \begin{pmatrix} \mathbf{0}_{3\times3} & \mathbf{1}_{3\times3} \\ \dfrac{\partial \mathbf{a}(t, \mathbf{r}, \mathbf{v}, \mathbf{p})}{\partial \mathbf{r}(t)} & \dfrac{\partial \mathbf{a}(t, \mathbf{r}, \mathbf{v}, \mathbf{p})}{\partial \mathbf{v}(t)} \end{pmatrix}_{6\times6} \cdot \mathbf{\Phi}(t, t_0), \tag{3.25}$$

which is a first order differential equation with the identity matrix as the initial value, $\mathbf{\Phi}(t_0, t_0) = \mathbf{1}_{6\times6}$. In a similar way the partials of the state vector with

respect to the force model parameters, captured in the $6 \times n_p$ dimensional (n_p being the number of estimated force model parameters) sensitivity matrix

$$\mathbf{S}(t) = \frac{\partial \mathbf{y}(t)}{\partial \mathbf{p}}, \tag{3.26}$$

are obtained. When differentiating eqn. 3.21 to the force model parameters,

$$\frac{d}{dt}\frac{\partial \mathbf{y}(t)}{\partial \mathbf{p}} = \frac{\partial \mathbf{f}(t, \mathbf{y}(t), \mathbf{p})}{\partial \mathbf{y}(t)} \cdot \frac{\partial \mathbf{y}(t)}{\partial \mathbf{p}} + \frac{\partial \mathbf{f}(t, \mathbf{y}(t), \mathbf{p})}{\partial \mathbf{p}}, \tag{3.27}$$

a first order differential equation, more specifically written as

$$\begin{aligned} &\frac{d}{dt}\mathbf{S}(t)_{6\times n_p} = \\ &\quad \begin{pmatrix} \mathbf{0}_{3\times 3} & \mathbf{1}_{3\times 3} \\ \dfrac{\partial \mathbf{a}(t, \mathbf{r}, \mathbf{v}, \mathbf{p})}{\partial \mathbf{r}(t)} & \dfrac{\partial \mathbf{a}(t, \mathbf{r}, \mathbf{v}, \mathbf{p})}{\partial \mathbf{v}(t)} \end{pmatrix}_{6\times 6} \cdot \mathbf{S}(t) + \begin{pmatrix} \mathbf{0}_{3\times n_p} \\ \dfrac{\partial \mathbf{a}(t, \mathbf{r}, \mathbf{v}, \mathbf{p})}{\partial \mathbf{p}} \end{pmatrix}_{6\times n_p}, \end{aligned} \tag{3.28}$$

is again obtained. Since the initial satellite state does not depend on any of the force model parameters the initial value of the sensitivity matrix yields $\mathbf{S}(t_0) = \mathbf{0}_{6\times n_p}$.

The derived expressions for both the state transition and sensitivity matrix can now be combined into the first order differential equation

$$\frac{d}{dt}(\mathbf{\Phi}, \mathbf{S}) = \begin{pmatrix} \mathbf{0}_{3\times 3} & \mathbf{1}_{3\times 3} \\ \dfrac{\partial \mathbf{a}}{\partial \mathbf{r}} & \dfrac{\partial \mathbf{a}}{\partial \mathbf{v}} \end{pmatrix}_{6\times 6} \cdot (\mathbf{\Phi}, \mathbf{S}) + \begin{pmatrix} \mathbf{0}_{3\times 6} & \mathbf{0}_{3\times n_p} \\ \mathbf{0}_{3\times 6} & \dfrac{\partial \mathbf{a}}{\partial \mathbf{p}} \end{pmatrix}_{6\times(6+n_p)} \tag{3.29}$$

also referred to as the variational equations. This form of the variational equations is adequate for use with numerical integration methods for the solution of first order initial value problems. Within the actual orbit determination process the integration of the satellite trajectory and the variational equations is typically performed at the same instance. As pointed out by *Montenbruck and Gill* [2000] common subexpressions in the set of differential equations are used to make the integration process more efficient in this way.

For integration of the trajectory, accurate force models are used to compute the gravitational and non-gravitational accelerations acting on the satellite. All expressions for the exact computation of these accelerations can be found in chapter 3 of *Montenbruck and Gill* [2000]. More specifically, the POD scenarios described later on use the GRACE GGM01S gravity field [*UT/CSR*, 2003] of selectable degree and order, up to 120×120, to obtain the acceleration due to the Earth's static gravity field. The effects of tidal displacements are accounted for by including solid Earth tides (4×4, diurnal), polar tides and ocean tides (UT/CSR 3.0 [*UT/CSR*, 2001] and TEG-2B) in the computation. Furthermore, accelerations due to point mass attraction by the Sun and Moon, computed using analytical expansions of luni-solar coordinates, described in *Montenbruck and Gill* [2000], are also taken

into account. Accelerations due to non-gravitational forces include the atmospheric drag and the solar radiation pressure acting on the spacecraft. Both are computed using a simple 'canon-ball' model for the satellite assuming a constant surface and mass on which the forces act. The atmospheric density is furthermore computed using the Jacchia 71 [*Jacchia*, 1971] atmospheric density model, and a conical Earth shadow model is applied indicating if solar radiation pressure is experienced. Since atmospheric density and solar activity are hard to model accurately a drag and solar radiation pressure scaling coefficient, C_D and C_R respectively, are estimated as part of the force model parameters.

Accuracy requirements for the partial derivatives are generally not as stringent as for the trajectory itself. This is due to the fact that some contributions are very small and that it concerns a linearized problem, which is typically adjusted for by a huge number of GPS observations over multiple iterations. It is therefore common to apply a simplified version of the force models in the integration of the variational equations. For this research the partials of the acceleration with respect to the spacecraft position solely depend on the Earth's static gravity field, using only the central term, GM, and the lowest zonal gravity field perturbation, $C_{2,0}$, in their computation. The partials of the acceleration with respect to the velocity are not set at all, i.e. they are always zero. Finally the partials of the acceleration with respect to the force model parameters are set using the simple expressions for the atmospheric drag and solar radiation pressure as described in *Montenbruck and Gill* [2000], and by the direction partials from eqn. 3.30 when the empirical accelerations, described in the next subsection, are considered.

3.4.2 Empirical accelerations

Within the two different reduced dynamic POD approaches empirical accelerations in the radial (subscript 'R'), along-track (transverse, subscript 'T') and cross-track (normal, subscript 'N') direction

$$\mathbf{e}_R = \frac{\mathbf{r}}{\|\mathbf{r}\|}, \quad \mathbf{e}_T = \mathbf{e}_N \times \mathbf{e}_R, \quad \mathbf{e}_N = \frac{\mathbf{r} \times \mathbf{v}}{\|\mathbf{r} \times \mathbf{v}\|} \tag{3.30}$$

are considered to compensate for any modeling deficiencies in the employed spacecraft dynamics. Although the amplitude of the individual acceleration components is not known beforehand, but estimated as part of the orbit determination process, realistic a-priori constraints have to be applied in each of the POD concepts to prevent a divergence of the estimated orbit solution.

Following *Bierman* [1977], the theory of random processes with exponentially correlated, also referred to as 'colored', process noise provides a suitable mathematical framework for the description of these unmodeled accelerations. A first-order Gauss-Markov process $p(t)$ [*Brown and Hwang*, 1997] exhibits an exponential autocorrelation

$$R(\Delta t) = E\big(p(t), p(t+\Delta t)\big) = \sigma^2 \mathrm{e}^{-|\Delta t|/\tau}, \tag{3.31}$$

where σ^2 denotes the steady-state variance of the process and τ is the correlation time scale. In a time-discrete form, the process satisfies the first-order difference equation

$$p(t_{i+1}) = m_i p(t_i) + w_i, \tag{3.32}$$

where the mapping factor is given as

$$m_i = \mathrm{e}^{-|t_{i+1}-t_i|/\tau}, \tag{3.33}$$

and where the process noise w_i is an uncorrelated random sequence with zero mean and variance

$$E(w_i^2) = \sigma^2(1 - m_i^2). \tag{3.34}$$

Although this framework can be directly applied to a recursive filtering scheme, as already done by *Lichten* [1990], it was found to be unsuitable for practical use by the batch LSQ. For this concept, the empirical accelerations are considered to be piecewise constant in pre-defined sub-intervals, which facilitates both the trajectory propagation and the overall parameter adjustment. Here, the entire data arc is divided into n_a intervals of equal duration τ and an independent set of empirical acceleration parameters $(a_R, a_T, a_N)_j$ is estimated for each interval, $j = 0, \ldots, n_a - 1$. The choice of an adequate interval length reflects a compromise between observability, computational effort and the capability to resolve time varying phenomena. Given an orbital period of roughly 6000 s for LEO satellites and a representative measurement interval of 30 s, intervals of 600 s duration have been found to be most suitable and are adopted throughout this research. While shorter intervals provide a smoother variation of the estimated accelerations, no relevant improvement of the overall orbit determination accuracy has been observed that would justify an associated increase in computation time. Longer intervals, in contrast, appeared insufficient to sample the characteristic time scales of the empirical acceleration variation. In accordance to the batch LSQ, the auto-correlation time used for handling the empirical accelerations in the Kalman filter is also set to 600 s. Although a variation in the auto-correlation time here does not influence the computational effort, it does affect the characteristics of the empirical acceleration variation and thus influences the orbit solution.

3.4.3 Batch LSQ

The major difference between the kinematic and reduced dynamic batch LSQ is the fact that the individual spacecraft positions at each measurement epoch are replaced by the spacecraft trajectory model. This of course has its effects on the modeling of the ionosphere free pseudorange and carrier phase data. Both data types are still parameterized with the GPS receiver clock offset, $c\delta t_r$, which again has to be determined at every measurement epoch, t_i. In exactly the same way, the GPS carrier phase observations contain the additional ionosphere free ambiguity or

bias parameter, $b_k = (\lambda_{\mathrm{IF}} A_{\mathrm{IF}})_k$. The rest of the estimation parameters are used for modeling the satellite trajectory in accordance with the previously discussed theories. They comprise the 6-dimensional initial spacecraft state vector, $\mathbf{y}_0 = \mathbf{y}(t_0)$ at a reference epoch t_0, relating to the S/C center of mass and expressed in the ICRF (EME2000), a solar radiation pressure coefficient C_R that acts as an adjustable scaling factor for the surface reflectivity in the modeling of solar radiation pressure forces, a drag coefficient C_D that acts as an adjustable scaling factor in the modeling of drag forces and the empirical accelerations $\mathbf{a}_j = (a_R, a_T, a_N)_j$ in consecutive time intervals $[t_0 + j \cdot \tau, t_0 + (j+1) \cdot \tau]$ for compensating deficiencies in the applied dynamical models.

When grouping the estimation parameters in the n_T-dimensional vector of GPS receiver clock offsets,

$$\mathbf{T} = \big(c\delta t_0; \ldots; c\delta t_{n_T - 1}\big), \tag{3.35}$$

the $n_Y = 8 + 3n_a$ dimensional vector concerning the satellite trajectory modeling, also referred to as the dynamic estimation parameters,

$$\mathbf{Y} = \big(\mathbf{y}_0; C_R; C_D; \mathbf{a}_0; \ldots; \mathbf{a}_{n_a - 1}\big), \tag{3.36}$$

and the n_B-dimensional vector of ionosphere free carrier phase biases,

$$\mathbf{B} = \big(b_0; \ldots; b_{n_B - 1}\big), \tag{3.37}$$

a similar partitioning as for the kinematic batch LSQ can be applied. The total number of estimation parameters in this minimization problem however, is less than for the kinematic case. When again considering a 24 hour data arc in which the measurements are processed in 30 second steps, this results in a total of $n_T = 2880$ clock offsets and the typical number of $n_B \approx 450 - 500$ carrier phase biases that need to be adjusted. In addition, when using 600 second intervals for the empirical accelerations this results in $n_Y = 440$ dynamical estimation parameters. The total number of estimation parameters now becomes approximately 3800, which is significantly less than for the kinematic case.

Similar to the kinematic batch LSQ, a linearization around initial values (subscript 0) of the estimation parameters takes place,

$$\begin{aligned} \mathbf{T} &= \mathbf{T}_0 + \Delta\mathbf{T}, \\ \mathbf{Y} &= \mathbf{Y}_0 + \Delta\mathbf{Y}, \\ \mathbf{B} &= \mathbf{B}_0 + \Delta\mathbf{B}, \end{aligned} \tag{3.38}$$

for which updates (preceding Δ) are computed in the LSQ estimation process, given by

$$\begin{aligned} &\left(\frac{\partial \mathbf{h}}{\partial(\mathbf{T}_0, \mathbf{Y}_0, \mathbf{B}_0)}\right)^T \mathbf{W} \left(\frac{\partial \mathbf{h}}{\partial(\mathbf{T}_0, \mathbf{Y}_0, \mathbf{B}_0)}\right) \begin{pmatrix} \Delta\mathbf{T} \\ \Delta\mathbf{Y} \\ \Delta\mathbf{B} \end{pmatrix} \\ &\quad = \left(\frac{\partial \mathbf{h}}{\partial(\mathbf{T}_0, \mathbf{Y}_0, \mathbf{B}_0)}\right)^T \mathbf{W}\big(\mathbf{z} - \mathbf{h}(\mathbf{T}_0, \mathbf{Y}_0, \mathbf{B}_0)\big). \end{aligned} \tag{3.39}$$

Here, again, the weighting matrix is the inverse of the measurement covariance, $\mathbf{W} = \mathbf{Q}_{\mathbf{z}}^{-1}$, and the overall design matrix

$$\left(\frac{\partial \mathbf{h}}{\partial(\mathbf{T}_0, \mathbf{Y}_0, \mathbf{B}_0)}\right) = \left(\mathbf{H}_T \ \mathbf{H}_Y \ \mathbf{H}_B\right), \tag{3.40}$$

is constructed from the three partitioned ones. Similar to the kinematic case the partials of the modeled GPS observation, h^s, of GPS satellite s with respect to the clock offset vector,

$$\frac{\partial h_i^s}{\partial \mathbf{T}} = \big(0_{(0)}, \ldots, 0_{(i-1)}, 1_{(i)}, 0_{(i+1)}, \ldots, 0_{(n_T-1)}\big), \tag{3.41}$$

are only set for the epoch, t_i, the measurement was taken. The same is again true when it concerns a carrier phase observation. In this case only the partial of the concerning bias parameter is set,

$$\frac{\partial h_i^s}{\partial \mathbf{B}} = \big(0_{(0)}, \ldots, 0_{(k-1)}, 1_{(k)}, 0_{(k+1)}, \ldots, 0_{(n_B-1)}\big). \tag{3.42}$$

Of course for pseudorange observations these partials are not set at all. Finally, the partials with respect to the dynamic estimation parameters refer to the point in the trajectory at which the measurement was taken,

$$\frac{\partial h_i^s}{\partial \mathbf{Y}} = \left(\frac{\partial h_i^s}{\partial \mathbf{y}_0}, \frac{\partial h_i^s}{\partial C_R}, \frac{\partial h_i^s}{\partial C_D}, \frac{\partial h_i^s}{\partial \mathbf{a}_0}, \cdots, \frac{\partial h_i^s}{\partial \mathbf{a}_{j-1}}, \frac{\partial h_i^s}{\partial \mathbf{a}_j}, \mathbf{0}_{(j+i)}^T, \cdots, \mathbf{0}_{(n_a-1)}^T\right), \tag{3.43}$$

meaning that if the measurement at epoch t_i falls within the j^{th} interval of empirical acceleration parameters, the partials up to this point are set accordingly. This follows from the physical explanation that the empirical accelerations in the past contributed to the trajectory shape in the present. No fading characteristics as for e.g. a Gauss-Markov process have been applied. A more generic expression for this last set of partials is given by

$$\frac{\partial h_i^s}{\partial \mathbf{Y}} = \left(\frac{\partial h_i^s}{\partial \mathbf{y}_0} \quad \frac{\partial h_i^s}{\partial \mathbf{p}}\right), \tag{3.44}$$

where the dynamic estimation parameters are divided into the initial state vector and the concerning force model parameters, $\mathbf{p}_i = (C_R; C_D; \mathbf{a}_0; \ldots; \mathbf{a}_j; \mathbf{0}; \ldots; \mathbf{0})$ up to epoch t_i. In addition, the partials of the measurement with respect to the current satellite state are given by

$$\frac{\partial h_i^s}{\partial \mathbf{y}_i} = \big(-(\mathbf{U}^T(t_i)\mathbf{e}^s(t_i))^T \quad \mathbf{0}_{1\times 3}\big), \tag{3.45}$$

where the line of sight vector, $\mathbf{e}^s(t_i)$, from eqn. 2.28 is transformed to the inertial reference frame using the 3×3 transformation matrix $\mathbf{U}(t_i)$ from eqn. 3.1. Combining the last two equations leads to an expression for the partials with respect to the dynamic estimation parameters:

$$\frac{\partial h_i^s}{\partial \mathbf{Y}} = \left(\frac{\partial h_i^s}{\partial \mathbf{y}_i}\frac{\partial \mathbf{y}_i}{\partial \mathbf{y}_0} \quad \frac{\partial h_i^s}{\partial \mathbf{y}_i}\frac{\partial \mathbf{y}_i}{\partial \mathbf{p}_i}\right) = \left(\frac{\partial h_i^s}{\partial \mathbf{y}_i}\mathbf{\Phi}(t_i, t_0) \quad \frac{\partial h_i^s}{\partial \mathbf{y}_i}\mathbf{S}(t_i)\right), \tag{3.46}$$

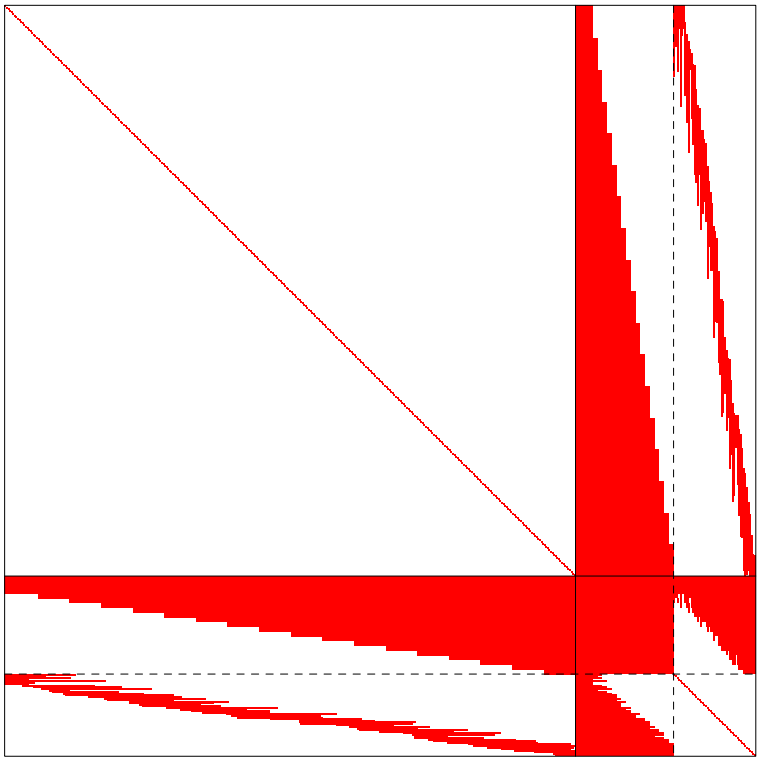

Figure 3.4 Structure of the normal equations for least-squares batch estimation of epoch-wise clock corrections, dynamic orbit parameters and carrier phase biases over continuous tracking arcs.

involving the state transition and sensitivity matrix.

In practice the construction of these partials and the accompanying measurement residual, $z - h(c\delta t_r(t_i), \mathbf{y}(t_i), b_k)$, are not so trivial anymore, since they require the numerical integration of the spacecraft trajectory along with the variational equations. Within the reduced dynamic batch LSQ this integration over the entire batch of observation data, with a restart at every new interval of empirical accelerations, is accomplished using the variable order variable step-size multi-step numerical integration method DE of *Shampine and Gordon* [1975], which has earlier been proven to be a highly efficient and flexible integrator for orbital dynamics problems with stringent accuracy requirements ([*Montenbruck and Gill*, 2000]; [*Montenbruck et al.*, 2005*a*]). Furthermore, it must be noted that the modeling of the GPS observations is done in the ITRF, using the GPS receiver antenna phase center position. The modeled observation, $h(c\delta t_r(t_i), \mathbf{y}(t_i), b_k)$, internally handles the appropriate transformations and corrections given earlier in section 3.2.

In a similar way as has been done for the kinematic batch LSQ, eqn. 3.39 can

be rewritten as

$$\begin{pmatrix} \mathbf{N}_{TT} & \mathbf{N}_{TY} & \mathbf{N}_{TB} \\ \mathbf{N}_{YT} & \mathbf{N}_{YY} & \mathbf{N}_{YB} \\ \mathbf{N}_{BT} & \mathbf{N}_{BY} & \mathbf{N}_{BB} \end{pmatrix} \begin{pmatrix} \Delta\mathbf{T} \\ \Delta\mathbf{Y} \\ \Delta\mathbf{B} \end{pmatrix} = \begin{pmatrix} \mathbf{n}_T \\ \mathbf{n}_Y \\ \mathbf{n}_B \end{pmatrix}. \tag{3.47}$$

Although the normal equations are generally not singular when both code and carrier phase observations are processed, and can thus be inverted, a free estimation is in general no longer possible. In order to prevent divergence of the satellite trajectory, uncorrelated a-priori information, $\mathbf{Y}_{apr}$, with a predefined weight, $\mathbf{\Lambda}_Y$, is added to the concerning part of the normal equations to constrain the dynamic estimation parameters. Similar to the kinematic case (uncorrelated) a-priori information must also be added to the carrier phase biases, $\mathbf{B}_{apr}$ and $\mathbf{\Lambda}_B$, if pseudorange observations are not processed. Again, ideally, this a-priori information only concerns one bias parameter for each carrier phase interconnected data arc. When incorporating this a-priori in formations the normal equations would read

$$\begin{pmatrix} \mathbf{N}_{TT} & \mathbf{N}_{TY} & \mathbf{N}_{TB} \\ \mathbf{N}_{YT} & \mathbf{N}_{YY} + \mathbf{\Lambda}_Y & \mathbf{N}_{YB} \\ \mathbf{N}_{BT} & \mathbf{N}_{BY} & \mathbf{N}_{BB} + \mathbf{\Lambda}_B \end{pmatrix} \begin{pmatrix} \Delta\mathbf{T} \\ \Delta\mathbf{Y} \\ \Delta\mathbf{B} \end{pmatrix} = \begin{pmatrix} \mathbf{n}_T \\ \mathbf{n}_Y + \mathbf{\Lambda}_Y\mathbf{Y}_{apr} \\ \mathbf{n}_B + \mathbf{\Lambda}_B\mathbf{B}_{apr} \end{pmatrix}, \tag{3.48}$$

where $\mathbf{\Lambda}_B$ is zero if both code and carrier phase observations are processed. The structure of the partitioned normal equations is visualized in Fig. 3.4 for a 3 hour data arc, processed in 30 second steps and a 600 second interval for the empirical accelerations. Here it can be seen directly that $\mathbf{N}_{TT}$ is a diagonal matrix whose inverse, $\mathbf{N}_{TT}^{-1}$, is readily computed. Furthermore, the specific structure of $\mathbf{N}_{TY}$ shows the contributions of all empirical accelerations prior to a concerned measurement epoch. When grouping the dynamic estimation parameters and the carrier phase biases into

$$\mathbf{X} = \begin{pmatrix} \mathbf{Y} \\ \mathbf{B} \end{pmatrix}, \tag{3.49}$$

the LSQ problem from eqn. 3.48 is redefined as

$$\begin{pmatrix} \mathbf{N}_{TT} & \mathbf{N}_{TX} \\ \mathbf{N}_{XT} & \mathbf{N}_{XX} \end{pmatrix} \begin{pmatrix} \Delta\mathbf{T} \\ \Delta\mathbf{X} \end{pmatrix} = \begin{pmatrix} \mathbf{n}_T \\ \mathbf{n}_X \end{pmatrix}. \tag{3.50}$$

Similar to the kinematic case the updates of the dynamic estimation and carrier phase bias parameters are efficiently obtained as

$$\Delta\mathbf{X} = \left(\mathbf{N}_{XX} - \mathbf{N}_{XT}\mathbf{N}_{TT}^{-1}\mathbf{N}_{TX}\right)^{-1}\left(\mathbf{n}_X - \mathbf{N}_{XT}\mathbf{N}_{TT}^{-1}\mathbf{n}_T\right), \tag{3.51}$$

which are subsequently back-substituted to obtain the updates for the clock offsets

$$\Delta\mathbf{T} = \mathbf{N}_{TT}^{-1}\left(\mathbf{n}_T - \mathbf{N}_{TX}\Delta\mathbf{X}\right). \tag{3.52}$$

Again, the formal covariances of the estimation parameters are given by

$$\mathbf{Q}_{XX} = \left(\mathbf{N}_{XX} - \mathbf{N}_{XT}\mathbf{N}_{TT}^{-1}\mathbf{N}_{TX}\right)^{-1}, \tag{3.53}$$

which was already computed when solving for the dynamic estimation and bias parameter updates, and by

$$\mathbf{Q}_{TT} = \mathbf{N}_{TT}^{-1} + \left(\mathbf{N}_{TT}^{-1}\mathbf{N}_{TX}\right)\mathbf{Q}_{XX}\left(\mathbf{N}_{TT}^{-1}\mathbf{N}_{TX}\right)^{T}. \tag{3.54}$$

After having obtained the updates for the estimation parameters the initial estimates are corrected for, and the newly obtained values are now used as initial values for a second run. Multiple iterations of this kind are required to cope with the non-linearity of the reduced dynamic estimation problem, and convergence is typically achieved within 3 to 4 iterations. Although the total number of estimation parameters is less than for the kinematic case, the numerical integration of the trajectory and the variational equations as well as the multiple iterations result in a much longer computation time. This however results in a continuous, smooth and (generally) more accurate solution of the satellite orbit.

3.4.4 Extended Kalman filter

A recursive formulation of the LSQ problem is captured in the standard Kalman filter [*Brown and Hwang*, 1997] for linearized models. Starting from a given set of initial conditions, measurements are processed at consecutive epochs. Non-linear estimation problems, such as reduced-dynamic orbit determination, can be coped with by adding an additional step to the Kalman filter where the filter state is updated to a value suitable for linearization. This concept is also referred to as the extended Kalman filter (EKF), which is described in e.g. *Montenbruck and Gill* [2000]. For this research the EKF is also used as a GPS based POD technique, which, due to its recursive nature, is particularly suitable for real-time applications.

In analogy with the reduced dynamic batch LSQ, the EKF state,

$$\mathbf{x} = \begin{pmatrix} \mathbf{Y} \\ c\delta t_r \\ \mathbf{B} \end{pmatrix}, \tag{3.55}$$

and accompanying covariance, $\mathbf{P}$, comprise the dynamic estimation parameters, $\mathbf{Y}$, the GPS receiver clock offset, $c\delta t_r$, and the ionosphere free carrier phase biases, $\mathbf{B}$, all relating to the current measurement epoch. This leads to a much smaller total number of estimation parameters to be handled at once since they are simply updated or removed over time. The dynamic estimation parameters,

$$\mathbf{Y} = \big(\mathbf{y};\mathbf{p}\big) = \big((\mathbf{r};\mathbf{v});(C_R;C_D;\mathbf{a})\big), \tag{3.56}$$

therefore comprise the 6-dimensional spacecraft state, $\mathbf{y} = (\mathbf{r};\mathbf{v})$, again relating to the center of mass and defined in the ICRF (EME2000), and a fixed number of force model parameters $\mathbf{p} = (C_R;C_D;\mathbf{a})$, including the 3 empirical accelerations, $\mathbf{a}$, resulting in a 11-dimensional vector of constant size. In a similar way the ionosphere free carrier phase biases, $b_j = (\lambda_{\mathrm{IF}} A_{\mathrm{IF}})_j$, in the filter state,

$$\mathbf{B} = \big(b_0,\ldots,b_n\big), \tag{3.57}$$

only concern the currently observed GPS satellites, resulting in an n-dimensional vector, that has to be re-ordered over time when new satellites become available and old satellites are no longer observed.

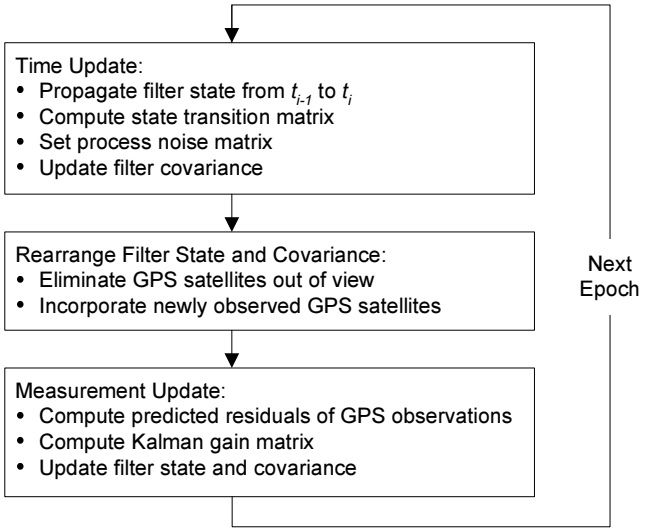

Figure 3.5 Extended Kalman Filter processing scheme for GPS based precise orbit determination

Starting from given initial values of the filter state and covariance at t_0, the EKF processes GPS observations at consecutive measurement epochs using the three step processing scheme visualized in Fig. 3.5. The first step covers the *time update*, where the filter state and covariance estimate from the previous epoch t_{i-1} (superscript '+') are propagated to a prediction (superscript '-') at the current epoch t_i, which is generally expressed as

$$\begin{aligned} \mathbf{x}_i^- &= \mathbf{x}\big(t_i; \mathbf{x}(t_{i-1}) = \mathbf{x}_{i-1}^+\big) \\ \mathbf{P}_i^- &= \mathbf{\Phi}_i \mathbf{P}_{i-1}^+ \mathbf{\Phi}_i^T + \mathbf{Q}_i \end{aligned} . \tag{3.58}$$

Propagation of the filter state and covariance involves numerical integration of the satellite trajectory and the variational equations from t_{i-1} to t_i. This requires usage of the estimated force model parameters, $\mathbf{p}_{i-1}^+$, which are kept constant during the integration. The numerical integration itself is accomplished using a simple 4^{th} order Runge-Kutta integration method, that is most suitable for the small measurement intervals (typically 30 seconds), with the need for a complete restart at every measurement epoch. After integration the empirical accelerations are propagated in accordance to the Gauss-Markov process model to

$$\mathbf{a}_i^- = \mathrm{e}^{-|t_i - t_{i-1}|/\tau} \mathbf{a}_{i-1}^+, \tag{3.59}$$

using the mapping factor cf. eqn. 3.33. All other estimation parameters in the filter state remain unchanged during the time update, i.e

$$\left(C_R; C_D; c\delta t_r, \mathbf{B}\right)_i^- = \left(C_R; C_D; c\delta t_r, \mathbf{B}\right)_{i-1}^+, \tag{3.60}$$

reflecting a white process noise model. Propagation of the filter covariance requires the filter state transition matrix,

$$\mathbf{\Phi}_i = \begin{pmatrix} \mathbf{\Phi_Y} & \mathbf{0} & \mathbf{0} \\ \mathbf{0}^T & 1 & \mathbf{0}^T \\ \mathbf{0} & \mathbf{0} & \mathbf{1} \end{pmatrix}, \tag{3.61}$$

where the part relating to the carrier phase ambiguities is given by the identity matrix, $\mathbf{1}_{n\times n}$, and the part relating to the receiver clock by the scalar 1. Except for the somewhat more complex structure of the submatrix $\mathbf{\Phi_Y}$, visualized in Fig. 3.6, all other entries are zero. Looking at the state transition matrix relating to the

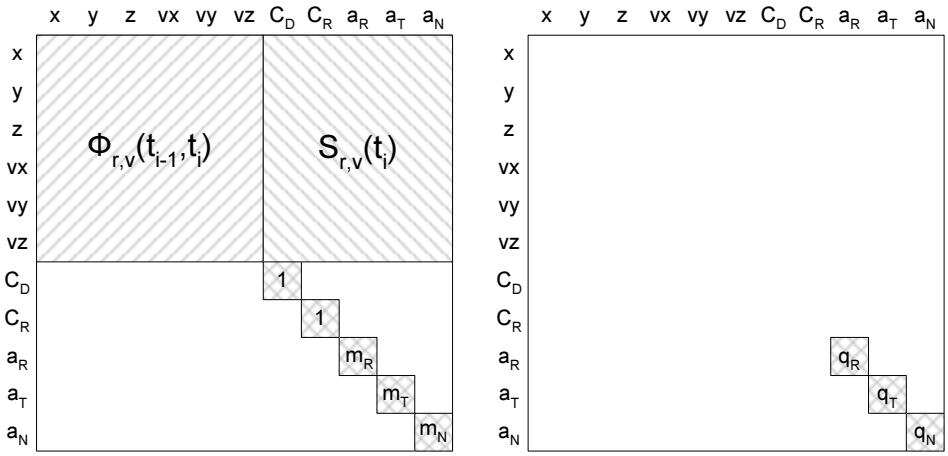

Figure 3.6 The structure of the transition ($\mathbf{\Phi_Y}$,left) and the process noise ($\mathbf{Q_Y}$,right) matrices, concerning the dynamic parameters in the EKF.

dynamic parameters it can be seen that for covariance propagation of the satellite state, the satellite state transition and sensitivity matrix are required, which were simultaneously obtained when solving the variational equations during trajectory integration. Furthermore, the entries corresponding to the empirical accelerations are set using the mapping factors from the Gauss-Markov process model cf. eqn. 3.33. In addition, process noise,

$$\mathbf{Q}_i = \begin{pmatrix} \mathbf{Q_Y} & \mathbf{0} & \mathbf{0} \\ \mathbf{0}^T & q_{c\delta t} & \mathbf{0}^T \\ \mathbf{0} & \mathbf{0} & \mathbf{0} \end{pmatrix}, \tag{3.62}$$

is added to the covariance matrix during the time update step in order to prevent filter divergence and to obtain more realistic covariance predictions for the

estimated accelerations. The process noise matrix is completely diagonal and the time-independent structure is also displayed in Fig. 3.6. Here, it can be seen that only the entries of the empirical acceleration parameters are set in accordance with the Gauss-Markov process model,

$$q_i = \sigma^2(1 - m_i^2), \tag{3.63}$$

using the corresponding mapping factor from the transition matrix. Although this process noise should actually be correlated with the position and velocity cf. *Teunissen* [2001] and *Tapley et al.* [2004*a*], it was found to have no impact on the satellite position when implemented for testing. This can be attributed to the fact that the numerical values of these process noise entries were negligible in comparison to the corresponding covariance matrix entries. More specifically, when applying the settings specified in Table 3.7 on page 67, the process noise for the empirical accelerations is between 10 and 11% of the corresponding covariance entry. For the position and velocity, as well as the cross correlations, the respective values were in the order of 10^{-7}%, 10^{-5}% and 10^{-4}%. The only remaining parameter for which process noise is added is the receiver clock offset. This parameter is treated as a stochastic variable with an underlying random walk process model, where the mapping factor is 1 (eqn. 3.61) and the process noise is given as

$$q_{c\delta t_r} = \left(\frac{\sigma^2_{c\delta t_r}}{\tau_{c\delta t_r}} \right) (t_i - t_{i-1}), \tag{3.64}$$

where $(\sigma^2_{c\delta t_r}/\tau_{c\delta t_r})$ is the noise spectral density. The process noise variance, $\sigma_{c\delta t_r}$ as well as the time scale, $\tau_{c\delta t_r}$, are only used (Table 3.7) to construct the noise spectral density of the process. No process noise is added to the carrier phase ambiguities, since they are constant over time. This means that their covariance becomes more precise as more data is accumulated over time, which is supposed to be the case.

Upon completion of the time update follows a step concerning a reordering of the filter state and covariance. This step incorporates the change in observed GPS satellites and therefore only involves the carrier phase biases. If at a certain epoch a specific GPS satellite is no longer observed, or if it experienced a carrier phase discontinuity, the corresponding bias parameter has to be removed from the filter state and covariance. In addition, whenever a new GPS satellite is tracked, its carrier phase bias has to be incorporated in the filter state and covariance. This assures that the total size of the filter state is always equal to $12+n$, where n equals the number of currently tracked satellites.

The final step in the EKF scheme is the actual incorporation of the GPS observation data to obtain the updated filter state, $\mathbf{x}_i^+$, and covariance, $\mathbf{P}_i^+$, at the current measurement epoch. This is accomplished during the linearized *measure-*

ment update,

$$\begin{aligned}\mathbf{K}_i &= \mathbf{P}_i^- \mathbf{H}_i^T \left(\mathbf{W}_i^{-1} + \mathbf{H}_i \mathbf{P}_i^{-1} \mathbf{H}_i^T\right)^{-1}, \\ \mathbf{x}_i^+ &= \mathbf{x}_i^- + \mathbf{K}_i \big(\mathbf{z}_i - \mathbf{h}(\mathbf{x}_i^-)\big), \\ \mathbf{P}_i^+ &= \big(\mathbf{1} - \mathbf{K}_i \mathbf{H}_i\big) \mathbf{P}_i^-,\end{aligned} \tag{3.65}$$

which starts with the computation of the Kalman gain, $\mathbf{K}_i$, from the predicted filter covariance, the design matrix, $\mathbf{H}_i$, and the diagonal measurement covariance or inverse weighting matrix, $\mathbf{W}_i^{-1}$. Subsequently the Kalman gain is used to map the predicted residuals, consisting of the ionosphere free GPS pseudorange and carrier phase observations,

$$\mathbf{z}_i = \begin{pmatrix} \mathbf{P}_{\mathrm{IF}} \\ \mathbf{L}_{\mathrm{IF}} \end{pmatrix} = \begin{pmatrix} (P_{\mathrm{IF},1}; \ldots; P_{\mathrm{IF},n}) \\ (L_{\mathrm{IF},1}; \ldots; L_{\mathrm{IF},n}) \end{pmatrix}, \tag{3.66}$$

minus their modeled values, $\mathbf{h}(\mathbf{x}_i^-)$, into a correction of the propagated state from which the updated filter state is obtained. Similar to the batch LSQ it must be noted that GPS measurement modeling is done in the ITRF using the position of the GPS receiver antenna phase center. Again, this means that the appropriate transformations and phase center offset correction discussed in section 3.2 have to be handled accordingly.

The design matrix contains the linearized partial derivatives with respect to the filter state,

$$\mathbf{H}_i = \begin{pmatrix} \dfrac{\partial \mathbf{h}}{\partial \mathbf{r}} & \dfrac{\partial \mathbf{h}}{\partial \mathbf{v}} & \dfrac{\partial \mathbf{h}}{\partial \mathbf{p}} & \dfrac{\partial \mathbf{h}}{\partial c\delta t_r} & \dfrac{\partial \mathbf{h}}{\partial \mathbf{B}} \end{pmatrix}, \tag{3.67}$$

which, due to the fact that the model can be linearized around the predicted state from the time update, can be more specifically written as

$$\mathbf{H}_i = \begin{pmatrix} \mathbf{E}_i & \mathbf{0} & \mathbf{0} & \mathbf{1} & \mathbf{0} \\ \mathbf{E}_i & \mathbf{0} & \mathbf{0} & \mathbf{1} & \mathbf{1} \end{pmatrix}. \tag{3.68}$$

Here, care must be taken to observe that the partials relating to the receiver clock are an $n \times 1$-dimensional vector of ones, and that the carrier phase ambiguity partials are given by the $n \times n$-dimensional identity matrix. This is however only true if the carrier phase measurements are put in the same order as their corresponding bias parameters in the filter state. The geometry matrix,

$$\mathbf{E}_i = \begin{pmatrix} -(\mathbf{U}^T(t_i)\, \mathbf{e}^1(t_i))^T \\ \vdots \\ -(\mathbf{U}^T(t_i)\, \mathbf{e}^n(t_i))^T \end{pmatrix}, \tag{3.69}$$

finally comprises the line of sight vectors (eqn. 2.28) to the different GPS satellites in the Earth fixed system, which have to be transformed to the ICRF by matrix $\mathbf{U}^T(t_i)$ from eqn. 3.1.

To improve the accuracy of the extended Kalman filter solution, the entire GPS data set is processed both in a forward, as well as a backward direction. At each epoch, a smoothed solution

$$\overline{\mathbf{x}}_i = \frac{\mathbf{P}_{i,fwd}^{-1}\mathbf{x}_{i,fwd} + \mathbf{P}_{i,bck}^{-1}\mathbf{x}_{i,bck}}{\mathbf{P}_{i,fwd}^{-1} + \mathbf{P}_{i,bck}^{-1}} \tag{3.70}$$

is then computed as the weighted average of the estimated filter states from both runs [*Brown and Hwang*, 1997]. The weights are determined by the information matrix, i.e. the inverse covariance, of the respective state estimates. By combining the forward and backward results, measurements from both before and after a given epoch contribute to the corresponding state estimate. As a result, a factor-of-two improvement in accuracy over the individual solutions can usually be achieved. However, a small degradation of the smoothed solution can usually be observed near the beginning and end of the data arc as well as over extended data gaps, where either the forward or backward filter is not yet fully converged.

3.5 GHOST toolkit

All of the previously discussed POD processing techniques are fully implemented in separate software tools as part of the GPS High precision Orbit determination Software Tools (GHOST, see [*Montenbruck et al.*, 2005*a*]). Besides the core POD tools, the toolkit furthermore comprises software for the generation of intermediate orbit and positioning products, data formatting, and satellite orbit comparisons. Similar to other POD software packages, such as GIPSY-OASIS [*ORMS*, 2005], Bernese [*Hugentobler et al.*, 2001] and GEODYN [*Rowlands et al.*, 1995], a strict processing scheme is to be followed when using GHOST for POD. This is required in order to assure a proper and robust editing of the GPS data within each of POD tools, prior to the actual orbit determination process. The following subsections provide an overview of both the GHOST processing scheme as well as the applied GPS data editing concept as used in this research.

3.5.1 Processing scheme

Within GHOST, precise orbit determination based on undifferenced GPS observations is a three step process, illustrated in Fig. 3.7. The first step is the generation of kinematic single point position solutions at discrete (measurement) epochs using only ionosphere free GPS pseudoranges, implemented in the *Single Point Positioning for LEO satellites* (SPPLEO) program. The second step involves the dynamical filtering of these kinematic positions using the reduced-dynamic batch LSQ approach described earlier in this chapter, with the only difference that position estimates, instead of GPS observations, are used as measurements. This is mechanized in the so-called *Position Fit* (PosFit) program. The output of this second step is a continuous and smooth orbit with medium precision (15-25 cm, 3-dimensional),

provided in the SP3 format. The third and final step of the process consists of the actual precise orbit determination, kinematic and/or reduced dynamic, where the just derived coarse a-priori orbit is used for GPS data editing, as described in the next subsection. Here, the kinematic batch LSQ from section 3.3 is implemented in the *Kinematic Point Positioning* (KIPP) program, the reduced dynamic batch LSQ from section 3.4.3 in the tool called *Reduced Dynamic Orbit Determination* (RDOD) and the EKF from section 3.4.4 in the *Filter for Adjustment of Satellite Trajectories* (FAST).

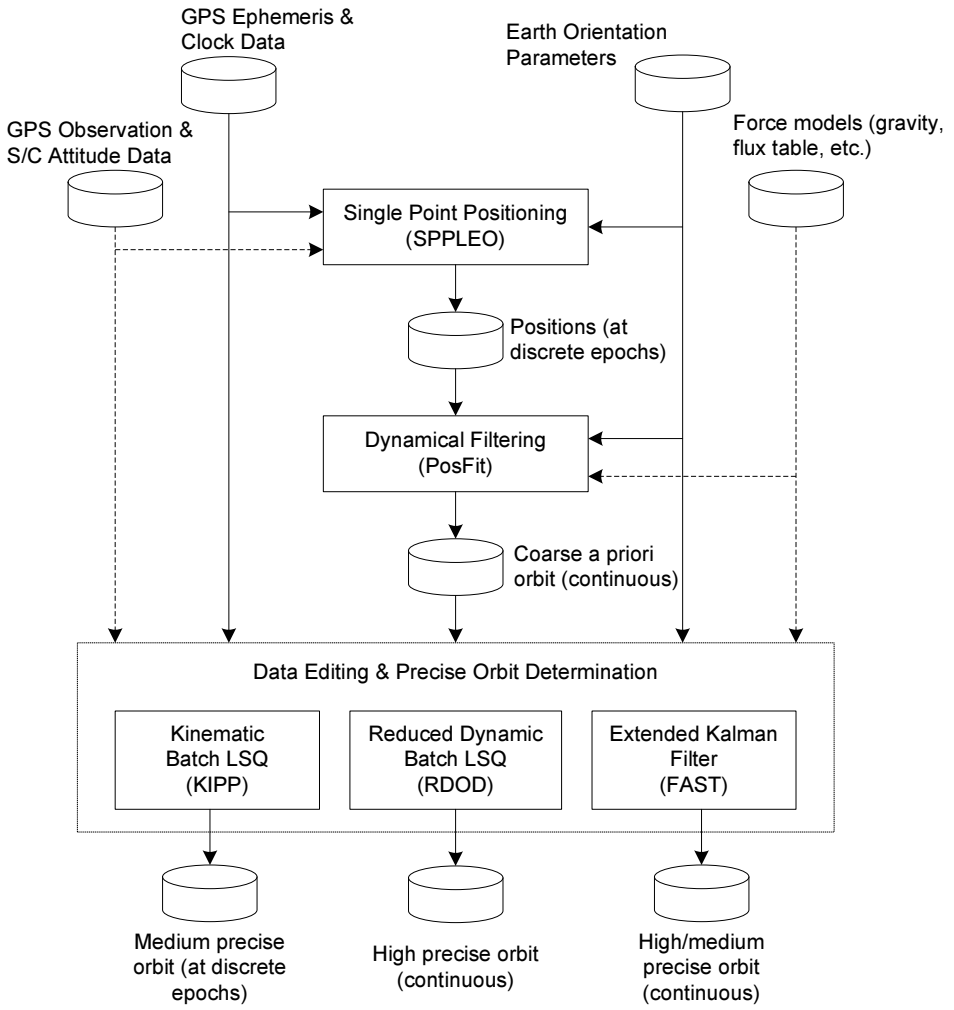

Figure 3.7 Processing scheme for GPS based precise orbit determination of LEO satellites using the GHOST toolkit.

The GHOST orbit determination process is typically conducted in single day (24 hour) data batches. If desired data batches of longer duration, e.g. 30 hours, can also be processed for conducting overlap analysis or the creation of semi-continuous orbits over an extended data arc. The toolkit works with standardized data formats, such as the Receiver INdependent EXchange (RINEX) [*Gurtner*, 1994] format for GPS observations and the SP3 format for the GPS satellite ephemerides and the reduced dynamic output orbits. Furthermore, Earth orientation parameters, required for the necessary reference frame transformations, can be provided in either the IERS yearly table, or the IGS Earth rotation parameter (ERP) format. Other required input data, such as the spacecraft attitude information used for correcting the GPS antenna phase center offset with respects to the center of mass, has to be put into a GHOST specific format [*Helleputte*, 2004].

The here presented processing scheme is fully self-contained and does not require any external reference ephemerides for purposes other than orbit comparisons in an effort to validate the orbit precision.

3.5.2 GPS data editing

A crucial factor of GPS based precise orbit determination is the quality of the data used. Therefore proper methods for data screening have to be applied in order to detect outliers and bad measurements, which are regularly encountered even in data obtained from geodetic grade spaceborne GPS receivers. Each of the three POD programs within the GHOST toolkit validate the GPS measurements prior to the actual orbit determination process using a combination of different statistical tests and simple limit checks. User configurable thresholds are, for example, used to discard any observations taken below a certain elevation or below a minimum SNR ratio. Also the presence of GPS satellite orbit and clock data is verified since this is required for processing the observations.

In addition to the more simple limit checks the quality of the GPS code and carrier-phase measurements is assessed in comparison with an a-priori reduced dynamic orbit, determined in the second step of the GHOST processing scheme. During construction of this orbit severe position outliers are also identified and removed. At each epoch modeled geometric ranges are computed, using the GPS receiver position obtained from this a-priori orbit, which are then used in conjunction with the observed ionosphere free pseudoranges to determine the GPS receiver clock offset value. From the set of n ≥ 2 observations an estimate

$$c\delta t_r(t_j) = \frac{1}{n}\sum_{i=1}^{n}\left(P^i_{\mathrm{IF},r}(t_j) - \left(\rho^i_r(t_j) - c\delta t^i(t_j)\right)\right) \tag{3.71}$$

of the receiver clock offset at the measurement epoch t_j and the associated residuals

$$res^i_r(t_j) = P^i_{\mathrm{IF},r}(t_j) - \left(\rho^i_r(t_j) + c\delta t_r(t_j) - c\delta t^i(t_j)\right) \tag{3.72}$$

are now obtained. Whenever the standard deviation of these residuals exceeds a predefined threshold, the code observation that contributes the dominating error is

identified and removed from the set of observations. If necessary, the process is repeated to reject multiple outliers at the same epoch. The GPS receiver clock offsets determined in this way can be used as a-priori values in the orbit determination process later on. This approach to pseudorange editing provides a safe and robust way to identify outliers. Although the receiver position from the a-priori orbit also exhibits an error, this is largely absorbed by the receiver clock offset. The small remaining contribution as well as pseudorange multipath, systematic errors and noise not absorbed can be compensated for by the size of the standard deviation threshold.

Whereas the code observations are subject to outliers, which need to be detected, the carrier phases have to be accurately screened for cycle slips, i.e. sudden jumps in the carrier phase bias. Since the carrier phase biases are constant over time a sudden jump can be detected by examining time differenced carrier phase measurements between two consecutive measurement epochs, t_{j-1} and t_j, in a similar process as for the code observations. Instead of the receiver clock offset the time difference of two consecutive clock offsets is determined. From the set of n ≥ 2 observations an estimate

$$c\delta t_r(t_{j-1}, t_j) = \frac{1}{n} \sum_{i=1}^{n} \left(L^i_{\mathrm{IF},r}(t_{j-1}, t_j) - \left(\rho^i_r(t_{j-1}, t_j) - c\delta t^i(t_{j-1}, t_j) \right) \right) \tag{3.73}$$

of the time differenced receiver clock offset between the measurement epochs t_j and t_{j-i} and the associated residuals

$$\begin{aligned} res^i_r(t_{j-1}, t_j) = \; & L^i_{\mathrm{IF},r}(t_{j-1}, t_j) - \left(\rho^i_r(t_{j-1}, t_j) + c\delta t_r(t_{j-1}, t_j) \right. \\ & \left. - c\delta t^i(t_{j-1}, t_j) \right) \end{aligned} \tag{3.74}$$

of the time differenced carrier phase observations are determined. Again, whenever the standard deviation of these residuals exceeds a predefined threshold, the carrier phase observation that contributes the dominating error is assumed to have experienced a cycle slip and is removed from the set of observations. If necessary, the process is repeated to identify multiple cycle slips. The threshold for this process however must be set small enough in order to guarantee no undetected cycle slips. This is possible due to the low noise level in the carrier phase data and the fact that errors in the a-priori positions used, even as highly time correlated multipath and systematic effects, cancel over short time spans.

Even though this data editing procedure puts an additional burden on the overall POD process, due to the required a-priori orbit generation, practical tests with CHAMP and GRACE GPS measurements have demonstrated this approach to be more reliable and accurate than 'on-the-fly' GPS data screening, such as e.g. outlier removal from post-fit residuals of the batch LSQ, or a scheme for model validation and adaption, as the detection, identification and adaption (DIA) method proposed in *Teunissen* [1990], for use in the extended Kalman filter.

3.6 POD results

This section contains the GPS based POD results of the CHAMP and GRACE spacecraft for a 101-day data arc in 2003 ranging from July 9 to October 17 (corresponding to day of year (DOY) 190 to 290 respectively), using the kinematic and reduced dynamic tools from the GHOST toolkit and following the processing scheme presented earlier. The CHAMP GPS and precise attitude data for this period are obtained from the CHAMP Information System and Data Center (ISDC) at the GeoForschungsZentrum (GFZ). In the case of GRACE this publicly available data, part of the so-called GRACE Level 1B products [*Case et al.*, 2002], is obtained from JPLs Physical Oceanography Distributed Active Archive Center (PODAAC). In addition to the mandatory GPS measurement and S/C attitude data, other input data required, and settings used, for the different POD programs are given in the next subsection. This is followed by a brief presentation of some additional output of the POD programs, the empirical accelerations and the post-fit residuals. In an effort to validate the quality of the final orbits, several orbit comparisons have been carried out, as well as an independent orbit validation using Satellite Laser Ranging (SLR) data. The results of both comparisons can be found in the last two subsections.

3.6.1 Settings and input data

Despite the fact that CHAMP and GRACE GPS measurements are provided at nominal intervals of 10 seconds, when excluding GPS data outages, they are processed at intervals of 30 seconds in the different POD applications. These epochs coincide with the high rate CODE GPS satellite clock offset data (section 3.1) that are, together with their accompanying GPS satellite orbits, used for the POD applications described here. Actually, the reduced dynamic and kinematic orbits show a small degradation in their precision when processing GPS data at the nominal 10 second data rate, most likely caused by the additional clock interpolation error now introduced, whilst the processing time of the different programs increases with roughly a factor 3.

As mentioned earlier, the first step within each of the POD programs concerns the GPS data editing, requiring the a-priori reduced dynamic orbit (PosFit). This orbit was found to have an overall precision of 5 cm in both radial and cross-track direction, and 15 cm in the along-track direction when compared to the reduced dynamic POD orbits (RDOD, FAST), using the orbit comparison methodology from section 3.6.4. Throughout all POD programs, and for all spacecraft, identical and constant setting are applied for GPS data editing. All GPS observations taken at elevations below 5° and with an SNR value of 5, corresponding to a C/N_0 of about 11 dB-Hz cf. eqn. 2.40, or lower are rejected from processing. In addition to these simple limit checks the ionosphere free pseudorange and carrier phase measurements are subjected to the robust comparison with the a-priori reduced dynamic orbit. The earlier discussed thresholds for the standard deviation of the ionosphere free

residuals are set to values of 0.5 m for the pseudorange and 2.5 cm for the carrier phase observations. These settings result in the average daily data editing statistics for the CHAMP and GRACE GPS observation data used, shown in Table 3.3.

Table 3.3 Average daily data editing statistics for the CHAMP and GRACE spacecraft. Displayed are the total number of observations and the percentages used.

	Total $P_{\mathrm{IF}}/L_{\mathrm{IF}}$ obs.	Used P_{IF} [%]	Used L_{IF} [%]
CHAMP	24317	78.8	87.1
GRACE A	24905	81.7	92.5
GRACE B	22062	87.2	93.8

The table displays the average daily number of ionosphere free pseudorange and carrier phase observations (taken at the 30 second processing interval) over the entire data arc, and the percentage of them that passed the data editing, which are thus used in the subsequent POD process. As can be seen most data is edited for CHAMP. This is a combined result of the lower GPS data quality, as discussed in section 2.6, and the higher number of observations taken below the elevation mask when compared to GRACE. When looking at the GRACE results it is noted that there is a structural lower number of GPS measurements for GRACE B, which is the result of a structural lower number of observations per epoch and is not related to large GPS data outages. However, it was shown in section 2.6 that the multipath and systematic errors were more or less the same for both GRACE satellites, but that the noise left on the pseudorange and carrier phase observations, Figures 2.6 and 2.7 respectively, is lower for GRACE B, meaning that the GPS data is of better quality here. This is also reflected is the data editing statistics, where higher percentages of the available GPS data, especially the pseudoranges, are used for the POD process.

In the presence of the unmodeled multipath and other systematic effects, as well as GPS ephemerides errors, an SNR or elevation dependent weighting of the GPS data was not found to be very suitable. Therefore, all GPS observations used for the POD process are given a unit weight, which of course differs between the observation types and also varies slightly for the different spacecraft. Based on the analysis in section 2.6, and given the fact that outliers have already been taken out, the ionosphere free measurement standard deviations used are set to the ones in Table 3.4.

Table 3.4 Unit standard deviations for the ionosphere free GPS observation data, used throughout all POD applications.

	CHAMP	GRACE A	GRACE B
$\sigma_{P_{\mathrm{IF}}}$ [cm]	50.0	40.0	40.0
$\sigma_{L_{\mathrm{IF}}}$ [cm]	1.0	1.0	1.0

Due to the higher accuracy of the carrier phase observations displayed here, the position or orbit determination process is basically dominated by this observation type. The pseudorange observations are required to discriminate the carrier phase bias parameters from the receiver clock offsets, and therefore only contribute indirectly, but crucially, in the positioning. It might be recalled that during the discussion of the kinematic and reduced dynamic batch LSQ it was mentioned that by adding a-priori information to the carrier phase bias parameters the kinematic positions or the satellite trajectory could be computed using solely carrier phase observations. Although this approach has been tried here as well, and the GHOST toolkit is able to handle this methodology, processing both ionosphere free pseudorange and carrier phase observations was found to provide better and more stable results. Since an equivalent approach by *Svehla and Rothacher* [2005] provides high quality orbit solutions it remains for further study to see if this methodology can be improved in the GHOST toolkit.

Table 3.5 GPS antenna phase center offsets with respect to the center of gravity, defined in the respective S/C body systems, for the CHAMP and GRACE satellites.

	X [m]	Y [m]	Z [m]
CHAMP	-1.4880	0.0000	-0.3928
GRACE A	0.0004	-0.0004	-0.4140
GRACE B	0.0006	-0.0008	-0.4143

No further input information is required for the kinematic batch LSQ (KIPP), although for completeness the used GPS antenna phase center offsets to the center of mass of the CHAMP and GRACE spacecraft still need to be given. These offsets, expressed in the respective S/C body frames, are listed in Table 3.5. It must also be mentioned that the positions from the a-priori reduced dynamic orbit are used as initial position values for linearization in the kinematic batch LSQ. Furthermore, the GPS receiver clock offsets are also initialized using the clock offset determination results from the pseudorange data editing. Since none are treated as a-priori information, and thus no weight is assigned to them, a free estimation is still performed. Due to the fact that the initial values are already close to the final positions (and clock offsets), only 1 iteration is required in the kinematic case.

For the reduced dynamic applications the dynamical models discussed in section 3.4.1 are used, which are listed in Table 3.6. Furthermore, the used reference frame transformations from ITRF2000 (implied by the CODE GPS ephemerides) to the EME2000 inertial frame, needed for integration of the trajectory, were already displayed in Table 3.2. For both the batch LSQ and the EKF the a-priori PosFit orbit is used to obtain the initial spacecraft state. Similar to the kinematic case, the GPS receiver clock offsets for the reduced dynamic batch LSQ (RDOD) are initialized using the values obtained from the pseudorange data editing process. For the EKF only the clock value on the initial state epoch requires initialization. Furthermore, for computation of the atmospheric drag and solar radiation pressure the mass and

Table 3.6 Overview of the dynamical models used for processing the GHOST reduced dynamic orbits.

Item	Description
Static gravity field	GGM01S 100 × 100
Tidal perturbations	Solid Earth tide (4 × 4, diurnal)
	Polar tide (IERS/IGS)
	Ocean tides (UT/CSR 3.0 + TEG2B)
3rd body gravity	Analytical series expansions of luni-solar coordinates
Satellite model	Canon-ball model (constant surface and mass)
Radiation pressure	Solar radiation pressure (conical Earth shadow)
Atmospheric drag	Jacchia 71 density model (NOAA solar flux (daily) and geomagnetic activity (3 hourly))

surface of both the CHAMP and GRACE spacecraft are set to values of 500 kg and 0.5 m^2 respectively. The atmospheric drag and solar radiation pressure scaling coefficients are also chosen similar for these spacecraft, 2.3 and 1.3 respectively, but are adjusted to unique values during the estimation process. Finally, in both the batch LSQ and EKF the empirical accelerations are all initialized to zero. For the batch LSQ a total of 3 iterations are required to adjust the estimation parameters to their final values, whereas the filter-smoother only processes the observation data once in forward and backward direction.

The just discussed (uncorrelated) a-priori information is constrained with the standard deviations displayed in Table 3.7. As can be seen in this table, the EKF has relatively tight constraints for the initial satellite state, otherwise convergence of the filter takes too long. This in contrast to the batch LSQ where the initial satellite state is left relatively free, and where even looser constraint could be applied. For the batch LSQ, the amplitudes for the empirical accelerations in the 600 s intervals are estimated as part of the orbit determination process. Here, a-priori constraints are applied to prevent divergence. Since the tangential (along-track) and radial component are difficult to separate due to the heavy in-plane dynamic coupling, tighter constraints are applied in radial direction. The along-track component should still be allowed to compensate for un- or mismodeled atmospheric drag. A similar philosophy has been applied to the empirical accelerations in the EKF, only here the process noise and the auto-correlation time were found to be more important than the a-priori constraints.

The just discussed settings for the different POD programs were found to provide the most precise orbits, and are therefore adopted for the entire data arc. The relevant outputs of the POD programs are discussed in the following subsections.

Table 3.7 Uncorrelated a-priori constraints and process noise used throughout the reduced dynamic POD programs for the entire data arc. Identical values are applied to the CHAMP and GRACE spacecraft.

	RDOD	FAST
A-priori standard deviation		
$\sigma_{\mathbf{r}}$ [m]	100.0	1.0
$\sigma_{\mathbf{v}}$ [m/s]	100.0	1.0
σ_{C_D} [-]	1.0	0.4
σ_{C_R} [-]	0.5	0.2
σ_{a_R} [nm/s^2]	5.0	10.0
σ_{a_T} [nm/s^2]	30.0	40.0
σ_{a_N} [nm/s^2]	10.0	20.0
$\sigma_{c\delta t_r}$ [m]	-	500.0
$\sigma_{b_{\mathrm{IF}}}$ [m]	-	10.0
Auto-correlation time/Interval size		
$\tau_{a_{(R,T,N)}}$ [s]	600.0	600.0
$\tau_{c\delta t_r}$ [s]	-	100.0
Process noise (steady state) σ		
σ_{a_R} [nm/s^2]	-	2.0
σ_{a_T} [nm/s^2]	-	8.0
σ_{a_N} [nm/s^2]	-	4.0
$\sigma_{c\delta t_r}$ [m]	-	500.0

3.6.2 Empirical accelerations

Typical results of the empirical accelerations estimated in orbit determination runs of the reduced-dynamic batch LSQ and EKF, using the just described program settings, are depicted in Fig. 3.8 (GRACE B, DOY 230). Here, only the dominant components in the tangential, or along-track, direction are shown. The normal components of the empirical accelerations are typically less than 20 nm/s^2 and might be related to albedo, mismodeled solar radiation pressure effects, unmodeled cross winds or unmodeled tidal perturbations. Due to the applied constraint in the radial component, the empirical accelerations in this direction are always near zero. The tangential component of the empirical acceleration for the batch LSQ in Fig. 3.8 (top) shows a small amplitude of 30 nm/s^2 during the first hours of DOY 230, followed by a peak of 120 nm/s^2 and a subsequent transition to again a quasi-periodic behavior. The observed pattern of the tangential acceleration component mainly reflects a mismodeling of atmospheric drag in the applied dynamical model.

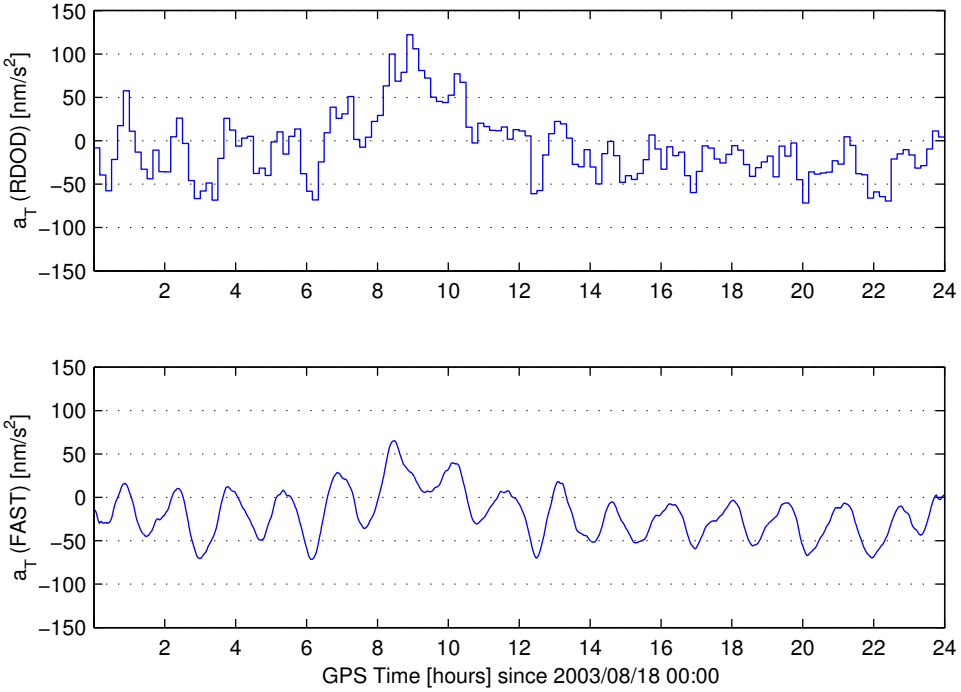

Figure 3.8 Empirical accelerations of GRACE B in the tangential, a_T, or along-track direction for both the reduced dynamic batch LSQ (top) and the EKF (bottom) for August 18, 2003 (DOY 230).

The peak value being the result of a non-modeled geomagnetic storm during that day. When comparing the empirical accelerations estimated by the batch LSQ (top) and the EKF (bottom), it becomes obvious that the observed phenomena are highly correlated. However, it is noted, that the estimated amplitudes differ by a factor of about 1.5. The origin of this discrepancy has not yet been resolved but might be due to a coupling between empirical accelerations and other estimation parameters, e.g. C_R and C_D, or simply by the different stochastic processes. It is further noted, that care must be taken when interpreting empirical acceleration patterns. The obtained values are highly dependent on the underlying dynamical and stochastic models, as well as the applied filter settings.

3.6.3 Post-fit residuals

A measure for consistency of the applied models with the GPS observation data is provided by the post-fit measurement residuals of the different POD programs. These residuals are readily obtained from the batch LSQ methods, for which the RMS of the ionosphere free pseudorange and carrier phase observations are shown

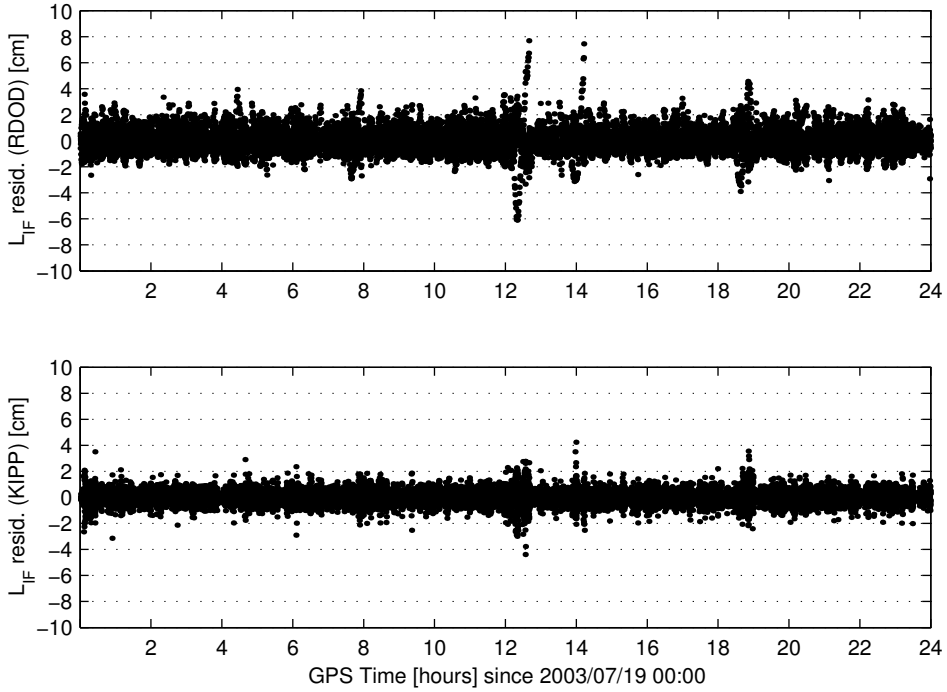

Figure 3.9 Post-fit residuals of the kinematic (KIPP, bottom) and reduced-dynamic (RDOD, top) batch LSQ orbit determination for GRACE A on July 19, 2003 (DOY 200).

in Table 3.8. The residuals were found to have a zero mean, which is expected given the underlying stochastic model applied.

Table 3.8 RMS of the ionosphere free pseudorange and carrier phase post-fit residuals for the entire data arc.

	RMS Res. (KIPP)		RMS Res. (RDOD)	
	P_{IF} [cm]	L_{IF} [cm]	P_{IF} [cm]	L_{IF} [cm]
CHAMP	39.09	0.48	38.90	0.77
GRACE A	34.68	0.47	34.93	0.87
GRACE B	34.23	0.41	34.23	0.89

As can be seen the pseudorange residuals are a little higher for CHAMP than they are for GRACE, reflecting the overall measurement quality. When looking at the carrier phase residuals it is readily observed that in the kinematic case these are much lower. Fig. 3.9 depicts the time series of typical carrier phase residuals from both the kinematic and reduced-dynamic batch LSQ for GRACE A on DOY

200. Here, it can be seen that systematic errors in the data as well as small errors in the CODE clock offsets are left outside the estimation parameters. This even applies to the larger errors visible around 12:00 and 14:00. Since these appeared in the CHAMP and GRACE B residuals as well they are not the result of undetected cycle slips, but were found to be related to a drift in the CODE GPS satellite clock offsets, occurring on a regular basis. In the kinematic case, the larger number of estimation parameters, as well as the absence of the dynamical constraints, cause all errors to be largely absorbed, and the residuals here mostly show observation noise. It must be noted that occasionally the reduced dynamic batch LSQ carrier phase residuals slightly diverge at the end of the daily data arc. This is caused by the long-arc integration performed within this method, making it more susceptive to the accumulation of numerical errors, as well as the (sometimes) not so good condition of the normal equations matrix. Additional iterations do not resolve this problem, but when occurring it only marginally degrades the orbit precision.

Unfortunately post-fit residuals are not easily obtained for the EKF in its current implementation. Normally, for recursive methods use can be made of the predicted residuals to test model consistency while running. An example of this is the earlier mentioned DIA procedure, described in *Teunissen* [1990] and implemented by e.g. *Tiberius* [1998] in a kinematic recursive estimation scheme. Due to the robust data editing procedure applied for this research, it is assumed that no model misspecifications, such as undetected cycle slips, remain and that large outliers in the observation data are completely removed. As can be seen in the post-fit (reduced dynamic) batch LSQ residuals this assumption is allowed here.

Although it must be said that slight variations in the POD program settings result in different empirical acceleration patterns and trajectory or position estimates, the post-fit residuals in general remain unaffected. Therefore they do not disclose any information on the orbit quality. The same must also be said about the formal (co)variances of the different estimation parameters. These values are in general too optimistic and solely depend on the program settings and the applied models. The two methods used for validation of the orbit results are discussed in the following two subsections

3.6.4 Orbit comparisons

In an effort to obtain some information on the precision of the CHAMP and GRACE orbits computed for this research they are compared to externally generated reduced dynamic GPS based POD solutions derived using different processing methodologies. Although this is certainly not an independent validation procedure, it is one of the most obvious tests, often used, to obtain a first indication of the overall orbit quality. It must be noted however that the so-called reference ephemerides used for the different comparisons are limited to a precision of, at best, several centimeters as well.

The orbit differences between the GHOST orbits and the reference ephemerides are computed in the radial, along-track and cross-track direction at the discrete

epochs in case of a kinematic orbit (KIPP) and at the nominal sampling rate of 30 seconds if reduced dynamic orbits are concerned (FAST, RDOD). These individual values are grouped in a daily statistic comprising of a mean and RMS (around zero) value in each of the directions mentioned. Statistics over multiple days are computed from the single day values, applying proper weighting to account for differences in the number of data points used. In practice this weighting only applies to the kinematic orbit comparisons, since these are the only ones that have positions at discrete epochs, which vary in number from day to day. It is furthermore noted that all reference ephemerides used are provided in the SP3 format, and are already defined in ITRF2000 coordinates. No additional reference frame transformations are therefore applied.

The CHAMP reference ephemerides are provided by the Department of Earth Observation and Satellite systems (DEOS) at the Technical University of Delft [*Van den IJssel et al.*, 2003]. These reduced dynamic orbits were created by processing ionosphere free triple difference GPS carrier phase observations with the GEODYN software package. Using the just described methodology, comparisons are made between the kinematic and reduced dynamic GHOST orbits and the DEOS reference ephemerides. In addition the kinematic and reduced dynamic batch LSQ GHOST orbits are also compared with each other, which gives an indication of the impact of the dynamic models applied. The results of this analysis are given in Table 3.9, showing the statistics of almost the entire data arc. Here, DOY 267 is left out of the reduced dynamic orbit comparisons (FAST-DEOS, RDOD-DEOS) due to an extended GPS data outage of nearly 5 hours at the end of the day. This however does not apply to the kinematic comparison since here there simply are no positions if no observation data is available. The reduced-dynamic statistics for this single day are given in Table 3.11 where it can be seen that when no observations are available the orbits show large discrepancies, especially when created using the EKF. It must be noted however that the reference ephemerides are also affected by this outage and no longer have sub-dm precision.

Table 3.9 Mean and RMS values in radial, along-track and cross-track direction for the CHAMP orbit comparisons of both the kinematic and the reduced-dynamic solutions over the period 2003 DOY 190 - 290, excluding DOY 267.

	Mean [cm]			RMS [cm]		
	Radial	Along-track	Cross-track	Radial	Along-track	Cross-track
Kin. - Red.Dyn.						
KIPP - DEOS	-0.32	0.72	1.56	5.11	4.90	4.56
KIPP - RDOD	-1.48	-0.20	1.45	4.89	3.60	4.16
Red.Dyn. - Red.Dyn.						
RDOD - DEOS	1.15	0.93	0.11	2.50	3.69	2.31
FAST - DEOS	0.60	0.70	-0.31	2.58	4.49	2.46

Table 3.10 Mean and RMS values in radial, along-track and cross-track direction for the GRACE A and B orbit comparisons of both the kinematic and the reduced-dynamic solutions over the period 2003 DOY 190 to 290. The external GRACE ephemerides data is provided by JPL and TUM.

	Mean [cm]			RMS [cm]		
	Radial	Along-track	Cross-track	Radial	Along-track	Cross-track
GRACE A						
Kin. - Red.Dyn.						
KIPP - JPL	2.27	0.05	-3.37	4.93	4.65	4.45
KIPP - RDOD	2.78	-0.28	-5.48	4.84	3.50	6.32
Red.Dyn. - Red.Dyn.						
RDOD - JPL	-0.50	0.35	2.11	1.75	2.88	2.98
FAST - JPL	-0.62	0.32	2.74	2.07	3.29	3.44
RDOD - TUM	-0.75	-1.86	2.80	2.77	3.68	3.91
FAST - TUM	-0.87	-1.89	3.45	2.96	3.99	4.43
TUM - JPL	0.25	2.21	-0.69	2.68	3.76	2.48
GRACE B						
Kin. - Red.Dyn.						
KIPP - JPL	3.09	-0.20	2.59	5.66	4.92	3.98
KIPP - RDOD	3.64	-0.15	1.23	5.61	3.63	3.75
Red.Dyn. - Red.Dyn.						
RDOD - JPL	-0.54	-0.05	1.37	1.85	2.98	2.59
FAST - JPL	-0.58	-0.08	1.46	2.05	3.12	2.47
RDOD - TUM	-1.63	-1.41	1.91	3.20	3.59	3.41
FAST - TUM	-1.67	-1.43	2.01	3.36	3.79	3.31
TUM - JPL	1.09	1.36	-0.53	2.76	3.19	2.21

For both GRACE satellites two sets of reference ephemerides are used in the comparison. The first one is provided by JPL and is distributed along with the GRACE GPS data [*Case et al.*, 2002]. These orbits are created by processing undifferenced ionosphere free pseudorange and carrier phase data with the GIPSY-OASIS software package. The other reference ephemerides are obtained from the Technical University of Munich (TUM) [*Svehla and Rothacher*, 2005]. They are created using the Bernese software package, by processing undifferenced ionosphere free carrier phase observations only. It must be mentioned that both sets of reference

ephemerides were generated using internally consistent GPS satellite orbit and clock offset solutions.

The orbit comparisons for the GRACE satellites are carried out in full analogy with the just described CHAMP orbit comparison, with the only difference that two sets of reference ephemerides are used here. Again, some outliers in the orbit comparisons were detected. For GRACE A, a GPS data outage of 6 hours was found in DOY 222, whereas for GRACE B an extended data gap of 10 hours stretching over DOY 239 and 240 was observed. Similar to CHAMP these days are not used in computing the reduced dynamic statistics presented in Table 3.10. The comparison statistic with the JPL ephemerides of these days can again be found in Table 3.11. It must be mentioned that for the comparison with the TUM orbits even more days had to be left out of the statistics. Due to reasons unexplained these orbits sometimes exhibit position errors of several hundreds of meters compared to both JPL and GHOST ephemerides.

Table 3.11 RMS values in radial, along-track and cross-track direction for the CHAMP and GRACE reduced dynamic GHOST orbit comparisons over days with extended data gaps.

	RMS [cm]		
	Radial	Along-track	Cross-track
CHAMP (DOY 267)			
RDOD - DEOS	15.9	55.3	40.0
FAST - DEOS	35.1	249.9	10.2
GRACE A (DOY 222)			
RDOD - JPL	3.0	23.1	2.7
FAST - JPL	42.4	536.4	3.3
GRACE B (DOY 239/240)			
RDOD - JPL	9.7	94.1	2.7
FAST - JPL	20.1	184.3	2.9

Nevertheless, it can be seen in the results of the CHAMP and GRACE orbit comparisons that overall the GHOST orbits are in good consistency with the reference ephemerides. It can also be observed that the largest RMS values occur in the comparisons of the kinematic solution, which is therefore assumed to be the least precise orbit of all. Furthermore, it is suspected that under normal circumstances the EKF (FAST) provides marginally worse results than the reduced dynamic batch LSQ (RDOD). During GPS data outages the performance is significantly worse (Table 3.11). It is noted however that care must be taken when further interpreting the orbit comparison statistics. No hard conclusions can be drawn on which ephemerides are the most accurate. The different biases, or means, and RMS

values can have a number of reasons and can be the result of several underlying effects, including differences in the dynamic models, GPS ephemerides data or observation modeling, reference frame transformations or GPS antenna phase center offset displacements. Although most of the statistics show a behavioral pattern

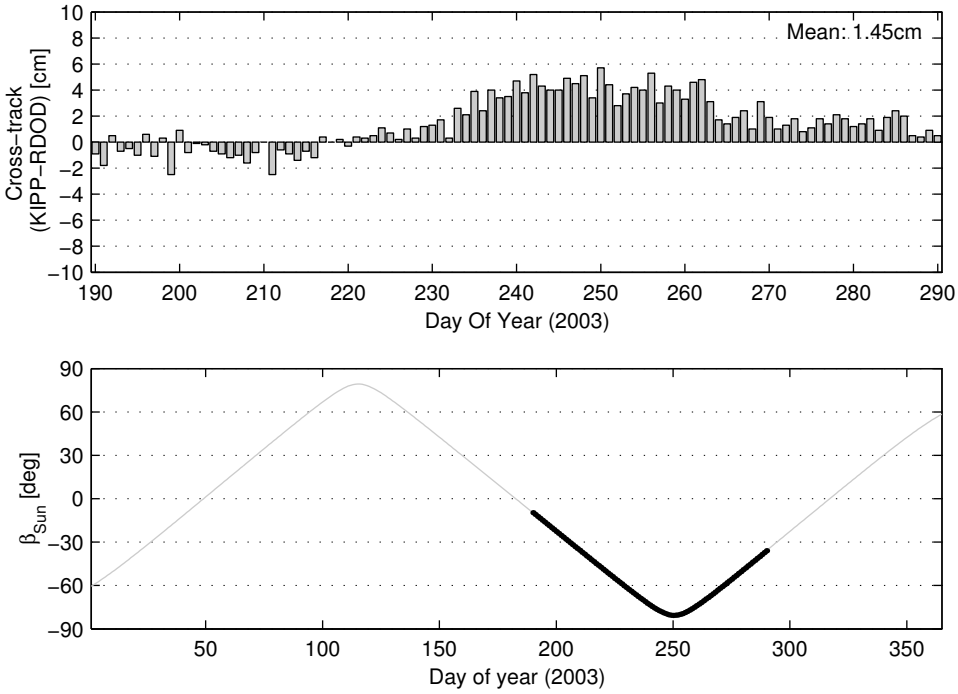

Figure 3.10 Cross-track mean offset for the CHAMP KIPP-RDOD comparison (top) over the entire data arc, together with the angle between the Sun vector and the CHAMP orbital plane (bottom) for 2003. The period corresponding to the data arc is highlighted.

that is more or less expected, such as a large radial RMS in the kinematic comparison and dominating along-track RMS values in the reduced-dynamic comparisons, a time varying behavior could be established in the cross-track direction. Although more dominant in some, all of the comparisons show the mean cross-track offset to gradually vary over time. For CHAMP the mean cross-track offset of the KIPP-RDOD comparison over the entire data arc can be found in Fig. 3.10. In addition the angle of the CHAMP orbital plane with the sun vector, β_{Sun}, is also shown here. The period relating to the data arc has been highlighted. An angle of $\pm 90°$ means that the orbital plane is perpendicular to the sun vector. For GRACE A the mean cross-track offsets for the RDOD-JPL comparisons is shown in Fig. 3.11, together with β_{Sun} for the GRACE orbital plane. In both cases the time variation seems to be correlated with β_{Sun}. Although clearly a longer time series needs to

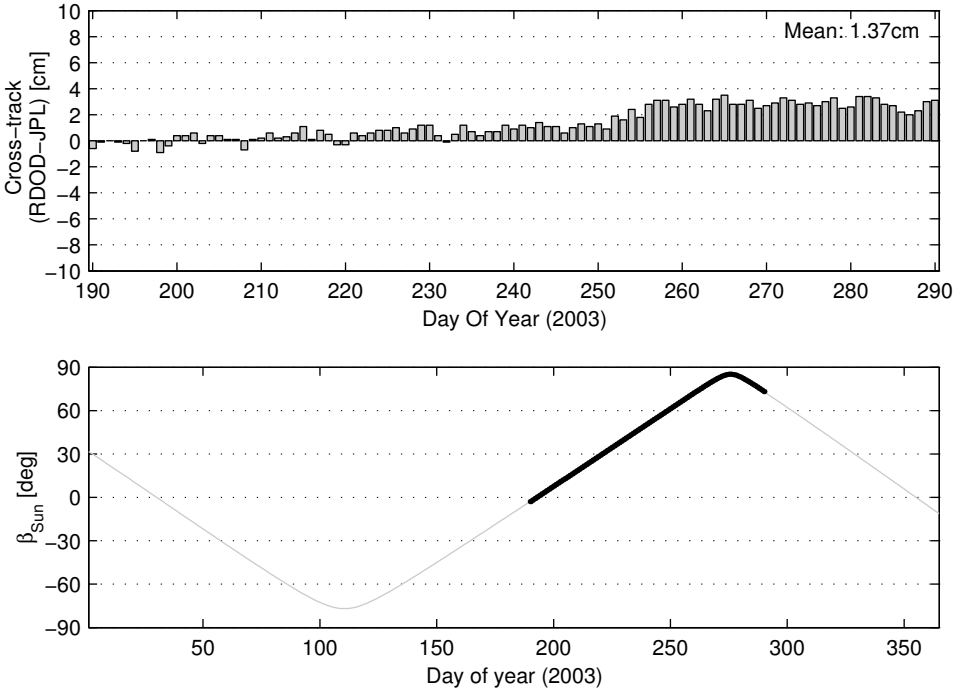

Figure 3.11 Cross-track mean offset for the GRACE B RDOD-JPL comparison (top) over the entire data arc, together with the angle between the Sun vector and the GRACE orbital plane (bottom) for 2003. The period corresponding to the data arc is highlighted.

be analyzed in order to draw any hard conclusions, it is suspected that the effect is caused by solar radiation pressure mismodeling in the reduced dynamic orbits. Apparently these discrepancies are not absorbed by the empirical accelerations. The effect seems to be most dominantly present in the GHOST reduced-dynamic orbits, which can be explained by the fact that the solar radiation pressure modeling is not very sophisticated (constant surface and mass) compared to e.g. JPL orbits, where satellite box models are used. Since the orbits are still precise enough for the purpose of a reference trajectory for relative spacecraft positioning, a possible solution to this potential problem remains for further study.

3.6.5 SLR validation

The orbit comparisons have the disadvantage that all the orbits involved are created using data from the same set of GPS observations. Although very unlikely, significant flaws in the data resulting in large orbit errors might remain undetected. An independent way for orbit validation is offered by comparing with SLR obser-

vation data, which for this research is done using the GEODYN software package. The SLR antenna offsets, with respect to the center of mass for the CHAMP and GRACE S/C, used for the comparison are displayed in Table 3.12, where they are given in the respective S/C body reference frames.

Table 3.12 SLR antenna offsets with respect to the center of gravity, defined in the respective S/C body systems, for the CHAMP and GRACE satellites.

	X [m]	Y [m]	Z [m]
CHAMP	0.0000	0.0000	0.2500
GRACE A	-0.6000	-0.3275	0.2178
GRACE B	-0.6000	-0.3275	0.2178

Typical results for the SLR comparison are depicted in Fig. 3.12 concerning the CHAMP RDOD orbits over the entire data arc. Here, the daily mean offset and the RMS of the SLR residuals is shown together with the number of SLR observations used to compute the statistics. As can be seen this number heavily fluctuates from day to day since the satellite is not always tracked by the same SLR ground stations on a daily basis. Overall the statistics look very good. The relatively high mean remains unexplained and is also observed for all SLR comparisons (Table 3.13) leading to the suspicion that this is caused by the SLR modeling. In the final SLR

Table 3.13 SLR validation statistics for the different reduced-dynamic CHAMP and GRACE orbits over the period 2003 DOY 190 - 290.

	Mean [cm]	RMS [cm]
CHAMP		
DEOS	-1.27	3.09
RDOD	-1.89	3.24
GRACE A		
JPL	-2.59	3.46
RDOD	-2.38	3.62
TUM	-2.85	4.42
GRACE B		
JPL	-2.15	3.00
RDOD	-1.35	2.81
TUM	-3.05	4.17

statistics over the entire data arc, displayed in Table 3.13, the outliers have again been excluded. For example, CHAMP DOY 267 shows an SLR RMS of 30 cm for the RDOD and 19 cm for the DEOS orbit, pointing out that both ephemerides are affected by GPS data outages.

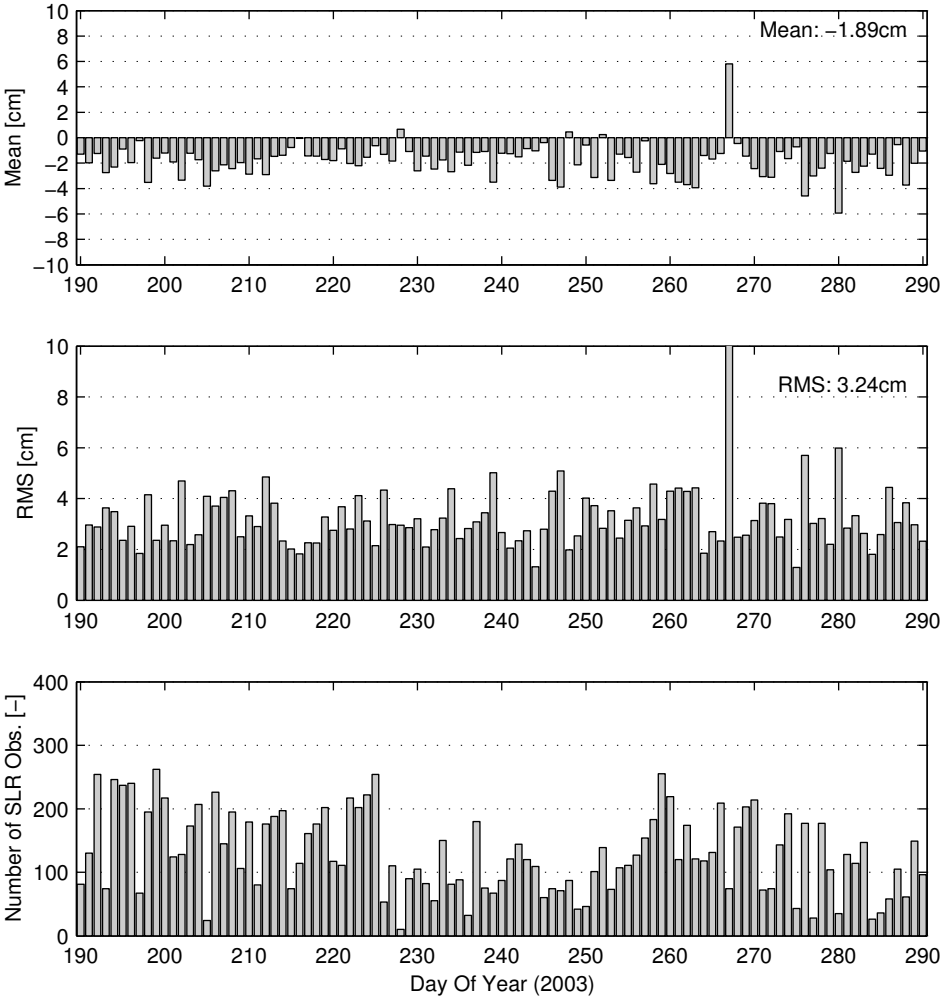

Figure 3.12 SLR comparison statistics for RDOD CHAMP ephemerides over the DOY 190 - 290, 2003 data arc. Shown are the mean offset (top) and the RMS (middle) of the SLR fit as well as the number of data points (bottom) used to obtain the statistics.

3.6.6 Conclusion

Based on the results from the previous subsections it has been decided to use the reduced dynamic batch LSQ (RDOD) orbits as reference trajectory for relative spacecraft positioning. The kinematic positions are only provided at discrete epochs and have shown to be the least precise of all. Although the EKF also produces good results, this method was found to be highly susceptive to GPS data outages. Despite an occasional numerical instability, observed in the post-fit residuals, the reduced dynamic batch LSQ estimation method was found to be the most robust of all, producing the highest precision orbits.

Chapter 4
Relative spacecraft positioning

Precise relative positioning between two or more GPS receivers is routinely exercised in terrestrial applications. This often involves an entire network of receivers with one dedicated reference station. As already mentioned in chapter 2, use is made of differenced GPS data for relative positioning applications in order to eliminate or reduce common data errors, such as the GPS satellite clock offset. Furthermore, it was shown that double difference GPS carrier phase ambiguities are integers. Once correctly resolved these integer ambiguities transform the corresponding carrier phase observations into highly precise relative ranges, with a noise level of only a few mm. Exploiting this integer property is therefore commonly regarded as the key to precise relative positioning.

From a purely kinematic perspective the problem of relative spacecraft positioning is almost similar to the terrestrial case of a GPS receiver on e.g. a rover that is positioned with respect to a reference station. In both cases one of the receivers is moving with respect to the other and so a new relative position vector has to be estimated every epoch. The major differences are the complete absence of tropospheric signal delays and the rapidly changing viewing geometry for the purely spaceborne scenario. These differences mainly influence the total number of estimation parameters, especially due to the larger number of carrier phase ambiguities, and the observation modeling. A clear advantage of the spaceborne case is the fact that, as seen in the previous chapter, spacecraft dynamics, and thus in a way also the relative dynamics between two spacecraft, can be modeled to a high degree of accuracy, whereas rover motion is, in general, unpredictable.

As already mentioned before, the previously discussed POD strategies form the conceptual basis for the developed relative positioning processing techniques. Therefore, in accordance, a kinematic and reduced dynamic batch least-squares estimator and an extended Kalman filter have been implemented and tested. In addition, a sequential kinematic filter, not based on any previously discussed scheme, has also been proposed. All strategies are based on processing differenced GPS data, and estimate the relative position between two spacecraft directly. This re-

quires amongst others accurate a-priori knowledge of one of the spacecraft, serving as the reference. It was already mentioned in chapter 3 that the reduced dynamic batch LSQ orbits are used for this purpose. The clear advantage of such an approach is that for multi-satellite formations each of spacecraft relative positions can be dealt with independently of the others, where one spacecraft serves as a dedicated reference. Out of the four proposed processing schemes both batch estimators and the sequential kinematic filter were found to have some limitations for use in real-world applications, due to the way they are currently implemented. These limitations are mostly related to problems with integer ambiguity resolution. The extended Kalman filter on the other hand has proven to be very adequate and robust for relative spacecraft positioning and is therefore described in full detail later on (section 4.3).

Due to the great importance of correctly resolving the integer DD ambiguities for relative positioning applications, the chapter starts with a description of the integer ambiguity resolution scheme applied throughout this research. This is followed by a discussion of the proposed processing strategies, especially focussing on the sequential kinematic filter and the two batch LSQ processing techniques, all investigated for GPS based spacecraft relative positioning, and why, in their current implementation, they were found to be inadequate for practical use in real-world applications. A thorough presentation of the extended Kalman filter is given thereafter. The chapter concludes with the test and validation results of the proposed EKF scheme using real-world data from the GRACE mission.

4.1 Integer ambiguity resolution

Over the past decades several strategies for resolving the integer double difference carrier phase ambiguities have been developed and implemented, some of course more successful than others. In addition to the required estimation of the integer carrier phase ambiguities, successful strategies also comprise a validation scheme of the obtained integer values. After validation, the integers, that are assumed to be the correct ones, have to be incorporated in the different processing techniques in order to obtain better estimates for the relative position solution. This section gives an overview of how integer ambiguity estimation and validation are dealt with in this research.

4.1.1 Integer ambiguity estimation

The first step in integer ambiguity resolution is the estimation of the integer DD carrier phase ambiguities. For this, the linear DD positioning model from section 2.5.2 is written in the general form

$$\mathbf{z} - \mathbf{h}(\mathbf{X}_0, \mathbf{A}_0) = \left(\frac{\partial \mathbf{h}}{\partial \mathbf{X}_0}\right) \Delta\mathbf{X} + \left(\frac{\partial \mathbf{h}}{\partial \mathbf{A}_0}\right) \Delta\mathbf{A}, \tag{4.1}$$

which is suitable for use in a LSQ adjustment, either a recursive or batch method. Here, the relative position(s), or dynamic baseline parameters, as well as the DD ionospheric path delays are captured in vector $\mathbf{X}$. The vector $\mathbf{A}$ holds the DD carrier phase ambiguities on each of the individual transmitting frequencies, expressed in units of cycles. The classical linear estimation methods however, can only be applied to models with real-valued parameters and cannot directly take the integer nature of the DD carrier phase ambiguities into account. Therefore estimation of the integer values is done in a separate step, after the real-valued, also referred to as the float, solution has been obtained. The float solution of the dual frequency DD carrier phase ambiguities and the accompanying covariance matrix, $\mathbf{Q}_{\mathbf{A}}$, both expressed in units of cycles, is given as

$$\mathbf{A} = \begin{pmatrix} \mathbf{A}_{L_1} \\ \mathbf{A}_{L_2} \end{pmatrix}; \quad \mathbf{Q}_{\mathbf{A}} = \begin{pmatrix} \mathbf{Q}_{\mathbf{A}_{L_1}\mathbf{A}_{L_1}} & \mathbf{Q}_{\mathbf{A}_{L_1}\mathbf{A}_{L_2}} \\ \mathbf{Q}_{\mathbf{A}_{L_2}\mathbf{A}_{L_1}} & \mathbf{Q}_{\mathbf{A}_{L_2}\mathbf{A}_{L_2}} \end{pmatrix}. \tag{4.2}$$

In general, the dual frequency ambiguities are highly correlated amongst each other, and the covariance matrix is therefore fully populated. From this float solution there are three commonly accepted ways of estimating an integer solution, namely by integer rounding, by integer bootstrapping or by means of integer least-squares (ILS). The exact details of each of these integer estimation methods can be found in appendix A, where their specific working is further illustrated using a numerical example.

The integer rounding estimator (section A.1), as the name suggests, simply rounds the float solution to the nearest integer values and hereby obtains the vector $\mathbf{N}_R$ of integer rounded (subscript 'R') ambiguities. Correlations between the DD ambiguities are completely ignored in this way. Integer bootstrapping (section A.2), also known as sequential or conditional rounding, takes some of the correlations between the DD ambiguities into account and therefore requires the covariance matrix of the real-valued DD ambiguities as well. First, the most precise ambiguity, based on the conditional variances derived from the covariance matrix (eqn. A.8), is rounded to the nearest integer value. This is followed by the subsequent rounding of the second most precise ambiguity, taking the correlation with the previously integer rounded ambiguity into account. This scheme, expressed in eqn. A.6, is repeated until the complete vector of integer bootstrapped DD ambiguities $\mathbf{N}_{BS}$ is obtained. Full correlation between all DD ambiguities is only accounted for in the ILS estimation method (section A.3). The vector of integer DD ambiguities obtained using ILS, $\mathbf{N}_{LS}$, is the one where the squared norm of the ambiguity residuals in the metric of the covariance, $(\mathbf{A} - \mathbf{N}_{LS})^T \mathbf{Q}_{\mathbf{A}}^{-1} (\mathbf{A} - \mathbf{N}_{LS})$, is the smallest. In contrast to the integer rounded and bootstrapped solutions, the ILS solution cannot be readily 'computed', but is the result of a, sometimes time-consuming, search process, illustrated in section A.3. However, it was shown earlier in *Teunissen* [1998] and *Teunissen* [1999] that the probability, or success rate, of actually having obtained the correct integer solution, $\mathbf{N}$, for the DD ambiguities is always higher or equal for ILS than for integer bootstrapping, which in turn has a higher or equal success

rate than integer rounding, i.e.

$$P(\mathbf{N}_{LS} = \mathbf{N}) \geq P(\mathbf{N}_{BS} = \mathbf{N}) \geq P(\mathbf{N}_R = \mathbf{N}). \tag{4.3}$$

Therefore, for this research use is made of ILS to perform the estimation of the integer DD carrier phase ambiguities. More specifically, the well known Least-Squares Ambiguity Decorrelation Adjustment (LAMBDA) method (see *Teunissen* [1995] or section A.4) has been implemented and used. The LAMBDA method is in fact nothing more than an optimized form of the ILS procedure outlined in section A.3. Its efficiency comes from an additional decorrelation step prior to the search for the integer solution yielding the smallest squared norm. The integer solution obtained from the LAMBDA method and the standard ILS procedure are the same. The only difference between both methods is the search time needed to arrive at it, which is usually significantly smaller in case of the LAMBDA method. In addition to the integer solution yielding the smallest norm, also referred to as the 'best' solution $\mathbf{N}_B$, the LAMBDA method, in its current implementation, also returns the solution with the one-but-smallest norm, also referred to as the 'second best' solution $\mathbf{N}_S$, and the vector of conditional variances of the decorrelated ambiguities, $\sigma_{n|N}$,

$$\left(\mathbf{A}, \mathbf{Q}_{\mathbf{A}}\right) \xrightarrow{LAMBDA} \left(\mathbf{N}_B, \mathbf{N}_S, \sigma_{n|N}\right), \tag{4.4}$$

all resulting from the real-valued or float solution. Of course the best solution is the one that is used in relative positioning applications. The second best solution and the conditional variances are given out for integer ambiguity validation purposes as described in the next subsection.

In many practical applications however ambiguity estimation is performed in a different way as for this research. For example, two well established software packages mentioned earlier, GIPSY-OASIS and Bernese, are also able to resolve the integer DD carrier phase ambiguities, but separately estimate the wide-lane and narrow-lane combinations (eqn. 2.20). In such a scheme, pseudorange observations are only required for resolving the wide-lane DD ambiguities, which could be, and is often, accomplished by simply using the DD Melbourne-Wübbena (eqn. 2.21) combination. Once resolved, the integer DD wide-lane ambiguities that are assumed to be correct are subsequently used in combination with a DD positioning model constructed of solely ionosphere free carrier phase observations to obtain integer estimates for the DD narrow-lane ambiguities. The advantage of such an approach is that the wide-lane ambiguities are in general easy to resolve due to their long wavelength and the pseudorange noise, and systematic error, reduction of this combination. The harder to resolve narrow-lane ambiguities are now only subject to the smaller carrier phase errors and noise. The drawback is that intermediate constraints are put onto the ambiguities since the 'fixed' integer wide-lane ambiguities are used to resolve the narrow lane. Incorrectly resolved DD wide lane ambiguities can seriously influence the subsequent narrow-lane ambiguity estimation process in a negative way. If a combined estimate of the dual frequency integer

DD ambiguities is made, as is the case in this research, they are basically left free and the correlations between the individual ambiguities are fully incorporated and exploited when using an ILS estimation scheme. However, it depends on the number of integer ambiguities that need to be estimated if using such a scheme is feasible in practice. Both GIPSY-OASIS and Bernese are often used to resolve thousands of integer DD ambiguities simultaneously, and on a daily basis, for entire (IGS) ground station networks. An ILS search procedure would in most cases be too time consuming, even when applied to the wide-lane and narrow-lane models, given that there is a covariance matrix available. Therefore integer rounding and bootstrapping approaches are often used, due to the fact that here the solution can be directly computed. Under such conditions, resolving the wide-lane and narrow-lane combinations separately is often the best that can be accomplished.

4.1.2 Integer ambiguity validation

Before using the obtained integer DD ambiguity estimates, $\mathbf{N}_B$, in any positioning model, a validation process should determine the likeliness of the estimates being correct. The reason for this is that erroneous integer values can seriously degrade the relative position solution instead of strengthening it. Therefore, for this research, a more conservative validation procedure is preferred, certainly for the sequential processing schemes where erroneous integer estimates can cause divergence of the filter solution. The proposed validation procedure for this research consists of a number of tests, which were calibrated primarily, and were found to work satisfying, for the EKF processing technique presented later on in section 4.3. Only few of these tests have some theoretical justification, others were derived from practical tests using the GRACE data and are therefore more or less custom tailored for the application at hand. Although the validation scheme was developed specifically for the EKF it is also applied to the other processing methodologies, where it was not always found to work satisfyingly, or at all. Nevertheless, the entire scheme is described here in detail, explaining the rationale behind the individual tests selected.

A very important measure for the quality of the obtained best integer solution is the probability or success rate of actually having estimated the correct integer ambiguities, $\mathbf{N}$. For the ILS class of estimation methods, computation of this probability is very complicated [*Verhagen*, 2004*a*]. However, a lower boundary for the bootstrapping success rate, that can be swiftly computed, is given in eqn. B.4. Using this success rate together with eqn. 4.3, it follows that

$$P(\mathbf{N}_B = \mathbf{N}) \geq \prod_{i=1}^{n} \left(1 - \mathrm{e}^{-\frac{1}{2}\left(\frac{1}{2\sigma_{i|I}}\right)^2} \right)^{\frac{1}{2}} \tag{4.5}$$

serves as a lower boundary for the LAMBDA, or ILS, success rate. In principle, the integer solution should only be trusted if the success rate is high enough. As can be seen the lower boundary is solely computed using the conditional variances that are returned by the LAMBDA method and are obtained from the decorrelated covariance matrix of the real-valued ambiguity solution. The success rate therefore

solely depends on the applied model, and does not take any unmodeled effects, such as pseudorange multipath, into account. Furthermore, the success rate decreases when the number of simultaneously estimated ambiguities increases. Since the estimation of subsets of DD ambiguities, also referred to as partial fixing as described in *Teunissen et al.* [1999], is not considered for this research, the value of the success rate in practice is limited to the sequential processing strategies. Here it serves as an initial indication to see if enough data has been accumulated to make a reliable integer estimate at all, prior to further validation tests that involve the integer ambiguity estimates themselves.

A good overview of various testing procedures that were proposed for practical use in the past can be found in *Verhagen* [2004*b*]. In this study various tests were compared to one another in an effort to arrive at a conclusion which one performed best under all circumstances. Unfortunately, it was found that such a conclusion could not be drawn. However, a preference for certain tests over others was given, based on the probability of correct acceptance of the integer solution. Therefore, in accordance with this previous study the most promising testing procedure has been used, consisting of a so-called integer test and a discrimination test. It must be mentioned that both tests assume that the integer DD ambiguities are deterministic, which in reality is not the case. In fact they are stochastic parameters, with a (discrete) distribution as e.g. depicted in Fig. 4.1 obtained from *Joosten and Tiberius* [2000], which is created by sampling (1800 samples to be exact). Here, the distribution of a DD ambiguity as real-valued (float, continuous distribution) and integer (fixed, discrete distribution) parameter is shown for a low success rate (left), where the stochastic nature cannot be neglected, and for a high success rate (right) where enough probability mass is located at the correct ambiguity (4 in this case) to assume a deterministic value. Both tests should therefore only be executed if the success rate is high enough.

The so-called integer test evaluates the squared norm of the ambiguity residuals of the best solution in the metric of the covariance,

$$R_B = (\mathbf{A} - \mathbf{N}_B)^T \mathbf{Q}_{\mathbf{A}}^{-1} (\mathbf{A} - \mathbf{N}_B), \tag{4.6}$$

which, if divided by the number of ambiguities n or in this case the degrees of freedom, is distributed as $F(n, \infty)$ when using the fact that the ambiguities are treated as deterministic. More specifically, the test reads

$$\frac{R_B}{n} < F_\alpha(n, \infty) = k_\alpha, \tag{4.7}$$

where α is the level of significance of the test and k_α the critical value obtained from the F-distribution. The rationale behind this test is that one would not have much confidence in the integer estimates if the distance to the float solution is large [*Verhagen*, 2004*b*]. Unfortunately, this test says nothing about the likelihood of the best solution compared to another integer solution. It can be that there is another integer solution for which the test is passed as well, although it is known that the likelihood of the best solution obtained from LAMBDA is higher than any other

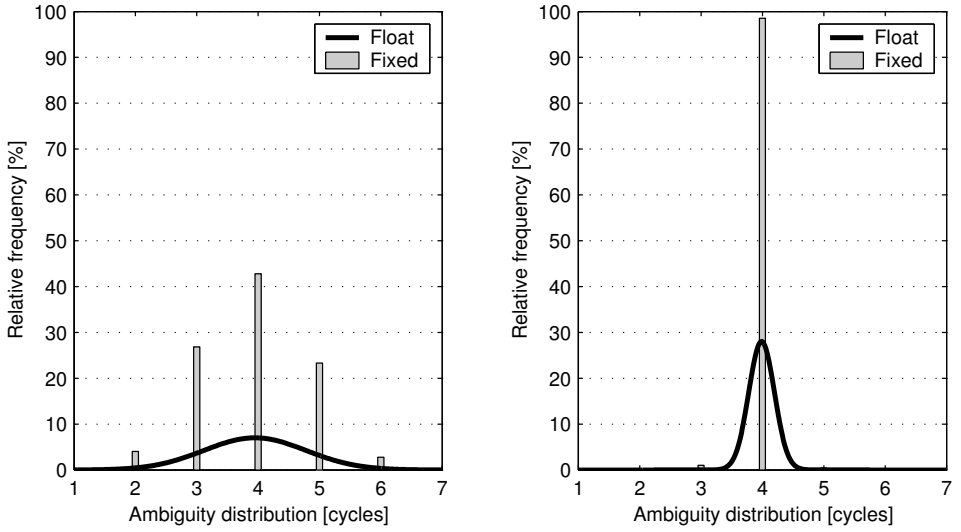

Figure 4.1 Distribution of a double difference ambiguity as real-valued (float) and accompanying integer (fixed) solution (Source: [*Joosten and Tiberius*, 2000]). In the left figure the probability mass for the correct value (4) is still low, in the right figure this might already be high enough to neglect the stochastic nature of the ambiguity.

integer solution. However, if the likelihood of the best solution is not significantly larger as the one associated with another integer solution, both solutions cannot be discriminated with enough confidence [*Verhagen*, 2004*b*]. Therefore the ratio of the squared norms of the ambiguity residuals in the metric of the covariance for the best and second best integer solution, as obtained from LAMBDA, is examined,

$$\frac{R_S}{R_B} > k_{S/B}, \tag{4.8}$$

where R_S is constructed in the analogy of eqn. 4.6. If this test is passed for the second best solution it will pass for any other integer vector, since its squared norm will always be larger (see section A.3 or A.4). In practice the problem is setting the critical value $k_{S/B}$, which is often accomplished using empirical results. Several literature sources however make suggestions, but these heavily depend on the underlying model used. In *Leick* [1994] it is mentioned that many software packages use a critical value of 3, which was also found to work adequately for the EKF scheme in this research.

Although the just discussed validation scheme should be conclusive, practical tests with the EKF using the GRACE data have shown that sometimes an integer solution (vector) was accepted where one of the individual integer ambiguity pairs was incorrect. Aside from the fact that this resulted in erroneous relative position estimates, the incorrectly resolved integers sometimes also lead to divergence of the

filter solution, due to the specific way they are handled here. A solution to this has been provided by extending the current validation scheme with two additional tests, screening favorable combinations of the individual ambiguity residuals, namely the wide-lane and the ionosphere free one. These residuals are constructed on ambiguity level using the transformation matrices

$$\mathbf{T}_{\mathrm{WL}} = \left(\mathbf{1}, -\mathbf{1}\right); \qquad \mathbf{T}_{\mathrm{IF}} = \left(77 \cdot \mathbf{1}, -60 \cdot \mathbf{1}\right). \tag{4.9}$$

for the wide-lane and ionosphere free ambiguities respectively, in which $\mathbf{1}$ is the identity matrix. The real-valued and integer DD wide-lane ambiguities are now constructed as

$$\mathbf{A}_{\mathrm{WL}} = \mathbf{T}_{\mathrm{WL}}\mathbf{A}; \qquad \mathbf{N}_{B_{\mathrm{WL}}} = \mathbf{T}_{\mathrm{WL}}\mathbf{N}_B, \tag{4.10}$$

and in a similar way the ionosphere free ones are obtained. The absolute values of the individual ambiguity residuals of the wide-lane,

$$|A_{\mathrm{WL}} - N_{B_{\mathrm{WL}}}| < k_{\mathrm{WL}}, \tag{4.11}$$

and ionosphere free,

$$|A_{\mathrm{IF}} - N_{B_{\mathrm{IF}}}| < \frac{k_{\mathrm{IF}}}{\lambda_{\mathrm{IF}}}, \tag{4.12}$$

combination can now be assessed, where the critical values k_{WL} and k_{IF} may not be exceeded. Here, k_{WL} is expressed in cycles and k_{IF} in units of meters. The ionosphere free wavelength, λ_{IF}, in this last test is given as $\lambda_{\mathrm{IF}} = 0.0063$ m.

Although these last two tests, as well as their critical values, were completely derived by empirical results from the EKF when testing on the GRACE data, some rationale behind them can still be given. It must be mentioned that care should be taken when simply applying them to different applications or processing methodologies, since they are more or less custom tailored for the application at hand. It was already shown by *Teunissen* [1997] that the wide-lane combination has a decorrelating property. Although correlations between the wide-lane ambiguity residuals still exist, they are reduced. Individual screening of the residuals could therefore be allowed. This can however not be said for the ionosphere free residuals. Correlations here are typically high. However, the functional model of the DD ionosphere free carrier phase observation only consists of the relative position and the ionosphere free DD carrier phase ambiguity. Over time this ambiguity combination will therefore become very well determined. It is thus unlikely that the real-valued and the integer solution of this combination, and thus the corresponding ambiguity residual, are far from each other.

How the integer estimates, that are assumed to be correct, are incorporated or handled by the different processing techniques is described in the following section. Most important is the assumption that integer ambiguities that are assumed to be correctly resolved have no uncertainty left in them, i.e. $\sigma_N = 0$, and are thus treated as deterministic.

4.2 Proposed processing strategies

As mentioned earlier, a total of four possible processing strategies were identified for GPS based relative spacecraft positioning. In accordance with the POD techniques discussed in chapter 3, a kinematic and reduced dynamic batch LSQ estimator and an extended Kalman filter, all processing single difference dual frequency GPS pseudorange and carrier phase observations, were implemented and tested. In addition, a sequential kinematic filter, using the more traditional double difference parametrization, has also been proposed.

When handled appropriately, meaning that all correlations are correctly accounted for, a SD and DD parametrization of the relative positioning model will yield the exact same results. This has amongst others been verified by practical tests carried out for this research. However, a SD formulation was found to have several implementation benefits over a DD one. First of all, the SD GPS observations already have the benefit of eliminating or reducing common errors in the data, such as the GPS satellite clock offset and ephemerides errors, whilst still remaining uncorrelated. This results in a less complex data handling, which is otherwise an additional burden, especially for the batch LSQ estimation methods. Second, a DD parametrization in a recursive or sequential estimation scheme requires a continuous re-ordering of some of the estimation parameters in the model, namely the DD ionospheric path delays and carrier phase ambiguities. This is due to the change in reference GPS satellite, required to construct the DD GPS observations, over time. Finally, and perhaps most important, despite a SD formulation, it is still possible to estimate and exploit the integer nature of DD carrier phase ambiguities.

Furthermore, when closely comparing the UD and SD observation models (eqn. 2.14 and 2.29 respectively), as well as the linearized form for use in positioning, it can be seen that the overall parametrization is basically identical. The only difference is the fact that the SD model uses 'relative' parameters whereas the UD model uses the 'absolute' ones. This means that the (ionosphere free) SD relative positioning models can be solved for in the exact same way as their POD 'equivalents' from chapter 3. The fact that dual frequency SD GPS data is used, in order to preserve the integer nature of the carrier phase ambiguities, introduces some additional estimation parameters (the SD ionospheric path delays and the dual frequency SD carrier phase ambiguities), but still does not change the general way the models can be solved.

The a-priori choice of the most appropriate processing methodology is not trivial. Each of the proposed strategies has its own advantages and disadvantages. This especially applies to the problem of integer ambiguity resolution and handling where a clear difference between the recursive, or sequential, and batch LSQ strategies exists. The sequential or recursive strategies have the advantage of being able to estimate and incorporate the integer DD ambiguities 'on-the-fly', where they will directly strengthen the relative position solution and also aid in the resolution of new integer ambiguities as they appear over time. A drawback of such a scheme is that an incorrectly resolved integer ambiguity can, besides the fact that it most likely

degrades the relative position solution accuracy, lead to the incorrect resolution of other integers as well, and hereby cause divergence of the filter solution. The batch LSQ estimation methods on the other hand first accumulate all available GPS observation data prior to making the integer estimate. Any incorrectly resolved integers are mostly a 'local' problem, meaning that they only influence the relative position solution on the epochs they relate to, and perhaps cause a few neighboring ambiguities to be incorrectly estimated as well. In general the effect lasts for 1 to 2 orbital revolutions of the spacecraft (Fig. 4.2 on page 91) and does not lead to complete divergence of the solution, that is if an ILS estimation procedure is used. The disadvantage is the large number of integer ambiguities that have to be estimated simultaneously. This certainly applies if an ILS estimation method is used, where the search time for the best solution can sometimes be excessively long.

Another choice to be made is the one between a kinematic or a reduced dynamic processing strategy. Despite the fact that for POD a purely kinematic methodology has shown to be less precise, there are two good reasons for still considering it for relative spacecraft positioning. The first one is the fact that once the integer DD carrier phase ambiguities are correctly resolved the accompanying carrier phase observations are transformed into highly precise relative ranges. A simple kinematic single point positioning (SPP) process using this data type (cf. eqn. 4.45 on page 103) might already be precise enough for the application at hand. The second reason is that no a-priori knowledge about the relative motion between both spacecraft is required, which simplifies matters. The reduced dynamic processing strategies on the other hand somehow have to incorporate this additional complexity. Although the earlier mentioned Clohessy-Wiltshire equations [*Clohessy and Wiltshire*, 1960], also known as the Hill equations, provide a first order framework describing the motion between two spacecraft, they are not accurate enough for application to a problem of this nature ([*Highsmith and Axelrad*, 2002]; [*Leung and Montenbruck*, 2005]). In fact, as far as is known, there are no direct models available at all that describe the relative spacecraft dynamics up to the required accuracy. This problem thus has to be coped with by obtaining the 'pseudo' relative spacecraft dynamics from the dynamical models of the individual spacecraft, hence pseudo. Similar to the POD case, the deterministic part of the relative dynamical modeling is supplemented with stochastic empirical accelerations, but this time the relative ones, in order to capture any modeling deficiencies.

Out of the total of four proposed processing schemes, both batch LSQ estimators and the sequential kinematic filter were found to have some serious limitations for practical use in their current implementation. This section therefore only presents a brief overview of the fundamentals of each of these methods and provides reasoning why they were found to be inadequate for the time being. The section concludes with an introduction of the extended Kalman filter, which was found to be very adequate and robust for relative spacecraft positioning in real-world applications (GRACE). A detailed description of this processing strategy is then provided in the next section, 4.3.

4.2.1 Sequential kinematic filter

The sequential kinematic filter was developed and initially tested using data from hardware-in-the-loop simulations, and is accurately described in *Kroes and Montenbruck* [2004]. This real time kinematic (RTK) type of approach uses double difference dual frequency GPS pseudorange and carrier phase data, which is processed on an epoch-to-epoch basis in a local LSQ adjustment (SPP process). In this way an estimate for both the relative spacecraft position as well as the DD carrier phase ambiguities (and the DD ionospheric path delays) is obtained on each epoch. The DD ambiguity estimates and their covariance are subsequently used as a-priori information for the next epoch, where their estimate is refined. This process is repeated until enough information is gathered over time to make a reliable integer estimate of the DD ambiguities using the LAMBDA method. After validation, the (assumed to be) correctly resolved integer ambiguities are treated as deterministic values and are kept constant. These integer DD ambiguities are now used by the filter as a-priori information instead of their float values, resulting in better estimates for both the relative position and the not yet resolved ambiguities. In this way the already resolved integers will automatically aid in resolution of new DD ambiguity pairs that appear over time.

The clear advantages of this kinematic scheme, as already lined out in the introduction of this section, are the relative simplicity and the fact that already resolved integer ambiguities aid in the resolution of new ones, resulting in a faster and (hopefully) more reliable resolution of these new integers. As also pointed out in the introduction to this section, the fact that a double difference formulation is used puts an additional burden on the data handling and filter parametrization since the reference GPS satellite, required to construct the DD observations and filter parameters, changes over time. Since only the parameters for the GPS satellites observed at a certain epoch are considered, which results in a small scale filter, this additional burden can be coped with.

As discussed in *Kroes and Montenbruck* [2004] the filter was found to work very adequately for several 2-hour hardware-in-the-loop scenarios, using two NovAtel OEM4-G2 GPS receivers. Due to the fact that a precise stochastic model was used for the GPS observation data ([*Kroes and Montenbruck*, 2004]; [*Montenbruck*, 2003]), the only integer validation test used for the HWIL simulations was the success rate. For two LEO scenarios, with a spacecraft separation of respectively 10 km and 110 km a 3-dimensional relative position accuracy (RMS) of 3.0 mm and 5.0 mm was found when resolving and incorporating the integer DD carrier phase ambiguities. No irregularities were encountered at all.

Unfortunately tests with real-world data from the GRACE mission were not so successful. Although the method proved to work fine over selected data arcs of 6-8 hours, leading to similar precision results as depicted in Fig. 4.13 on page 120, it was found to have a severe shortcoming. Despite the ambiguity validation scheme applied, none of the 24-hour arcs tested could be processed without one or more incorrectly resolved integer ambiguities that got incorporated at a certain moment. As already stated earlier, this did not only result in erroneous relative position

estimates, but also in the incorrect resolution of new DD ambiguities, which, in all cases, was found to lead to divergence of the filter solution. These incorrectly resolved ambiguities were not detected by the underlying SPP process based on integer ambiguity corrected carrier phase data only (in essence similar to the one from eqn. 4.45), indicating that they locally 'fit' the data very well. The resulting divergences, or the incorrectly resolved ambiguities causing them, were thus not always (instantaneously) detected. As a result, the filter could not be restarted from the epoch an incorrectly resolved ambiguity got allocated, since this point could not always be determined. The filter was simply found to lack the required robustness for the real-world application at hand.

4.2.2 Kinematic batch LSQ

The kinematic batch LSQ for relative spacecraft positioning accumulates, similar to its POD equivalent described in section 3.3, all available GPS observation data over a selected data arc. All SD observations are, according to the linearized dual frequency SD positioning model from section 2.5.1, parameterized with the relative position between the antenna phase centers of both GPS receivers, the relative GPS receiver clock offset and a SD ionospheric path delay. For n mutually observed GPS satellites on epoch t_i, a total of $4 + n$ time dependent parameters, $\mathbf{x}_{AB,i} = (x, y, z, c\delta t, I^1, \ldots, I^n)_{AB,i}$, have to be estimated. In addition, the carrier phase observations are also parameterized with the time constant SD ambiguity parameters, A_{1AB} and A_{2AB}, on each of the transmitting frequencies. For a total of n_X measurement epochs and n_B phase connected SD passes this results in the following vector for the time dependent estimation parameters

$$\mathbf{X}_{AB} = \left(\mathbf{x}_{AB,0}; \cdots; \mathbf{x}_{AB,i}; \cdots; \mathbf{x}_{AB,n_X-1}\right), \tag{4.13}$$

and the SD carrier phase ambiguities on the individual frequencies

$$\mathbf{A}_{AB} = \left(A^1_{1AB}; \cdots; A^{n_B-1}_{1AB}; A^1_{2AB}; \cdots; A^{n_B-1}_{2AB}\right), \tag{4.14}$$

which respectively replace the vectors in eqn. 3.6 and 3.7 of the kinematic POD model. The accompanying vectors with the partials also change in accordance to the SD positioning model. For the SD ionospheric path delays the partials respectively become 1, f_1^2/f_2^2, -1 and $-f_1^2/f_2^2$ for the P_1, P_2, L_1 and L_2 SD observation. These partials are of course only set for the ionospheric path delay corresponding to the current SD observation. In addition, the carrier phase ambiguities are expressed in units of cycles, meaning that the partial accompanying the carrier phase bias on L_1 becomes λ_1 and the one on L_2 becomes λ_2. It can be seen however that despite the larger dimension of the estimation parameter vectors, the model is still partitioned in the same way as the POD variant, and can thus also be solved by first obtaining the updates for the SD carrier phase ambiguities that are subsequently back-substituted to obtain the updates for the other estimation parameters.

After having obtained the estimates for the SD ambiguities, they are transformed to DD float estimates together with the accompanying covariance matrix. This is

accomplished by means of a linear transformation, similar to eqn. 2.36, using one of the SD ambiguity pairs, (A^j_{1AB}, A^j_{2AB}), as a reference. The obtained real-valued DD ambiguities are then processed by the integer ambiguity resolution scheme, described in section 4.1, to obtain the vector of integer DD ambiguities. These are subsequently used to create a relative position estimate on an epoch-to-epoch basis using only ionosphere free SD carrier phase data corrected for the just found integer DD ambiguity offsets (cf. the SPP principle from eqn. 4.45). This also allows for some additional validation since incorrectly resolved ambiguities might be detected, after which the corresponding measurement can be removed from the SPP process.

The just described kinematic batch LSQ method has been tested using several 24-hour data arcs from the GRACE mission. The SD GPS data was processed at the 10 second interval in which it is provided. Furthermore, in order to guarantee proper real-valued DD ambiguity estimates, only SD phase connected passes containing at least 60 epochs of good quality SD pseudorange observations were taken into the model. For the 24-hour data arcs tested, 2003 DOY 210-215, this still corresponded to between 330 and 350 SD passes, and consequently between 658 and 698 DD ambiguities that had to be estimated simultaneously. This is where the first problem arose. For none of these days was the LAMBDA method able to provide a solution within 12 hours search time (actual CPU time on a Pentium 4, 2.4 GHz), after this the search was aborted. When using the kinematic batch LSQ over smaller time intervals, e.g. 6 hours, where more or less 160 DD ambiguities are searched for simultaneously, the search time varied between less than 1 second, to again more than 12 hours. For a practical application the search times were simply experienced to be too long and too unpredictable. This is the main reason why the kinematic batch LSQ was found to be inadequate for practical use in its current implementation.

A second problem that became apparent was that if a vector of integer estimates was returned (within a reasonable time) the ambiguity validation procedure outlined

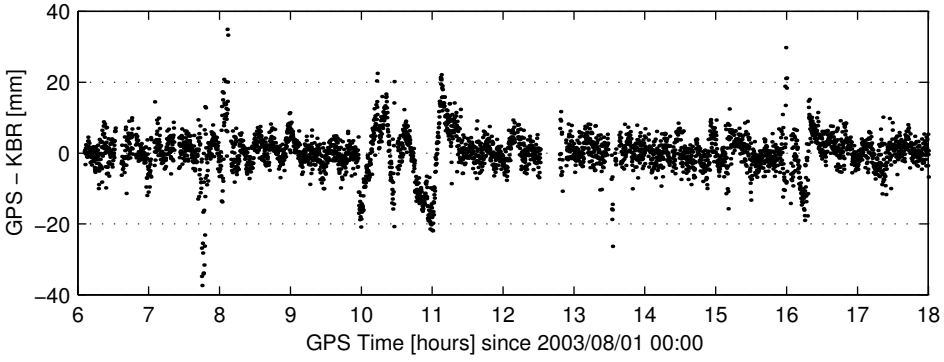

Figure 4.2 KBR Fit of the kinematic single point positions using integer ambiguities, obtained from the kinematic batch LSQ.

in section 4.1.2 was not found to be applicable at all. It would always reject over 90% of the estimated values, even if they were found to provide high precision position estimates when compared to the GRACE KBR observations. In e.g. Fig. 4.2 the GRACE relative position fit with the KBR is shown for 2003, DOY 213. As can be seen the kinematic batch LSQ was used over the 06-18 h time interval. The integer vector of 336 DD ambiguities was found in slightly over 20 minutes, and contains a few incorrectly estimated values. This is visible in the relative position estimates between 10:00 and 11:30 and around 16:15. These were also not detected by the SPP process, indicating that they 'fit' the data. Important is the fact that these incorrectly resolved integers, as explained earlier, affect the solution only over 1 to 2 orbital revolutions. They are thus more a 'local' problem, and do not cause divergence of the relative position solution as experienced with the sequential kinematic filter.

It must be mentioned that it is not claimed that a kinematic batch LSQ would not work at all. On the contrary. A study by *Svehla and Rothacher* [2004*a*] presents ambiguity fixed kinematic GRACE relative positioning results of similar precision as depicted in Fig. 4.13. For this a kinematic batch LSQ estimation method implemented in the Bernese software was used. The major difference with the kinematic batch LSQ of this research is the ambiguity estimation scheme applied, briefly mentioned in section 4.1.1, based on integer rounding/bootstrapping of the DD wide-lane and narrow-lane ambiguities, as well as another type of ambiguity validation procedure [*Hugentobler et al.*, 2001].

4.2.3 Reduced dynamic batch LSQ

From all tested POD concepts, the reduced dynamic batch LSQ has shown to provide the most precise and smoothest orbits. Despite the LAMBDA search time problems encountered in the kinematic batch LSQ, the reduced dynamic equivalent for relative spacecraft positioning has therefore still been investigated. In order to see if the (pseudo) relative dynamics can be properly modeled, it has first been tested on ionosphere free SD GPS data. The parametrization of the SD observations in this case is basically identical to the POD variant from section 3.4.3, with the only difference that 'relative' parameters are used instead of the 'absolute' ones. The GPS receiver clock offsets in eqn. 3.35 are replaced with the epoch wise relative receiver clock offsets, captured in $\mathbf{T}_{AB}$, eqn. 3.37 is replaced with the SD ionosphere free carrier phase biases, captured in $\mathbf{B}_{AB}$, and finally the dynamic spacecraft parameters from eqn. 3.36 are replaced with the dynamic baseline parameters

$$\begin{aligned}\mathbf{Y}_{AB} &= \big(\mathbf{y}_{AB}(t_0); \mathbf{p}_{AB}\big) \\ &= \big((\mathbf{r}_{AB}(t_0); \mathbf{v}_{AB}(t_0)); (C_{D_{AB}}; C_{R_{AB}}; \mathbf{a}_{AB,(0)}; \ldots; \mathbf{a}_{AB,(n_a-1)})\big).\end{aligned} \tag{4.15}$$

As can be seen this vector comprises the initial relative spacecraft state as well as the relative force model parameters. The relation with the individual spacecraft dynamic parameters is given by $\mathbf{Y}_B = \mathbf{Y}_A + \mathbf{Y}_{AB}$.

Due to the selected parametrization a direct integration of the relative spacecraft state, $\mathbf{y}_{AB} = \mathbf{y}_B - \mathbf{y}_A$, has been facilitated. For this the first order differential equation for the relative state (cf. eqn. 3.21) is defined as

$$\frac{d}{dt}\mathbf{y}_{AB}(t) = \begin{pmatrix} \mathbf{v}_{AB}(t) \\ \mathbf{a}_B(t, \mathbf{r}_B, \mathbf{v}_B, \mathbf{p}_B) - \mathbf{a}_A(t, \mathbf{r}_A, \mathbf{v}_A, \mathbf{p}_A) \end{pmatrix}. \tag{4.16}$$

Here it can be seen that the relative spacecraft acceleration still has to be obtained from the individual dynamical force models. To this extent the dynamic parameters of the reference trajectory, S/C A in this case, so $\mathbf{Y}_A$, are loaded a-priori and are propagated together with the dynamic baseline parameters using the same numerical integration method (DE, [*Shampine and Gordon*, 1975]) as for the POD case. Whenever the individual accelerations have to be evaluated, the dynamic parameters for S/C B are obtained by the earlier given relation $\mathbf{Y}_B = \mathbf{Y}_A + \mathbf{Y}_{AB}$. It is noted that only the the dynamic baseline parameters are being estimated. The dynamic parameters for the a-priori reference trajectory of S/C A are kept fixed to their initial values.

When constructing the normal equations of the batch LSQ the partials with respect to the dynamic baseline parameters are required. These on their turn require the knowledge of the relative state transition and sensitivity matrix, $\mathbf{\Phi}_{AB}(t, t_0)$ and $\mathbf{S}_{AB}(t)$, which for the individual spacecraft are obtained from integration of the variational equations (section 3.4.1). In order to arrive at an expression for the relative case, the state transition matrix from eqn. 3.22 for both S/C are first expressed as $\partial\mathbf{y}_A(t) = \mathbf{\Phi}_A(t, t_0)\,\partial\mathbf{y}_A(t_0)$ and $\partial\mathbf{y}_B(t) = \mathbf{\Phi}_B(t, t_0)\,\partial\mathbf{y}_B(t_0)$. By now subtracting both expressions, $\partial\mathbf{y}_B(t) - \partial\mathbf{y}_A(t) = \mathbf{\Phi}_B(t, t_0)\,\partial\mathbf{y}_B(t_0) - \mathbf{\Phi}_A(t, t_0)\,\partial\mathbf{y}_A(t_0)$, and by substituting $\partial\mathbf{y}_{AB} = \partial\mathbf{y}_B - \partial\mathbf{y}_A$, it follows that

$$\partial\mathbf{y}_{AB}(t) = \mathbf{\Phi}_B(t, t_0)\,\partial\mathbf{y}_{AB}(t_0) - \big(\mathbf{\Phi}_A(t, t_0) - \mathbf{\Phi}_B(t, t_0)\big)\,\partial\mathbf{y}_A(t_0). \tag{4.17}$$

When using the fact that the trajectory of the reference spacecraft, S/C A, is given a-priori, and it's initial state vector $\mathbf{y}_A(t_0)$ is thus kept fixed, i.e $\partial\mathbf{y}_A(t_0) = \mathbf{0}$, it can be seen that the relative state transition matrix is equal to the one of S/C B,

$$\mathbf{\Phi}_{AB}(t, t_0) = \mathbf{\Phi}_B(t, t_0). \tag{4.18}$$

In a similar way it can shown that the relative sensitivity matrix equals the one of S/C B as well,

$$\mathbf{S}_{AB}(t) = \mathbf{S}_B(t). \tag{4.19}$$

Both expressions are more or less in analogy with eqn. 2.33, where the relative position partials also solely depend on S/C B, when the position of S/C A is kept fixed. This also means that if the orbit of S/C A would be estimated simultaneously, a correlation is introduced. The resulting normal equations have the identical structure as for the POD case and can be solved in exactly the same way as described in section 3.4.3.

The just discussed reduced dynamic batch LSQ has been tested over several time intervals (daily and sub-daily) with GRACE SD ionosphere free GPS data. Unfortunately, another problem became apparent. In no single test case did the resulting baseline solution fully converge, even after many iterations (up to 10 has been tested). The 24-hour (daily) solutions even started to diverge after several hours (10-12) into the integration. Divergence is these last cases could only be partly resolved by performing more iterations. The growing number of empirical accelerations (and carrier phase ambiguities) over these long time spans might result in the accumulation of (numerical) instabilities. The obtained results are the reason why the reduced dynamic batch LSQ for relative S/C positioning, was found to be inadequate for practical use in its current implementation. It has therefore also not been expanded to process dual frequency SD observations, and it is left for further study to see if the encountered problem can be resolved.

Similar to the kinematic case, it is not claimed that a reduced dynamic batch LSQ is not suitable at all for the application at hand. On the contrary. Besides the kinematic batch LSQ, *Svehla and Rothacher* [2004*a*] also used a reduced dynamic batch LSQ method, implemented in the Bernese software, for estimating the GRACE baseline, and obtained highly precise relative position results by it when fixing the DD ambiguities (3 mm precision (1-dimensional)). Although the exact details of the processing are not published, it is known that the baseline integration is not facilitated as it is done in this research, but is based on an absolute formulation.

4.2.4 Extended Kalman filter

Within the current implementations of all proposed processing strategies, the extended Kalman filter was the only one that works well under all circumstances tested. It was found to be very robust and adequate for highly precise relative spacecraft positioning. Similar to the batch LSQ strategies the filter processes dual frequency SD GPS observations. Nevertheless, the integer nature of the DD ambiguities can still be exploited, in an even easier and more elegant way than for the other processing strategies. The strength of the filter is, similar to the sequential kinematic method, the fact that integer ambiguities can be resolved 'on-the-fly' and instantaneously used. In this way the relative position solution directly improves, and the already resolved integer ambiguities automatically aid in the resolution of new ones as they appear over time. The (pseudo) relative spacecraft dynamics can be handled in an easier way than for the reduced dynamic batch LSQ since the integration restarts at every measurement epoch. Although the relative dynamics were found to offer some robustness against incorrectly resolved integer ambiguities it was noted that the filter solution could still diverge. Therefore, the filter is complemented with the rigorous ambiguity validation scheme from section 4.1.2. Similar to the POD case, the EKF also processes the measurements in forward and backward direction, and smoothes the relative S/C position estimates. Exact details of all aspects of the extended Kalman filter/smoother are presented in section 4.3. In

section 4.4 the results of testing the EKF on the actual GRACE GPS data is given. Here it is shown that when using this proposed methodology relative spacecraft positioning with (sub-)mm precision is feasible in real-world applications.

4.3 Details of the extended Kalman filter

Although the extended Kalman filter for relative spacecraft positioning has many similarities with the POD version from section 3.4.4, there are a few important differences. Aside from the fact that now 'relative' instead of 'absolute' parameters are used, the filter furthermore processes the dual-frequency SD GPS observations in order to preserve the integer nature of the DD carrier phase ambiguities. Therefore, in accordance with the SD observation model from eqn. 2.29, the filter state,

$$\mathbf{x} = \begin{pmatrix} \mathbf{Y}_{AB} \\ c\delta t_{AB} \\ \mathbf{I}_{AB} \\ \mathbf{A}_{AB} \end{pmatrix}, \tag{4.20}$$

and covariance, $\mathbf{P}$, at each epoch comprise, next to the dynamic estimation parameters, $\mathbf{Y}_{AB}$, and the relative receiver clock offset, $c\delta t_{AB}$, the SD ionospheric path delays, $\mathbf{I}_{AB}$, and the SD carrier phase ambiguities, $\mathbf{A}_{AB}$, on each of the transmitting frequencies. The dynamic estimation parameters,

$$\mathbf{Y}_{AB} = \big(\mathbf{y}_{AB}; \mathbf{p}_{AB}\big) = \big((\mathbf{r}_{AB}; \mathbf{v}_{AB}); (C_{R_{AB}}; C_{D_{AB}}; \mathbf{a}_{AB})\big), \tag{4.21}$$

comprise the 6-dimensional relative S/C state, $\mathbf{y}_{AB}$, containing the relative position and velocity between the centers of mass of both S/C (in EME2000), and the 5-dimensional vector of relative force model parameters, $\mathbf{p}_{AB}$. This last vector furthermore contains the relative drag and solar radiation pressure coefficient as well as the relative empirical accelerations in radial, along-track and cross-track direction, that are used to capture any discrepancies or mismodeling of the (pseudo) relative spacecraft dynamics. Similar to the POD implementation, the n-dimensional vector of SD ionospheric path delays

$$\mathbf{I}_{AB} = \big(I^1_{AB}; \ldots; I^n_{AB}\big), \tag{4.22}$$

and the $2n$-dimensional vector of SD carrier phase ambiguities, expressed in units of cycles,

$$\begin{aligned} \mathbf{A}_{AB} &= \big(\mathbf{A}_{1AB}; \mathbf{A}_{2AB}\big) \\ &= \big((A^1_{1AB}; \ldots; A^n_{1AB}); (A^1_{2AB}; \ldots; A^n_{2AB})\big), \end{aligned} \tag{4.23}$$

only comprise the parameters of the GPS satellites that are mutually tracked, at the same instant, by the GPS receivers onboard both spacecraft concerned.

Similar to the POD implementation the updated filter state and covariance at t_{i-1} are first propagated to a prediction at the current measurement epoch t_i during

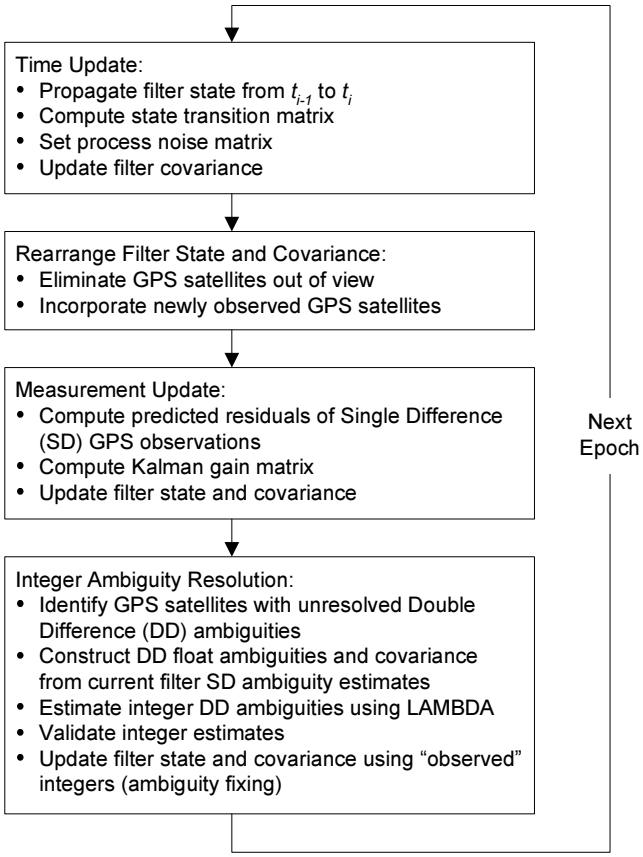

Figure 4.3 Epoch wise processing scheme of the Extended Kalman Filter for relative positioning of spacecraft.

the *time update*. This is followed by a reordering step to accommodate the change in mutually tracked GPS satellites, only concerning the SD ionospheric path delays and carrier phase ambiguities. After this step the SD GPS measurements are added to the filter during the *measurement update*, resulting in the updated filter state at the current epoch. In addition to these 3 steps the EKF contains a 4^{th} step concerning the estimation and validation of the integer DD ambiguities (*integer ambiguity resolution*), as well as their incorporation into the filter. This four step processing scheme is visualized in Fig. 4.3, and is discussed in full detail in the following.

Time update

During the time update, the updated filter state and covariance at t_{i-1} (superscript '+') are first propagated to a prediction (superscript '-') at the current measurement

epoch t_i, yielding

$$\begin{aligned} \mathbf{x}_i^- &= \mathbf{x}\big(t_i; \mathbf{x}(t_{i-1}) = \mathbf{x}_{i-1}^+\big) \\ \mathbf{P}_i^- &= \mathbf{\Phi}_i \mathbf{P}_{i-1}^+ \mathbf{\Phi}_i^T + \mathbf{Q}_i \end{aligned} . \tag{4.24}$$

Propagation of the filter state however requires the integration of the relative S/C state. As mentioned in the introduction of section 4.2, there is no direct model describing the relative S/C motion with the required accuracy. The relative S/C motion is thus obtained from the dynamical models of the individual spacecraft, hence the 'pseudo' relative dynamics. In contrast to the reduced dynamic batch LSQ where a direct integration of the relative spacecraft state was facilitated (eqn. 4.16), the EKF handles this problem in a slightly different way, which was found to be more flexible and easier when implementing. Here, integration of the relative state, from t_{i-1} to t_i, is accomplished by independent integration of the two absolute S/C states, $\mathbf{y}_A$ and $\mathbf{y}_B$, over the same time interval and subtracting them in the end. This approach was already successfully demonstrated by *Leung and Montenbruck* [2005] and during an earlier stage of this research in *Kroes et al.* [2005]. More specifically, at epoch t_{i-1} the absolute state from the reference spacecraft, again S/C A, is obtained from a reduced dynamic a-priori reference orbit (in SP3 format), $\mathbf{y}_A^{\text{ref}}(t_{i-1})$. The (auxiliary) state of the other spacecraft, S/C B, is obtained by adding the updated filter estimate of the relative state at t_{i-1} to the state of the reference spacecraft,

$$\mathbf{y}_B^{\text{aux}}(t_{i-1}) = \mathbf{y}_A^{\text{ref}}(t_{i-1}) + \mathbf{y}_{AB,i-1}^+. \tag{4.25}$$

The absolute force model parameters, required for integration of the individual S/C states, are obtained in a similar way. The force model parameters for S/C A, $\mathbf{p}_A^{\text{ref}}$, are set to realistic predefined values and are kept constant over time. The (auxiliary) force model parameters for S/C B are obtained by adding the relative force model parameters from the filter state to the ones of S/C A at t_{i-1}, yielding

$$\mathbf{p}_B^{\text{aux}}(t_{i-1}) = \mathbf{p}_A^{\text{ref}}(t_{i-1}) + \mathbf{p}_{AB,i-1}^+. \tag{4.26}$$

Integration of the individual spacecraft states, leading to their predicted values

$$\mathbf{y}_i^- = \mathbf{y}_{i-1}^+ + \int_{t_{i-1}}^{t_i} \mathbf{f}(t, \mathbf{y}(t), \mathbf{p}) dt, \tag{4.27}$$

is now accomplished using a 4^{th} order Runge-Kutta numerical integration method, similar to the POD case. The predicted relative state,

$$\mathbf{y}_{AB,i}^- = \mathbf{y}_{B,i}^- - \mathbf{y}_{A,i}^-, \tag{4.28}$$

is now constructed as the difference of the predictions of the absolute states. This process is repeated at every epoch and visualized in Fig. 4.4.

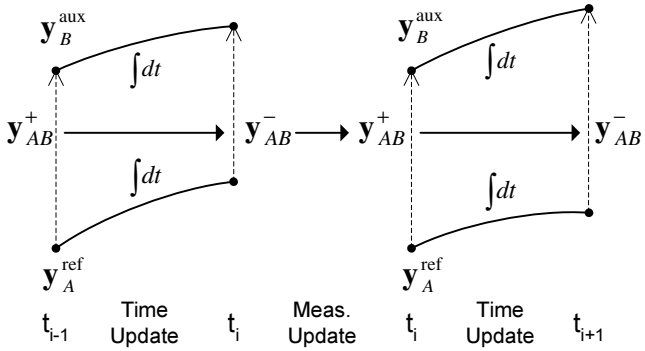

Figure 4.4 Illustration of the propagation of the relative spacecraft state over the time and measurement update. (Source: [*Kroes et al.*, 2005])

Although analytically the integration of the individual S/C states is identical to the direct integration of the relative state from eqn. 4.16, there is a difference when numerically evaluating both expressions. Therefore, as a test, the direct integration has also been facilitated. Here, the state of S/C A is integrated in a similar way as just described, but with simultaneous integration of the relative S/C state. During integration the state of S/C B as well as the accompanying force model parameters, all required to evaluate the accelerations, are obtained as $\mathbf{Y}_B = \mathbf{Y}_A + \mathbf{Y}_{AB}$. Both formulations resulted in relative position differences of up to 0.05 mm for a 10 second integration interval when fixing ambiguities. Due to the fact that the integration is restarted at every epoch, and the GPS measurements are added in between, the numerical discrepancy between both approaches does not accumulate over time. When both solutions were compared to the KBR measurements a difference of up to 0.02 mm in the precision was noticed in the advantage of the here illustrated, and finally used integration scheme. Therefore, and due to the fact that implementation is more straightforward, the integration of the relative state remains facilitated by integrating the individual S/C states as just illustrated.

Similar to the EKF for POD, the relative empirical accelerations are propagated over time using the Gauss-Markov process model (cf. eqn. 3.33),

$$\mathbf{a}_{AB,i}^{-} = \mathrm{e}^{-|t_i - t_{i-1}|/\tau} \mathbf{a}_{AB,i-1}^{+}. \tag{4.29}$$

The other estimation parameters are again kept constant during the entire filter time update phase

$$\left(C_{R_{AB}}; C_{D_{AB}}; c\delta t_{AB}, \mathbf{I}_{AB}, \mathbf{A}_{AB}\right)_i^{-} = \left(C_{R_{AB}}; C_{D_{AB}}; c\delta t_{AB}, \mathbf{I}_{AB}, \mathbf{A}_{AB}\right)_{i-1}^{+}, \tag{4.30}$$

reflecting a white process noise model. Propagation of the filter covariance requires

the filter state transition matrix

$$\mathbf{\Phi}_i = \begin{pmatrix} \mathbf{\Phi_Y} & \mathbf{0} & \mathbf{0} & \mathbf{0} \\ \mathbf{0}^T & 1 & \mathbf{0}^T & \mathbf{0}^T \\ \mathbf{0} & \mathbf{0} & \mathbf{1} & \mathbf{0} \\ \mathbf{0} & \mathbf{0} & \mathbf{0} & \mathbf{1} \end{pmatrix}, \tag{4.31}$$

which is completely diagonal and filled with ones except for the submatrix regarding the dynamic estimation parameters, $\mathbf{\Phi_Y}$. Since the trajectory of S/C A is again given a-priori and is kept fixed (no parameters are estimated for it), the relative S/C state transition and sensitivity matrix are similar to the ones of S/C B, $\mathbf{\Phi}_{AB}(t, t_0) = \mathbf{\Phi}_B(t, t_0)$ and $\mathbf{S}_{AB}(t) = \mathbf{S}_B(t)$, as was shown earlier in eqn. 4.18 and eqn. 4.19 respectively. This means that $\mathbf{\Phi_Y}$ has exactly the same structure as for the POD process (Fig. 3.6), where the relative S/C state transition and sensitivity matrix have to be substituted by the ones of S/C B. In addition, process noise,

$$\mathbf{Q}_i = \begin{pmatrix} \mathbf{Q_Y} & \mathbf{0} & \mathbf{0} & \mathbf{0} \\ \mathbf{0}^T & q_{c\delta t} & \mathbf{0}^T & \mathbf{0}^T \\ \mathbf{0} & \mathbf{0} & \mathbf{Q_I} & \mathbf{0} \\ \mathbf{0} & \mathbf{0} & \mathbf{0} & \mathbf{0} \end{pmatrix}, \tag{4.32}$$

is also added to the covariance. This entirely diagonal matrix only has entries for the empirical accelerations, the relative GPS receiver clock offset and the SD ionospheric path delays. The entries for the empirical accelerations are again set according to the Gauss-Markov process model (Fig. 3.6),

$$q_i = \sigma^2(1 - m_i^2). \tag{4.33}$$

Similar to the POD case (section 3.4.4), it can again be argued to incorporate the correlations of the process noise of the empirical accelerations with the relative position and velocity. When implemented for testing using the settings from Table 4.1 on page 107, the process noise entries, as a percentage of their corresponding covariance matrix entry, were found to be even lower than encountered in the POD case. Inclusion did introduce a very small difference (up to 0.01 mm) between the relative position estimates in both cases. Compared to the KBR however, both solutions still had the same precision. Therefore incorporating these correlations was only found to be an additional burden.

Similar to the EKF for POD, the relative receiver clock is handled as a random walk process, meaning a mapping factor of 1 and the corresponding process noise entry

$$q_{c\delta t} = \left(\frac{\sigma_{c\delta t}^2}{\tau_{c\delta t}}\right)(t_i - t_{i-1}). \tag{4.34}$$

Here, again, $(\sigma_{c\delta t}^2/\tau_{c\delta t})$ is the noise spectral density, consisting of a process noise variance, $\sigma_{c\delta t}$, as well as a time scale, $\tau_{c\delta t}$, that are once more only used (Table 4.1)

to construct the noise spectral density of the process. Although physically not entirely correct the random walk process model is also applied to the SD ionospheric path delays. These parameters are only estimated since this is required for proper ambiguity resolution over long baselines (section 4.4.3). To guarantee a 'free' estimation of these parameters, a high enough process noise is added at every time update of the filter (Table 4.1).

Reordering

Upon completion of the time update step a reordering of the filter state and covariance takes place. This in order to incorporate the change in mutually observed GPS satellites, again only concerning the GPS satellite parameters, i.e. the SD ionospheric path delays and carrier phase ambiguities. Here, GPS satellites no longer mutually observed, or which have experienced a (SD) carrier phase discontinuity are removed from the filter state and covariance. Whenever a new commonly observed GPS satellite becomes available, a-priori values of these parameters are added to both the filter state vector and covariance matrix. This again assures that the total size of the filter state is always equal to $12 + 3n$, where n equals the number of currently commonly tracked satellites.

Measurement update

The measurement update of the EKF is performed directly after the reordering step and is again expressed as

$$\begin{aligned} \mathbf{K}_i &= \mathbf{P}_i^- \mathbf{H}_i^T \big(\mathbf{W}_i^{-1} + \mathbf{H}_i \mathbf{P}_i^{-1} \mathbf{H}_i^T\big)^{-1} \\ \mathbf{x}_i^+ &= \mathbf{x}_i^- + \mathbf{K}_i \big(\mathbf{z}_i - \mathbf{h}(\mathbf{x}_i^-)\big) \qquad , \\ \mathbf{P}_i^+ &= \big(\mathbf{1} - \mathbf{K}_i \mathbf{H}_i\big) \mathbf{P}_i^- \end{aligned} \tag{4.35}$$

in which the measurement covariance, or inverse weighting matrix, $\mathbf{W}^{-1}$, is still completely diagonal due to the fact that the SD GPS observations

$$\mathbf{z}_i = \begin{pmatrix} \mathbf{P}_{1AB} \\ \mathbf{P}_{2AB} \\ \mathbf{L}_{1AB} \\ \mathbf{L}_{2AB} \end{pmatrix} = \begin{pmatrix} (P^1_{1AB}; \ldots; P^n_{1AB}) \\ (P^1_{2AB}; \ldots; P^n_{2AB}) \\ (L^1_{1AB}; \ldots; L^n_{1AB}) \\ (L^1_{2AB}; \ldots; L^n_{2AB}) \end{pmatrix} \tag{4.36}$$

are assumed uncorrelated for this research. The filter design matrix

$$\mathbf{H}_i = \left(\frac{\partial \mathbf{h}}{\partial \mathbf{r}_{AB}} \; \frac{\partial \mathbf{h}}{\partial \mathbf{v}_{AB}} \; \frac{\partial \mathbf{h}}{\partial \mathbf{p}_{AB}} \; \frac{\partial \mathbf{h}}{\partial c\delta t_{AB}} \; \frac{\partial \mathbf{h}}{\partial \mathbf{I}_{AB}} \; \frac{\partial \mathbf{h}}{\partial \mathbf{A}_{1AB}} \; \frac{\partial \mathbf{h}}{\partial \mathbf{A}_{2AB}} \right), \tag{4.37}$$

again contains the partial derivatives of the modeled measurements with respect to the filter state. More specifically, when the SD observations are put in the same

order as the corresponding estimation parameters, the design matrix reads

$$\mathbf{H}_i = \begin{pmatrix} \mathbf{E}_i & \mathbf{0} & \mathbf{0} & \mathbf{1} & \mathbf{1} & \mathbf{0} & \mathbf{0} \\ \mathbf{E}_i & \mathbf{0} & \mathbf{0} & \mathbf{1} & \frac{f_1^2}{f_2^2}\mathbf{1} & \mathbf{0} & \mathbf{0} \\ \mathbf{E}_i & \mathbf{0} & \mathbf{0} & \mathbf{1} & -\mathbf{1} & \lambda_1\mathbf{1} & \mathbf{0} \\ \mathbf{E}_i & \mathbf{0} & \mathbf{0} & \mathbf{1} & -\frac{f_1^2}{f_2^2}\mathbf{1} & \mathbf{0} & \lambda_2\mathbf{1} \end{pmatrix}, \tag{4.38}$$

where all partials are constant over time except for the ones relating to the relative position. The partials follow from the dual frequency observation model in eqn. 2.29. It must be noted that the partials with respect to the relative receiver clock are an $n \times 1$ dimensional vector of ones, whereas the partials with respect to the SD ionospheric path delays and carrier phase ambiguities are given by the identity matrix, whether or not multiplied with either the ionospheric refraction factor, (f_1^2/f_2^2), or the signal wavelengths. Since the trajectory of S/C A is given a-priori and does not change, the position partials only depend on the line of sight vectors to S/C B (eqn. 2.28). The geometry matrix,

$$\mathbf{E}_i = \begin{pmatrix} -(\mathbf{U}^T(t_i) \cdot \mathbf{e}_B^1(t_i))^T \\ \vdots \\ -(\mathbf{U}^T(t_i) \cdot \mathbf{e}_B^n(t_i))^T \end{pmatrix}, \tag{4.39}$$

comprises these line of sight vectors to the different GPS satellites, which, due to the fact that they are given in the Earth fixed system, have to be transformed to the ICRF by matrix $\mathbf{U}^T(t_i)$ from eqn. 3.1.

Integer ambiguity resolution

Upon completion of the measurement update, the filter is enhanced with an additional step regarding the resolution of integer DD ambiguities and their incorporation into the filter. As mentioned earlier, the continuous change in mutually observed GPS satellites, results in the allocation of new SD ambiguities to the filter, and the removal of no longer observed ones, over time. This propagates into the DD estimation problem. At every epoch, the current filter state has to be evaluated to see if any of the present SD ambiguities can form not-yet-resolved DD ambiguity pairs (a pair being the SD L_1 and L_2 ambiguities belonging together). If this is the case, the concerned DD float ambiguity estimates are formed by differencing the corresponding filter SD ambiguities with respect to the ones from a reference GPS satellite j, A_{1AB}^j and A_{2AB}^j. Selection of this reference satellite is subject to the presence of already resolved integer DD ambiguities in the filter state and covariance. When present, the reference SD ambiguity pair has to be selected from the subset forming these already resolved integer values. This assures a proper connection of the to-be-resolved integer DD ambiguities with the pre-existing ones in the filter. At filter startup or after a complete GPS phase break, no integer ambiguity constraints are present in the filter state and covariance, meaning that the

reference SD ambiguity can be freely selected. Selection in this last case is based on the highest (mutual) elevation of the GPS satellite to which the SD ambiguity pair belongs. For the integer estimation process, the real-valued SD and DD float ambiguities are, when keeping the notations of the respective observation models (eqn. 2.29 and eqn. 2.35), defined as:

$$\begin{aligned} \mathbf{A}_{SD} &= \left((A^k_{1AB};\ldots;A^m_{1AB};A^j_{1AB});(A^k_{2AB};\ldots;A^m_{2AB};A^j_{2AB})\right) \\ \mathbf{A}_{DD} &= \left((N^{jk}_{1AB};\ldots;N^{jm}_{1AB});(N^{jk}_{2AB};\ldots;N^{jm}_{2AB})\right) \end{aligned} . \tag{4.40}$$

Here, the vector $\mathbf{A}_{SD}$ contains only those SD ambiguities that are not yet part of an already resolved DD ambiguity (except for the reference j if applicable) and therefore differs from the vector of SD ambiguities in the filter state (eqn. 4.23). Besides a float estimate of the DD ambiguities their accompanying covariance matrix, $\mathbf{P}_{\mathbf{A}DD}$, is also required. Both are easily obtained from their SD counterparts,

$$\begin{aligned} \mathbf{A}_{DD} &= \mathbf{T}\mathbf{A}_{SD} \\ \mathbf{P}_{\mathbf{A}DD} &= \mathbf{T}\mathbf{P}_{\mathbf{A}SD}\mathbf{T}^T \end{aligned} , \tag{4.41}$$

by means of a transformation with the block diagonal *dual frequency* ambiguity transformation matrix,

$$\mathbf{T} = \begin{pmatrix} \mathbf{T}_* & \mathbf{0} \\ \mathbf{0} & \mathbf{T}_* \end{pmatrix}, \tag{4.42}$$

in which the *single frequency* transformation matrix yields

$$\mathbf{T}_* = \begin{pmatrix} 1 & 0 & \cdots & 0 & -1 \\ 0 & 1 & & \vdots & -1 \\ \vdots & & \ddots & 0 & \vdots \\ 0 & \cdots & 0 & 1 & -1 \end{pmatrix}. \tag{4.43}$$

The hereby obtained real-valued DD ambiguity estimates as well as their covariance are used as input for the LAMBDA method, where, cf. eqn. 4.4, the best and second best integer DD ambiguity estimates, $\mathbf{N}_B$ and $\mathbf{N}_S$ respectively, as well as the vector of accompanying conditional variances, $\sigma_{i|I}$, are returned. The validation of the best integer solution is subsequently conducted. Here, the individual tests of the validation procedure are executed in the order they are discussed in section 4.1.2. If the success rate (eqn. 4.5) is not high enough, or if either the integer (eqn. 4.7) or the discrimination (eqn. 4.8) test are not passed, the validation process rejects the entire vector of integers. If these 3 tests are passed, the individual wide-lane and ionosphere free ambiguity residuals are screened. Here it can, and does frequently, occur that only one or a few integer ambiguity pairs are found to be incorrectly estimated. These are subsequently removed from the vector $\mathbf{N}_B$, which then only contains the integers that are assumed to be correctly resolved.

Allocation of the integers that have passed the validation procedure is accomplished by means of an additional measurement update (eqn. 4.35) with the following settings:

$$\begin{array}{ll} \mathbf{z} & = \mathbf{N}_B \\ \mathbf{h}(\mathbf{x}) & = \mathbf{A}_{DD} = \mathbf{T}\mathbf{A}_{SD} \\ \mathbf{W}^{-1} & = \mathbf{0} \\ \mathbf{H} & = \begin{pmatrix} \mathbf{0} & \mathbf{0} & \mathbf{0} & \mathbf{T} \end{pmatrix}. \end{array} \tag{4.44}$$

Here it can be seen that the integers are actually allocated as 'observations' with no uncertainty left in them, $\mathbf{W}^{-1} = \mathbf{0}$. They are modeled by the SD ambiguities, and have the transformation matrix $\mathbf{T}$ as the corresponding partials. Although strictly speaking incorrect, since they are no observations, handling them like this restructures the covariance in such a way that they act as integer constraints throughout their existence in the filter. No additional bookkeeping is thus required. It must be noted that whenever a subset of integers is allocated, due to the fact that some pairs were removed by either one of the ambiguity residuals screening tests, the corresponding rows of the vectors and matrices of the measurement update have to be removed as well.

Kinematic single point positioning

As soon as the filter has integer DD ambiguities allocated, it is no additional burden to retrieve them at any time. It is therefore possible to construct a precise kinematic carrier phase only relative position solution at each epoch as long as there are enough integer DD ambiguities known (4 or more for redundancy). The single point positioning principle used here processes SD ionosphere free carrier phase observations corrected for the integer DD carrier phase ambiguities, and satisfies the simple positioning model

$$\begin{pmatrix} L^j_{\mathrm{IF},AB} - \rho^{j0}_{AB} \\ L^k_{\mathrm{IF},AB} - \rho^{k0}_{AB} - N^{jk}_{\mathrm{IF},AB} \\ \vdots \\ L^m_{\mathrm{IF},AB} - \rho^{m0}_{AB} - N^{jm}_{\mathrm{IF},AB} \end{pmatrix} = \begin{pmatrix} (\mathbf{e}^j_B)^T & 1 \\ (\mathbf{e}^k_B)^T & 1 \\ \vdots & \\ (\mathbf{e}^m_B)^T & 1 \end{pmatrix} \begin{pmatrix} \Delta\mathbf{r}_{AB} \\ c\delta t_{AB} + A^j_{\mathrm{IF},AB} \end{pmatrix}, \tag{4.45}$$

also given by *Misra and Enge* [2001]. As can be seen the relative receiver clock offset becomes biased with the ionosphere free SD ambiguity of GPS satellite j, serving as the reference. The SPP process performs a check on the post-fit residuals obtained. Whenever the standard deviation of these residuals exceeds a predefined threshold, the integer corrected SD carrier phase observation that contributes the dominating error is identified and removed from the set of observations. If necessary, the process is repeated to reject multiple outliers at the same epoch. Incorrectly resolved integer ambiguities could be identified in this way.

Smoother

Just as for the EKF for POD, the entire SD GPS data set is processed both in a forward, as well as a backward direction. At each epoch, a smoothed solution

$$\overline{\mathbf{x}}_i = \frac{\mathbf{P}_{i,fwd}^{-1}\mathbf{x}_{i,fwd} + \mathbf{P}_{i,bck}^{-1}\mathbf{x}_{i,bck}}{\mathbf{P}_{i,fwd}^{-1} + \mathbf{P}_{i,bck}^{-1}} \tag{4.46}$$

is again computed as the weighted average of the estimated filter states from both runs. The weights are determined by the information matrix, i.e. the inverse covariance, of the respective state estimates. By combining the forward and backward results, measurements from both before and after a given epoch contribute to the corresponding state estimate. This is now especially important due to the fact that the integer DD ambiguities are freely estimated on both runs, i.e. none of the integer DD ambiguities obtained during the forward run is a-priori allocated to the backward run. The smoothing process therefore assures that integer information, which is not available on a certain epoch in one of the runs, is still accounted for. Again, as a result, a significant improvement in accuracy over the individual solutions is achieved. This can no longer directly be quantified (for the POD case this was roughly a factor of 2), but depends if both runs have integers allocated, which influences the weight of the individual information matrices. As an example, near the beginning and end of the data arc as well as over extended data gaps, where either the forward or backward filter has no integer ambiguities allocated yet, the other solution will dominate the smoothing process.

The same process is applied to the kinematic SPP solutions, created independently during the forward and the backward run, but it would be more appropriate to speak of averaging instead of smoothing in this case. Here, the SPP solution will not be smoothed, but the process assures that the information of integer ambiguities, that are not part of both the forward and backward SPP solution, can still contribute. The resulting solution is the one where all available (integer corrected measurement) information is accounted for.

4.4 Extended Kalman filter results

This section contains the results of the EKF for relative positioning of spacecraft, when tested using the GRACE data from the same 101-day data arc, 2003 DOY 190 to 290, as for the GPS based POD tools from the previous chapter. First, the specific EKF settings and the processing scheme are discussed. This is followed by some words on the relative empirical accelerations and SD ionospheric path delays resulting as additional output of the EKF runs. The actual validation of the relative position solution is presented thereafter. This starts with an overview on how exactly the GRACE KBR observation data is used for this purpose, followed by the KBR comparison of four different relative position solution types. These include the relative position computed from two individual GRACE POD orbits, the EKF

float solution, created without resolving the integer DD ambiguities, and the high precision EKF ambiguity fixed solution as well as the simultaneously constructed kinematic SPP solution. Due to the fact that the KBR only provides a 1-dimensional validation possibility and cannot detect constant biases in the solution, a comparison of the different EKF position solutions, as an additional consistency check, along with an analysis of the formal filter errors (variances) associated, concludes this section.

4.4.1 Filter settings

The EKF for relative positioning of spacecraft has been implemented in the *Filter for Relative Navigation of Spacecraft* (FRNS) as an extension of the GHOST toolkit discussed in section 3.5. Similar to the POD tools in this software package, a strict processing scheme is to be followed when using the FRNS tool. This is first of all implied by the fact that one of the S/C serves as a reference (GRACE A) and therefore its orbit should already be known to the best possible extent. Second, and perhaps even more important, a similar GPS data editing procedure as for the POD tools (section 3.5.2) is implemented, requiring a reduced-dynamic reference orbit for both S/C concerned. It has earlier been decided to use the RDOD orbits (section 3.6) of both S/C for this purpose, and therefore prior to running the FRNS tool, the GHOST processing scheme (section 3.5.1) for each of the individual S/C has to be executed.

Similar to the POD tools, the FRNS program processes the GRACE GPS data in 24 hour, so daily, batches. One of the differences compared to the POD tools is the fact that the SD GPS data is processed at the higher data rate of 10 seconds, at which it is provided. This can now be done since the SD formulation no longer requires knowledge of the GPS satellite clock offsets. Therefore, if desired, use can even be made of the final IGS ephemerides (section 3.1) for this application, instead of the ones from CODE. When processing at this data rate, it was found that for the entire 101-day data arc there are on average 64088 observed SD code and carrier phase observations on each of the individual frequencies, on a 24 hour basis. This number is in good agreement with the values found in Table 3.3, where GRACE B is the limiting factor. Of course one has to account for the 3 times higher data rate and the fact that GPS satellites are not always mutually observed by both S/C for the 220 km GRACE separation. For the FRNS tool this total number of SD observations is edited using a similar scheme as for the POD tools. If an individual GPS observation, on either one of the GRACE S/C, has an elevation lower than 5° or an SNR value lower than 5, corresponding to a C/N_0 threshold of about 11 dB-Hz cf. eqn. 2.40, the SD observation is rejected. The two other tests no longer use the UD ionosphere free pseudorange and carrier phase observations, but the SD ones instead. In accordance the standard deviation threshold for the pseudorange data editing has been incremented with roughly a factor $\sqrt{2}$ to 0.7 m, to accommodate the higher noise of the SD ionosphere free observations. The standard deviation threshold of the time differenced SD carrier phase test for cycle slip detection on

the other hand has been lowered to 1 cm. This could be done due to the fact that the error reduction of the SD carrier phases was actually found to be higher than the increment in noise. This lower threshold assures an even better detection of (SD) cycle slips and other irregularities in the carrier phase data. These data editing settings allowed for an average of 86.3% of the observed SD pseudoranges to be used and a much higher 94.8% of the carrier phase data. A distribution of the SD observation data over the epochs is depicted in Fig. 4.5. Here the relative

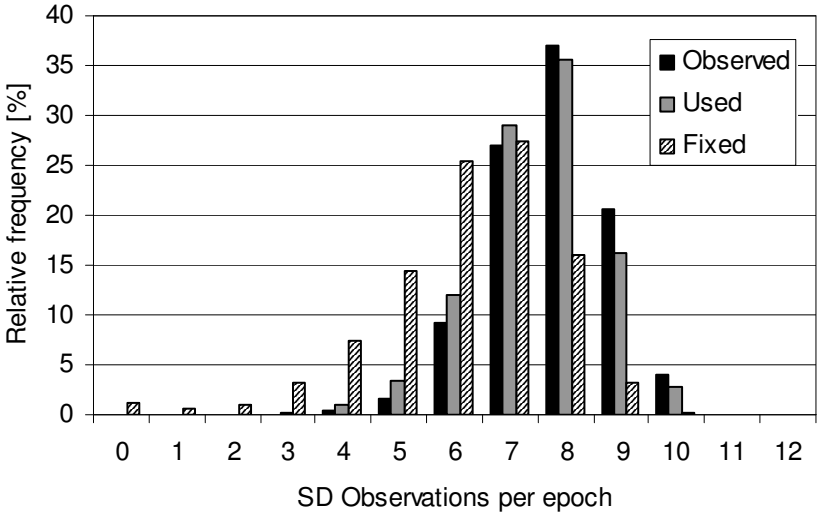

Figure 4.5 Average distribution, for the entire 101-day GRACE data arc, of the number of SD observations per epoch. Shown are the available SD observations ('Observed'), the ones used ('Used') by the filter and the ones of which the SD carrier phase ambiguity is part of an already resolved integer DD ambiguity ('Fixed').

frequency of the number of SD observations per epoch are given, averaged over the entire data arc. Shown are the total number of observed single differences and the ones that passed data editing and are thus used by the filter. More than 98% of all epochs has 5 or more SD observations that passed data editing and are used by the filter. In addition, the distribution of the SD carrier phase ambiguities that are part of an already resolved integer DD ambiguity is also depicted, but will be further discussed in section 4.4.7.

In accordance to the POD case, the SD GPS observations that are used by the filter are given an (uncorrelated) unit variance. For the SD pseudoranges (P_1 and P_2) and carrier phase (L_1 and L_2) observations, respective values of 0.5 m and 5.0 mm have been selected. For the pseudoranges this might seem a little conservative, but assures a better robustness for ambiguity resolution since more data needs to be accumulated before the success rate is high enough. Other (uncorrelated) a-priori variances and filter settings applied for the entire data arc can be found

Table 4.1 Overall settings for the *Filter for Relative Navigation of Spacecraft* (FRNS) used throughout the entire 101-day GRACE data arc.

Parameter	Value	Parameter	Value
A-priori standard deviation		*Process noise (steady state)* σ	
$\sigma_{\mathbf{r}}$ [m]	1.0	σ_{a_R} [nm/s^2]	0.1
$\sigma_{\mathbf{v}}$ [m/s]	1.0	σ_{a_T} [nm/s^2]	1.0
σ_{C_D} [-]	0.1	σ_{a_N} [nm/s^2]	0.3
σ_{C_R} [-]	0.1		
		$\sigma_{c\delta t}$ [m]	500.0
σ_{a_R} [nm/s^2]	0.5	σ_I [m]	1.0
σ_{a_T} [nm/s^2]	3.0		
σ_{a_N} [nm/s^2]	1.0	*Integer ambiguity validation*	
		$P(\mathbf{N}_B = \mathbf{N})$ [%] (eqn. 4.5)	99.9
$\sigma_{c\delta t}$ [m]	500.0	k_α [-] ($\alpha = 0.01$, eqn. 4.7)	1.8
σ_I [m]	20.0	$k_{S/B}$ [-] (eqn. 4.8)	3.0
$\sigma_{A_{L1}}$,$\sigma_{A_{L2}}$ [cycles]	10000.0	k_{WL} [cycles] (eqn. 4.11)	0.2
		k_{IF} [cm] (eqn. 4.12)	1.0
(Auto-corr.) Time scale			
$\tau_{a_{(R,T,N)}}$ [s]	600.0	*GPS SD observation (unit)* σ	
$\tau_{c\delta t}$ [s]	100.0	σ_{P_1},σ_{P_2} [m]	0.500
τ_I [s]	10.0	σ_{L_1},σ_{L_2} [m]	0.005

in Table 4.1. The filter uses the same high fidelity force models to propagate the individual S/C states that are used for the POD tools, provided earlier in Table 3.6. For both GRACE A and GRACE B the mass and surface area onto which the atmospheric drag and solar radiation pressure act are chosen similar to the POD process, 500 kg and 0.5 m^2 respectively. The initial values of the drag and solar radiation pressure coefficient for the reference S/C are kept fixed and have been set to the average ones resulting from the FAST program when running with the GRACE data (not documented earlier), resulting in $C_D = 4.45$ and $C_R = 1.60$. The empirical accelerations for the reference S/C are kept fixed to zero for the short integration time. The relative force model parameters are all initialized to zero, but are adjusted during the filter run.

The just described filter settings have been applied throughout the remainder of this section. In case the float solution is considered the ambiguity tests are of course not executed. Similar to the FAST program, all results presented in this section refer to the smoothed FRNS solution, computed according to eqn. 4.46.

4.4.2 Empirical accelerations

In accordance with the POD tools, and already displayed in Table 4.1, the auto-correlation time of the relative empirical accelerations have been set to 600 s. This

value was found to work very adequately for the application at hand. Of course the a-priori and steady state variances are chosen much smaller than for the POD process since only the differential modeling deficiencies have to be captured. Similar to the POD tools, tighter a-priori and process noise constraints are put onto the radial component due to the heavy in-plane dynamic coupling, as well as the lower sensitivity in this direction. The along-track component is thus left more free to absorb amongst others the effects of unmodeled differential drag. Typical results for

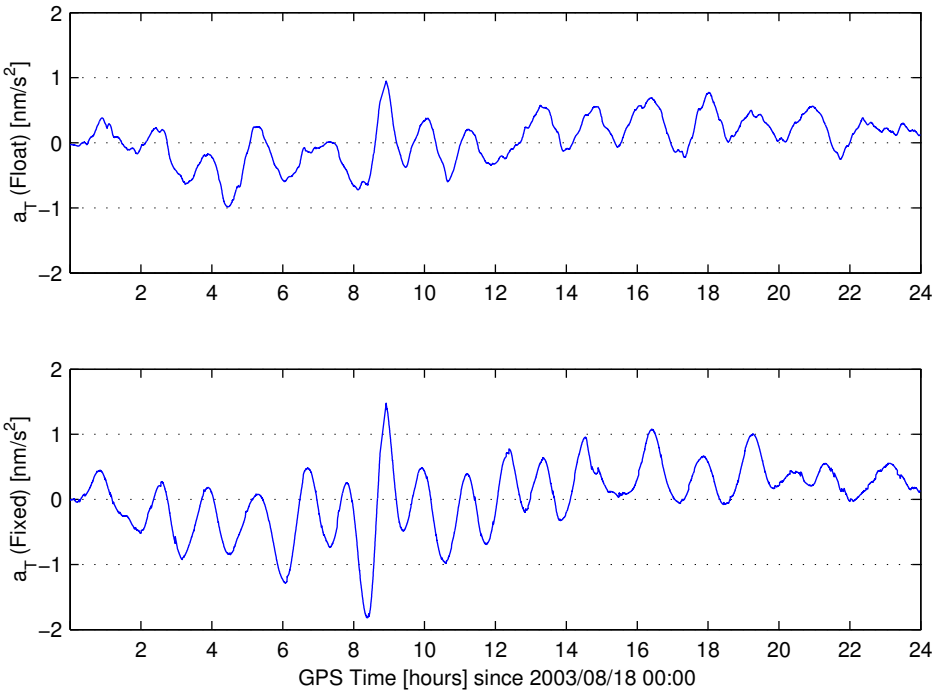

Figure 4.6 Relative empirical accelerations in the along-track direction (a_T) for the FRNS program for August 18, 2003 (DOY 230). Shown are the situations with float (top) and fixed (bottom) ambiguities

the relative empirical accelerations are given in Fig. 4.6 for DOY 230, concerning both the ambiguity float (top) and fixed (bottom) solution. Similar to the POD case (Fig. 3.8) only the dominant along-track component is shown here for both situations. As can be seen the effects of the geomagnetic storm present in Fig. 3.8 do not show up here with the same dominance. If at all, this is most clearly visible by the 'phase shifted' pattern between 8:00 and 10:00 in the ambiguity fixed empirical acceleration. It is interesting to see that there still is a relatively large difference between the empirical accelerations of the float and fixed solution, although the overall pattern is largely identical. In the ambiguity fixed case the 'integer corrected' carrier phase observations dramatically strengthen and dominate

the relative position solution. Any discrepancies with the force models are kept outside the position solution and are thus put into the relative empirical acceleration parameters. In the ambiguity float scenario on the other hand these deficiencies seem to be more absorbed by the position since they do not always appear in the empirical accelerations. Again, caution must be taken when interpreting the empirical acceleration patterns. Similar to the different POD scenarios the obtained values are highly dependent on the underlying dynamical and stochastic models, as well as the applied filter settings.

4.4.3 Ionospheric path delays

Typical values for the SD ionospheric path delays obtained from the EKF when using GRACE GPS data are depicted in Fig. 4.7. In addition, the DD values are also shown which were formed from the SD filter estimates. As can be seen the SD delays are quite significant over the long S/C (nominally 220 km) separation, even for the high altitude of 470 km. The fairly constant mean value of around -2.8 m however represents the SD differential code bias between both GRACE GPS receivers, which is absorbed by the SD ionospheric path delay. Since both GRACE

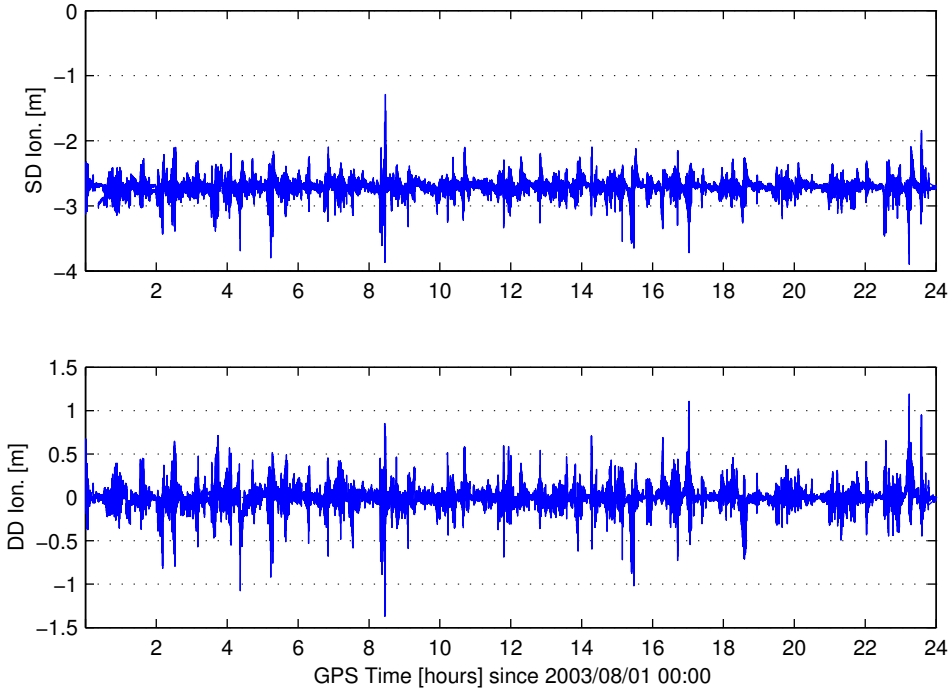

Figure 4.7 The SD (top) and DD (bottom) ionospheric path delays between the GRACE S/C for August 1, 2003 (DOY 213).

S/C rapidly move over the day and night side of the Earth, the SD ionosphere shows a pattern of higher and lower activity. It is clear that if the DD ambiguities are to be resolved correctly using a SD filter formulation, the SD ionospheric path delays have to be estimated, as has been done here. The underlying random walk process, that is used to model the SD ionospheric path delays, shows to work adequately, which is mainly caused by the fact that an adequate, high enough process noise (Table 4.1) is added to allow for a more or less 'free' estimation of these parameters at every epoch. Although this approach already works very satisfying, it might be worthwhile to model the SD ionospheric path delays more precisely, including a rate of change or even the acceleration of the change in ionosphere, in a future variant of the EKF. This would namely speed up the re-estimation of integer ambiguities after a cycle slip has occurred. It can furthermore be seen in Fig. 4.7 that the DD ionospheric path delays can be more than 1 m, corresponding to 5 and 4 integer cycles in respectively the L_1 and L_2 observation. A DD parametrization of the filter would therefore still require the estimation of the accompanying ionospheric path delays, where the additional burden of continuous re-ordering the parameters also has to be coped with.

4.4.4 GRACE K/Ka-Band Ranging System modeling

In addition to the GPS and attitude quaternion data, the GRACE K/Ka-Band Ranging System observations are also provided as part of the Level 1B GRACE data distributed by PODAAC. A Level 1B KBR observation, L_{KBR}, is an ionosphere free phase or biased range measurement, constructed from the dual frequency, or Level 1A [*Case et al.*, 2002], K- and Ka-Band Ranging observations that have a noise level, ϵ, of 10 μm at 1 Hz sampling [*Dunn et al.*, 2003]. The Level 1B KBR observation data is already flagged for bad data points and cycle slips [*Case et al.*, 2002] and can therefore be used directly for the purpose of validating the norm of the relative position solution, corresponding more or less to the along-track component, between both GRACE satellites. The KBR observation, at time t_i, is modeled as

$$L_{KBR}(t_i) = \rho_{AB}(t_i) + B_{KBR} + \Delta_{ant}(t_i) + \Delta_{c\tau}(t_i) + \epsilon(t_i), \tag{4.47}$$

where ρ_{AB} is the distance between the center of mass of both GRACE S/C, B_{KBR} is the real-valued KBR observation bias that is constant over time until a cycle slip occurs, Δ_{ant} is the correction concerning the offset between the KBR antenna phase center and the center of mass, on each of the individual GRACE S/C (Table 4.2), and $\Delta_{c\tau}$ is the so called light time correction. More specifically, the light time correction is the correction applied for the distance travelled by both GRACE satellites during the KBR signal travelling time. Both the antenna offset correction and light time correction are also provided in the Level 1B KBR data files [*Case et al.*, 2002] and can directly be used for the purpose of this research. Validation of the relative position solution is done for each of the individual 24 hour, so daily, batches at which the GPS data is provided, and thus the interval used to construct

Table 4.2 The KBR antenna phase center offsets with respect to the center of gravity for each of the GRACE S/C, defined in the respective S/C body systems.

	X [m]	Y [m]	Z [m]
GRACE A	1.472581	0.002663	0.001548
GRACE B	1.472580	-0.000088	0.003319

the relative position solution. The Level 1B KBR observations are also provided in identical 24 hour (daily) periods, synchronized to the GPS integer time tags. The only difference here is the higher output rate of the KBR observations, which are nominally provided at 5 second intervals. In order to validate the relative position solution, the constant KBR bias must first be calibrated. This is accomplished using the norm of the relative position solutions, $\rho_{AB}(t_i) = \|\mathbf{r}_{AB}(t_i)\|$, obtained at each of the GPS measurement epochs t_i. For a total of n epochs over a day (at the 10 second GPS observation intervals this would be a maximum for n of 8640) the bias would read

$$B_{KBR} = \frac{1}{n}\sum_{i=1}^{n} L_{KBR}(t_i) - \rho_{AB}(t_i) - \Delta_{ant}(t_i) - \Delta_{c\tau}(t_i). \tag{4.48}$$

It must be noted that when a cycle slip in the KBR data is detected, which frequently occurs, between e.g. t_m and t_{m+1}, two biases must be calibrated over the respective period, one from t_1 to t_m and one from t_{m+1} to t_n.

After having calibrated the daily bias or biases, they are subsequently used to construct a (24 hour) time series of residuals between the norm of the relative position solution and the bias corrected KBR observations, the so-called 'KBR fit'. Since the KBR observation noise is negligible compared to the errors in the relative position solution, the (daily) standard deviation of this time series presents a direct 1-dimensional precision measure of the relative position solution. It must be noted that this standard deviation only reflects the true daily standard deviation in case there has been no cycle slip in the KBR data, meaning that only one bias needs to be calibrated. If multiple biases are present the standard deviation could reflect a too positive assumption on the quality. It is once more emphasized that the KBR measurements can only validate the norm of the relative position solution (1-dimensional precision) and cannot detect any constant biases in the solution since these are automatically absorbed in the just discussed calibration process.

4.4.5 KBR comparison of the GRACE POD solutions

In order to see how well the relative position can be constructed from two independently generated POD solutions of the S/C concerned, a KBR fit of the GRACE POD orbits from section 3.6 is presented here. For the KBR bias calibration process the relative position is simply constructed as $\rho_{AB}(t_i) = \|\mathbf{r}_B(t_i) - \mathbf{r}_A(t_i)\|$. For this analysis the GRACE RDOD orbits, serving as reference trajectories within the

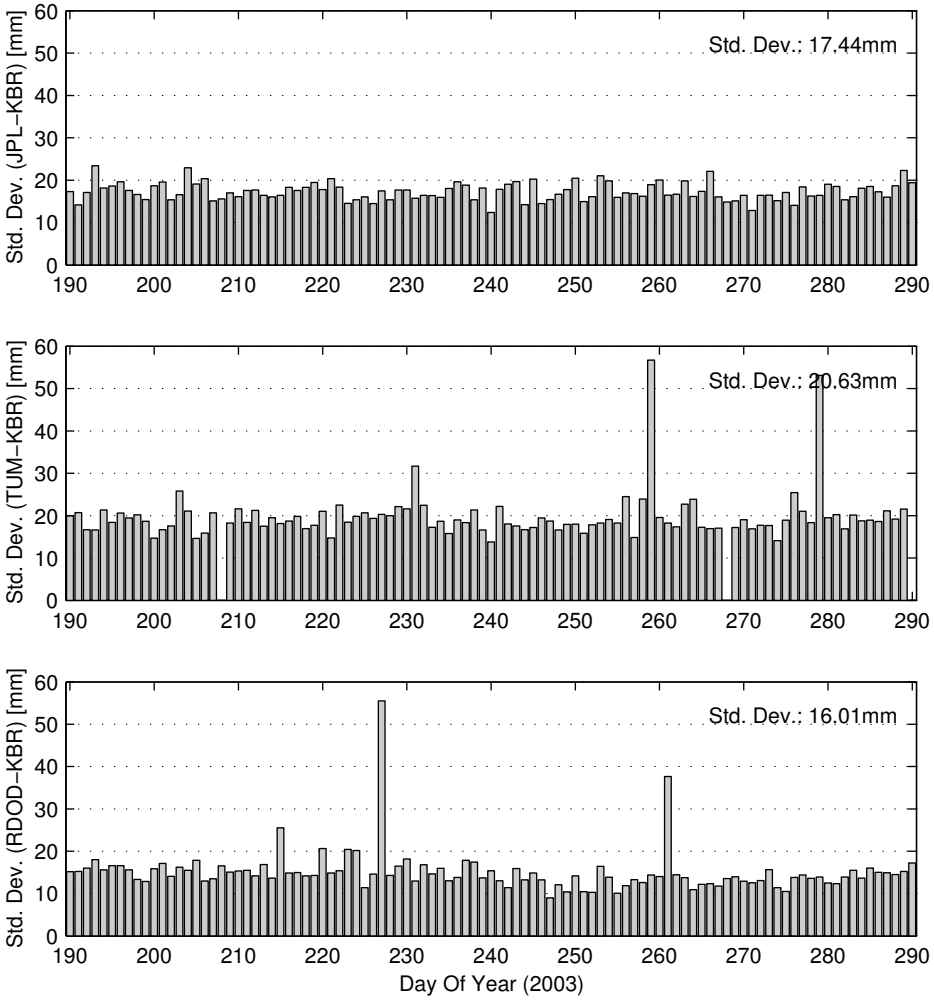

Figure 4.8 Daily standard deviations of the GRACE relative position, constructed from the individual satellite orbits, when compared to the KBR measurements.

FRNS tool, as well as the JPL and TUM reference ephemeris for the orbit comparisons made in section 3.6.4 are used. The daily standard deviations of this comparison for the entire 101-day data arc are depicted in Fig. 4.8. In addition, the standard deviation over the entire series is also provided in the upper right corner of each of the plots. This value is computed from the daily standard deviations, whilst properly accounting for the number of underlying residuals on each day. As can be seen the JPL GRACE orbits (top plot) have a really constant fit with the KBR data without any outliers. As already mentioned in section 3.6.4,

the TUM orbits (middle plot) have a few very large outliers of several hundreds of meters (DOY 268 and 290), which have been left out of the comparison. Aside from the fact that the RDOD orbits (bottom plot) also have some outliers in the KBR comparison, they seem to have the most precise overall KBR fit of 16 mm. Although an analysis of this kind can be used as a consistency check for the individual satellite orbits, it must be mentioned that it does not provide additional information on their precision or accuracy. Nevertheless, it is now known what the obtainable precision is for the baseline when constructed from 2 absolute positions.

4.4.6 Float ambiguity solution

As mentioned before, running the FRNS tool without estimating any integer ambiguities results in the so-called float solution for the relative position estimates. This solution is constructed using the same overall settings as for the ambiguity fixed solution (Table 4.1), except of course for the ambiguity validation tests, that are not required at all in this case. The float solution provides a direct measure for the improvement that can be gained over the just described baseline created from the individual orbits, by using (single) differenced GPS observation data and applying the (pseudo) relative S/C dynamics. The KBR comparison time series of the float solution, constructed as described in section 4.4.4, are depicted in Fig. 4.9 for four selected days (top down are shown DOY 195, 217, 222 and 258). The first thing that is clearly visible in each of the time series is the strong periodic signal, corresponding more or less to the orbital revolution period of each of the GRACE satellites (around 94 minutes), a so called once per revolution signal. This indicates that the resulting relative position solution heavily depends on the spacecraft dynamics, that are usually responsible for introducing such signals. Furthermore, in the plot of DOY 222 it can be seen that the EKF for relative S/C positioning is not as susceptible to data outages as its POD variant, FAST. The formulation of the relative dynamics implemented propagates the relative S/C state over the nearly 6 hour GPS (and KBR) data gap without any difficulty. Although in either the forward or backward solution this leads to an error in the relative position solution of about 15 cm (compared to KBR), this is still in the linear domain and allows for a rapid convergence of the filter after the data gap. It must however be mentioned that a performance comparison with the POD variant (FAST) for such cases is not completely fair. This is due to the fact that the relative S/C state is propagated by means of integrating the individual spacecraft states in the same manner as for the POD variant, as discussed in section 4.3. Each of these individual states experiences an error of several meters after such a data gap, as was shown in section 3.6.4, or more specifically in Table 3.11. The difference between these errors on the other hand, which resembles the integration error of the relative S/C state, is apparently (relatively) small. In addition, the GRACE S/C fly in the same orbital plane, with a separation of not even 30 seconds (220 km). The individual satellites are thus subject to more or less the same forces, leading to a more or less similar dynamic

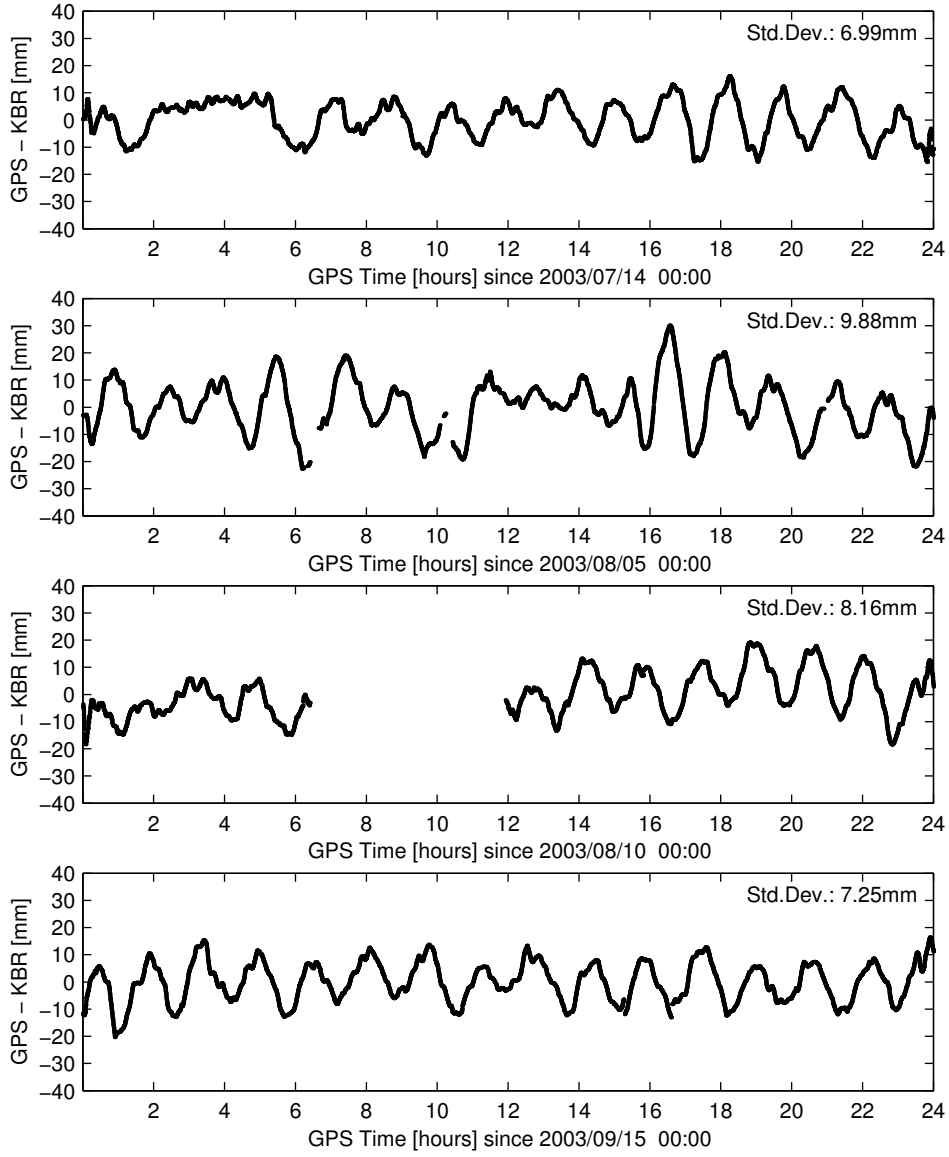

Figure 4.9 Time series of the KBR comparison residuals of the GRACE relative position solution. The relative position is obtained from the EKF with float ambiguities. Shown are (top down) DOY 195, DOY 217, DOY 222 and DOY 258.

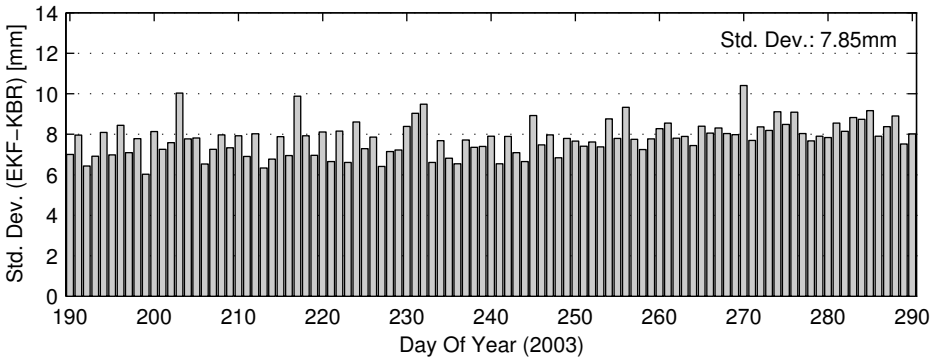

Figure 4.10 Daily standard deviations of the GRACE relative position, constructed by processing SD code and carrier phase observations with float ambiguities, when compared to the KBR measurements.

model uncertainty induced error in the individual positions. It remains for further study to see how the filter would respond to an out of plane system in such cases.

As can be seen the precision of the four KBR fit time series is already much higher than for the case where the relative position is constructed from the individual orbits. Although it must be mentioned that in the time series of DOY 217 a total of 4 KBR biases had to be calibrated (KBR phase breaks around, 6:15, 10:15 and 21:00; GPS phase breaks at 6:15 and 10:15). In this case for example, the computed residuals between the calibrated KBR and the relative position solution over the time interval 6:15 - 10:15 might be a little too optimistic, resulting in a too optimistic overall precision. The standard deviations of the KBR fit with the float solution over the entire data arc are given in Fig. 4.10. Here it is immediately observed that when differenced GPS data is used together with the implemented formulation of the relative dynamics, a significant precision improvement of (more than) a factor 2 in the (along-track component of the) relative position is gained compared to the baseline constructed from the individual orbits.

4.4.7 Fixed ambiguity solution

The highest achievable accuracy for the relative position solution is obtained when fixing the DD ambiguities to their resolved integer values and incorporating them as described in section 4.3. Here, the most important assumption is that the integer DD ambiguities are deterministic and have no uncertainty left in them, $\sigma_N = 0$. As mentioned earlier this not only dramatically strengthens the relative position but also aids in the swift and successful resolution of new DD integer ambiguities as they appear over time.

The rigorous and conservative ambiguity validation scheme, presented in section 4.1.2 using the settings from Table 4.4.1, still allows for a successful resolution of a seemingly constant average of 82% of the, on average, 494 DD ambiguity pairs

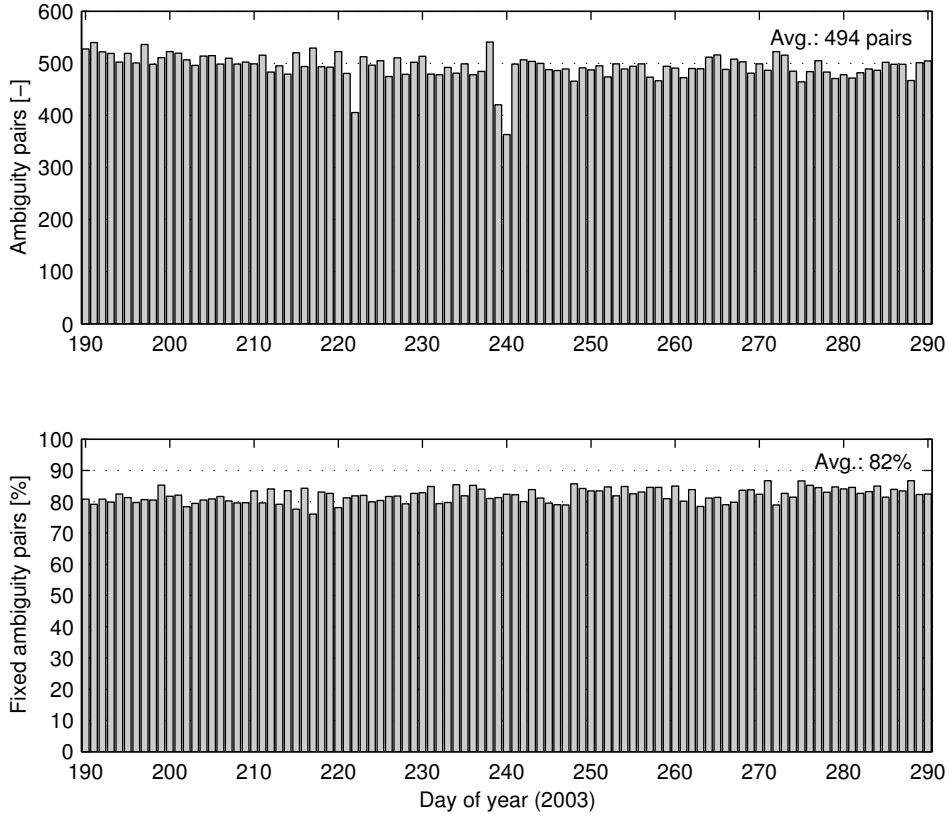

Figure 4.11 The total number of SD ambiguity pairs processed by the EKF on a daily basis (top), as well as the percentage of them that are eventually part of a fixed integer DD value (bottom).

per day (Fig. 4.11). This is a very decent number. When only considering DD pairs formed from continuous SD carrier phase tracking arcs with a length of at least 300 s (or 30 measurement epochs at the 10 s measurement interval) an again fairly constant, and even higher, 91% out of 400 pairs meeting this criterion, are fixed. This means that only around 40% of the DD ambiguities part of a continuous SD tracking arcs shorter than 300 s is fixed. This is logical since such short arcs are mostly the result of a detected cycle slip at the end of a SD pass. Here the pseudorange observations are not of a very good quality, which, combined with the short time these ambiguities are present in the filter, makes them hard to resolve. SD ambiguities for which the DD integer value cannot be resolved remain in the filter and still participate in, and contribute to, the EKF estimation process.

So far, Fig. 4.11 only depicts the DD ambiguities that are eventually fixed to their integer value. The distribution of the number of SD ambiguities that are

part of an already resolved, and incorporated, integer DD value over the epochs was already shown in Fig. 4.5. Here it can be seen that the distribution of the 'fixed' SD ambiguities per epoch appears shifted with respect to the distribution of the good SD observations, actually used on a per epoch basis. The reason for this is that the resolution of integer DD ambiguities formed from newly allocated SD ambiguities in general takes a few epochs, or is sometimes not possible at all. The shift in the distribution thus depicts the fact that ambiguity resolution takes some epochs. The figure furthermore shows that less than 10% of the epochs has a maximum of 3 SD ambiguities part of an already resolved integer DD value. This is the result of the initial filter startup and complete GPS phase breaks, mostly occurring after a data outage, where there are no integers known at all. On average it takes somewhere between 20 to 30 minutes after filter startup before at least 3 integer DD (4 SD) ambiguities are correctly resolved and incorporated. This also applies to large GPS data outages, where the filter no longer has any integer ambiguities allocated. Once the filter already has enough integer ambiguities incorporated, the resolution of new ones that appear over time is, in general, done swiftly. There is however no overall 'duration of resolution' that can be specified for such cases. It depends on issues like the number of simultaneous estimated ambiguities, the quality of the data and the viewing geometry. Sometimes it only takes one or two epochs of data accumulation before the ambiguities can be fixed, another time it might take several minutes.

Out of the 5 ambiguity validation tests that are applied, using the settings from Table 4.1, the most critical one is the test that evaluates the ionosphere free ambiguity residual (eqn. 4.12). This test basically dominates the ambiguity validation procedure and stops even the most 'subtle' incorrectly resolved ambiguities. The test evaluating the wide-lane ambiguity residual (eqn. 4.11) only stops the most critical integer estimation errors. Nevertheless, both test were found to be required during the development of the validation scheme. Occasionally, ambiguities that pass the ionosphere free ambiguity residual test were still found to be incorrect by the wide-lane test. This is due to the fact that the ionosphere free ambiguity does not heavily depend on the pseudorange data, whereas the wide-lane does. Incorporation of such ambiguities were found to lead to position errors as discussed and depicted in section 4.5.3, but not to divergence of the filter solution. The other tests, the success rate (eqn. 4.5), the integer test (eqn. 4.7) and the discrimination test (eqn. 4.8), were found to more or less 'precondition' the integer estimates to a level where the just discussed ambiguity residual tests only stop the real critical decisions. For example, if the success rate is not high enough more data should be accumulated before a reliable integer estimate can be made at all. In almost all cases the integer test is simultaneously passed with the success rate. Only occasionally a few additional epochs of data need to be accumulated before it is passed. The discrimination test was found to be more critical as soon as more ambiguities are estimated simultaneously. This is logical due to the fact that if only one ambiguity pair is different between the best and second best solution, the resulting ratio of both squared norms can be small. Therefore this test is harder to pass if no integer ambiguities are incorporated yet, i.e during initialization, and thus the integer

estimation vector is larger. Here, sometimes multiple epochs (up to 3 minutes) of additional data have to be accumulated before this test is passed. However, if there are already resolved integer ambiguities present in the filter, this test is, similar to the integer test, in nearly all cases simultaneously passed with the success rate.

The just discussed ambiguity fixing statistics depicted in Fig. 4.11 and Fig. 4.5 as well as the performance of the individual validation tests apply to both the individual forward and backward filter run. As mentioned earlier the integer ambiguities on both runs are estimated independently from each other, i.e. no integers estimated in the forward run are allocated a-priori in the backward run. For the entire data arc processed, no differences were found in an afterwards comparison between the integer DD ambiguities allocated to the filter during both runs. It is encouraging to see such a result, since it indicates a good consistency between the individual estimation processes. However, it must also be mentioned that such an additional test can only be used to identify discrepancies between both solutions, but cannot provide conclusive evidence about which integer ambiguity would be (more) in error in case a discrepancy is detected.

The smoothed relative position solutions from the EKF whilst fixing the ambiguities have of course also been compared to the KBR measurements. Similar to the EKF float solution the KBR comparison time series of (top down) DOY 195, 217, 222 and 258 are presented in Fig. 4.12. It can directly be seen that fixing the ambiguities, and incorporating them accordingly into the filter, dramatically improves the precision of the relative position solution, compared to the ambiguity float case. In addition, it is clearly visible that the 'once per revolution' periodicity, encountered in the EKF float solution, has (largely) disappeared. This is due to the fact that the 'integer corrected' carrier phase observations dominate the solution due to the strength of this measurement type. The pattern that has now become visible is thus mostly the result of unmodeled systematic effects, such as multipath, present in the GPS carrier phase observation data.

The best overall precision for the entire data arc is obtained for DOY 258 where the standard deviation of the KBR comparison is only 0.63 mm. It is furthermore encouraging to see that the worst case scenario for the entire data arc, DOY 217, has a precision of 1.62 mm, largely due to one outlying period between 15:00 and 16:00 that day. It is unclear if this is related to an incorrectly resolved ambiguity since the corresponding kinematic solution (Fig.4.13) shows no such traces (like the ones earlier depicted in Fig. 4.2 between 10:00 and 11:30) and did not reject any observations for that time. In the kinematic solution it can be observed that around this period there are some gaps in the KBR comparison, meaning that not enough integer ambiguities are available to construct the SPP solution. The outlying period in the reduced dynamic ambiguity fixed solution is most likely related to this fact. However, since such a 'dramatic' situation only occurred twice during the entire data arc (once more on DOY 231, as can be seen from the standard deviation series for the entire data arc in Fig. 4.14) no further effort has been put into resolving the exact nature of this discrepancy. Furthermore, it can be seen in the KBR fit of DOY 222 that also in the ambiguity fixed case the relative position solution

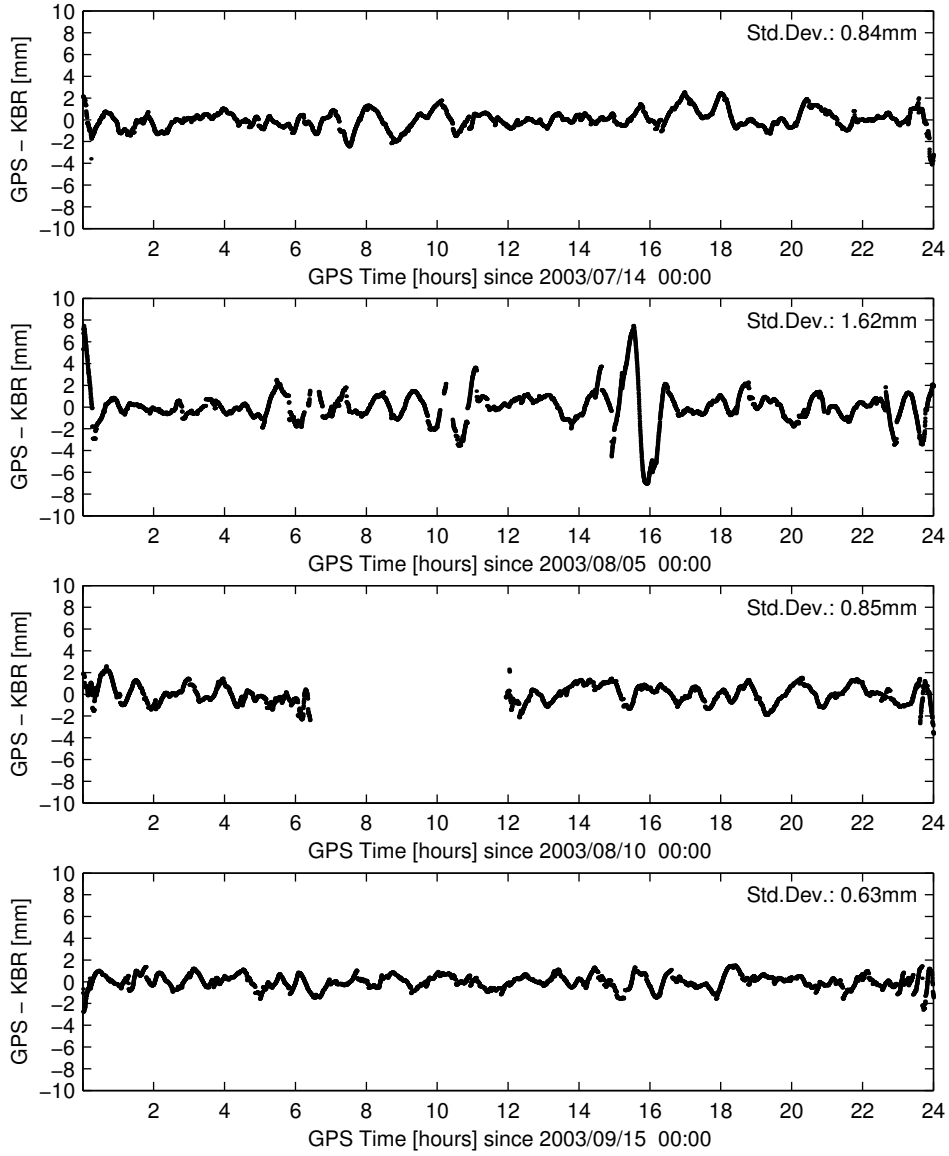

Figure 4.12 Time series of the KBR comparison residuals of the GRACE relative position solution. The relative position is obtained from the EKF when fixing DD ambiguities to integer values. Shown are (top down) DOY 195 (average situation), DOY 217 (worst case), DOY 222 (extended data gap) and DOY 258 (best overall fit).

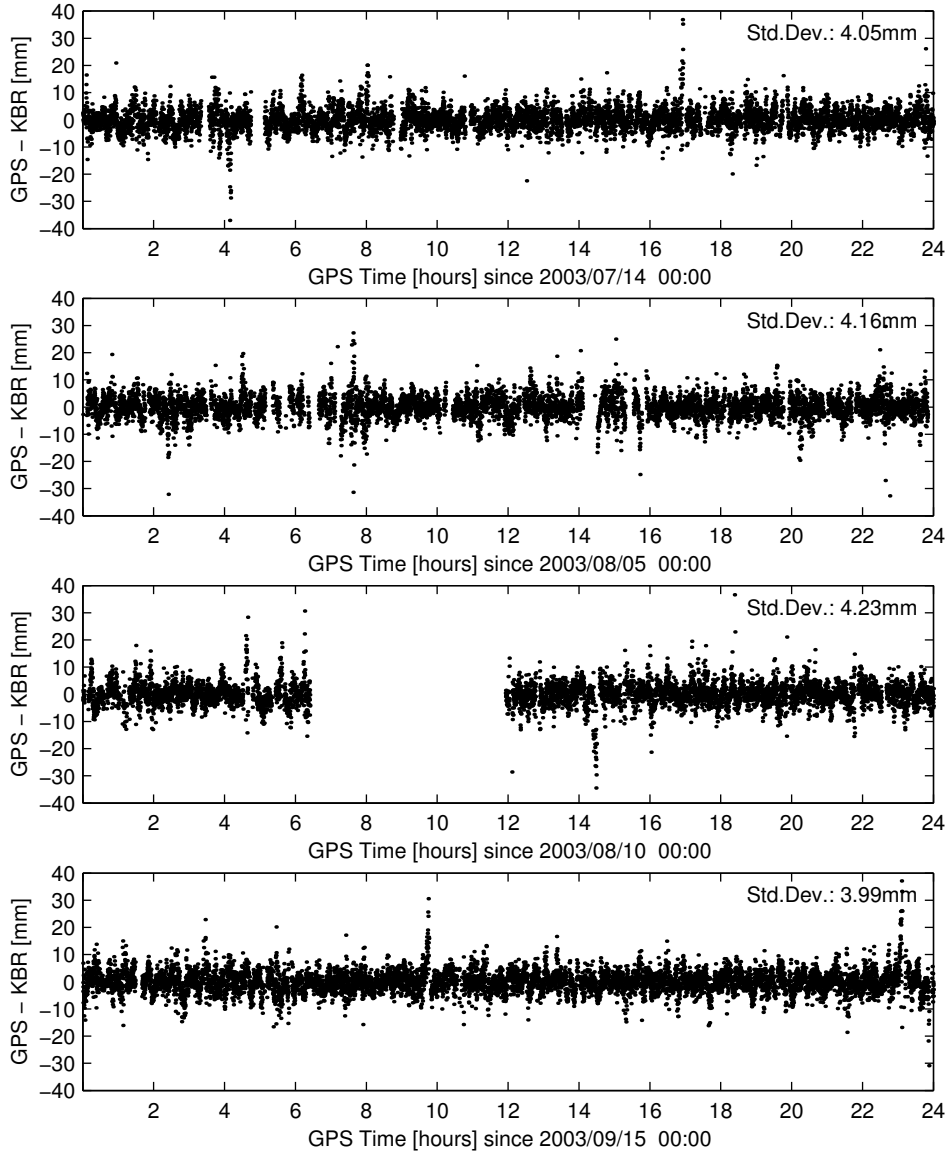

Figure 4.13 Time series of the KBR comparison residuals of the GRACE relative position solution. The relative position is obtained from the kinematic carrier phase data only SPP process, using the fixed ambiguities from the EKF. Only solutions with a PDOP value of 7 or lower are displayed and used. Shown are (top down) DOY 195, DOY 217, DOY 222 and DOY 258.

is propagated over extended data gaps without difficulty. The relative position errors in either the forward and backward solution are on the same level as for the ambiguity float scenario (15 cm compared to the KBR), and do not show up in the smoothed solution. This is due to the fact that either one of the solutions no longer has any integer ambiguities allocated and thus has a significantly lower weight in the smoothing process from eqn. 4.46. This same analogy can be applied to the 'ramps' that occur at the beginning and the end of a daily data arc, e.g. the beginning of DOY 217 or the end of DOY 195. Here the covariance of either the forward or backward solution has not yet any integers allocated and is not fully converged. A solution to this can be provided by extending the length of the daily data arc with e.g. 1 hour on each side, but only use the middle 24-hours for the KBR comparison. A similar, but smaller, effect can also be seen around the GPS phase breaks at 6:15 and 10:15 during DOY 217. Unfortunately, no simple solution, like the data arc extension, can be provided for such cases. It can furthermore be seen that the KBR comparison time series experience several smaller and larger jumps, e.g. DOY 217 0:30 or DOY 258 1:45 and 5:00, not coinciding with GPS or KBR phase breaks. These jumps are related to the sudden allocation of multiple integer ambiguities in either the forward or backward run from a state where not many, or no, integer ambiguities are already present in the filter. Aside from the fact that the kinematic solution (depicted in Fig. 4.13 for again (top down) DOY 195, 217, 222 and 258, where only relative position solutions with a PDOP of 7 or lower are included) is much noisier, correlations in the overall pattern of systematic carrier phase data errors with the EKF fixed solution can be observed and is expected. However, it can also be clearly seen in the KBR comparison time series of both the kinematic and EKF fixed solution, that the relative S/C dynamics offer protection against some systematic position outliers at e.g. DOY 195 4:00 and 17:00, DOY 222 14:30, or DOY 258 9:45 and 23:00.

The KBR fit standard deviations for the entire 101 day data arc for both the kinematic (bottom) and EKF fixed (top) solution are given in Fig. 4.14. Despite a few, relatively small, outliers in each of the solutions, the overall precision of the (along-track component of) the relative position in the kinematic case is 4.19 mm and in case of the EKF fixed solution even 0.91 mm. Compared to the relative position constructed from the individual GRACE POD solutions or the EKF float solution a precision improvement of more than respectively a factor 17 and 8 is achieved. For truly high precision post-facto relative positioning of formation flying S/C it is thus of the utmost importance to correctly resolve and use the integer carrier phase ambiguities.

As mentioned earlier in chapter 1 there has so far been only one other study, by *Svehla and Rothacher* [2004*a*], focussing on high precise post-facto reconstruction of the relative position between both GRACE satellites. In this study a slightly larger, but fully overlapping, data arc (2003, DOY 182 to 302) has been processed using the Bernese software package. As mentioned in section 4.2.3 the specific processing strategy and details are not published, but it is known that a batch LSQ estimation method has been used based on the absolute S/C dynamics and not the relative

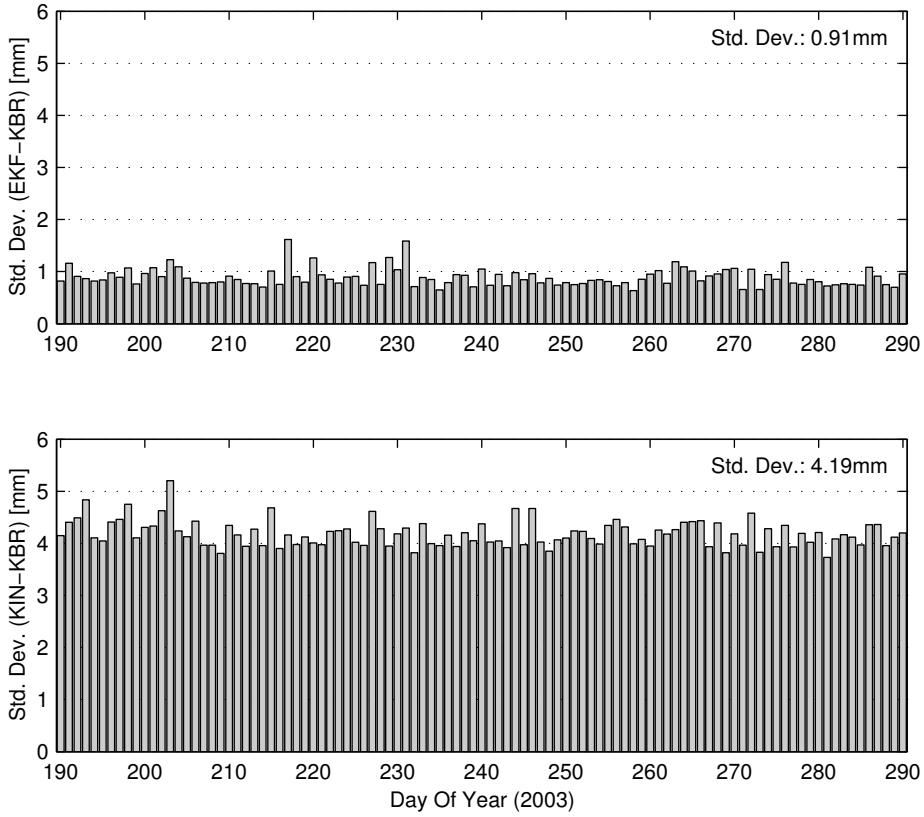

Figure 4.14 Daily standard deviations of the GRACE relative position, constructed by processing SD code and carrier phase observations with fixed ambiguities, when compared to the KBR measurements. The top figure shows the reduced dynamic solution from the EKF, the bottom one the kinematic SPP position solution constructed using carrier phase data in conjunction with the integer DD ambiguities from the EKF.

formulation as presented in section 4.2.3. Furthermore, a DD parametrization is used, where the wide-lane and narrow-lane ambiguities are estimated separately, in a similar fashion briefly described at the end of section 4.1.1. Out of an average daily number of 416 DD ambiguity pairs for the entire data arc presented, 98.4% of the wide-lane and 92.8% of the narrow-lane ambiguities are stated to be resolved, which is in good agreement with this research, where 91% out of 400 pairs (that are present for more than 300 s) are resolved. The resulting reduced dynamic (batch LSQ) ambiguity fixed relative position solution has also been compared to the KBR in a similar way as performed here. The best precision found by *Svehla and Rothacher* [2004*a*] is about 2.8 mm, which is even higher than the worst case presented in this dissertation (1.62 mm). Furthermore, for the period between DOY

210 and 235, several outliers in the KBR comparison standard deviations, varying between 12 and 16 mm, were found for the reduced dynamic (batch LSQ) ambiguity fixed solution. This might indicate that an EKF, or another recursive estimation method, is more suitable for an application of this nature.

4.4.8 Relative position comparisons

As mentioned in the first chapter, many studies in the field of relative positioning of formation flying spacecraft are based on hardware-in-the-loop or software simulations. In both cases the actual accuracy of the resulting relative position estimates can be computed since the reference trajectories of the S/C concerned are exactly known. For this research such values can unfortunately not be computed. It has however already been shown in the previous subsections that the true precision of the along-track component of the relative position between the GRACE S/C could be computed using the KBR measurements. Aside from the fact that this already is a very unique aspect for a real-world spaceborne scenario, information about the precision of the other components is unfortunately not obtained in this way. However, an indicative measure of these quantities can be obtained by comparing the different filter solutions, discussed in the previous subsections. This comparison is performed in exactly the same way as for the POD scenarios, described in section 3.6.4, with the only difference that it now concerns relative position solutions instead. For each of the comparisons the statistical mean and RMS of the data series are computed. The EKF ambiguity fixed solution has been selected as reference for the comparisons, since it has been shown to be the most precise when compared to the KBR measurements. It is therefore also assumed to be the most accurate solution that has been created. The first comparison concerns the kinematic fixed solution minus the EKF fixed solution, for which the daily mean and RMS values over the entire data arc are depicted in Fig. 4.15 and Fig. 4.16 respectively. The second comparison concerns the EKF float minus the EKF fixed solution, for which the daily mean and RMS values over the entire data arc are depicted in Fig. 4.17 and Fig. 4.18 respectively. It must be mentioned that the EKF fixed solution is expected to be (highly) correlated with both solutions, since not only the same GPS data has been used, but also, in case of the float solution, the same estimation method and settings, or, in case of the kinematic solution the same integer ambiguities. Therefore the results of this comparison should even be more carefully interpreted than for the POD scenarios. A more independent measure for consistency would therefore also be the comparison of the kinematic solution with the EKF float one, which has also been performed. The results obtained were found to be in perfect agreement with the other comparisons and are therefore not depicted here.

As can be seen in Fig. 4.15 and Fig. 4.16 a fairly large but seemingly constant mean and RMS are present in the radial component of the comparison between the kinematic and the EKF fixed solution. Since it is commonly known that the radial component of the purely kinematic case is not as well determined as the

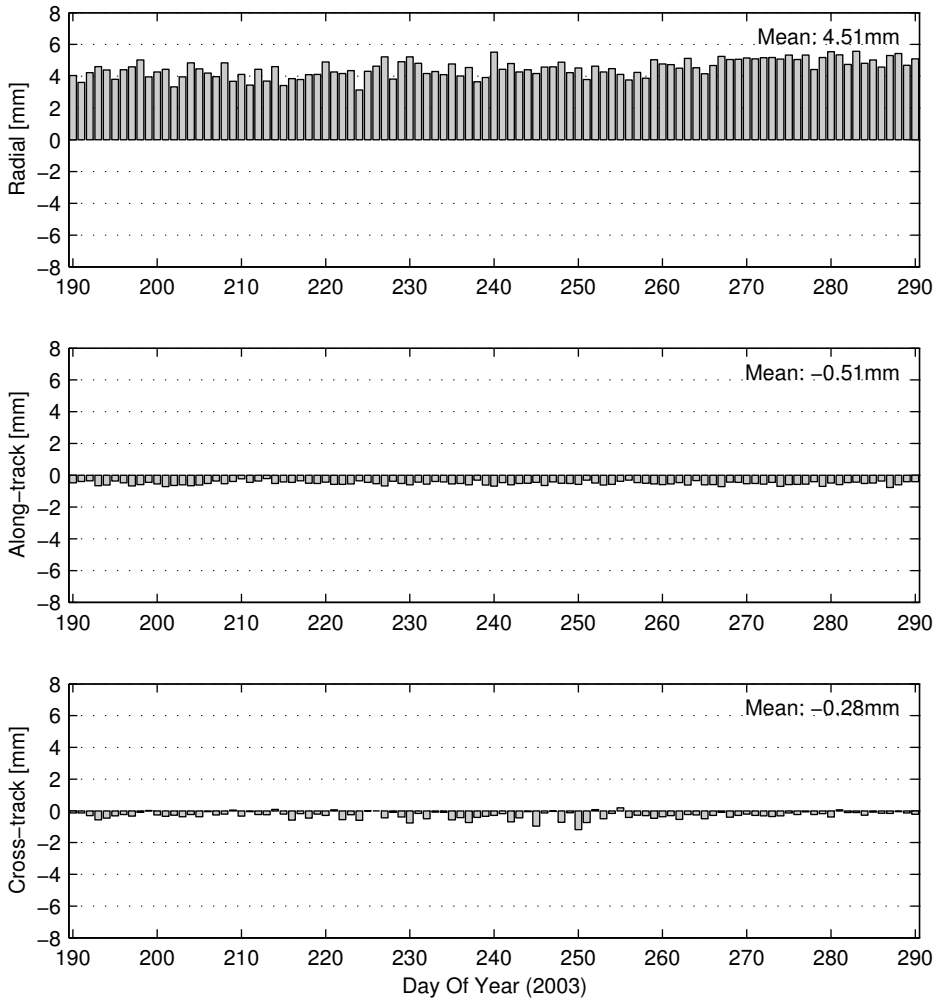

Figure 4.15 Daily mean offset in radial, along-track and cross-track direction between the kinematic and reduced dynamic relative position solution, both constructed using fixed integer ambiguities.

other components, due to the GPS viewing geometry, it is logical to assume that this can mainly be contributed to the kinematic solution. The along-track and cross-track component show an expected behavioral pattern as well, although it remains unclear if the mean values, again seemingly constant, can be fully or largely attributed to the kinematic solution. For example, the along-track component is the one worst determined for a reduced-dynamic solution (as can also be seen in Fig. 4.17 and Fig. 4.18) and it is not claimed that the EKF fixed solution, serving

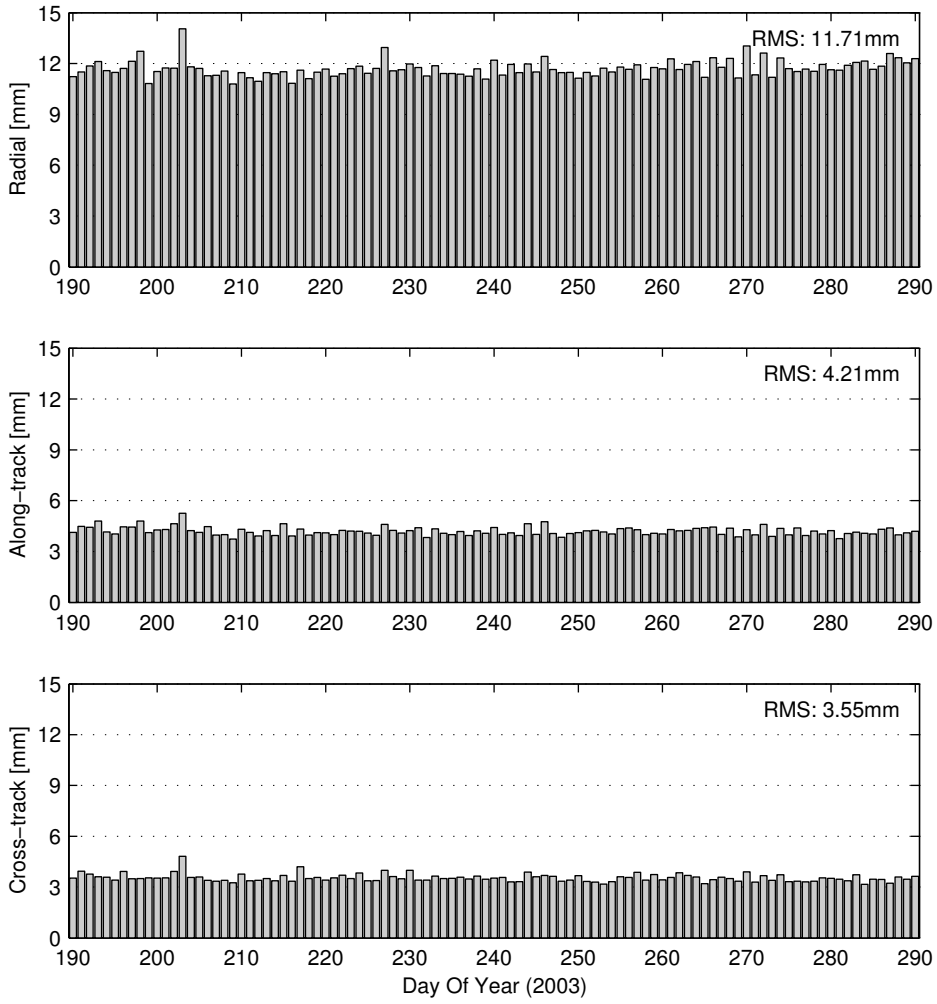

Figure 4.16 Daily RMS values in radial, along-track and cross-track direction of the comparison between the kinematic and reduced dynamic relative position solution, both constructed using fixed integer ambiguities.

as the reference for the comparison, is bias free. Correlations between the solutions can be substantiated for the along-track component. When propagating the overall precision of the KBR comparisons of both solutions, obtained from Fig. 4.14, the standard deviation (precision) of the along-track component should more or less be $\sqrt{4.19^2 + 0.91^2} = 4.28$ mm. For the current relative position comparison, the standard deviation however is $\sqrt{4.21^2 - (-0.51)^2} = 4.18$ mm. This indicates that only a small correlation is present between the along-track components of

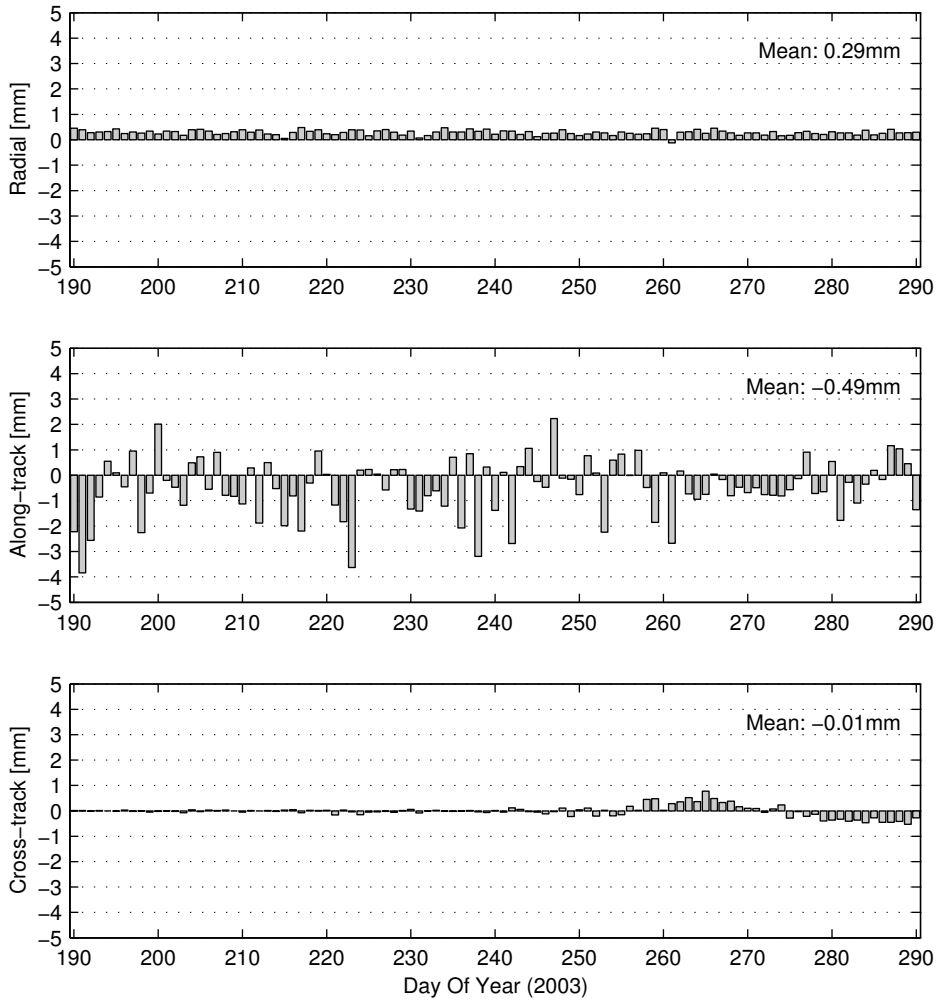

Figure 4.17 Daily mean offset in radial, along-track and cross-track direction between the float and fixed ambiguity reduced dynamic (EKF) relative position solutions.

both solutions. It is assumed that similar small correlations are present in the other components. Therefore, the RMS values presented for the radial and cross-track component of this comparison, 11.71 mm and 3.55 mm respectively, are only indications, but most likely very good ones, for the precision (standard deviation) of the kinematic relative position solution in these directions.

When looking at the comparison between the EKF float and fixed solution the mean and RMS values of all components describe an expected behavioral pattern as well, i.e. a high RMS for the along-track direction, and lower ones for the radial

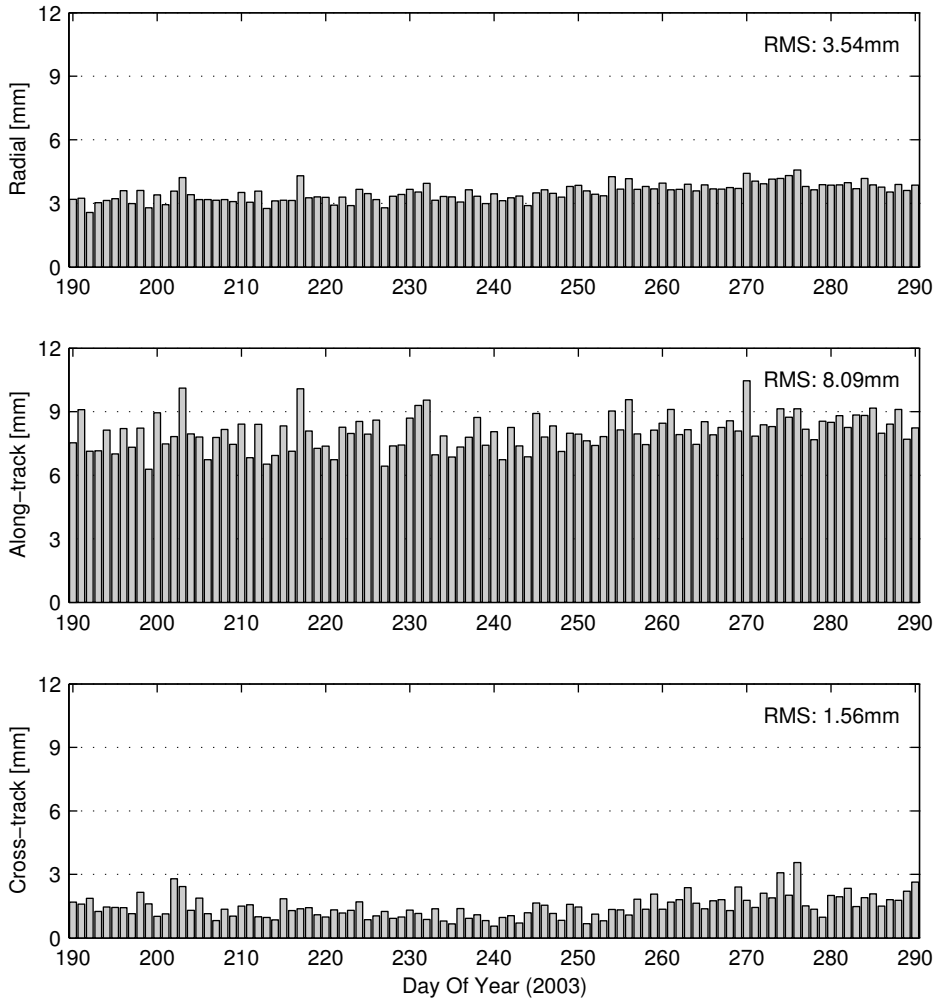

Figure 4.18 Daily RMS values in radial, along-track and cross-track direction of the comparison between the float and fixed ambiguity reduced dynamic (EKF) relative position solutions.

and cross-track components. In the same way as done for the previous comparison the correlation in the along-track component of both solutions can be substantiated. From the KBR comparisons (Fig. 4.14 and Fig. 4.10) it follows that the along-track standard deviation of the relative position comparison should be 7.91 mm. This one however reads 8.07 mm, again indicating a, this time positive, correlation. Similar small correlations are assumed to be present in the other components of the comparison. Therefore, similar to the kinematic comparison, the RMS values presented

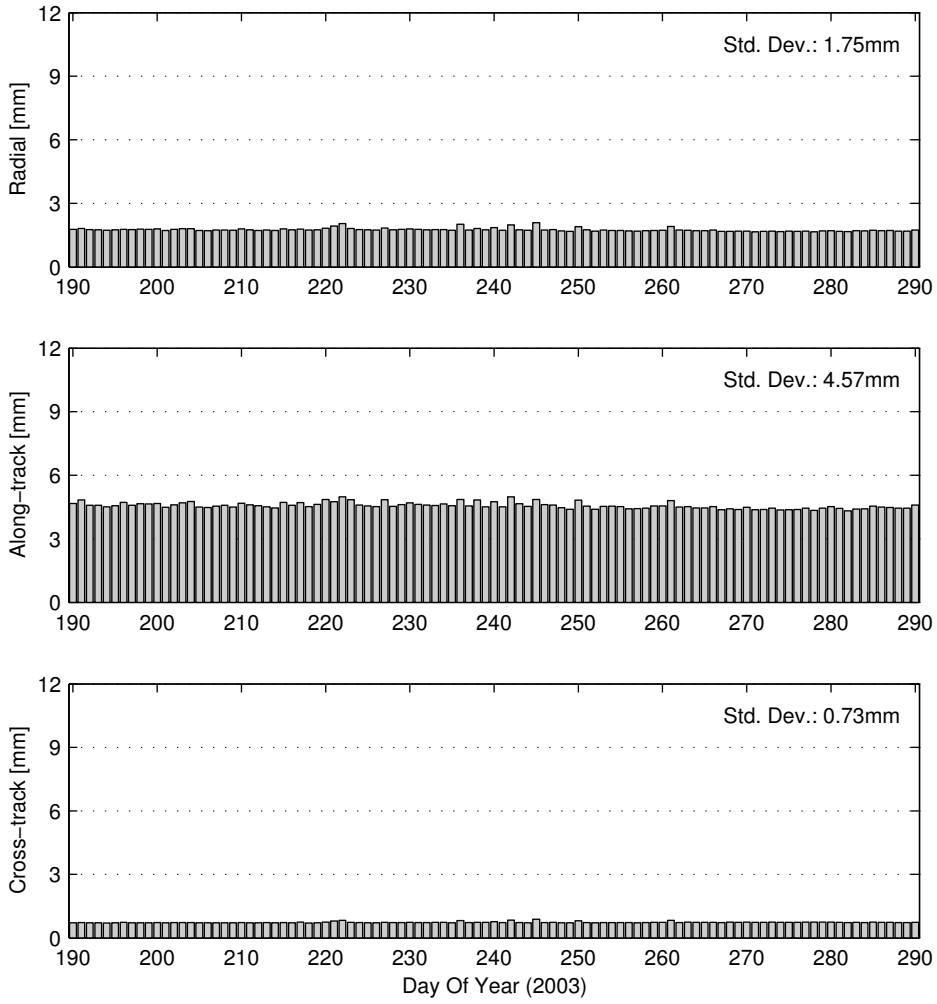

Figure 4.19 Daily formal variances of the extended Kalman filter in radial, along-track and cross-track direction, in the comparison between the float and fixed ambiguity relative position solutions.

for the radial and cross-track component of the EKF float comparison, 3.54 mm and 1.56 mm respectively, are only indications, but most likely very good ones, for the precision (standard deviation) of the EKF float relative position solution. As can be seen these RMS values are much lower than for the kinematic case, which is normal since for a reduced-dynamic solution the along-track component is in general the least precise one. Some evidence for this is provided by looking at the formal filter precision (variances) for the relative position comparison at hand, depicted in

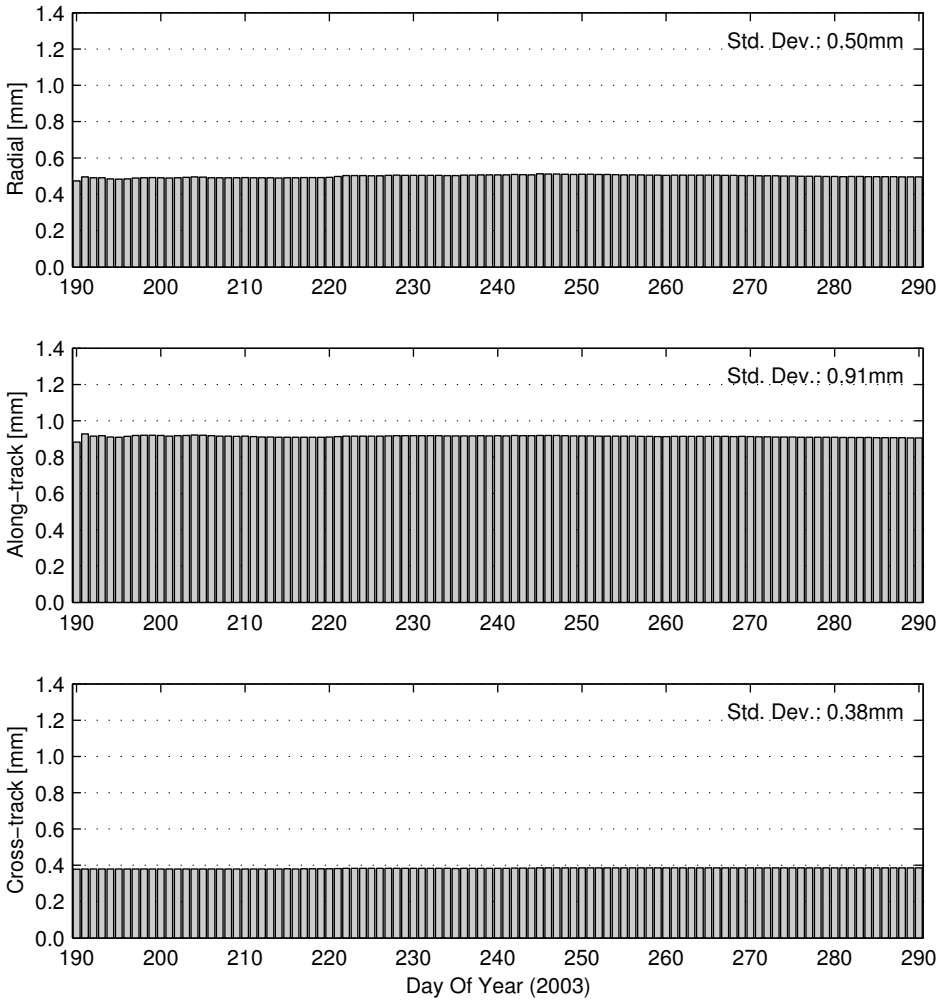

Figure 4.20 Daily formal variances of the extended Kalman filter in radial, along-track and cross-track direction, when constructing the fixed ambiguity relative position solution.

Fig. 4.19. This figure is constructed by properly propagating the filter covariances from the individual solutions in the comparison. Despite the fact that the formal precision is too optimistic by more or less a factor 2, the overall ratios between the different directions is more or less identical as for the RMS values derived from the comparison.

Although the KBR comparisons presented in the previous subsections depict the kinematic solution as the one more precise than the EKF float solution, the relative position comparisons show a different picture. As expected the radial and

cross-track component of the EKF float solution have shown to be more precise than the ones from the kinematic solution. The 3-dimensional float solution is therefore also expected to be more precise, and more accurate, than the kinematic one. This could not be concluded based on the KBR comparisons alone. Besides being more precise, the float solution also has the benefit of being continuous and smooth, whereas the kinematic one is only available at discrete epochs. The mean values of the float minus fixed comparison, depicted in Fig. 4.17, can also be explained to some extent. The fluctuation of the mean of the along-track component can be fully contributed to the EKF float solution, since it was not present in the mean of the kinematic comparison (Fig. 4.15). This is mainly caused by day-to-day differences in the differential atmospheric drag. It was already shown in Fig. 4.6 that the empirical accelerations between the float and fixed solution are slightly different. In case of the float solution not all force model discrepancies seemed to be properly captured by them, meaning that these errors are absorbed in the position. The fixed solution however is constructed from a much stronger measurement type and is thus able to keep the discrepancies out of the position components. An interesting phenomenon is again visible in the cross-track mean, where at the end of the data arc a periodic effect starts to show up, similar to the POD comparison. This is probably again related to solar radiation pressure mismodeling, and can most likely be fully attributed to the float solution since it did not show in the kinematic comparison. The reason it did not show in the fixed solution is again the fact that the measurements used in this case are much stronger, and thus dominate the solution. The seemingly constant radial offset can have several reasons, the most likely ones are that, again, the dynamics are more dominant in the float solution, or that there is a different antenna phase center for the pseudorange observations, which still contribute to the float solution to some extent.

Unfortunately, the just discussed comparisons do not reveal any indication about the precision of the EKF fixed solution serving as the reference. However, the formal filter variances of the radial, along-track and cross-track component of this solution are given in Fig. 4.20. Although it is observed that the true precision from the KBR validation (Fig. 4.14) fluctuates over the data arc and the formal precision does not, the overall values (0.91 mm) are in perfect agreement. This mostly indicates that the a-priori weights for the GPS (carrier phase) observations as well as the dynamic constraints are realistically chosen. Despite the fact that it is tempting to believe that the overall precision in the radial and cross-track component are thus also similar to the formal ones, 0.50 mm and 0.38 mm respectively, no substantial evidence for such a claim can be provided. The only thing pointing in such a direction would be the fact that a similar ratio for the individual component precision was also found for the EKF float solution, based on the EKF float minus EKF fixed solution comparison. If any statements about the precision of the radial and cross-track component of the fixed solution should be made, it is more realistic to assume a similar precision as found for the along-track direction from the KBR fit, meaning 0.91 mm for both the radial and cross-track component as well. This would result in a 3-dimensional precision of 1.56 mm. Unfortunately, potential biases in

the solution remain undetected and cannot be quantified. An example source of a constant bias in any component would be a shift or mismodeling in either one, or both, of the GRACE GPS receiver antenna phase center offsets. Such a shift would also remain undetected in the solution comparison performed here due to the fact that each solution is constructed using the same offsets. It is possible that such biases are larger than the precision. It is however unlikely that they are too large, without quantifying this statement, otherwise the resolution of the integer DD carrier phase ambiguities might not have been so successful, as validated with the KBR.

4.5 Some words on ...

This section contains an overview of some additional tests that have been carried out using the FRNS tool. First, the impact of higher systematic errors in the GRACE data on the relative position is analyzed, followed by a presentation of the improvements that can be obtained when using the C/A code and, especially, the accompanying carrier phase observable instead of the P_1 code and carrier phase. The section is concluded with a brief analysis on using some different ambiguity resolution approaches.

4.5.1 ... the effects of higher systematic or multipath errors

The GPS data used to create the results presented in section 4.4 was already subject to a mild form of systematic or multipath errors as depicted and discussed in section 2.6.2. In this last section it was also demonstrated that once the GPS occultation antenna on GRACE B was activated for testing purposes, higher systematic errors on the pseudorange data from the GPS POD antenna were encountered. For the carrier phase data this can so far only be suspected. For relative positioning applications the effects of higher systematic errors in the GPS data can contribute to the baseline solution on two levels. First of all, high errors in the pseudorange data could lead to incorrectly resolved integer DD ambiguities, which would then degrade the relative position solution accuracy. Second, if the integer ambiguities can be resolved correctly, high systematic errors in the carrier phase data could prevent a mm-level precision for the resulting relative position solution.

In order to assess the impact of higher systematic errors in the GPS data on the relative position solution, the GPS data collected during the occultation antenna test on GRACE B in July 2004 have been processed by the EKF, and the resulting baseline solutions compared to the KBR. The settings used for this test are the same as discussed in section 4.4.1. Only the ambiguity fixed case is considered, since the effects on ambiguity resolution and mm-level precision of the relative position solution are assessed. The KBR residuals of the reduced dynamic ambiguity fixed solution for 2004 DOY 209 through 212 (top down) are given in Fig. 4.21. The period where the GPS occultation antenna on GRACE B was activated, more specifically from July 28 (DOY 210) 06:05 until July 29 (DOY 211) 07:10, is marked

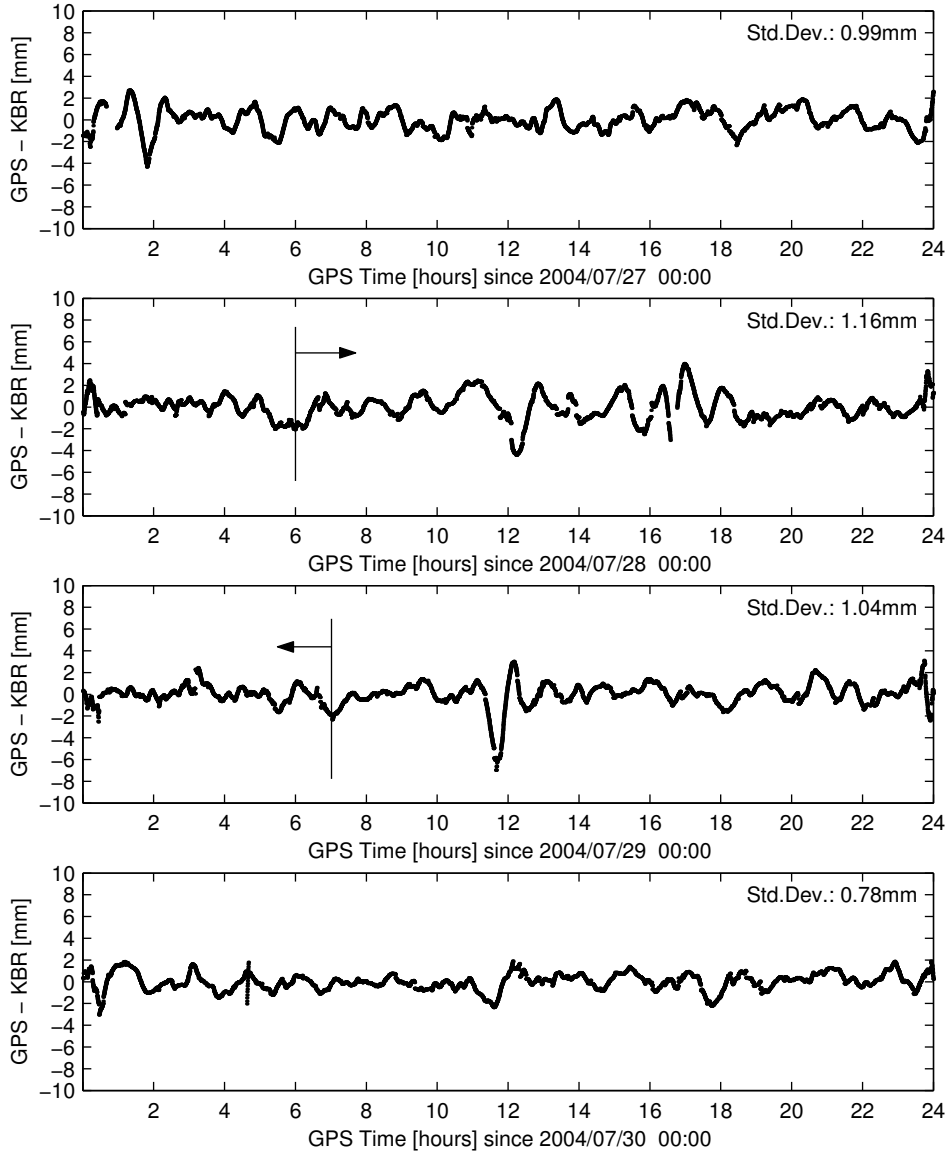

Figure 4.21 Time series of the KBR comparison residuals of the GRACE relative position solution. The relative position is obtained from the EKF when fixing ambiguities to integer values. Shown are (top down) DOY 209, DOY 210, DOY 211 and DOY 212 of 2004. The period over which the GPS occultation antenna was activated (DOY 210 and 211) has been marked.

here. As can be seen in this figure no significant changes are encountered in the KBR residuals during the activation, meaning that the relative position solution seems to remain unaffected. It must be noted that the higher residuals between 12:00 and 18:00 on DOY 210 were found to be related to 2 small GPS, and KBR, data gaps after which the filter no longer has any fixed integer ambiguities allocated. Situations like this were also encountered during the 2003 data arc analyzed for this research (section 4.4.7, e.g. DOY 217 in Fig. 4.12) and have nothing to do with higher systematic errors in the GPS data. In addition, a similar percentage of DD ambiguities (82.3% and 85.5% for DOY 210 and 211 respectively) could be fixed as under other circumstances. Furthermore, the kinematic solution, not depicted here, also shows no evidence of higher systematic effects in the carrier phase data. Although clearly a longer data arc with such higher systematic errors, as the earlier mentioned December 2004 period (section 2.6.2), should be analyzed to draw any conclusions, the relative position solution as well as the (quality of the) integer ambiguity resolution scheme, seem to remain unaffected.

4.5.2 ... using the C/A code and carrier phase observations

So far, all relative position solutions presented in section 4.4 were created using the P_1-code and accompanying L_1-carrier phase observable. It was already mentioned in chapter 2 that the BlackJack GPS receiver onboard the GRACE S/C supports and gives out all three code and accompanying carrier phase observations. It was also shown in Fig. 2.6 that the noise of the C/A code observable is notably lower than the noise on P_1 under all circumstances tested. Furthermore, the carrier phase observable, L_A, accompanying the C/A code was used for visualizing the assumed upper limit for the noise on the L_1 observable, depicted in Fig. 2.7. In order to verify if the noise of the L_A observable is indeed lower, and to see if any further improvements in the relative position solution can be obtained, it has been used by the FRNS tool for a brief test, together with the accompanying C/A code observable. The overall settings chosen for this test are identical as lined out in section 4.4.1. Only the ambiguity fixed case is considered here. The test has been carried out over the same days for which the KBR comparison time series were given earlier, DOY 195, 217, 222 and 258. No significant changes were found in the reduced dynamic solution, where the standard deviation of the KBR comparison time series changes with no more than 1-2%. A very notable and significant improvement however was encountered in the kinematic SPP solution, constructed using the ionosphere free carrier phase observable derived from L_A and L_2, which is depicted in Fig. 4.22. Here, again only solutions with a PDOP value of 7 or lower are included. It can immediately be seen that the noise on the L_A observable is indeed (significantly) lower compared to the one on L_1 (Fig. 4.13). The standard deviation of the KBR comparison is more than 25% lower, corresponding to more than 1 mm. A similar result is found for the other components of the kinematic solution, when comparing the reduced dynamic and kinematic relative position solutions in the same way as described in section 4.4.8. The biases between

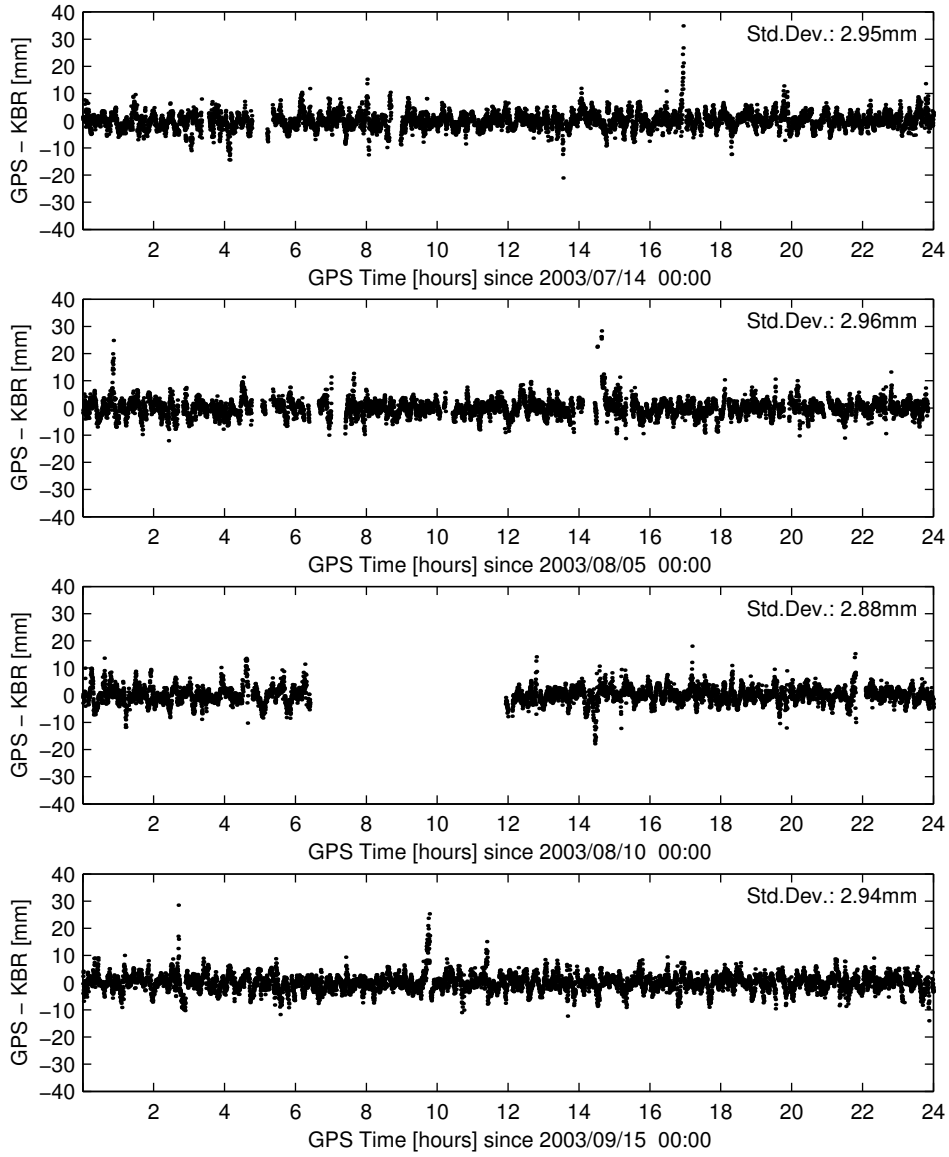

Figure 4.22 Time series of the KBR comparison residuals of the GRACE relative position solution. The relative position is obtained from the kinematic SPP process using the ionosphere free carrier phase observable constructed from L_A and L_2, complemented with the integer ambiguities from the EKF. Only solutions with a PDOP value of 7 or lower are displayed and used. Shown are the results for (top down) DOY 195, DOY 217, DOY 222 and DOY 258.

both solutions seem to remain unchanged, but the RMS of the residuals in radial, along-track and cross-track direction respectively become around 9.5 mm, 3.7 mm and 3.1 mm, indicating that the overall precision of the kinematic solution increased. Furthermore, a pattern of systematic errors in the data can clearly be observed in Fig. 4.22, which, when closely examining Fig. 4.13, can also be discovered if the L_1 observable is used. It is thus logical that the reduced dynamic solution does not alter dramatically if only the noise level of the data lowers, since the EKF is not very susceptible to such a change.

4.5.3 ... testing different ambiguity resolution approaches

It was already mentioned earlier that without applying the integer validation tests based on screening the individual ambiguity residuals (eqn. 4.11 and eqn. 4.12) incorrect integer values were incorporated in the EKF, sometimes leading to divergence of the filter solution. In this section a brief demonstration of a (non-diverging) result from the EKF is given when using only the success rate and the integer (eqn 4.7) and discrimination (eqn. 4.8) test for ambiguity validation. This is done since many software packages apparently use such a validation scheme as conclusive ([*Verhagen*, 2004*b*]; [*Leick*, 1994]). In addition, the results of testing another ambiguity validation and handling concept are also briefly presented. Here, the integer ambiguities are not incorporated in the EKF, but resolved every epoch and only used on that instance.

Both concepts were tested on a shorter (sub) data arc, 2003 DOY 210 to 220, initially used for development of the final FRNS tool [*Kroes et al.*, 2005]. Here it was found that when using only the first 3 integer validation test, without screening the individual ambiguity residuals and furthermore applying the same settings as given in Table 4.1, this leads to complete divergence on DOY 214 and 217. Therefore, a more conservative value for the (more critical) discrimination test has been selected, $k_{S/B} = 5.0$, still allowing incorrectly resolved integer ambiguities to be incorporated in the filter, but preventing divergence for any day in the short data arc at hand. The results of the relative position compared to the KBR for DOY 213 are depicted in Fig. 4.23. The top plot shows the situation where the entire validation scheme, including the individual ambiguity residual screening tests, is applied. The one below this shows the situation with the 'incomplete' validation procedure, just discussed. As can be seen some incorrectly resolved ambiguities have been incorporated, leading to erroneous relative position fixes. A comparison between both solutions learns that the effect of the incorrectly resolved, but incorporated, integer values is most dominantly present in the along-track direction under all circumstances tested, which is most likely related to the fact that this direction has the highest uncertainty in the filter. The position errors in the radial and cross-track components were found to be smaller by at least a factor 2. It must be mentioned that in this case the incorrectly resolved ambiguities were rejected by the SPP process of the kinematic solution. It has therefore also been tried to incorporate the kinematic SPP solution as an additional 'test' in the integer ambiguity

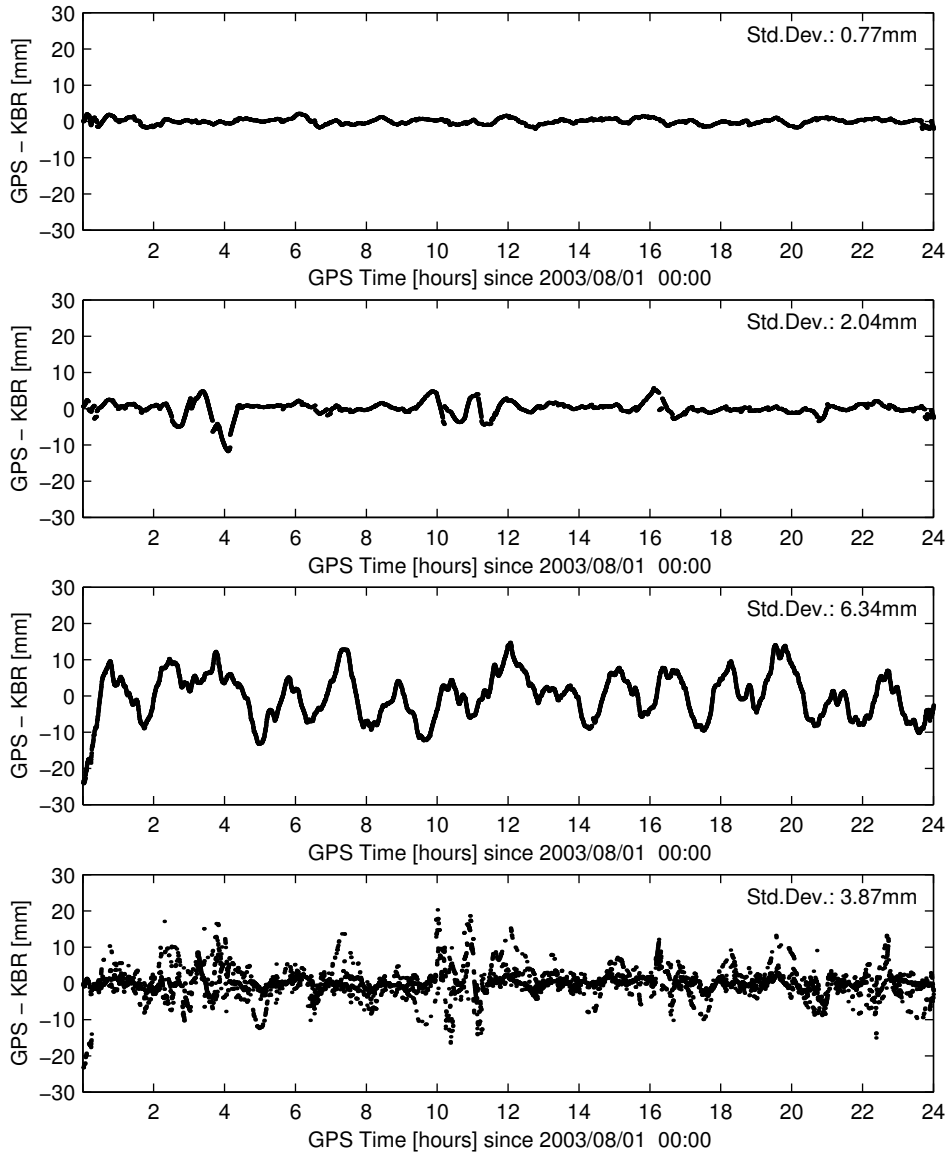

Figure 4.23 Time series of the KBR comparison residuals of the GRACE relative position solution. Shown are the results of different ambiguity resolution and fixing concepts for DOY 213. Top-down are given the solution with the overall integer validation scheme applied, the solution with an integer validation scheme not screening the individual ambiguity residuals, the float solution, and the solution with 'locally' fixed integers.

validation scheme (also in the complete validation procedure discussed in section 4.1.2). Although this seems attractive at first, it did not work for the following reasons. First of all, there are not always 4 integer DD ambiguities present, meaning that a (redundant) kinematic solution cannot always be constructed. This in contrast to the other tests in the validation scheme that can be executed under all circumstances. Second, an incorrect integer ambiguity is sometimes first detected after it has already been incorporated into the filter. Finally, the SPP process does not always seem to properly 'identify' the integer ambiguity that has been resolved incorrectly, and can also reject another one instead.

An alternative approach to handling the integer ambiguities is to estimate them every epoch and subsequently use them only once to improve the relative position solution locally, without incorporating them as described in section 4.3. The filter state and covariance are thus kept filled with float values only, which prevents divergence of the solution under all circumstances tested. The third plot from the top in Fig. 4.23 shows the relative position constructed using solely float ambiguities compared to the KBR for DOY 213. The bottom plot shows the solution where the filter gets local updates from integer ambiguities. The only test that is carried out here is to see if the success rate is high enough (99.0%), which can be seen by the fact that sometimes the float solution is used. Still, incorrectly resolved integers can be identified between 10:00 and 11:30, the same also present in Fig. 4.2. It can also be argued to always use the estimated integer ambiguities in this case without applying any kind of test. However, when lowering the limit of the success rate to 90% it was found that outliers of 10 cm were already encountered in the KBR comparison. Therefore the 99.0% success rate limit remained in effect. As can be seen in Fig. 4.23 the resulting solution is neither continuous nor 100% discrete in nature. Its precision however, when compared to the EKF fixed solution, is somewhere between the EKF fixed and EKF float solution. This might be an attractive alternative for some applications where a possibility of precise validation of the solution, presented by the KBR in this case, is not available and incorrectly resolved ambiguities, leading to a divergence of the solution, can thus not always be detected.

Chapter 5
Conclusions and outlook

The primary objective of this research work was to develop, implement, test and validate a method for high precision post-facto relative positioning of formation flying spacecraft. Based on the results from the previous chapter it can be concluded that this objective has been fulfilled. When tested using GRACE GPS observation data, the developed extended Kalman filter has shown to provide relative position solutions with (sub-)mm precision (1-dimensional), after validation with the GRACE KBR measurements. For the 101-day GRACE data arc processed, an overall relative position precision of 0.91 mm was found from the KBR comparisons. Although this represents only the precision of, more or less, the along-track component, it is believed that the precision of the other components (radial and cross-track) is of the same order of magnitude (section 4.4.8). It is again emphasized that the KBR validation does not provide conclusive information about the accuracy of the solution. Constant biases are namely absorbed in the calibration process (section 4.4.4).

However, in order to arrive at the high precision solution it can be concluded that a few prerequisites have to be met. These are briefly mentioned here, and discussed in more detail in the following. First, and most important of all, the integer nature of the double difference carrier phase ambiguities has to be exploited. Once again, this has proven to be the key to precise relative (spacecraft) positioning. Second, a reduced dynamic processing strategy should be used. Aside from the fact that this results in a smooth and (semi-)continuous solution with a much higher precision (3-dimensional) than for the kinematic ambiguity fixed case (section 4.4.8, Fig. 4.16), the inclusion of the spacecraft dynamics have shown to provide the additional robustness required for reliable integer ambiguity resolution. Furthermore, the GPS observation data used has to be of a good quality, and it is therefore recommended to use dual frequency geodetic grade GPS receivers for applications of this nature. Closely related to this fact is the facilitation of a robust GPS observation data editing procedure. This is of great importance since undetected cycle slips, or outliers in the pseudorange data, can seriously deteriorate the resulting solution. In addition, precise a-priori knowledge of the orbit of one of the spacecraft, serving

as the reference, is required for relative positioning. Therefore, and this is the final prerequisite, a strict processing scheme is to be followed, involving the generation of a precise orbit for each of the individual (GRACE) satellites.

Regarding integer ambiguity resolution itself, it can be concluded that the sequential or recursive processing methodologies have shown to be more flexible in dealing with this problem. They allow on-the-fly resolution and incorporation of the integer ambiguities, directly strengthening the relative position solution. This however comes with the associated risk of divergence of the filter solution as soon as incorrectly resolved integers are still allocated. The batch LSQ estimation methods do not have this last problem. Practical tests with the kinematic batch LSQ on the other hand demonstrated unacceptably long search times when using the LAMBDA method. Although not verified, it is not expected that the reduced dynamic batch LSQ behaves any different in this respect. The large numbers of ambiguity pairs combined with the short SD pass length for the spaceborne scenario might make it hard for any kind of ILS scheme to be successfully applied. It is left for further study to see if e.g. an improved stochastic measurement model could be beneficial in such cases. In contrast, the LAMBDA method has demonstrated to work well for the sequential or recursive methods where the number of simultaneously estimated integer ambiguities is much smaller. For these processing strategies however, proper integer ambiguity resolution for real-world spaceborne applications, with unmodeled multipath and systematic errors in the GPS observation data, requires the inclusion of the relative spacecraft dynamics. This was demonstrated with the sequential kinematic filter, which simply lacked the robustness to properly cope with this problem. In addition to the dynamics, a conservative ambiguity validation procedure, more or less custom tailored for the GRACE application at hand, was required by the EKF in order to prevent incorrectly estimated integer values to be allocated to the filter.

With respect to the relative spacecraft dynamics, it can be concluded that the way they are facilitated within the EKF scheme works properly in the context of the GRACE mission. Next to the fact that the dynamics provides the robustness for proper ambiguity resolution, it is also required for the highly precise relative position solution. However, since the EKF ambiguity fixed solution clearly shows traces of multipath or systematic errors in the carrier phase data (section 4.4.7, Fig. 4.12), it is not believed that improved dynamical modeling for e.g. the atmospheric drag or solar radiation pressure will result in an even more precise solution. For the EKF ambiguity float solution on the other hand it was demonstrated that the effects of some mismodeled forces, most likely the solar radiation pressure, still showed up in the relative position. Improved dynamical modeling might therefore be beneficial in this last case.

Another factor of critical importance is the quality of the GPS observation data used. Despite the fact that under normal circumstances the GRACE GPS data is relatively low on multipath and systematic errors (section 2.6.2), a conservative integer ambiguity validation scheme was still required due to the presence of these unmodeled (pseudorange) errors. In addition, as mentioned before, the EKF relative

position solution is clearly affected by carrier phase multipath (Fig. 4.12). Although a first test over a single day with even higher multipath and/or systematic errors in the GRACE (pseudorange) observation data (Fig. 2.5) did not seem to have any influence on either ambiguity resolution or the precision of the resulting relative position solution (section 4.5.1), it is left for further study, involving data collected over longer time spans, to see if this is truly the case.

It can furthermore be concluded that the entire processing scheme works very adequately. The reduced dynamic orbits generated with the GHOST RDOD tool have shown to be precise enough for the purpose of relative positioning. This has first of all directly been verified by the independent SLR comparisons (section 3.6.5). An indirect validation is offered by the relative position solution results obtained, since errors in the RDOD orbit of the reference spacecraft directly influence the modeled SD observations (eqn. 2.34), and thus the resulting solution.

Applicability of the developed filtering scheme

The EKF processing strategy developed for precise relative positioning of spacecraft is in principle applicable to any kind of (LEO) satellite formation, provided that enough SD GPS observations can be formed at all, or most, measurement epochs. Of course it also depends on the GPS receivers that are used. Due to issues like, again, observation data quality (multipath suppressing characteristics) geodetic grade spaceborne GPS receivers are preferred. The formulation of the relative S/C dynamics is basically independent of the composition of the formation. However, if the formation requires a lot of active control by means of thruster activity this might have to be facilitated in the dynamical model. Another issue that might be important for out-of-plane formations with long baselines is the fact that after large GPS data outages the filter might require a restart. This is due to the fact that the resulting integration error caused by the dynamical model uncertainty might cause the filter to run out of the linear domain.

For satellite formations with short separations between the spacecraft, such as the envisaged TerraSAR-X/TanDEM-X formation in bistatic operation mode, some potential benefits for relative positioning can be identified. First of all, a shorter baseline should be beneficial for the number of SD observations that are available at each epoch, although the distribution for GRACE was already very good (Fig. 4.5), and might hereby positively influence the reliability or chance of obtaining a solution with a high precision. Another potential benefit is a more reliable and faster resolution of the integer carrier phase ambiguities. This is based on the same assumption as for the terrestrial case that the DD ionospheric path delays can be ignored, or at least be reduced by a simple model to a level that they can be ignored, for short baselines. However, the ionospheric effect should still be properly accounted for in the final position solution if high precision is to be obtained. Aside from these two benefits, it is most likely that the precision of the relative position solution itself will also (slightly) increase. This is first of all due to the fact that the maximum error in the modeled SD observation (eqn. 2.34) decreases as soon

as the spacecraft separation becomes smaller. In addition, the (potentially) higher number of SD observations will in principle result in a better determined solution. However, the GRACE EKF ambiguity fixed solution has shown to be affected by systematic errors in the GPS carrier phase data (Fig. 4.12), which do not depend on the spacecraft separation. Therefore the obtainable precision remains limited to a certain level (for GRACE the best precision obtained that was obtained is 0.63 mm for DOY 258), dictated by the quality of the observation data.

The only remaining issue with the applicability of the developed EKF to other scenarios is the ambiguity validation procedure. As stated earlier this procedure is more or less custom tailored to the GRACE application at hand. The great detection power of the KBR observation data is able to visualize every flaw in the resulting relative position solution, allowing for a good calibration of the critical values of the different ambiguity validation tests (section 4.1.2). Although the developed procedure is in principle applicable to other spaceborne scenarios as well, the absence of an external validation possibility in these cases might make the calibration of the scheme very hard.

Recommendations for further study

Although the developed EKF is in principle applicable to other spaceborne scenarios as well, a question that remains for such cases is how to validate the precision of the relative position solution without an external validation possibility like the KBR observations. Closely related to this is the proper calibration of the currently implemented integer ambiguity validation procedure. Although a large divergence of the ambiguity fixed relative position solution can certainly be detected under other circumstances as well, it is questionable if the more subtle errors caused by incorrectly resolved integers, as demonstrated in section 4.5.3, can be identified as well without such an external validation possibility. These issues form the basis for the recommendations for further study.

One of the first issues for further study should be the development of a more generic ambiguity validation procedure for the existing filter. Although the kinematic SPP process has demonstrated to have some detection power for incorrectly resolved ambiguities, its use for inclusion in such a scheme is limited (section 4.5.3). The first step in the development of a more generic procedure might be the use of corrective models for multipath and systematic errors in the GPS observation data, and, simultaneously, the application of a better stochastic model, facilitating a C/N_0 dependent data weighting and perhaps even taking correlations between the observations, and in time, into account. If this would be implemented, the resulting ambiguity success rate might become more reliable (meaning that it reflects the true situation better), and might even make screening of the individual ambiguity residuals, for which determination of the critical values was found to be the most difficult, unnecessary. The GRACE scenario still serves as the perfect test-bed for such as study. As a start, the systematic errors for the pseudorange data from Fig. 2.3 and Fig. 2.4, presented earlier, can be used. The pseudorange data weights

can also be obtained from the earlier derived results in Fig. 2.6. For the carrier phase data, the results from *Haines et al.* [2005] might somehow provide a good starting point, as well as the noise curves from Fig. 2.7.

Another consideration might be to step away from the on-the-fly ambiguity resolution approach. This in order to prevent complete divergence of the filter solution under all circumstances as soon as incorrectly resolved integer ambiguities are allocated. An alternative approach might be to resolve the integer ambiguities on each epoch after the smoothed float (ambiguity) solution has been computed first. The found integers can then be used to update the solution on the epoch they relate to. This is not entirely identical to the method discussed in section 4.5.3, where the ambiguities are still estimated during both filter runs. It is left for further study to see if the obtainable precision of the suggested alternative is as good as the precision obtained so far.

The validation of the (ambiguity fixed) relative position solution might already be partly solved if corrective models for multipath and systematic errors as well a proper stochastic model are applied. It might namely be that the formal variances of the relative position comparison between e.g. the EKF float and EKF fixed solution match the obtained (RMS) values better. However, it is left for further study to see if this is truly the case. Another consideration might be the use of the reduced dynamic batch LSQ estimation method for relative spacecraft positioning. The batch LSQ allows for an additional consistency check of the results, by screening the post-fit residuals to see if any discrepancies exist (as for the POD case 3.6.3). It is however left for further study to see if a way exists to properly cope with the problems encountered earlier with this processing strategy. If (re-)implemented, it is advised to use the resolved integer ambiguities from the EKF in the batch LSQ and not (re-)estimate the integers using the LAMBDA method. It is namely still believed that the earlier encountered search time problem is hard to solve.

Some satellite formations might offer an indirect validation possibility for the relative position solution. It was already demonstrated by *Kohlhase et al.* [2003] that interferometric SAR images can be used to disclose information on the absolute position accuracy of the satellite that took the images. The interferometric SAR images from the envisaged TerraSAR-X/TanDEM-X formation could possibly be used for this purpose as well, but than for the relative position. If this is truly feasible remains for further study.

A final recommendation is the use of the GRACE GPS observation data for a real-time relative spacecraft positioning study. This is certainly of interest as soon as the GRACE satellites would be in close proximity of each other, which is the case if the envisaged switch manoeuvre [*Kirschner et al.*, 2004] truly takes place. It could then be proven if many of the (single-frequency) concepts from previous studies truly work under real-world conditions, or if the assumptions made in here, especially regarding ambiguity resolution, are too optimistic.

Future developments of GPS and Galileo

In the near future the GPS system will be enhanced with the modulation of a civil code on the second transmitting frequency, as well as with a new to come third transmitting frequency. In contrast to the $L1$ and $L2$ frequencies, the third frequency, $L5$, will only be modulated with a civil code. In addition, the European Galileo system, consisting of a total of 30 satellites, will become operational. These satellites will transmit on a total of four frequency bands, partly overlapping the GPS transmitting frequencies. A basic overview of these developments was already given in *Hofmann-Wellenhof et al.* [2001].

These new developments will have some impact on the relative spacecraft positioning problem as well. First of all there are benefits for ambiguity resolution. It has already been shown by *Tiberius et al.* [2002] that, especially for short baselines, a somewhat higher ambiguity success rate (eqn. 4.5) can in general be obtained in case of 3 transmitting frequencies. Significant benefits for ambiguity resolution however, again measured by the ambiguity success rate, were reported when the total number of simultaneously observed GPS or Galileo satellites increases. Furthermore, the new Galileo codes are expected to outperform the existing, and new to come, GPS civil codes with respect to multipath sensitivity as well as noise. This would even be more beneficial for the ambiguity resolution problem.

The future availability of more GPS and Galileo spacecraft will also lead to a better viewing geometry in (nearly) all cases. Although in principle this should be beneficial for the obtainable precision of the relative spacecraft position solution, it must again be mentioned that the precision will most likely still be dictated, and thus limited, by the multipath and systematic errors present in the carrier phase observation data.

Furthermore, it has been shown in section 4.5.2 that the use of the C/A code and (especially the) carrier phase observable improves the precision of the kinematic solution. Since the main cause of this improvement was a noise reduction in the carrier phase observation data, but the multipath or systematic errors were still present, the EKF solution remained largely unaffected. The future availability of the civil code (and carrier phase) observable on the second GPS transmitting frequency will most likely bring an additional improvement in the kinematic relative position solution. However, based on the earlier obtained results, it is not directly believed that this will improve the precision of the EKF solution much further. Nevertheless, a future study is required to see if this is truly the case.

Appendix A
Integer Ambiguity Estimation

This appendix provides an overview of the basic operation of the three commonly accepted methods for integer estimation, namely integer rounding, integer bootstrapping, also referred to as sequential or conditional rounding, and integer least squares (ILS). In addition, the Least Squares Ambiguity Decorrelation Adjustment (LAMBDA) method, an efficient implementation of ILS and the integer estimation method used for this research, is also described and compared to the standard ILS procedure.

Although for this research integer estimation concerns the double difference carrier phase ambiguities on the individual frequencies, the just mentioned estimation methods can be applied to other integer estimation problems as well. As already mentioned in section 4.1.1 integer estimation is performed from a real-valued solution of the double difference ambiguities. The quality of the integer estimate strongly depends on the quality of this real-valued solution, as well as the integer estimation method used. In order to arrive at an adequate real-valued solution, a batch or recursive LSQ processing technique should be used. The general form of the n-dimensional real-valued DD ambiguity vector, $\mathbf{a}$, and the accompanying fully populated covariance matrix, $\mathbf{Q_a}$, both expressed in units of cycles, obtained from a LSQ method, are defined as

$$\mathbf{a} = \begin{pmatrix} a_1 \\ a_2 \\ \vdots \\ a_n \end{pmatrix}; \quad \mathbf{Q_a} = \begin{pmatrix} \sigma^2_{a_1} & \sigma_{a_1 a_2} & \dots & \sigma_{a_1 a_n} \\ \sigma_{a_2 a_1} & \sigma^2_{a_2} & \dots & \sigma_{a_2 a_n} \\ \vdots & \vdots & \ddots & \vdots \\ \sigma_{a_n a_1} & \sigma_{a_n a_2} & \dots & \sigma^2_{a_n} \end{pmatrix}. \tag{A.1}$$

An n-dimensional integer DD ambiguity vector, derived from this real-valued solu-

tion is denoted as

$$\mathbf{n} = \begin{pmatrix} n_1 \\ n_2 \\ \vdots \\ n_n \end{pmatrix}. \tag{A.2}$$

In the following the working of the integer estimation methods is discussed with the aid of the 2-dimensional numerical example

$$\mathbf{a} = \begin{pmatrix} 2.51 \\ 2.23 \end{pmatrix}; \quad \mathbf{Q_a} = \begin{pmatrix} 0.2767 & 0.2152 \\ 0.2152 & 0.1680 \end{pmatrix}, \tag{A.3}$$

obtained from *Odijk* [2002].

A.1 Integer rounding

The easiest way of obtaining an integer estimate from the real-valued solution is by simply rounding to the nearest integer value. In this way the correlations between the individual ambiguities are completely ignored. The vector of integer rounded ambiguities, $\mathbf{n}_R$, simply reads

$$\mathbf{n}_R = \begin{pmatrix} [a_1] \\ \vdots \\ [a_n] \end{pmatrix}, \tag{A.4}$$

where $[\cdot]$ represents rounding to the nearest integer. Applying this to the numerical example yields

$$\mathbf{n}_R = \begin{pmatrix} [2.51] \\ [2.23] \end{pmatrix} = \begin{pmatrix} 3 \\ 2 \end{pmatrix} \tag{A.5}$$

for the integer ambiguities. In general integer rounding is a dangerous way of obtaining an integer estimate, since the correlations between the individual ambiguities are typically high and cannot be easily ignored.

A.2 Integer bootstrapping

A more proper way of obtaining an integer estimate is by means of sequential or conditional integer rounding, also referred to as integer bootstrapping. In contrast to integer rounding, the integer bootstrapping estimator takes the correlations between the ambiguities into account to some extent, and therefore requires the covariance matrix. The bootstrapped integer ambiguities follow from a sequential conditional LSQ adjustment with a conditioning on the integer ambiguity values from the previous steps. In other words this means that the first ambiguity is simply rounded to

the nearest integer value, the second integer is obtained with a conditioning on the first, the third one with a conditioning on the second and the first, etc. In general the bootstrapped integer estimator can be written as

$$\begin{aligned} n_{1,B} &= [a_1], \\ n_{2,B} &= [a_{2|1}] = [a_2 - \sigma_{a_2 a_1}\sigma_{a_1}^{-2}(a_1 - n_{1,B})], \\ &\vdots \\ n_{n,B} &= [a_{n|N}] = \left[a_n - \sum_{i=1}^{n-1} \sigma_{a_n a_{i|I}} \sigma_{a_{i|I}}^{-2} (a_{i|I} - n_{i,B}) \right], \end{aligned} \tag{A.6}$$

where $a_{i|I}$ is the real valued i-th ambiguity obtained through a conditioning on the previous $I = 1, \ldots, (i-1)$ sequentially rounded ambiguities. These real-valued sequentially least-squared ambiguities are obtained by a triangular decomposition of the covariance matrix, $\mathbf{Q_a} = \mathbf{LDL}^T$. Here, $\mathbf{L}$ is a lower triangular matrix and $\mathbf{D}$ a diagonal matrix, both defined as

$$\mathbf{L} = \begin{pmatrix} 1 & & & \\ \frac{\sigma_{a_2 a_1}}{\sigma_{a_1}^2} & 1 & & \\ \vdots & \ddots & \ddots & \\ \frac{\sigma_{a_n a_1}}{\sigma_{a_1}^2} & \cdots & \frac{\sigma_{a_n a_{n-1|N-1}}}{\sigma_{a_{n-1|N-1}}^2} & 1 \end{pmatrix}; \quad \mathbf{D} = \begin{pmatrix} \sigma_{a_1}^2 & & & \\ & \sigma_{a_{2|1}}^2 & & \\ & & \ddots & \\ & & & \sigma_{a_{n|N}}^2 \end{pmatrix}, \tag{A.7}$$

with the elements of $\mathbf{D}$ specified as the so-called conditional variances, given by

$$\sigma_{a_{i|I}}^2 = \sigma_{a_i}^2 - \sum_{j=1}^{i-1} \sigma_{a_i a_{j|J}}^2 \sigma_{a_{j|J}}^{-2}. \tag{A.8}$$

When applying the $\mathbf{LDL}^T$ decomposition to the 2-dimensional numerical example,

$$\mathbf{L} = \begin{pmatrix} 1 & 0 \\ 0.7777 & 1 \end{pmatrix}; \quad \mathbf{D} = \begin{pmatrix} 0.2767 & 0 \\ 0 & 0.0006 \end{pmatrix}, \tag{A.9}$$

the bootstrapped integer ambiguities can be computed as

$$\mathbf{a}_B = \begin{pmatrix} [2.51] \\ [2.23 - 0.7777(2.51 - 3)] \end{pmatrix} = \begin{pmatrix} 3 \\ 3 \end{pmatrix}. \tag{A.10}$$

When re-ordering the ambiguities in the numerical example,

$$\mathbf{a} = \begin{pmatrix} 2.23 \\ 2.51 \end{pmatrix}; \quad \mathbf{Q_a} = \begin{pmatrix} 0.1680 & 0.2152 \\ 0.2152 & 0.2767 \end{pmatrix}, \tag{A.11}$$

and hereby bringing the most precise ambiguity to the first position entry, the $\mathbf{LDL}^T$ decomposition yields

$$\mathbf{L} = \begin{pmatrix} 1 & 0 \\ 1.280 & 1 \end{pmatrix}; \quad \mathbf{D} = \begin{pmatrix} 0.1680 & 0 \\ 0 & 0.0010 \end{pmatrix}, \tag{A.12}$$

and the bootstrapped integer estimate becomes

$$\mathbf{a}_B = \begin{pmatrix} [2.23] \\ [2.51 - 1.280(2.23 - 2)] \end{pmatrix} = \begin{pmatrix} 2 \\ 2 \end{pmatrix}. \tag{A.13}$$

It can be immediately seen that both bootstrapped integer estimates differ from eachother. In general the most reliable integer bootstrapped solution is the one where the most precise ambiguity is rounded first, followed by the one with the most precise conditional variance based on eqn. A.8, etc. A re-ordering algorithm might be necessary to accomplish this.

A.3 Integer Least-Squares

The optimum solution for the integer ambiguities is obtained by solving a non-standard LSQ problem, referred to as integer least-squares [*Teunissen*, 1993]. The integer ambiguities obtained in this way, $\mathbf{n}_{LS}$, follow from solving the following minimization problem

$$\min_{\mathbf{n}_{LS} \in \mathbb{Z}^n} \|\mathbf{a} - \mathbf{n}_{LS}\|^2_{\mathbf{Q_a}}. \tag{A.14}$$

The solution of this minimization problem cannot simply be computed as was the case with integer rounding and bootstrapping. Instead a search is required. Therefore, according to the minimization problem, a search space can be defined as

$$(\mathbf{a} - \mathbf{n}_{LS})^T \mathbf{Q}_{\mathbf{a}}^{-1} (\mathbf{a} - \mathbf{n}_{LS}) \leq \chi^2, \tag{A.15}$$

which is an n-dimensional ellipsoid with size χ^2. The shape of this ellipsoid is governed by the covariance matrix. Using the $\mathbf{LDL}^T$ decomposition derived earlier the search space can be rewritten as a sum of n squares,

$$\sum_{i=1}^{n} \frac{a_{i|I} - n_{i,LS}}{\sigma^2_{a_{i|I}}} \leq \chi^2, \tag{A.16}$$

which, when written out in full, result in n constraint equations for the integer search:

$$\begin{aligned} (a_1 - n_{1,LS})^2 &\leq \sigma^2_{a_1} \chi^2, \\ (a_{2|1} - n_{2,LS})^2 &\leq \sigma^2_{a_{2|1}} (\chi^2 - \tfrac{(a_1 - n_{1,LS})^2}{\sigma^2_{a_1}}), \\ &\vdots \\ (a_{n|N} - n_{n,LS})^2 &\leq \sigma^2_{a_{n|N}} (\chi^2 - \textstyle\sum_{i=1}^{n-1} \frac{(a_{i|I} - n_{i,LS})^2}{\sigma^2_{a_{i|I}}}). \end{aligned} \tag{A.17}$$

The sequential conditional ambiguities, $a_{i|I}$, are similar as for the bootstrapping estimator

$$\begin{aligned} a_1 &= a_1, \\ a_{2|1} &= a_2 - \sigma_{a_2 a_1}\sigma_{a_1}^{-2}(a_1 - n_{1,LS}), \\ &\vdots \\ a_{n|N} &= a_n - \textstyle\sum_{i=1}^{n-1} \sigma_{a_n a_{i|I}}\sigma_{a_{i|I}}^{-2}(a_{i|I} - n_{n,LS}), \end{aligned} \tag{A.18}$$

with the difference that they are not rounded to integers and that they are continuously recomputed during the search for the optimum integer values. The size of the ellipsoid, χ^2, should be set in such a way that at least one solution is present, but yet not too many for the integer search to be efficient. This is where the previous integer estimators come in handy. It is known from *Teunissen* [1998] and *Teunissen* [1999] that the integer solution obtained by rounding is less optimal than bootstrapping, which is less optimal than integer least squares, i.e.:

$$\|\mathbf{a} - \mathbf{n}_{LS}\|^2_{\mathbf{Q_a}} \leq \|\mathbf{a} - \mathbf{n}_B\|^2_{\mathbf{Q_a}} \leq \|\mathbf{a} - \mathbf{n}_R\|^2_{\mathbf{Q_a}}. \tag{A.19}$$

Therefore the integer bootstrapped solution could be used to set the size of the search space

$$\chi^2 = (\mathbf{a} - \mathbf{n}_B)^T \mathbf{Q}_\mathbf{a}^{-1}(\mathbf{a} - \mathbf{n}_B) \tag{A.20}$$

In the following the ILS search is demonstrated using the 2-dimensional numerical example. First, the search space is computed using the bootstrapped solution. The first solution $\mathbf{n}_B = (3, 3)^T$ yields a search space $\chi^2 = 240.62$, and the second solution $\mathbf{n}_B = (2, 2)^T$ yields $\chi^2 = 44.96$. For comparison, the integer solution based on rounding would yield a size of $\chi^2 = 592.81$. The search space belonging to the most precise bootstrapped solution, which also yields the smallest size, is used.

The second step is to search through the range of integer values bounded by the first constraint equation

$$\begin{aligned} n_{1,LS} &\leq a_1 - \sqrt{\sigma_{a_1}^2 \chi^2}, \\ n_{1,LS} &\geq a_1 + \sqrt{\sigma_{a_1}^2 \chi^2}. \end{aligned} \tag{A.21}$$

With the earlier derived search space size it follows that $-1.02 \leq n_{1,LS} \leq 6.04$, so $n_{1,LS} \in [-1, 0, 1, 2, 3, 4, 5, 6]$. The third step is to evaluate the constraint equation of the second ambiguity for each possible integer value of the first ambiguity:

$$\begin{aligned} n_{2,LS} &\leq a_{2|1} - \sqrt{\sigma_{a_{2|1}}^2 \frac{\chi^2 - (a_1 - n_{1,LS})}{\sigma_{a_1}^2}}, \\ n_{2,LS} &\geq a_{2|1} + \sqrt{\sigma_{a_{2|1}}^2 \frac{\chi^2 - (a_1 - n_{1,LS})}{\sigma_{a_1}^2}}. \end{aligned} \tag{A.22}$$

This process is displayed in Table A.1. Here it can be seen that not every possible integer value for the first ambiguity has an accompanying integer value for the second ambiguity within the search space, and results in a so called 'dead end' of the search. Only 2 integer ambiguity pairs are found within the search space, the

Table A.1 Search procedure for the second integer ambiguity.

$n_{1,LS}$	$a_{2\|1}$	low	upp	$n_{2,LS}$	$(\mathbf{a}-\mathbf{n}_{LS})^T\mathbf{Q}_{\mathbf{a}}^{-1}(\mathbf{a}-\mathbf{n}_{LS})$
-1	-0.50	-0.52	-0.48	-	-
0	0.28	0.16	0.40	-	-
1	1.06	0.90	1.21	1	13.14
2	1.83	1.67	2.00	2	44.96
3	2.61	2.44	2.76	-	-
4	3.39	3.24	3.54	-	-
5	4.17	4.05	4.26	-	-
6	4.94	4.92	4.97	-	-

bootstrapped solution and a solution with the smallest possible norm in the metric of the covariance matrix, which is also the ILS solution,

$$\mathbf{n}_{LS} = \begin{pmatrix} 1 \\ 1 \end{pmatrix}. \tag{A.23}$$

When conducting the ILS search using the re-ordered real-valued ambiguities (eqn. A.11) it follows that $-0.52 \leq n_{1,LS} \leq 4.98$, meaning that $n_{1,LS} \in [0, 1, 2, 3, 4]$. Again the search for the second ambiguity is displayed in Table A.2. Here it can be

Table A.2 Search procedure for the second integer ambiguity, conducted on the re-ordered ambiguities

$n_{1,LS}$	$a_{2\|1}$	low	upp	$n_{2,LS}$	$(\mathbf{a}-\mathbf{n}_{LS})^T\mathbf{Q}_{\mathbf{a}}^{-1}(\mathbf{a}-\mathbf{n}_{LS})$
0	-0.34	-0.47	-0.22	-	-
1	0.94	0.74	1.13	1	13.14
2	2.22	2.00	2.43	2	44.96
3	3.50	3.29	3.70	-	-
4	4.78	4.61	4.94	-	-

directly seen that the solution is the same as for the 'original' ambiguities, this in contrast to the bootstrapping estimator. This is due to the fact that a search for the optimum value, the minimized squared norm, is conducted. The only difference is the shorter search tree required due to the fact that the process was started with the most precise ambiguity. Therefore similar as for bootstrapping the most precise ambiguity should be started with, followed by the second most precise one (based on the conditional variance), etc. This assures the shortest search time, which can

be quite significant with a large number of ambiguities, whilst still returning the optimum solution.

A.4 Optimized Integer Least Squares: The LAMBDA Method

The biggest problem with the standard ILS search procedure are the long search times for large numbers of ambiguities, caused by the highly elongated ellipsoidal search space, resulting in numerous dead ends and possible solutions that have to be evaluated for their squared norm. The highly elongated shape of the search space is again the result of the heavy correlations between the ambiguities. In order to overcome this problem *Teunissen* [1995] proposed the Least Squares Ambiguity Decorrelation Adjustment (LAMBDA) method where the integer search procedure is optimized.

The optimization of this method comes from a decorrelation of the original ambiguities by means of a transformation with matrix $\mathbf{Z}$,

$$\mathbf{z} = \mathbf{Z}^T\mathbf{a}; \quad \mathbf{Q_z} = \mathbf{Z}^T\mathbf{Q_a}\mathbf{Z}, \tag{A.24}$$

and conduct the ILS search over a more spherical search space spanned by the newly obtained ambiguities $\mathbf{z}$ with covariance matrix $\mathbf{Q_z}$. After having found the ILS solution, $\mathbf{z}_{LS}$, the integer estimates of the original ambiguities are obtained as

$$\mathbf{n}_{LS} = \mathbf{Z}^{-T}\mathbf{z}_{LS}. \tag{A.25}$$

The so-called Z-transformation must be admissible meaning that the integer nature of the ambiguities must be preserved, i.e. $\mathbf{Z}$ and $\mathbf{Z}^{-1}$ must have integer entries, and that the volume and size of the search space is preserved, i.e $|\mathbf{Z}| = \pm 1$. Using the $\mathbf{LDL}^T$ decomposition of $\mathbf{Q_a}$ it can immediately be seen that full decorrelation is achieved when $\mathbf{Z} = \mathbf{L}^{-T}$, after which $\mathbf{Q_z} = \mathbf{D}$. Since it is very unlikely that $\mathbf{L}$ has any lower triangular integer entries full decorrelation cannot be achieved. A detailed overview of the construction algorithm of the Z-transformation matrix can be found in *De Jonge and Tiberius* [1996]. It is based on a sequence of integer Gauss transformations on the lower triangular matrix $\mathbf{L}$ and a continuous reordering of its columns and the corresponding entries in $\mathbf{D}$.

For the 2-dimensional numerical example the transposed Z-transformation matrix and its inverse are given by

$$\mathbf{Z}^T = \begin{pmatrix} 1 & -1 \\ -3 & 4 \end{pmatrix}; \quad \mathbf{Z}^{-T} = \begin{pmatrix} 4 & 1 \\ 3 & 1 \end{pmatrix}, \tag{A.26}$$

which are then used to create the transformed ambiguities

$$\mathbf{z} = \begin{pmatrix} 0.28 \\ 1.39 \end{pmatrix}; \quad \mathbf{Q_z} = \begin{pmatrix} 0.0143 & 0.0043 \\ 0.0043 & 0.0135 \end{pmatrix}. \tag{A.27}$$

As can be seen the correlations between the ambiguities are not so strong anymore, resulting in a much more circular search space. This decorrelation process is illustrated in Fig. A.1 where a stepwise Z-transformation changes the shape of the search space from the original very elongated (top) shape to a more circular one (bottom). The size of the search space is still the same, which is easily verified by transform-

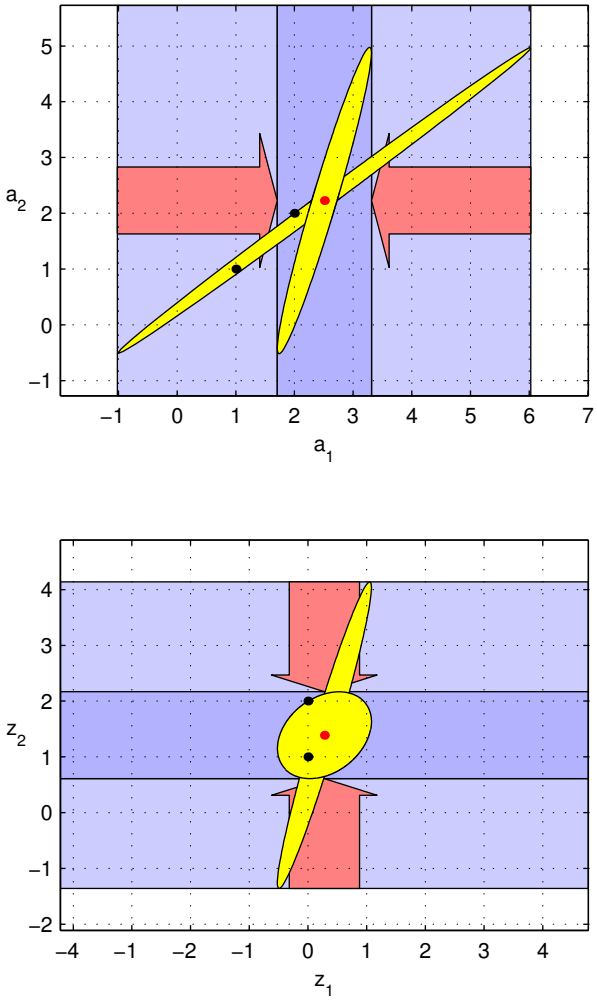

Figure A.1 Illustration of the stepwise decorrelation of the 2-dimensional search space by means of an integer Z-transformation. The original very elongated ellipsoidal search space (top) and the almost fully decorrelated nearly circular one (bottom) have the same size and are centered around the original ambiguities. (Figures courtesy of Peter Joosten).

ing the most precise bootstrapped integer ambiguities, $\mathbf{z}_B = \mathbf{Z}^T\mathbf{n}_B = (0,2)^T$, and compute the search space size in the new metric $\chi^2 = (\mathbf{z}-\mathbf{z}_B)^T\mathbf{Q}_\mathbf{z}^{-1}(\mathbf{z}-\mathbf{z}_B) = 44.96$.

The remaining search process is identical as previously described (section A.3). The boundaries of the first ambiguity are thus given as $-0.52 \leq z_{1,LS} \leq 1.08$, so $z_{1,LS} \in [0,1]$. Compared to standard ILS this is a much smaller interval to be searched. The search for the second ambiguity is displayed in Table A.3 where only one dead end is left.

Table A.3 Search for the second ambiguity in the transformed search space.

$z_{1,LS}$	$z_{2\|1}$	*low*	*upp*	$z_{2,LS}$	$(\mathbf{z}-\mathbf{z}_{LS})^T\mathbf{Q}_\mathbf{z}^{-1}(\mathbf{z}-\mathbf{z}_{LS})$
0	1.31	0.61	2.00	1	13.14
				2	44.96
1	1.61	1.28	1.93	-	-

If the search is performed over the re-ordered transformed ambiguities

$$\mathbf{z} = \begin{pmatrix} 1.39 \\ 0.28 \end{pmatrix}; \quad \mathbf{Q}_\mathbf{z} = \begin{pmatrix} 0.0135 & 0.0043 \\ 0.0043 & 0.0143 \end{pmatrix}, \tag{A.28}$$

and thus starts with the most precise ambiguity, no dead end is present. In this case the first ambiguity is bounded as $0.61 \leq z_{1,LS} \leq 2.17$, and thus $z_{1,LS} \in [1,2]$, the search for the second ambiguity is listed in Table A.4. This indicates that

Table A.4 Search for the second ambiguity in the transformed search space, conducted on the re-ordered ambiguities

$z_{1,LS}$	$z_{2\|1}$	*low*	*upp*	$z_{2,LS}$	$(\mathbf{z}-\mathbf{z}_{LS})^T\mathbf{Q}_\mathbf{z}^{-1}(\mathbf{z}-\mathbf{z}_{LS})$
1	0.16	-0.50	0.82	0	13.14
2	0.47	0.00	0.95	0	44.96

also within the transformed search space it is recommended to start with the most precise ambiguity and continue with the second most precise, etc. The ILS solution in the transformed search space

$$\mathbf{z}_{LS} = \begin{pmatrix} 0 \\ 1 \end{pmatrix}, \tag{A.29}$$

has the same squared norm in the transformed metric as the previously found ILS solution in the original search space. When transforming back using eqn. A.25 the same ILS solution as for the original ambiguities is found, $\mathbf{n}_{LS} = (1,1)^T$.

The LAMBDA implementation used for this research is the one described in *De Jonge and Tiberius* [1996] and internally re-orders the ambiguities from most precise to least precise, according to the conditional variances of the decorrelated ambiguities. This optimizes the ambiguity search tree, and thus search time, as was

shown to be important. The conditional variances of the decorrelated ambiguities are also returned by LAMBDA and are used for integer validation purposes as described in section 4.1.2. Furthermore, the LAMBDA method returns two integer solutions, the one with the smallest and the one-but-smallest squared norm of the ambiguity residuals in the metric of the covariance. This is again used for integer validation purposes. To assure the presence of at least two solutions, χ^2 is set using the one-but-smallest squared norm from the integer solution obtained from subsequent rounding to the nearest and one-but-nearest decorrelated ambiguities. Applied to our numerical example it would mean that the following integer rounded solutions would need to be evaluated: $\mathbf{z}_R = (0, 1)^T$, $\mathbf{z}_R = (1, 1)^T$ and $\mathbf{z}_R = (0, 2)^T$. The accompanying squared norms are respectively given as 13.14, 66.39 and 44.96, where it can be seen that 44.96 should be used as search space size, which has also been done throughout the examples. As mentioned in the previous subsection, χ^2 can also be set using the bootstrapped solution of the decorrelated ambiguities. This however does not guarantee the presence of at least two solutions, so the one-but-smallest squared norm from bootstrapping should be used. This has however not been done for this research.

Appendix B

Lower boundary for the bootstrapping success rate

From *Teunissen* [1999] or *Joosten and Tiberius* [2000] it is learned that the success rate or probability of having actually estimated the correct vector of integers, $\mathbf{n}$, using the integer bootstrapping estimation method (section A.2) is defined as

$$P(\mathbf{n}_B = \mathbf{n}) = \prod_{i=1}^{n} \left(2\Phi(\frac{1}{2\sigma_{i|I}}) - 1. \right). \tag{B.1}$$

Here, $\sigma_{i|I}$ is the conditional variance of the i^{th} bootstrapped ambiguity cf. eqn. A.8. Furthermore, $\Phi(x)$ is the cumulative normal distribution, given as

$$\Phi(x) = \int_{-\infty}^{x} \frac{1}{\sqrt{2\pi}} e^{-\frac{1}{2}z^2} dz \; . \tag{B.2}$$

Although many software packages, e.g. MATLAB, are able to instantaneously evaluate eqn. B.1, this is not always the case within other practical applications, e.g. onboard S/C computers. In *Dórtenzio* [1965] a lower boundary for $\Phi(x)$ is given as

$$\Phi(x) \geq \frac{1}{2} \left(1 + \left(1 - e^{-\frac{x^2}{2}} \right)^{\frac{1}{2}} \right). \tag{B.3}$$

When combining this last expression with eqn. B.1, a lower boundary for the bootstrapping success rate is found,

$$P(\mathbf{n}_B = \mathbf{n}) \geq \prod_{i=1}^{n} \left(1 - e^{-\frac{1}{2}(\frac{1}{2\sigma_{i|I}})^2} \right)^{\frac{1}{2}}, \tag{B.4}$$

which can be swiftly computed under all circumstances.

Bibliography

Astrium (2002), A GPS Receiver for LEO, MEO, and GEO applications, Mosaic fact sheet, November 2002.

Bierman, G.J. (1977), *Factorization Methods for Discrete Sequential Estimation*, Academic Press, Inc., New York.

Binning, P.W. (1997), *Absolute and relative satellite to satellite navigation using GPS*, Ph.D. dissertation, University of Colorado.

Birmingham, W. P., B. L. Miller, and W. L. Stein (1983), Experimental Results of Using the GPS for Landsat 4 Onboard Navigation, *Navigation, The Journal of the Institute of Navigation*, *30*(3), 244–251.

Braasch, M.S. (1995), Multipath effects, in *Global Positioning System: Theory and Applications, Volume 1*, edited by B.W. Parkinson and J.J. Spilker, American Institute for Aeronautics and Astronautics, Washington.

Brown, R.G., and P.Y.C. Hwang (1997), *Introduction to Random Signals and Applied Kalmann Filtering*, John Wiley and Sons, New York.

Bruinsma, S., D. Tamagnan, and R. Biancale (2003), Atmospheric densities from CHAMP/STAR accelerometer observations, *Planetary and Space Sciences*, *52*, 297–312, DOI: 10.1016/j.pss.2003.11.004.

Busse, F.D. (2003), *Precise Formation-State Estimation in Low Earth Orbit Using Carrier Differential GPS*, Ph.D. dissertation, Dept. of Aeronautics and Astronautics, Stanford University.

Case, K., G. Kruizinga, and S. Wu (2002), *GRACE Level 1B data product user handbook*, NASA Jet Propulsion Laboratory, Pasadena, JPL Publication D-22027.

Clohessy, W.H., and R.S. Wiltshire (1960), Terminal guidance for satellite rendezvous, *Journal of Aerospace Sciences*, *27*, 653.

Dórtenzio, R.J. (1965), Approximating the normal distribution function, *Systems Design*, *9*, 4–7.

Dunn, C., W. Bertiger, Y. Bar-Sever, S. Desai, and B. Haines (2003), Instrument of GRACE, *GPS World*, February 2003.

Ebinuma, T. (2001), *Precision spacecraft rendezvous using GPS: an integrated hardware approach*, Ph.D. dissertation, University of Texas.

ENEIDE (2005), Experiment Tests EGNOS on Space Mission, *GPS World*, *16*(5).

Estey, L. H., and C. M. Meertens (1999), TEQC: The Multi-Purpose Toolkit for GPS/GLONASS Data, *GPS Solutions*, *3*(1), 42–49.

Flechtner, F. (2003), Relative baseline determination for a tandem SAR mission using GPS code and phase measurements, *Technical Note*, GeoForschungsZentrum, Potsdam, August 2003.

Gurtner, W. (1994), RINEX: The Receiver Independent Exchange Format, *GPS World*, pp. 48–52.

Haines, B., Y. Bar-Sever, W. Bertiger, S. Byun, S. Desai, and G. Hajj (2005), GPS satellite antenna phase center variations: new perspectives from the GRACE mission, presentation at Dynamic Planet 2005, Joint Meeting of the IAG, IAPSO and IABO, Abstract Vol. p. 157, Cairns, Australia.

Hartrampf, M., E. Gottzein, M. Mittnacht, C., and Mller (2002), Relative Navigation of Satellites Using GPS Signals, in *Proceedings of Deutscher Luft- und Raumfahrt Kongress*.

Helleputte, T. Van (2004), *GPS High Precision Orbit Determination Software Tools: User Manual*, Doc. No. FDS-SUM-3110.

Highsmith, D., and P. Axelrad (2002), Relative State Estimation Using GPS Flight Data from Co-Orbiting Spacecraft, in *Proceedings of the ION GPS-99 meeting*, pp. 401–409, Nashville, TN, September 2002.

Hofmann-Wellenhof, B., H. Lichtenegger, and J. Collins (2001), *GPS Theory and Practice*, Springer Verlag, WienNewYork.

Hugentobler, U., S. Schaer, and P. Fridez (2001), *Bernese GPS Software Version 4.2*, February 2001, Manual.

Husti, G.J. (2000), *Global Positioning System, een inleiding*, Serie on Mathematical Geodesy and Positioning, Delft University Press, Delft, The Netherlands, In Dutch.

IGSCB (2005), IGS Products, http://igscb.jpl.nasa.gov/components/prods.html, Last accessed: September 2005.

IJssel, J. van den, P.N.A.M. Visser, and E.P. Rodriguez (2003), CHAMP Precise Orbit Determination Using GPS Data, *Adv. Space Res.*, *31*(8), 1889–1895, doi: 10.1026/S0273-1177(03)00161-3.

Jacchia, L.G. (1971), Revised Static Models of the Thermosphere and Exosphere with Empirical Temperature Profiles, *SAO Special Report 332*.

Jonge, P.J. de, and C.C.J.M. Tiberius (1996), The LAMBDA method for integer ambiguity estimation: implementation aspects, *LGR Series No. 12*, Delft Geodetic Computing Centre, Delft.

Joosten, P., and C.C.J.M. Tiberius (2000), Fixing the ambiguities. Are you sure they're right?, *GPS World*, *11*(5), 46–51.

Kedar, S., G.A. Hajj, B.D. Wilson, and M.B. Heflin (2003), The effect of the second order GPS ionospheric correction on receiver positions, *Geophysical Research Letters*, *30*(16).

Kirschner, M., O. Montenbruck, and S. DAmico (2004), Safe Switching of the GRACE Formation using an Eccentricity/Inclination Vector Separation, in *Proceedings of the 18th International Symposium on Space Flight Dynamics*, Munich, Germany, 11–15 October 2004.

Kohlhase, A.O., K.L. Feigl, and D. Massonnet (2003), Applying differential InSAR to orbital dynamics: a new approach for estimating ERS trajectories, *Journal of Geodesy*, *77*(9), 493–502.

Kouba, J. (2002), *A Guide to Using IGS Products*, Geodetic Survey Division, Natural Resources Canada, Ottowa, Ontario.

Kroes, R., and O. Montenbruck (2004), Spacecraft Formation Flying, Relative Positioning Using Dual-Frequency Carrier Phase, *GPS World*, *15*(7), 37–42.

Kroes, R., O. Montenbruck, W. Bertiger, and P.N.A.M. Visser (2005), Precise GRACE baseline determination using GPS, *GPS Solutions*, *9*(1), 21–31, DOI: 10.1007/s10291-004-0123-5.

Kursinski, E.R., G.A. Hajj, J.T. Schofield, R.P. Linfield, and K.R. Hardy (1997), Observing Earth's atmosphere with radio occultation measurements using the Global Positioning System, *Journal of Geophysical Research*, *23*, 429–465.

Langley, R.B., O. Montenbruck, M. Markgraf, C.S. Kang, and D. Kim (2004), Qualification of a commercial dual-frequency GPS receiver for the e-POP platform onboard the Canadian CASSIOPE spacecraft, in *2nd ESA Workshop on Satellite Navigation User Equipment Technologies, NAVITEC'2004*, Noordwijk, The Netherlands, December 8–10 2004.

Leick, A. (1994), *GPS Satellite Surveying*, John Wiley and Sons, New York.

Leung, S., and O. Montenbruck (2005), Real-Time Navigation of Formation-Flying Spacecraft using Global Positioning System Measurements, *Journal of Guidance, Control and Dynamics*, *28*(2), 226–235.

Leva, J.L., M. Uijt de Haag, and K. Van Dyke (1996), Performance of Standalone GPS, in *Understanding GPS, Principles and Applications*, edited by E.D. Kaplan, Archtec House, Boston.

Lichten, S.M. (1990), Estimation and filtering for high-precision GPS positioning applications, *Manuscripta Geodaetica*, *15*, 159–176.

Marradi, L., E. Banfi, and A. Mambretti (2001), The Lagrange receiver: design and in-flight demonstration, in *Proceedings of NAVITECH'2001*, Noordwijk, The Netherlands, December 10–12 2001.

McCarthy, D.D. (1996), IERS Conventions, 1996, *IERS Technical Note 21*, Central Bureau of IERS, Observatoire de Paris, Paris.

Melbourne, W.G. (1985), The case for ranging in GPS-based geodetic systems, in *Proceedings of the 1st Intenational Symposium on Precise positioning with the Global Positioning System*, pp. 373–386, Rockville, Maryland.

Misra, P., and P. Enge (eds.) (2001), *Global Positioning System: Signals, Measurements and Performance*, Ganga-Jamuna Press, Lincoln, MA.

Montenbruck, O. (2000), Quaternion Representation of BIRD Orientation and Reference System Transformations, *Technical Note TN 00–03*, German Space Operations Center.

Montenbruck, O. (2003), Performance Assessment of the NovAtel OEM4-G2 Receiver for LEO Satellite Tracking, *Technical Note TN 03–05*, German Space Operations Center.

Montenbruck, O., and E. Gill (2000), *Satellite Orbits: Models, Methods and Applications*, Springer Verlag, Heidelberg.

Montenbruck, O., and R. Kroes (2003), In-flight performance analysis of the CHAMP BlackJack GPS Receiver, *GPS Solutions*, *7*(2), 74–86, DOI: 10.1007/s10291-003-0055-5.

Montenbruck, O., B. Nortier, and S. Mostert (2004), A Miniature GPS Receiver for Precise Orbit Determination of the SUNSAT2004 Micro-Satellite, ION NTM 2004 Conference, San Diego, January 26–28 2004.

Montenbruck, O., T. van Helleputte, R. Kroes, and E. Gill (2005*a*), Reduced dynamic orbit determination using GPS code and carrier measurements, *Aerospace Science and Technology*, pp. 261–271.

Montenbruck, O., E. Gill, and R. Kroes (2005*b*), Rapid orbit determination of LEO satellites using IGS clock and ephemeris products, *GPS Solutions*, DOI: 10.1007/s10291-005-0131-0.

Montenbruck, O., J. Williams, T. Wang, and G. Lightsey (2005*c*), Preflight Validation of the IGOR GPS Receiver for TerraSAR-X, *Technical Note GTN–TST–0200*, German Space Operations Center.

Moreira, A. (2003), A TerraSAR-X Add-On for digital elevation measurements, *Proposal Study Doc. No. 2003–3472739*, Deutsches Zentrum fuer Luft- und Raumfahrt.

Moreira, A., G. Krieger, I. Hajnsek, D. Hounam, M. Werner, S. Riegger, and E. Settelmeyer (2004), TanDEM-X: A TerraSAR-X Add-On Satellite for Single-Pass SAR Interferometry., *Proceedings of IGARSS*, September 2004.

NASA (2002), Studying the Earth's gravity from space: the Gravity Recovery and Climate Experiment (GRACE), *NASA Facts, Doc. No. FS–2002–1–029–GSFC*, NASA.

Odijk, D. (2002), *Fast precise GPS positioning in the presence of ionospheric delays*, Ph.D. dissertation, Delft University of Technology.

ORMS (2005), GIPSY-OASIS Software Package, http://gipsy.jpl.nasa.gov/orms/goa/, Last accessed: September 2005.

Parkinson, B.W., and J.J. Spilker (eds.) (1995), *Global Positioning System: Theory and Applications, Volume 1*, American Institute for Aeronautics and Astronautics, Washington.

Reigber, C., H. Lühr, and P. Schwintzer (eds.) (2003), *First CHAMP Mission Results for Gravity, Magnetic and Atmospheric Studies*, Springer Verlag, Berlin.

Reigber, Ch., R. Bock, C. Förste, L. Grunwaldt, N. Jakowski, H. Lühr, P. Schwintzer, and C. Tilgner (1996), CHAMP Phase B - Executive Summary, *STR96/13*, GeoForschungsZentrum, Potsdam.

Reigber, Ch., G. Balmino, P. Schwintzer, R. Biancale, A. Bode, J.M Lemoine, R. König, S. Loyer, H. Neumayer, J.C. Marty, F. Barthelmes, F. Perosanz, and S.Y. Zhu (2002), A high quality global gravity field model from CHAMP GPS tracking data and accelerometry (EIGEN-1S), *Geophysical Research Letters*, *29*(14), DOI: 10.1029/2002GL015064.

Remondi, B.W. (1991), NGS second generation ASCII and binary orbit formats and associated interpolation studies, in *Proceedings of the twentieth general assembly, International Union of Geodesy and Geophysics*, Vienna, Austria, August 11–14 1991.

Rowlands, D., J.A. Marshall, J. McCarthy, D. Moore, D. Pavlis, S. Rowton, S. Luthcke, and L. Tsaoussi (1995), GEODYN II system description, Vols. 1-5, *Contractor report*, Hughes STX Corp., Greenbelt, MD.

Shampine, L.F., and M.K. Gordon (eds.) (1975), *Computer Solution of Ordinary Differential Equations*, Freeman and Comp., San Francisco.

Silvestrin, P., R. Bagge, M. Bonnedal, A. Carlström, J. Christensen, M. Hägg, T. Lindgren, and F. Zangerl (2000), Spaceborne GNSS radio occultation instrumentation for operational applications, in *Proceedings of ION-GPS-2000 Conference*, pp. 872–880, Salt Lake City.

SSTL (2003), SSTL SGR-10 Space GPS Receiver, fact sheet, Issue No. SSTL-9001-05, September 23 2003.

Svehla, D., and M. Rothacher (2003), CHAMP Double Difference Kinematic POD with Ambiguity Resolution, in *First CHAMP Mission Results for Gravity, Magnetic and Atmospheric Studies*, edited by C. Reigber *et al.*, Springer Verlag, Berlin.

Svehla, D., and M. Rothacher (2004*a*), CHAMP and GRACE in Tandem: POD with GPS and K-Band Measurements, presentation at the Joint CHAMP/GRACE Science Meeting, Potsdam, Germany, July 6–8 2004.

Svehla, D., and M. Rothacher (2004*b*), Two Years of CHAMP Kinematic Orbits for Geosciences, in *Geophysical Research Abstracts, European Geophysical Society*, Nice, France, ISSN:1029-7006.

Svehla, D., and M. Rothacher (2005), Kinematic positioning of LEO and GPS satellites and IGS stations on the ground, *Advances in Space Research*, DOI:10.1016/j.asr.2005.04.066.

Tapley, B.D., B.E. Schutz, and G.H. Borne (2004*a*), *Statistical Orbit Determination*, Elsevier Academic Press, Burlington, MA.

Tapley, B.D., S. Bettadpur, J.C. Ries, P.F. Thompson, and M. Watkins (2004*b*), GRACE measurements of mass variability in the Earth system, *Science*, *305*(5683), 503–505.

Teunissen, P.J.G. (1990), An integrity and quality control procedure for use in multi sensor integration, in *Proceedings of ION-GPS-1990*, pp. 513–522, Colorado Springs.

Teunissen, P.J.G. (1993), Least-squares estimation of the integer GPS ambiguities, in *Section IV Theory and Methodologym, IAG General Meeting, August 1993*, Beijing.

Teunissen, P.J.G. (1995), The least-squares ambiguitiy decorrelation adjustment: a method for fast GPS integer ambiguity estimation, *Journal of Geodesy*, *70*, 65–82.

Teunissen, P.J.G. (1997), On the GPS widelane and its decorrelating property, *Journal of Geodesy*, *71*, 577–587.

Teunissen, P.J.G. (1998), Success probability of integer GPS ambiguity rounding and bootstrapping, *Journal of Geodesy*, *72*, 606–612.

Teunissen, P.J.G. (1999), An optimality property of the integer least-squares estimator, *Journal of Geodesy*, *73*, 587–593.

Teunissen, P.J.G. (2000), *Adjustment theory, an introduction*, Serie on Mathematical Geodesy and Positioning, Delft University Press, Delft, The Netherlands.

Teunissen, P.J.G. (2001), *Dynamic data processing, recursive least-squares*, Serie on Mathematical Geodesy and Positioning, Delft University Press, Delft, The Netherlands.

Teunissen, P.J.G., and A. Kleusberg (1998), GPS Observation Equations and Positioning Concepts, in *GPS for Geodesy*, edited by P.J.G. Teunissen and A. Kleusberg, Springer Verlag, Heidelberg.

Teunissen, P.J.G., P. Joosten, and C.C.J.M. Tiberius (1999), Geometry-free Ambiguity Success Rates in Case of Partial Fixing, in *Proc. of National Technical Meeting and 19th Biennal Guidance Test Symposium, ION 1999*, pp. 201–207.

Tiberius, C., N. Jonker, and F. Kenselaar (1999), The Stochastics of GPS Observables, *GPS World*, pp. 49–54, February 1999.

Tiberius, C., T. Pany, B. Eissfeller, P. Joosten, and S. Verhagen (2002), 0.99999999 confidence ambiguity resolution with GPS and Galileo, *GPS Solutions*, *6*, 96–99.

Tiberius, C.C.J.M. (1998), *Recursive data processing for kinematic GPS surveying*, Ph.D. dissertation, Delft University of Technology.

UT/CSR (2001), UT/CSR Ocean Tide Model from Schwiderski and Interpolation/Extrapolation, ftp://ftp.csr.utexas.edu/pub/grav/OTIDES.CSRC, University of Texas, Center for Space Research, Issue 10, September 2001, Last accessed: September 2005.

UT/CSR (2003), GRACE Gravity Model GGM01, http://www.csr.utexas.edu/grace/gravity/ggm01/GGM01_Notes.pdf, University of Texas, Center for Space Research, Last accessed: September 2005.

Verhagen, S. (2004*a*), *The GNSS integer ambiguities: estimation and validation*, Ph.D. dissertation, Delft University of Technology.

Verhagen, S. (2004*b*), Integer ambiguity validation: an open problem?, *GPS Solutions*, *8*(1), 36–46, DOI: 10.1007/s10291-004-0087-5.

Ward, P. (1996), Satellite Signal Acquisition and Tracking, in *Understanding GPS, Principles and Applications*, edited by E.D. Kaplan, Archtec House, Boston.

Woo, K.T. (1991), Optimum semicodeless carrier-phase tracking for L2, *Navigation*, *47*(2), 82–99.

Wu, S.C., T.P. Yunck, and C.L. Thornton (1991), Reduced-dynamic technique for precise orbit determination of low Earth satellites, *Journal of Guidance Control and Dynamics*, *14*(1), 24–30.

Wübbena, G. (1985), Software developments for geodetic positioning with GPS using TI 4100 code and carrier measurements, in *Proceedings of the 1st Intenational Symposium on Precise positioning with the Global Positioning System*, pp. 403–412, Rockville, Maryland.

Xu, G. (2003), *GPS - Theory, Algorithms and Applications*, Springer Verlag, Heidelberg.

Yunck, T.P. (2003), Spaceborne GPS for POD and Earth Science, in *First CHAMP Mission Results for Gravity, Magnetic and Atmospheric Studies*, edited by C. Reigber *et al.*, Springer Verlag, Berlin.

Yunck, T.P., S.C. Wu, J.T. Wu, and C.L. Thornton (1990), Precise tracking of remote sensing satellites with the Global Positioning System, in *IEEE Transactions on Geoscience and Remote Sensing*, vol. 28, pp. 108–116.

Zumberge, J.F., and G. Gendt (2001), The demise of selective availability and implications for the International GPS Service, *Physics and Chemistry of the Earth*, *26A*(6–8), 637–644.

Curriculum Vitae

Remco Kroes was born in Voorburg, the Netherlands, on September 1, 1977. He attended secondary school (the Dutch VWO) from 1989 until 1995 at the Pallas College in Zoetermeer. After that he studied aerospace engineering at the Delft University of Technology. In April 2001 he graduated cum laude with a Master's thesis on software development for a Low Earth Orbit GPS receiver, for which he spent more than one year at Kayser-Threde GmbH in Munich, Germany.

After his graduation, in May 2001, he took on a PhD position at the Astrodynamics and Satellite Systems group where he also graduated, under the supervision of Prof. B.A.C. Ambrosius and Dr. P.N.A.M. Visser. During his PhD research he visited the DLR German Space Operations Center in Oberpfaffenhofen on two occasions, from August through December in 2002 and from July through December in 2004, to work together with his external supervisor Dr. O. Montenbruck. He furthermore spent another 6 months, from September 2003 through February 2004, at the NASA Jet Propulsion Laboratory in Pasadena, CA, as a visiting scientist. From January 2006 on, he will work at the A.T. Kearney Amsterdam office as a Business Analyst.